Interpretation of Gravity Data to Delineate the Geothermal Reservoir Extent and Assess the Geothermal Resource in the Municipality of Isa, Southern Kyushu, Japan

カルロス, オスミン, ポカサングレ, ジメネズ

https://doi.org/10.15017/2534415

出版情報：Kyushu University, 2019, 博士（工学）, 課程博士
バージョン：
権利関係：

九州大学

Interpretation of Gravity Data to Delineate the Geothermal Reservoir Extent and Assess the Geothermal Resource in the Municipality of Isa, Southern Kyushu, Japan

by

Carlos Osmín Pocasangre Jiménez

A Dissertation Submitted in Partial Fulfilment of the
Requirement for the Degree of

Doctor of Engineering

Supervised by

Professor Dr. Yasuhiro Fujimitsu

Laboratory of Geothermics
Department of Earth Resources Engineering
Graduate School of Engineering
Kyushu University, Japan

September, 2019

To everything, there is a season,
and time to every purpose under the heaven:

שְׁמַ֖ע יִשְׂרָאֵ֑ל יְהוָ֥ה אֱלֹהֵ֖ינוּ יְהוָ֥ה אֶחָֽד

(Shema Yisrael Adonai eloheinu Adonai ehad)

Hear, O Israel: The Lord our God, the Lord is one.
Love the Lord your God with all your heart,
and with all your soul and with all your strength.

(Deuteronomy 6:4-5)

Table of Contents

List of Figures

List of Tables

Acknowledgments

> *"It is very common to remember that someone*
> *owes us some gratitude, but it is more common*
> *not to think about who we owe our gratitude."*
>
> *Johann Wolfgang von Goethe (1749-1832)*

I thank God Almighty because he has given me the strength, wisdom, health, impetus to have studied the Doctoral Course in Geothermal Energy throughout these hard four years, and also to have completed this investigation.

To my parents, Esperanza Elba Jiménez and Osmín Pocasangre, for giving me life and guiding me on the right path, in addition for providing me with the necessary education which has made me the person I am.

To My wife, Kelly Meza, you will always be in my heart, for being with me in the final stage and during the hardest times. For sacrificing yourself for me, so that I can fulfill this dream and thus allowing me fight for you, for being by my side and helping me to move forward. For giving me your love, peace of mind, and making me so happy.

To my friend's and labmates whose supported me and encouraged me to achieve this dream that has come true. A special thank you to Isaac Kanda and Justus Maithya for your valuable inputs and proofreading that added a lot of value to my research.

To my Supervisors, Dr. Yasuhiro Fujimitsu and Dr. Jun Nishijima, whose wisely guided the development of this research; sometimes I felt discouraged to finish, but they always knew how to direct me. Their advice and endless discussions were beneficial to me and guided me towards completing my study within schedule. I

could not have imagined having better advisors and mentors for my Doctorate study in the Geothermics laboratory.

Besides my Supervisors, I would like to thank the rest of my thesis committee: Prof. Noriyuki Yasufuku (Department of Civil Engineering), Prof. Takeshi Tsuji (Department of Earth Resources Engineering), Assoc. Prof. Saeid Jalilinasrabady (Department of Earth Resources Engineering), and Assoc. Prof. Tatsuya Wakeyama (Global Energy Research Alliance Unit), for their insightful comments and encouragement, but also for the hard question which incentivized me to widen my research from various perspectives.

Finally, I want to thank the Authorities of the Faculty of Engineering and Architecture of the University of El Salvador, Kyushu University, Japan, and Japan International Cooperation Agency, JICA, for having reached an agreement and achieving an understanding for the benefit of each of the countries. This cooperation initiative has taken a step further in improving the quality of life of our population in El Salvador. Besides, a special mention to Sumitomo Metal Mining Co., Ltd. for having provided several papers and documents, which were very useful for fulfilling this dissertation.

This list of acknowledgments can only capture a small fraction of the people who supported my work. I send my deepest gratitude to all. Your contributions to this thesis were vital, but the inevitable mistakes in it are very much my own.

Abstract

The municipality of Isa is located in the southern part of Kyushu Island, and it is considered one of the wealthiest places in Japan because one of the most important gold mine, Hishikari mine, is found in this area. Additionally, there are many hydrothermal manifestations, e.g., Hishikari, Yunoo, Kawanami, and Kintaro hot springs, which can be exploited by the community as an electric power source. Until now, the geothermal resource has not been used for power generation purpose although Geological Survey of Japan had carried out some preliminary geothermal assessments, which show that the power potential density is between 10 and 20 kW/km^2. To calibrate the previous value, first, this study attempts to analyze and interpret the gravity data for delineating the geothermal reservoir boundary and the assessment of geothermal resource. Accordingly, the 2-D and 3-D gravity modeling in the current research were conducted. This modeling is an essential stage of the complete gravity analysis in the region, because the filtering gravity methods, i.e., Horizontal-Derivative and Tilt-Derivative, can quickly detect steep gradients and indicate the location of faults or geological boundaries, however, they cannot estimate geological structure depth and shape. For this purpose, an area of 10 × 10 km was selected and analyzed considering a Bouguer Density of 2.458 g/cm^3. The Bouguer Anomaly result shows a high value at the center, which extends 5.61 km^2 and could represent the inferred geothermal resource. In addition, integrating the NEDO reports, the probable geothermal resource might be 4.006 km^2. According to the Kagoshima geological map, volcanic and sedimentary rocks are the dominant type of rocks in this area. Cretaceous Shimanto Supergroup controls the fundamental structure of the deepest element. This arrangement is typically composed of sandstone, shale, acidic tuff with subordinate conglomerates, and their alterations, also Pliocene volcanic rocks and alluvial deposits. Similarly, Kakuto and Okuchi Basin, which are located at east and west respectively, control the region. The 2-D gravity modeling was carried out requiring a density contrast between the two assumed layers, i.e., the basement and the low-density deposit, and thus a value of 0.4 g/cm^3 was assigned. Likewise, the horizontal size of the cells was set at 100 m. The profile trending NW- SE shows a significant depression 400 m to 700 m deep located next to Hishikari hot spring, implying the hydrothermal fluids might be flowing up to the surface forming altered rocks and hot springs by using a possible geological fault. For a better understanding of the region, the authors also carried out 3-D gravity modeling. The result shows an area which has density values below 2.4 g/cm^3 and the zone NE-SW direction that starts at the Uonogoe area and ends at the Yamada area. Besides, a large anomaly located in the central area that has density values above 2.5 g/cm^3 is evident. This anomaly represents the hydrothermal alteration zone that hosts the propylitic altered rocks having precious minerals such as gold and silver. Between these evidenced zones, the location of the probable geothermal reserve which has an area of 4.006 km^2 could be inferred. Integrating past research reports carried out by NEDO, using the Volumetric method with the calculated geothermal reserve area, and a Monte Carlo simulation, which is coded on Python (GPPeval: A Python-based stochastic library for assessing geothermal power potential), a possible inference that the output is greater than or equal to 4.27 MWe and 121.9 kWe is 90 % for the inferred and probable geothermal resource respectively was estimated. After that, the preliminary power potential assessment density is 174.1 kWe/km^2 and 30.4 kWe/km^2 for the inferred and probable geothermal resource respectively for a period of 20 years. Nevertheless, this result needs to be corrected by further geoscientific investigations including inversion modeling of the Isa area because in this dissertation only gravity data was analyzed. The studies could be a precise gravity survey, magneto-telluric (MT), time-domain electromagnetic methods (TDEM), seismic logging, as well as numerical simulation, e.g., USGS Hydrotherm[1] and TOUGH2[2].

Keywords: Isa region, gravity data, propylitic alteration, hot springs, gravity modeling, geothermal power assessment, Monte Carlo, Bouguer Anomaly, Python.

---

[1] https://volcanoes.usgs.gov/software/hydrotherm/

[2] https://tough.lbl.gov/

Chapter 1

General Introduction

1.1 World installed capacity

Heat is a form of energy, and geothermal energy is literally the heat contained within the Earth that generates geological phenomena on a planetary scale. Geothermal energy is often used nowadays, however, there is a requirement to indicate that part the Earth's heat that could be recovered and exploited by humankind (Dickson & Fanelli, 2006).

There are renewable energy resources in different forms, such as wind, waves, ocean currents, tidal, hydro, solar, and geothermal which is the essence of this study. Geothermal resource has the highest net capacity factor or plant factor because it is not dependent on weather variations (floods and droughts), seasonal variations (rain, dry season), day and night. Geothermal energy is available all year (DiPippo, 2012).

A new world energy economy is emerging as fossil fuel prices rise, oil insecurity deepens, nuclear power plant accident recently in Japan and moreover concerns with pollution and climate instability cast a shadow over the future of coal. Consequently, the great energy transition from fossil fuels to renewable sources of energy is in progress. Geothermal energy provides one of such an important alternatives. The relationship of intense volcanic activity with the Earth's tectonic plate boundary has resulted in a world-wide distribution of geothermal energy which is an important alternative renewable energy source for the developed and developing countries as a whole (Harsh & Sukanta, 2007). Figure 1-1 shows the worldwide distribution of the geothermal fields which happened to be located near to the plate boundaries.

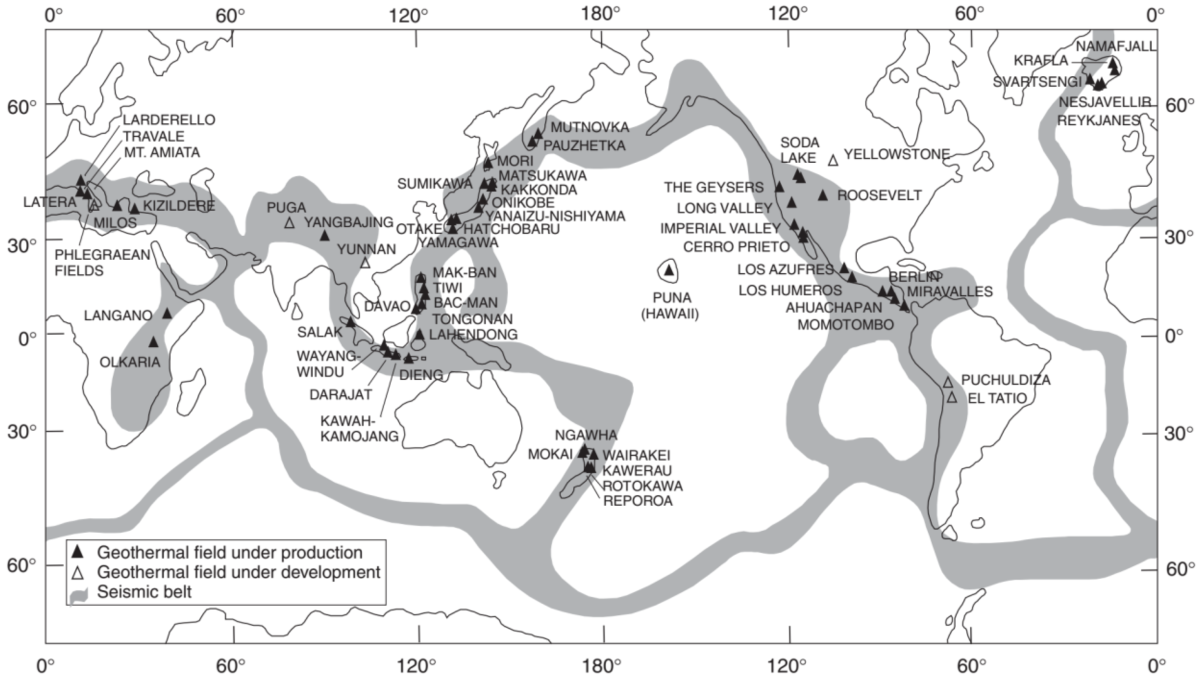

Figure 1-1. Worldwide distribution of geothermal fields. Under production and under development (Harsh & Sukanta, 2007).

Electricity generation from geothermal energy has a long history of more than one hundred years. In 1904, the first device was installed to produce electricity from geothermal steam by Prince Piero Ginori Conti in Landerello, Italy (Dickson & Fanelli, 2006). Later, the associated technology has progressed to the stage where the geothermal resources can now represent some extremely reliable and economic means to both electricity generation and non-electrical proposes as industrial processing, domestic heating and cooling. In the first stage, only developed countries used large scale geothermal energy like Italy, the United States, New Zealand and Japan, but later the potential developing countries developed their geothermal resources for electricity generation and non-electrical proposes. Since the first installment, 24 countries have already developed geothermal power plants using high temperature reservoirs (Dickson & Fanelli, 2006). Today, the world installed electricity capacity is more than 10 GWe, and annual energy produced is near 70,000 GWh from geothermal resources, that represent only a small percentages, about less than 0.5 % of world needs (GEA, 2015), see Table 1-1.

Table 1-1. Installed capacity and produced energy for 2010, 2015 and forecasting for 2020 (GEA, 2015).

Rank	Country	Installed in 2010 [MWe]	Installed in 2015 [MWe]	Forecast for 2020 [MWe]	Increase since 2010 [MWe]	Increase since 2010 [%]
1	USA	3098	3450	5600	352	11
2	Philippines	1904	1870	2500	-34	-2
3	Indonesia	1197	1340	3500	143	12
4	Mexico	958	1017	1400	59	6
5	New Zealand	762	1005	1350	243	32
6	Italy	843	916	1000	74	9
7	Iceland	575	665	1300	90	16
8	Kenya	202	594	1500	392	194
9	Japan	536	519	570	-16	-3
10	Turkey	91	397	600	306	336
11	Costa Rica	166	207	260	42	25
12	El Salvador	204	204	300	0	0
13	Nicaragua	88	159	200	72	82
14	Russia	82	82	190	0	0
15	Guatemala	52	52	140	0	0
16	Papua New Guinea	56	50	70	-6	-11
17	Portugal	29	29	60	0	0
18	China	24	27	100	3	12
19	Austria	1.4	1.2	6	-0.2	-14
20	Australia	0.1	1.1	20	1	
21	Thailand	0.3	0.3	1	0	0
	TOTAL	10868.8	12585.6	20667	1720.8	

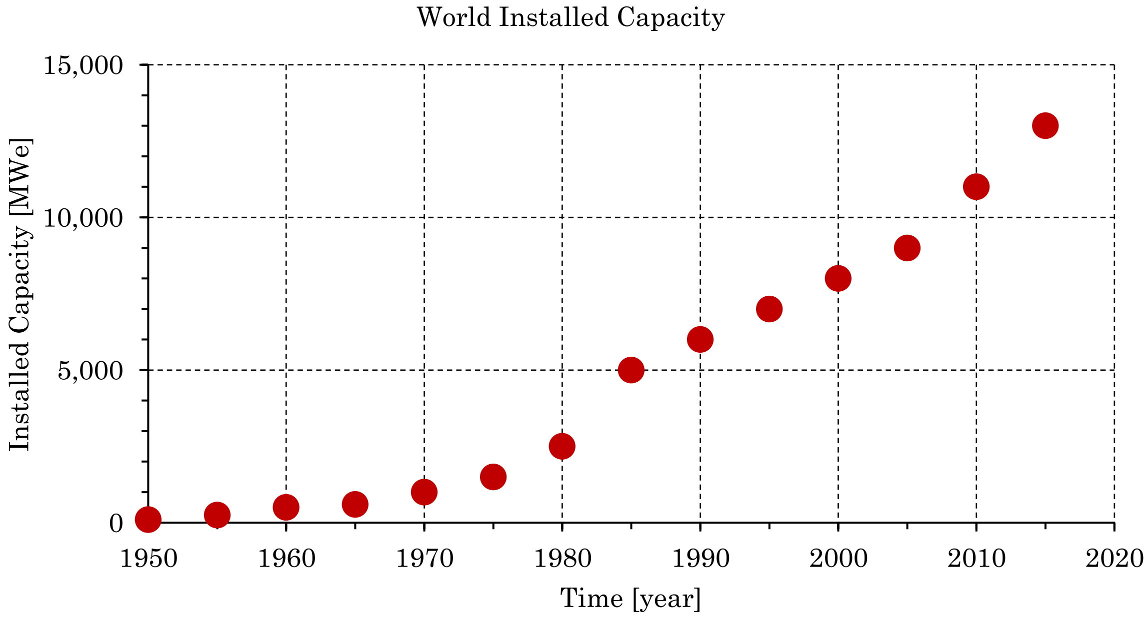

Figure 1-2. World Geothermal Installed capacity from 1950 up to 2015 (Bertani, 2015).

Every five years, a constant increase of about 1,000 MWe is observed from 1980 to 2015, see Figure 1-2. Otherwise, a bigger rise geothermal energy production was observed due to the effect of oil crisis in 1973 (Bertani, 2015). In recent years, the interest of renewable energy is increasing in general and particularly geothermal energy resources around the world as clean energy.

1.2 Geothermal energy status in Japan

The first experimental geothermal power generation in Japan was conducted by Dr. H. Tachikawa in 1925 (capacity: 1.12 kWe). The first and second geothermal power plants in Japan began their operation in 1966 and 1967 at Matsukawa and Otake, respectively. After the first oil shock in 1973, the Ministry of International Trade and Industry (presently the Ministry of Economy, Trade and Industry) initiated the Sunshine Project to promote new energy, including geothermal research and development (R&D). Four more power plants in the '70s (Onuma in 1974, Onikobe in 1975, Hatchobaru I 1977, and Kakkonda I in 1978), three plants in the '80s (Suginoi in 1981, Mori in 1982, Kirishima-Kokusai in 1984), and nine plants + two units opened in the '90s (Hatchobaru II in 1990, Takenoyu in 1991, Uenotai in 1994, Sumikawa, Kakkonda II, Yanaizu-Nishiyama, and Yamagawa in 1995, Ogiri and Takigami in 1996, Kuju in 1998, and Hachijo-jima in 1999). The location of the geothermal power plants is shown in Figure 1-5. This improvement led to hosting World Geothermal Congress that was held in Oita and Iwate, Japan in 2000. Development had been very slow since then, but surveys for new power plants were restarted recently (GRSJ, 2010).

1.2.1 Tasks in promoting developments

As an environment-friendly energy system, geothermal power generation should be promoted (Yasukawa et al., 2010). Figure 1-3a shows the Japan's future matrix plan for the year 2050 proposed by Institute for Sustainable Energy Policies (ISEP, 2015). Likewise, the Ministry of Economy, Trade and Industry (2015) has a prospect for the year 2030 (Figure 1-3b), which the basic principle for the power supply-demand structure is to lower dependency on nuclear power generation to the extent possible through energy efficiency and conservation and introducing renewable energy as well as improving the efficiency of thermal power generation.

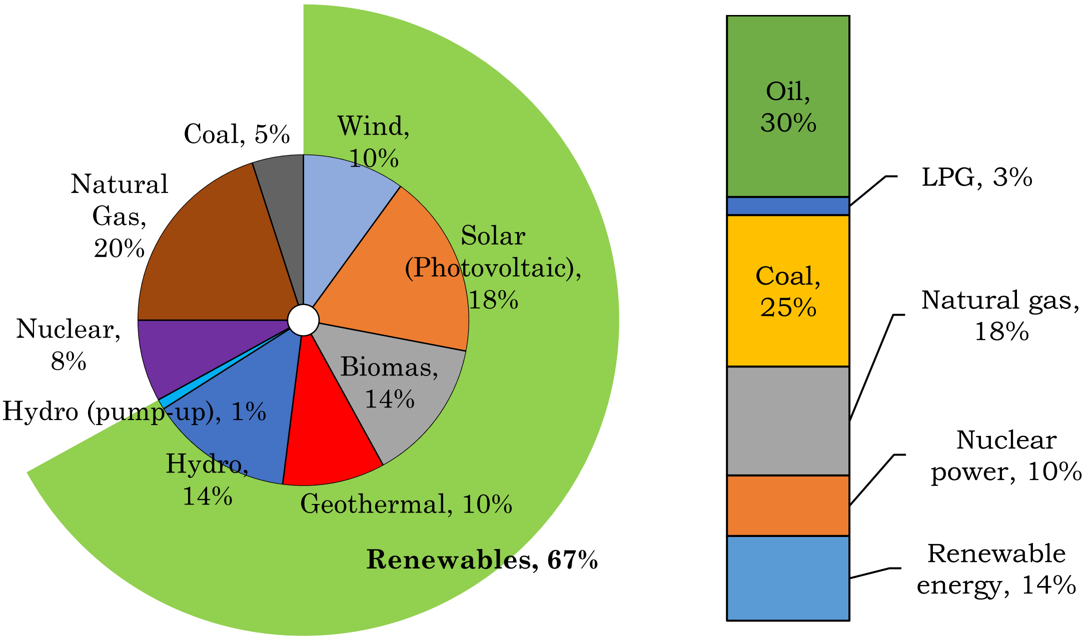

(a) FY2050

(b) FY2030

Figure 1-3. Power supply prospect in Japan: (a) for the year 2050 (ISEP, 2015), and (b) for the 2030 (METI, 2015).

One of the obstacles against geothermal development in Japan is the fact that most of the promising fields are located near or inside national parks or spa resorts. In geothermal development, careful steps must be taken to preserve the scenic beauty and hot spring resources for the local residents. Another obstacle is its high development costs, which is the nature of this type of energy. The industry, the academia and the government need to make more efforts to reduce the costs by improving technology and changing related regulations for bigger and wider utilization of geothermal energy.

1.2.2 Assessment of power generation close to hot springs areas

High temperature hot spring water (about 80-120°C) can be utilized for power generation by applying either the Kalina cycle system or the ORC cycle (Organic Rankine Cycle). Japan has about 28,000 hot springs that are naturally discharging or artificially drilled. An estimation suggests that, using 1,500 hotter wells and springs among them, as much as 723 MWe could be generated without additional drillings (GRSJ, 2010). Japan is one of the most tectonically active countries in the world, with nearly 200 volcanoes and tremendous geothermal energy resources.

Because of this tectonic activities, Japan has two periods before the earthquake in 2011 and later. The event changed the energy prospect of renewable energy. The geological phenomenon occurred in northern Japan in March 11, 2011 and in which two nuclear plants were damaged.

The geothermal development started in 1925, with an experimental unit, and the first independent power plant at Matsukawa, Iwate started in 1966 and followed by the Otake, Oita power station for commercial power generation in 1967 (Bertani, 2012). Estimated potential of geothermal power generation is 23.47 GWe from hydrothermal reservoirs to a depth of 3 km (GRSJ, 2010). Currently, 21 electric power units at 18 geothermal sites are in operation with a total capacity of 542 MWe, which amounts to about 2.3 % of the country demand. Most are located in Tohoku and Kyushu regions. Figure 1-4 shows the trend of the installed capacity and produced electricity from 1995 to 2015. Total geothermal power capacity in Japan has changed little since 1995. There are various geothermal plants installed in Japan. Table 1-2 and Figure 1-5 describe the geothermal power plants locations up to 2015 (AIST, 2014; JOGMEC, 2015; Yasukawa, 2017). Geothermal energy is expected to be an important role for zero-carbon era but main reason of such a low utilization rate is mainly due to its high initial cost and impact on ambient surrounding of power plant (Bertani, 2015). Figure 1-6 highlights the geothermal activity; a higher number indicates higher subsurface temperature expected, e.g., Hokkaido, Akita, Miyagi, Toyama, Oita, and Kagoshima.

In an early stage, a 46.199 MWe (installed capacity) geothermal power generation project at Wasabizawa, Akita, has been carried out by Electric Power Development Co., Ltd., Mitsubishi Materials Corporation, and Mitsubishi Gas Chemical Company, Inc., and expected to be commenced to operate in the middle of 2019 (JOGMEC, 2015). In addition, a new geothermal power plant went online in Japan newly. The plant in Iwate started operations already in late January 2019 with a rated output of 7.499 MWe in Matsuo-Hachimantai District (Richter, 2019).

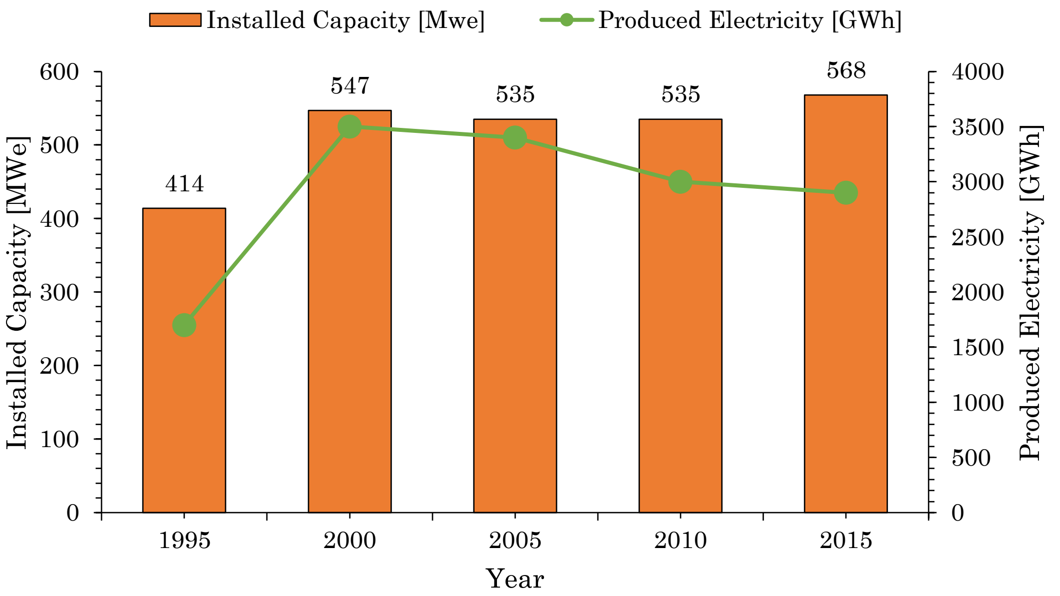

Figure 1-4. Installed capacity and produced electricity in Japan from 1995 (Bertani, 2015).

Table 1-2. Geothermal power plans installed in Japan until 2015 (JOGMEC, 2015).

Name	Installed Capacity [kWe]	Prefecture	Coordinates [°]	
			Latitude	Longitude
Onuma	9,500	Akita	39.98	140.78
Sumikawa	50,000	Akita	39.98	140.78
Uenotai	28,800	Akita	39.00	140.60
Yanaizu-Nishiyama	65,000	Fukushima	37.44	139.69
Mori	50,000	Hokkaido	42.13	140.46
Kakkonda	80,000	Iwate	39.83	140.86
Matsukawa	23,500	Iwate	39.93	140.93
Yamagawa	30,000	Kagoshima	31.19	130.61
Ogiri	30,000	Kagoshima	31.93	130.80
Kirishima Kokusai Hotel	100	Kagoshima	32.09	131.11
Kumamoto	2,000	Kumamoto	33.12	131.07
Takenoyu	50	Kumamoto	32.92	130.85
Onikobe	12,500	Miyagi	38.81	140.71
Otake	12,500	Oita	33.12	131.19
Suginoi	3,000	Oita	33.28	131.48
Takigami	28,000	Oita	33.21	131.27
Hatchobaru	112,000	Oita	33.11	131.19
Kuju	2,000	Oita	33.11	131.22
Hachijojima	3,300	Tokyo	33.11	139.78
TOTAL INSTALLED	542,250			

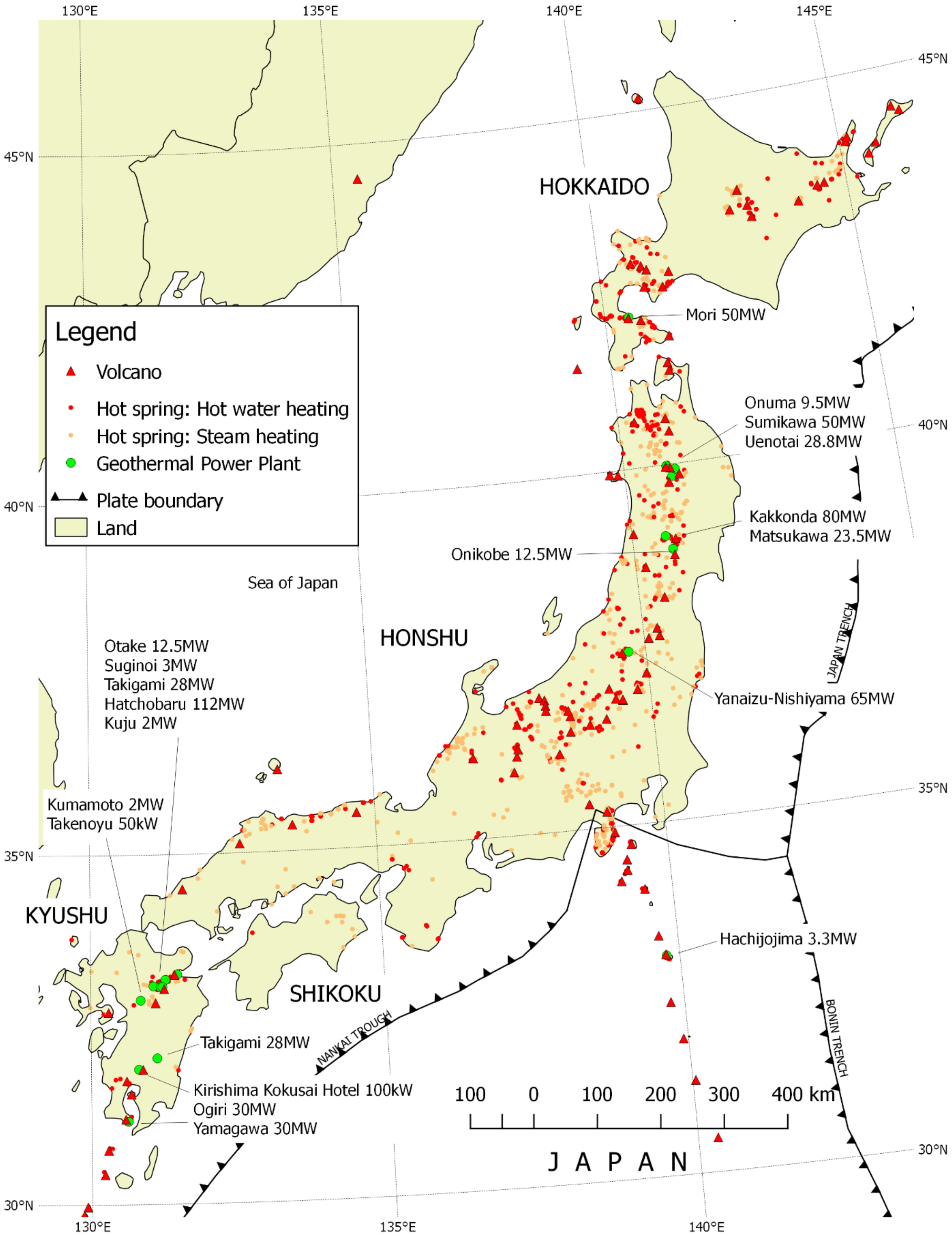

Figure 1-5. Hydrothermal manifestations and Geothermal Power Plants location in Japan (JOGMEC, 2015).

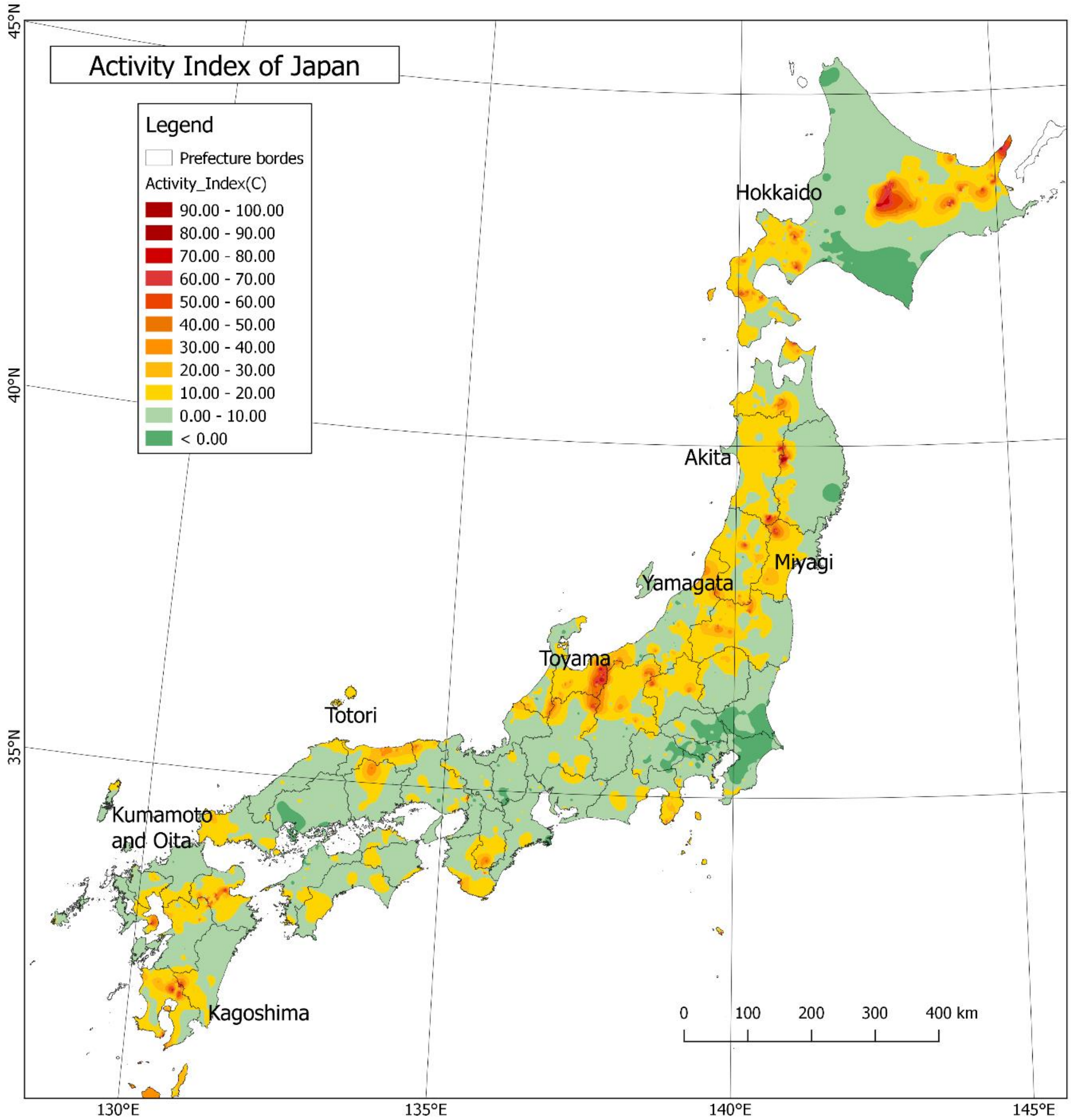

Figure 1-6. Activity index. Higher number indicates higher subsurface temperature expected (AIST, 2009).

Despite the large geothermal potential of the country, estimated about 20 GWe, the present total capacity of geothermal power plant is still around 540 MWe, almost unchanged for more than a decade. After the nuclear accident in March 2011, the government restarted an incentive scheme for geothermal development and mitigation of constraints in national parks, encouraging new geothermal exploration activities by private sectors as well as quick installation of small binary systems.

1.2.3 Prospects of geothermal power generation in Japan

The geothermal potential areas in Japan are:

- Approximately 80 % of energy potential of geothermal is located within the areas of Natural Parks stipulated by Natural Park Activity.
- Consequently, geothermal power plants have been developed mainly outside of these natural parks.
- However, after the accident at nuclear power plant in Fukushima, Ministry of Environment issued the guideline which lifted restrictions on drilling at National Parks.

The Table 1-3 shows the category of Natural Parks and the Geothermal Power Potential, also Figure 1-7 shows the geothermal potential in Natural Parks indicating that 80 % is located in those areas (JOGMEC, 2015). The classification of zones in National Parks is shown in Table 1-4 (Sawamura, 1995).

Table 1-3. Geothermal Potential located in National parks (JOGMEC, 2015).

Category of Natural Parks	Potential [MWe]			Potential location
Special Protection Zone	7,000	29.9%	78.6%	Within Natural Parks
Special Zone I	2,600	11.1%		
Special Zone II and III	7,700	32.9%		
Ordinary Zone	1,100	4.7%		
Outside of Natural Parks	5,000	21.4%	21.4%	Outside of Natural Parks
TOTAL	23,400	100%	100%	

Despite the geothermal energy virtues like stable generation, high power factor, not dependent on climatic aspects or day and night, not important source of CO_2 and the relationship between energy generated and inverted to obtain is high, the production of electricity from geothermal energy has been stagnant in Japan. Some reasons for geothermal energy being stagnant are:

1. Potentially energy fields are in national parks or nature reserves, nearly 80 % of geothermal energy is in these places.

2. Geothermal fields are private therefore the owners are negative to the operation and construction of wells and plants on their land by environmental degradation and the quality of hydrothermal manifestations may vary because people use the hot water in hotels, spa, cooking, etc.
3. Nowadays, building a new geothermal power plant is expensive (the initial capital cost is high) if it is compared to a thermal power plant using oil, as a result, the investors are uninterested.

After 2011, several regulations have been enacted to improve the geothermal energy situation, as the geothermal exploitation is not an enemy to national parks. The only problem is to convince the people, who are the owners, to accept the exploitation of hot springs because it will bring many benefits for their homes and cities. There are some initiatives reported by the Energy Agency Ministry of Economy of Japan METI, which gives funding for well drilling. In addition, the energy sales rate is fixed for the next 15 years (FIT[3]), power plant lower than 15 MWe is ¥40/kWh + tax and higher than or equal to 15 MWe of ¥26/kWh + tax.

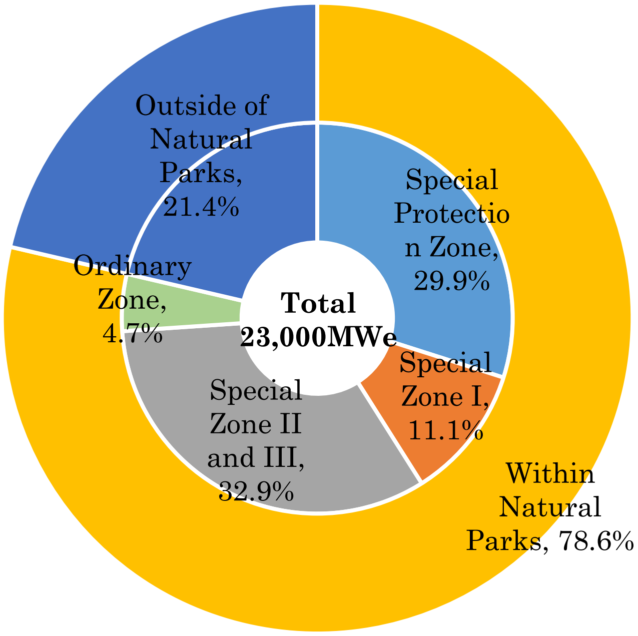

Figure 1-7. Geothermal Potential percent located in Natural parks (JOGMEC, 2015).

---

[3] The feed-in tariff FIT system, was launched in Japan in 2012, with the aim of encouraging the introduction of renewable energy equipment.

Table 1-4. Classification of Zones in National Parks (Sawamura, 1995).

Classification	Description	Prohibitions
Special protection zone	Areas required to maintain scenic beauty strictly	Erection of structures is prohibited in principle.
Class I special zone	Areas ranking after special protection zone and required to maintain scenic beauty somewhat strictly and required to conserve the present scenic beauty as far as possible	Erection of structures is prohibited in principle. Namely, the regulation of special protection zone applies correspondingly to this zone.
Class II special zone	Areas required to adjust the activities of agriculture, forestry and fisheries as far as possible	Establishment of facilities required for the daily life of local people such as housing and other facilities relating to normal activities of agriculture, forestry and fisheries, is permitted in principle. Also establishment of resting facilities, villas, cottages and the like which are not obstructive to scenic beauty will be allowed.
Class III special zone	Areas other than Class I special zone and Class II special zone, and where there is little fear of affecting the maintenance of scenic beauty in principle even though ordinary activities of agriculture, forestry and fisheries are performed.	Regarding erection of structures, regulation is almost same as in the Class II special zone. With regard to forestry, clear cut is allowed.
Marine park zone	Areas where seascapes are excellent due to abundant marine animals and plants	Same regulation as in the special protection zone.
Ordinary zone	Areas surrounding special zone of scenic beauty and they are required to conserve scenery as buffer zones in a sense. In many cases there are some settlements and farms. Sea area is also included in this zone.	As for large buildings which may obstruct scenic beauty, administrative action can be taken for the purpose of conservation.

1.3 Utilization of hot springs in Japan

1.3.1 History of utilization of hot springs

It is said that Japanese people like to take baths most in the world, and in fact this has already became an indispensable custom for Japanese people. But the forerunner of the custom is concerned with hot springs (Komagata et al., 1970). All Japanese people feel the necessity of taking a bath in cold or hot water during the most humid summer season in Japan, and this is not only important for people in the modern age but probably was so in ancient times. Japan abounds with fresh springs and rivers. In addition, many hot springs are widely distributed in the volcanic zones cross-wise. It is not strange that ancients were in the habit of taking baths from earliest times. Weather on one hand, and the land containing many fresh springs, rivers and hot springs on the other hand, would have stimulated them into doing this. The origin of body purification dates far back to times when people washed and purified their bodies to remove dirt and filth. Japanese people were in the habit of purifying themselves in fresh springs and mountain streams to pray for divine protection whenever anything serious occurred, and this has been done not only in cold water but also hot water or natural hot springs. The reason why ancient people attached great importance to hot springs is not merely that they carried out purification there. There is a more important factor, that is, the constituents contained in hot springs have a miraculous godlike effects upon human sicknesses.

A particular example in which hot springs had great importance attached to them as medical hot water is Tamazukuri Hot Spring, Shimane Prefecture, where there are records stating that as far back in 729 men and women, young and old, swarmed together and formed a city for the curing of their sicknesses. As spring resources known “god hot water” or “medical hot water” are widely distributed, similar facts have been transmitted since olden times in various places such as Yumura in Shimane Prefecture, Arima in Hyogo Prefecture, Dogo in Ehime Prefecture, Hakone in Kanagawa Prefecture, etc. In view of many shrines which are built around hot springs, it is observed the importance for ancient Japanese people attached to hot springs.

Blessed with many springs, rivers, mountains streams and hot springs, the custom of the Japanese people to take baths was closely related to religious belief, and the effect of taking baths led to the discovery of the hot springs remedy. Thus the custom of taking baths eventually developed up to a utilization of hot springs without precedent in the world.
Attempts have been made to utilize hot springs practically for industrial purposes other than that of taking baths. Such facilities, on a fairly large scale, are, for example, those in Shimokamo, Shizuoka Prefecture, Beppu City, Oita Prefecture, Ibusuki City and Kagoshima City, Kagoshima Prefecture, etc. In Shimokamo hot water of about 90 °C used to be drawn into the glasshouse through s steel pipe, dating from 1916. This was for cultivating melons, flowers, etc., and in 1919 the glasshouse was extended up to 825 m^2. Today the facilities not only cultivate garden plants but also hatch eggs, raise poultry, breed alligators, eels, carp, etc., as well as being used in brewing, distillation, or other processing. As of the end of 1968, in the case of Beppu City which is famous for its hot springs, 54 of the 2,132 spring sources were utilized for horticulture, and 254 for tourism and other commitments. In Ibusuki City, as of the end of 1967, 106 of 571 spring sources were utilized for horticulture, six for fish breeding and one for brewing and distillation, according to local government (Komagata et al., 1970).

The utilization of geothermal energy for power generation has recently become the most important field of geothermal utilization. Industries have been awaiting geothermal power generation because of the abundant hot volcanic springs in Japan. The first attempt was made by H. Tachikawa, who carried out a trial power generation of 1.12 kWe at Beppu in 1925. But the enthusiasm for and interest in power generation by geothermal energy have gradually fade away, mainly due to the rapid progress of hydraulic and thermal power plants thereafter. During the postwar years of electric power shortage, some trial geothermal power generations were attempted on small scale at Atagawa, Shizuoka Prefecture, Narugo, Miyagi Prefecture, Beppu, Oita Prefecture, and Hakone, Kanagawa Prefecture. The

Beppu plant was operating at an output of 30 kWe in 1956. An upward trend of enthusiasm for geothermal power generation reappeared. As a result, in 1966, a 20 MWe plant and in 1967 a 13 MWe plant were constructed at Matsukawa and Otake respectively. Further, exploitation is being actively carried out at present at Hachimantai in Akita Prefecture, Onikobe in Miyagi Prefecture, and Hatchobaru in Oita Prefecture.

1.3.2 Distribution of hot springs in Japan

Situated in the circular Pacific Oceanic Zone, Japan is one of the leading volcanic countries in the world with 196 Quaternary volcanoes distributed nationwide. It can be easily seen that there is a close relationship between the distribution of volcanoes and hot springs. Figure 1-5 shows the distribution of hot springs supplying hot water at temperatures above 90 °C. Many of these hot springs are issuing from volcanic ejecta of Quaternary age and from the Tertiary formations constituting the bases of volcanoes, and some others are issuing directly from Tertiary, Mesozoic, Paleozoic formations or granites. Table 1-5 shows the number of hot springs in each Prefectures above 90 ℃ in Kyushu, Shikoku, Honshu, and Hokkaido regions. There are many hot springs in prefectures distributed along Quaternary volcanic zone, and very few are distributed in prefectures situated outside the volcanic zone along the Pacific coastline. For example, the Kochi, Kagawa, and Tokushima Prefectures on Shikoku Island are little blessed with hot springs. The same thing can be said of Saitama, Shiga and Nara Prefectures. Also many of the hot springs with temperatures below 40 °C are distributed in Ibaraki, Chiba, Aichi, Mie, Kyoto, Osaka, and Okayama Prefectures and Tokyo, all of which are situated outside the volcanic zone. As an exceptional instance, a comparatively large number of hot springs are distributed in the Wakayama Prefecture situated outside the volcanic zone, and this indicates that hot springs are distributed also in the surrounding areas of quartz porphyry and granite porphyry crossing Tertiary and Paleozoic formations (Komagata et al., 1970).

Table 1-5. Number of Hot Springs in each Prefecture above 90 °C[4] (Komagata et al., 1970).

Prefecture	Number of hot springs	Prefecture	Number of hot springs
Aichi	62	Miyagi	401
Akita	214	Miyazaki	105
Aomori	420	Nagano	1144
Chiba	48	Niigata	202
Ehime	117	Nara	21
Fukui	108	Nagasaki	173
Fukuoka	217	Oita	4540
Fukushima	400	Okayama	56
Gifu	318	Osaka	39
Gunma	225	Saitama	3
Hiroshima	38	Saga	100
Hokkaido	969	Shiga	16
Hyogo	210	Shimane	145
Ibaraki	41	Shizuoka	2216
Ishikawa	108	Tochigi	402
Iwate	170	Tokyo	64
Kanagawa	576	Tottori	314
Kagawa	4	Tokushima	1
Kochi	10	Toyama	112
Kagoshima	1463	Wakayama	344
Kumamoto	677	Yamagata	303
Kyoto	63	Yamaguchi	238
Mie	52	Yamanashi	207

1.3.3 Financial support and costs on geothermal activities

Geothermal projects get double financial incentives from government (drilling support and FIT). The Energy Agency of METI supports domestic geothermal businesses by:

a) Financial support

1. Drilling: Government's support for geothermal drilling was to be abolished in FY2011. But after the big earthquake, government increased the budget from US$15 to US$90 million in FY2012. It covers up to 50 % of exploration well drilling cost.

---

[4] The gray background highlights the Prefectures whose number of hot spring rise above 500 locations.

2. Public acceptance PA: New budget covers 100 % of public acceptance activities by private sectors.

b) Feed in Tariff (FIT): FIT law for geothermal power generation was enacted and price fixed in 2012 (METI, 2016).
   1. 15 MWe or bigger: ¥26/kWh + tax for 15 years.
   2. Smaller than 15 MWe: ¥40/kWh + tax for 15 years.

1.3.4 Example of utilization of low enthalpy geothermal fluid

The GERD[5] and AIST[6] have been conducting a demonstration project in Niigata sponsored by MoE[7] using a Kalina cycle which enables power generation by about 85 °C water. Many hot springs owners have interest in such small plants for their own use (Yasukawa, 2017).

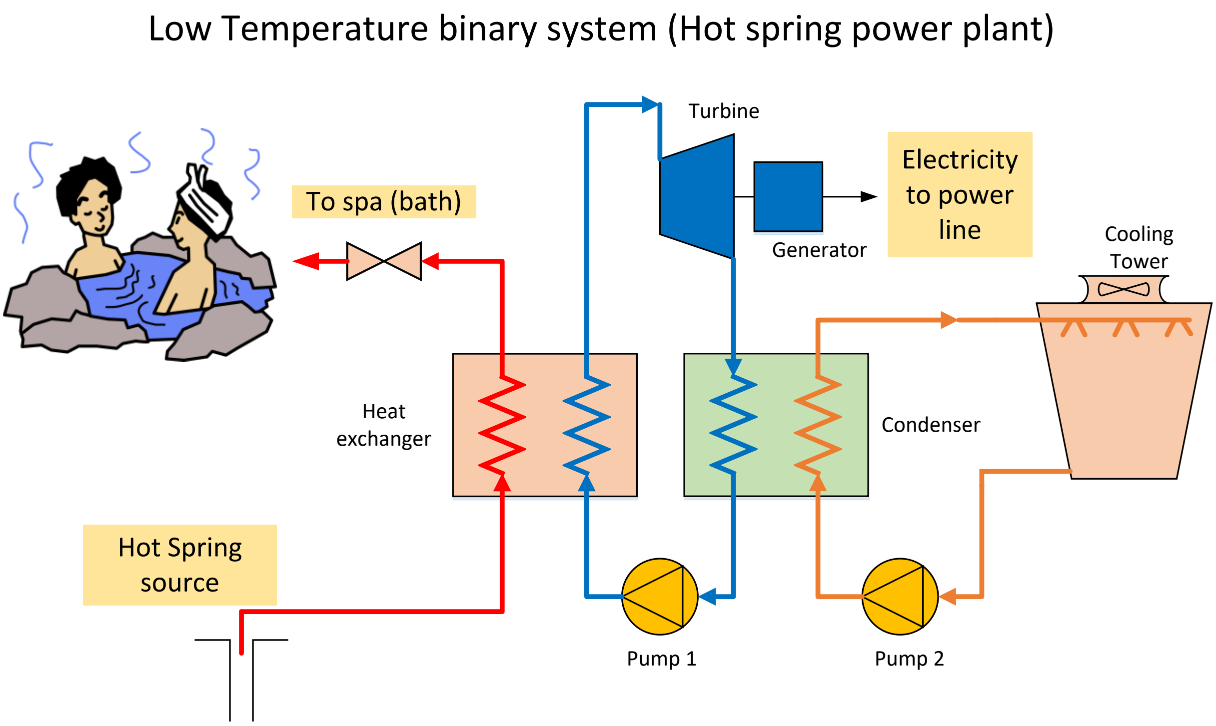
Low Temperature binary system (Hot spring power plant)

Figure 1-8. Hot spring power plant project at Niigata (Yasukawa, 2017).

---

[5] GERD: Geothermal Energy Research & Development Co., Ltd.

[6] AIST: National Institute of Advanced Industrial Science and Technology

[7] MoE: Ministry of Environment

The use of hydrothermal manifestations can be achieved without affecting the owners of hotels or resorts, or landowners, by using small geothermal power plant lower than 500 kWe (AIST, 2014). This can be achieved by the use of a heat exchanger in parallel with the low enthalpy hydrothermal fluid, e.g., a hot spring with a temperature of 80 °C could generate around 10 kWe. It depends on the power plant size. The electricity generated could be sold by connecting it to the electrical network as distributed generation or be used by hotel or nearby community (Figure 1-8). The Ministry of the Environment (2013) suggested in its reports that the exploitation of low-temperature resources (hot springs) might be carry out outside the National Parks and without additional excavations.

1.4 Geothermal activities in the Municipality of Isa

Isa City (伊佐市) in Kagoshima Prefecture, is located in the inland area at the northern end of Kagoshima Prefecture, approximately 75 km north of Kagoshima City. On the north side is Kumamoto Prefecture, and on the east side is Miyazaki Prefecture, and the Sendai River runs through the city. The central urban area forms part of the Okuchi Basin, with an elevation of about 180 m. Located in the southern part of Kyushu Island, it is considered one of the wealthiest places in Japan. The zone is blessed as a result of the hydrothermal manifestations and volcanic activity as they have been depositing several minerals into geologic structures or fractures, e.g., gold. Because of the mineral depositions in this area, one of the most important gold mines is found here, Hishikari mine.

Inside the municipality, and at East, a study area for this dissertation was selected. Figure 1-9 shows the topographic map. One of the biggest collapsed caldera, Kakuto Basin, is located in the municipality of Ebino, which has numerous hydrothermal manifestations. Also, an ancient caldera called Okuchi Basin is localized in the city of Isa, which has several hot springs as well. However, it is difficult to recognize Okuchi Basin due to the fact that the caldera has been covered by river sediments and volcanic deposits that were put down by Yamada River, Sendai River, and ancient volcanic eruptions. The study area of this dissertation is located in the center of the geothermal activity map, as shown in Figure 1-10. The area is mainly built of sedimentary rocks and volcanic rocks (Quaternary, Q1).

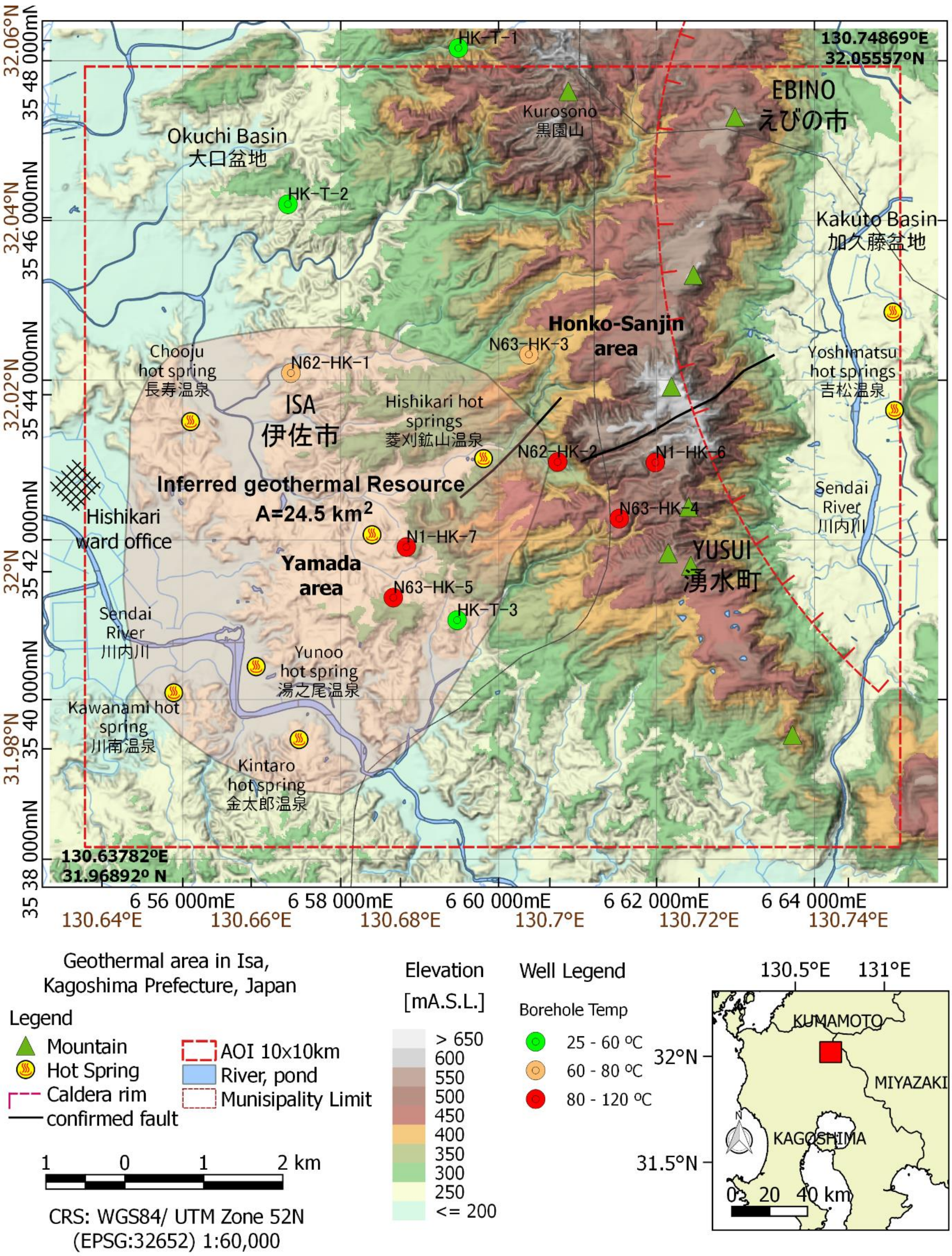

Figure 1-9. Topographic map of Isa, Kagoshima Prefecture. Center point is located at 32.01° N, 130.69° E, and 220 m A.S.L. The marked red area is the inferred geothermal resource of 24.5 km² (Geospatial Information Authority of Japan, 2017).

For this dissertation, the study was focused on hydrothermal manifestations of low enthalpy fluids in Isa area, i.e., Hishikari, Yunoo, Kawanami, and Kintaro hot springs. The temperature at the surface and in the borehole is around 60 °C and 120 °C respectively (Sakaguchi et al., 2000). The geothermal resources are abundant in the southern part of Kyushu region. Figure 1-10 show the geothermal resources associated with geological structures. The map, with coordinates 31.25º - 32.25º N and 130º - 131.25º E, was compiled at 1:500,000 scale to understand the outline of geothermal resources areas and geothermal heat resources based on geology, gravity (Bouguer anomaly) and geochemistry (Sakaguchi et al., 2000). Hot springs were classified by water temperature, pH, chemical concentration, fumaroles areas, and geothermal exploration wells by maximum temperature and well condition.

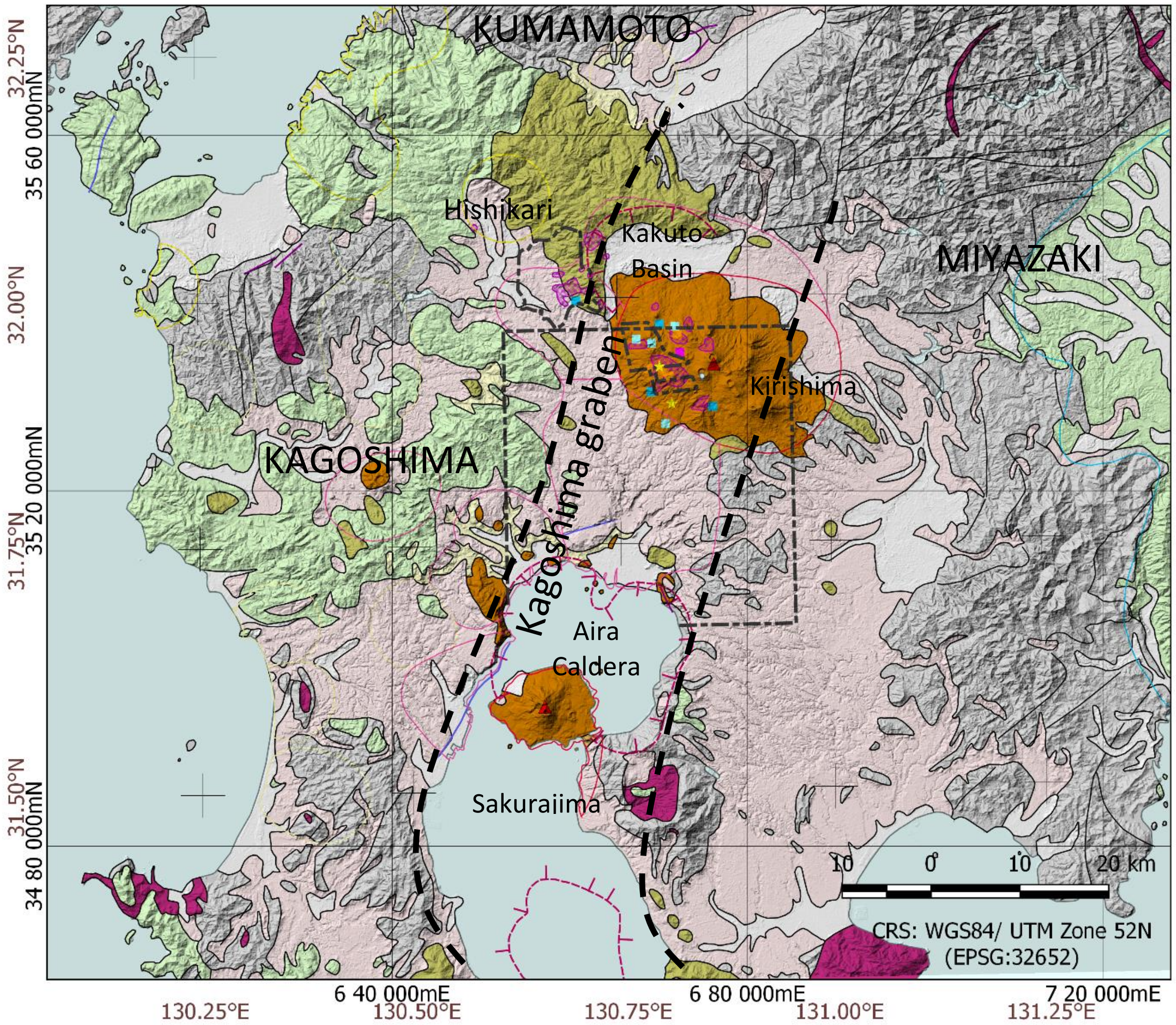

(a)

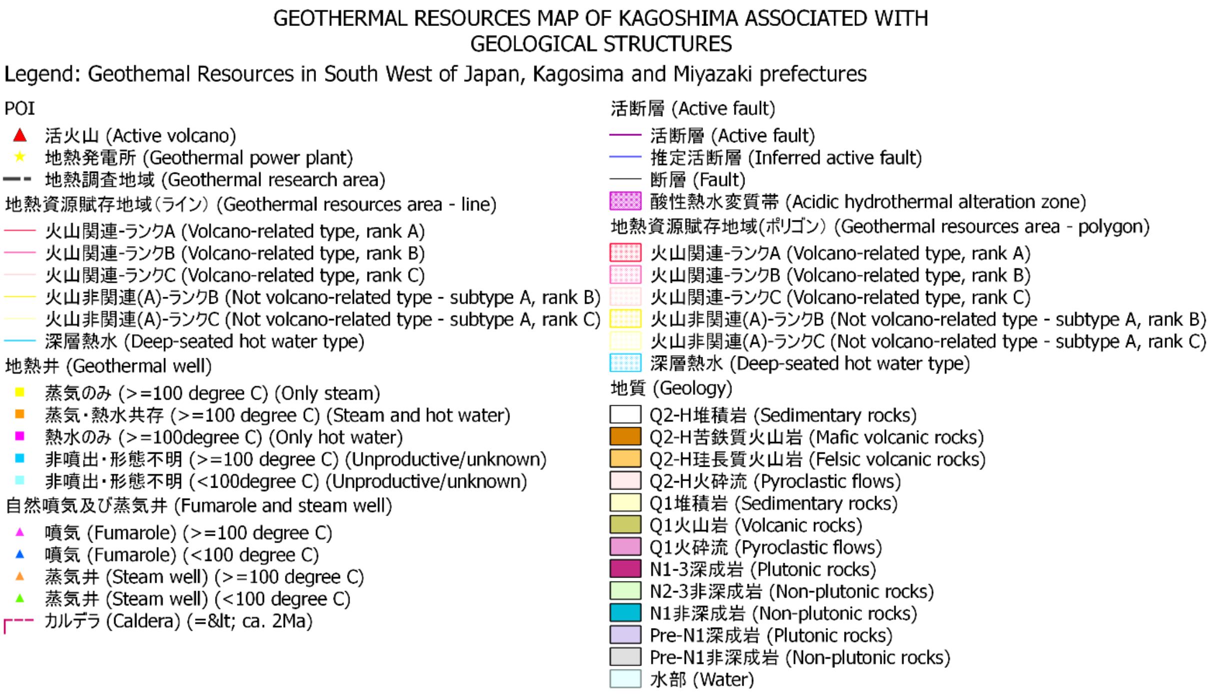

(b)

Figure 1-10. Geothermal resources in South West of Japan, Kagoshima and Miyazaki prefectures. (a) Regional geological Map of Kagoshima and Miyazaki prefectures showing relief, faults, geology, calderas, volcanoes, geothermal resources in black dotted region; (b) legend (Sakaguchi et al., 2000).

Geothermal resource areas are categorized into the following 4 types: 1. geothermal resource area related to Quaternary volcanoes; 2. Deep-seated hot water resource areas; 3. geothermal resource area not related to Quaternary volcanoes which is located back-arc side or within 20 km fore-arc side of volcanic front (type A); 4. Geothermal resources area not related to Quaternary volcanoes which is located more than 20 km fore-arc side of the volcanic front (type B). Geothermal resource areas, except deep-seated hot water resources areas, are classified into 3 ranks based on their geothermal potential as shown: Rank A has production of geothermal fluid of >= 90 °C, or with both of surface manifestation of >=70 °C and acidic alteration zone larger than 1 km^2; Rank B has geochemical geothermometers temperatures of >=150 °C among non-rank A areas and Rank C includes areas where either the data is missing or less power potential is available. The criteria of classification of geothermal resources areas is shown in Figure 1-11. According to this criteria, in the Kyushu area, 19 Quaternary volcano-related geothermal resources (rank A: 11, B: 7, C: 11), 26 geothermal resources areas not related to Quaternary volcanoes (rank B: 7, C: 19), 3 deep-seated hot water resources areas are delineated. This shows that Kyushu area has a high potential.

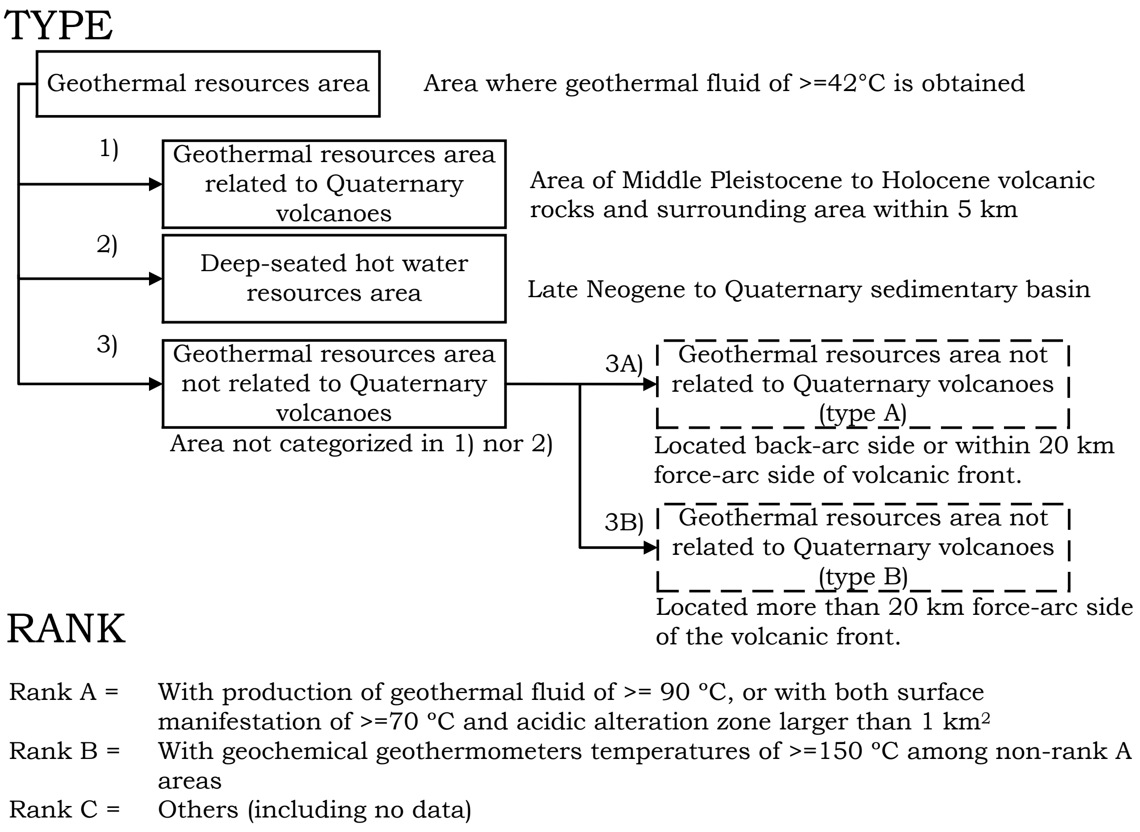

Rank A = With production of geothermal fluid of >= 90 °C, or with both surface manifestation of >=70 °C and acidic alteration zone larger than 1 km^2
Rank B = With geochemical geothermometers temperatures of >=150 °C among non-rank A areas
Rank C = Others (including no data)

Figure 1-11. Criteria of classification of geothermal resource types and ranks (Sakaguchi et al., 2000).

1.4.1 Renewable energy introduction potential map

Until now, the geothermal resource in the hot spring close to the Municipality of Isa has not been used for power generation purpose although Geological Survey of Japan had carried out several preliminary geothermal assessments. They show that the power potential density is around 20 kW/km^2 in the Municipality of Yusui in the Abundance map (Ministry of the Environment Government of Japan, 2011), see Figure 1-12. This map shows the Renewable Energy Introduction Potential Map and Basic Zoning Information, Fiscal Year 2011. The Map data are being published as reference material to aid in discussions towards the introduction of renewable energy. In this project, the abundance, the introduction potential, and the potential under different scenarios are being calculated for Photovoltaic power (PV) (nondomestic), wind power, small and medium-scale hydropower, and geothermal power (including hot spring power generation), and PV in individual buildings (including households). However, for this dissertation, the geothermal abundance map was chosen.

For calibrating the previous value obtained by Government of Japan, the abundance[8] of 20 kW/km^2, the gravity data for figuring out geothermal reservoir border and the geothermal power potential assessment was analyzed. For this purpose, an area of 10 × 10 km, whose coordinates are 31.97°N to 32.06°N and 130.64°E to 130.75°E, was selected. After having processed gravity data, an evaluation of geothermal potential was carried out, i.e., the amount of thermal energy that can be transformed from a geothermal reservoir and used economically by people for different kinds of applications such as either power generation or direct uses. For estimating the geothermal resource in new areas, there are various methods around the world that have been developed for calculating the available energy. When a geothermal exploration starts, sometimes the provided data are either limited or missing. Consequently, a simple technique called volumetric method is used for estimating the energy available from the geothermal reservoir (Muffler & Cataldi, 1978). The calculation of the geothermal energy stored in a volume is based on reservoir characteristics and carried out by using the stochastic Monte Carlo simulation, see Chapter 2.

---

[8] Abundance: This is the amount of energy resources which can be theoretically estimated by the feasible area for system installation, mean wind velocity, river discharge or other relevant factors. It excludes the amount of energy which is difficult to utilize based on the current technological level and does not take various limiting factors (such as land inclination, legal restrictions, land use, distance from a residential area and others) into consideration (Simiyu, 2010).

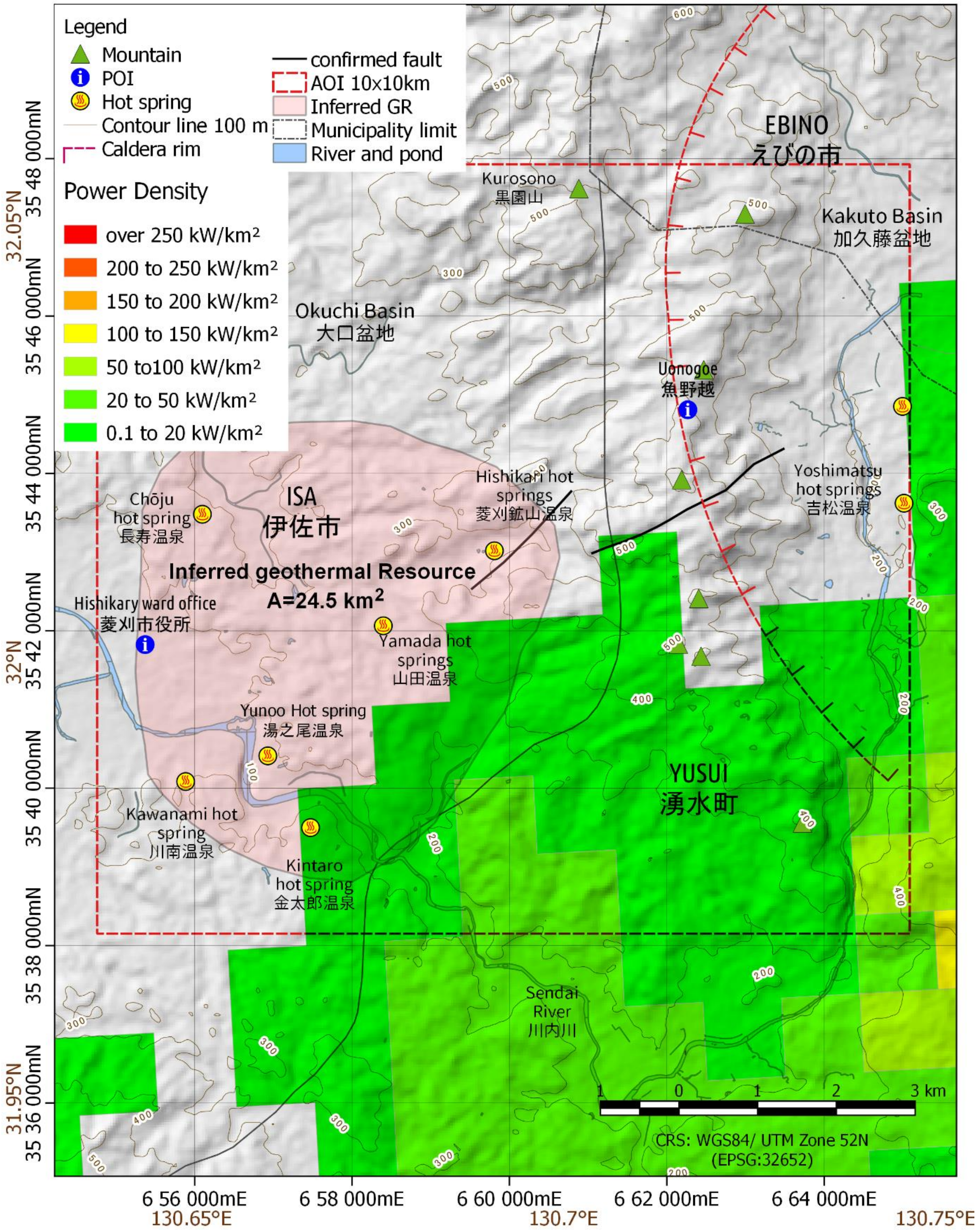

Figure 1-12. Geothermal abundance map of the municipalities of Isa, Ebino, and Yusui (Ministry of the Environment Government of Japan, 2011).

1.5 Outline of the dissertation

This dissertation consists of 6 chapters, which describe the research carried out on the integration of previous studies conducted by NEDO, geology, geophysical studies for delineating the geothermal reservoir extent and assess the geothermal resource in the municipality of Isa, southern Kyushu, Japan.

Chapter 1: This chapter describes the general background of the study as well as the global information about the geothermal status in Japan also documented studies that were conducted by preceding researchers. The history and current state of geothermal development in Japan, with a particular focus on low enthalpy fluid, i.e., hot springs, are given. Likewise, a description of the purpose, the plan and the structure of the thesis are also made.

Chapter 2: This chapter presents a Python-based stochastic library for assessing geothermal power potential using the volumetric method in a liquid-dominated reservoir. The specific aims of this study are to use the volumetric method, "heat in place," to estimate electrical energy production ability from a geothermal liquid-dominated reservoir, and to build a Python-based stochastic library with useful methods for running such simulations. Although licensed software is available, the open-source programming language Python for this task was selected.

Chapter 3: This chapter elaborates on the various characteristics that define the Isa geothermal area. The chapter starts with a detailed review of the geology and structural setting of the area from both local and regional viewpoints. Then a description of the methodology used in the study of lineaments from Landsat images is presented. The description includes the extraction of lineaments from the satellite image, their analysis, and interpretation, and presentation of the results using rose diagrams.

The last section reviews the previous studies carried out by NEDO such as well loggings and conceptual model of the eastern part of the municipality of Isa, Kagoshima.

Chapter 4: This chapter describes the gravity study. A comprehensive review of the gravity method both theory and applications is given then a description of gravity data and how the survey was conducted in the field. Besides, some corrections were done in the field, which were later applied to the data are also discussed. Bouguer anomaly map is presented and the methods used to estimate the Bouguer density are discussed. The 3-D inversion technique used is described, and the resulting model is presented and discussed in the last part of this chapter.

Chapter 5: This chapter brings together the results from previous chapters and assessment of the geothermal power potential in the eastern part of Isa, Kagoshima which is one of the main aims of this dissertation. Two scenarios are simulated: inferred and probable geothermal resource.

Chapter 6: This chapter presents the conclusions of the study, and this includes a summary of the conclusions made in preceding chapters.

Chapter 2

Geothermal Power Assessment Tool

2.1 Outline of geothermal power assessment

The geothermal resource assessment is an estimation of the amount of thermal energy ("heat in place") that can be transformed from a geothermal reservoir for economic use in a variety of applications. However, such data are often limited or difficult to obtain during initial geothermal exploration, and a basic assessment method is needed (Saibi, 2018). In the 1970s, researchers at the United States Geological Survey (USGS) developed a method to quantify geothermal resource estimate uncertainties associated with a given hydrothermal area. This simple technique, called the USGS volumetric "heat in place" method, (Cataldi et al., 1978; Garg & Combs, 2015; Muffler & Cataldi, 1978), is therefore also employed in the present study.

The primary purpose of this study are to use the volumetric method to estimate electrical energy production ability from a geothermal liquid-dominated reservoir, and to develop a Python-based stochastic library, called the Geothermal Power Potential Evaluation (GPPeval), with suitable methods for running the simulations. The calculation of geothermal energy stored in a given volume is based on a range of reservoir parameters, carried out using a stochastic Monte Carlo simulation, and applies a probabilistic method for evaluating reserves or resources and the associated estimation uncertainties. Given the geological complexity and heterogeneity of most geothermal reservoirs, this method is more appropriate than the usual deterministic approach that assumes a single value for each parameter to represent the entire reservoir. Instead of assigning a fixed value to a reservoir parameter, numbers within a range of the distribution model are randomly selected and drawn for each calculation cycle over a thousand iterations (Sarmiento & Steingrímsson, 2011; Wakeyama & Ehara, 2009).

Licensed software is available for carrying out this simulation, however the algorithm was programmed using the open-source programming language Python (Python Software Foundation, 2016). Python is a platform-independent, full-feature, object-oriented programming language that has grown in popularity over the last decade due to its versatility and explicit syntax. Furthermore, Python is widely used throughout the geophysics community (Krieger & Peacock, 2014). The stochastic library developed in this study is distributed as it is without charge. The Numpy and Scipy modules allow handling of large numerical data sets, and the built-in file handling and flexibility of string manipulations allow for confident processing of files in arbitrary formats, e.g., CSV. In addition to the standard modules within Python, GPPeval utilizes the Matplotlib module for graphical visualization, the Beautifultable module for easily printing tabular data in a visually appealing ASCII format to a terminal, and the Mcerp module for performing non-order specific error propagation[9] or uncertainty analysis (Lee, 2014).

The GPPeval is structured as three essential objects including a geothermal power plant module, a Monte Carlo simulation module, and a tools module. The geothermal power plant abstraction or object contains the necessary properties and methods employed in the Monte Carlo simulation. The Monte Carlo abstraction or object has the essential properties and methods for running the Monte Carlo

---

[9] The "Non-order specific error propagation" means that Mcerp does not make any assumptions or approximations in how uncertainty in the input variables is converted into uncertainty in the output functions. This Python library, being a random sampling based approach, takes the result as it is. It is possible to perform various statistical analyses on the data to find out information about the resultant distribution (Lee, 2014).

simulation and obtaining the geothermal power potential. The tools abstraction or object has the necessary properties and methods for showing the simulation results. Hot spring data from the municipality of Nombre de Jesus, El Salvador (Campos, 1988) was used to demonstrate how the GPPeval can be used to assess geothermal power potential.

2.2 Thermal energy calculations

A typical geothermal reservoir and the required model parameters are shown in Figure 2-1. Two distinct purposes are identified in this task:

1. To address the question of geothermal energy, the study area should have specific attributes including a geothermal aquifer or reservoir, cap rock, bedrock, either a fractured-rock environment or permeable rock, convection-driven movement of hot fluid, and a heat source such as an intrusive magma chamber, fossilized dike, or relevant regional activity (DiPippo, 2012).
2. To assess reservoir power generation, the geothermal area should have defined parameters such as the reservoir area (A), thickness (h), and temperature (Tr), the abandon temperature (Ta), average rock porosity (ϕ), rock specific heat (Cr) and density (ρr), fluid specific heat (Cf) and density (ρf), a heat recovery factor (RF), electrical conversion efficiency (ηe), plant net capacity factor (PF), and lifespan (t).

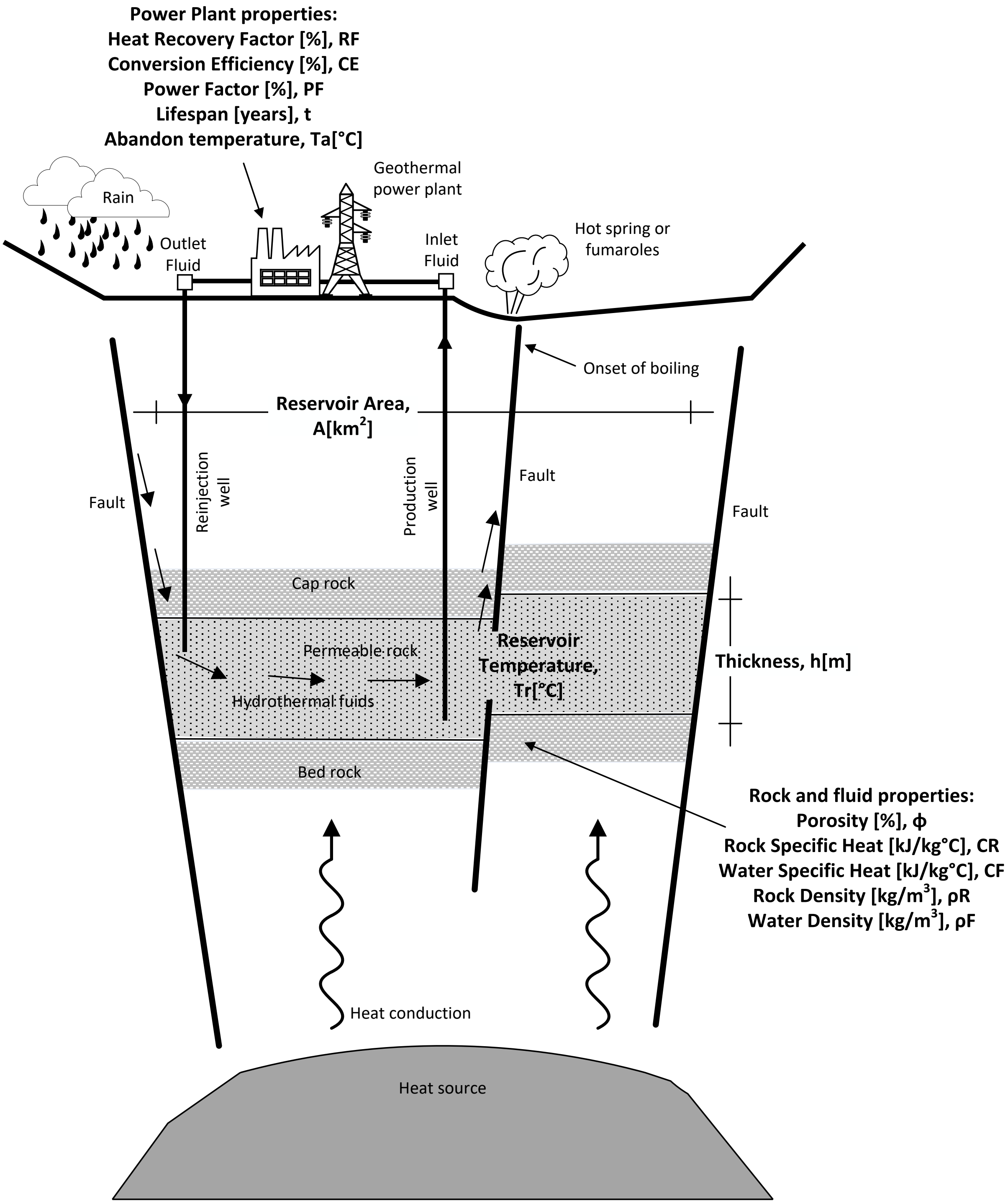

Figure 2-1. A typical hydrothermal geothermal reservoir with parameters required for assessing the geothermal power potential (DiPippo, 2012).

The volumetric method refers to the calculation of thermal energy in a rock and fluid that can be extracted based on a specified reservoir volume, temperature, and reference or final temperature. This approach is based on methods applied by the

USGS to assess geothermal resources of the United States (Muffler & Guffanti, 1978). The final or reference temperature using those methods is based on an ambient temperature of 15 °C (or a condensing temperature of 40 °C) that was commonly used in previous USGS applications. However, the use of an arbitrary low reference temperature (i.e., ambient or condensing temperature) often results in an overestimate of the available thermal energy. The abandon temperature, or temperature below which a geothermal reservoir is not producible, should therefore be used as the reference temperature to obtain realistic estimates of the available thermal energy.

Abandon temperature values depend on the power cycle. Thus, for a flash-type power plant, the lower limit of the abandon temperature is given by the saturation temperature, which corresponds to the separator pressure, and the so-called pinch point temperature for a binary power plant. Under appropriate space heating conditions, the abandon temperature is usually 30–40 °C, while a typical high-temperature geothermal resource has an average reservoir temperature of 250 °C. Assuming that a single flash cycle has a separator pressure of 5 bar (saturation temperature of 151.831 °C), the abandon temperature would be equal to 151.831 °C. Similarly, a conventional low-enthalpy fluid with an average temperature of 150 °C is used to heat a secondary working fluid (isobutane) with an assumed pressure of 20 bar and saturation temperature of 100.36 °C. Therefore, considering a temperature difference of 5 °C at the pinch point, the abandon temperature is 105.36 °C (Garg & Combs, 2015; National Institute of Standards and Technology NIST, 2017). The equation used in thermal energy calculations for a liquid-dominated reservoir is as follows:

$$Q_T = Q_r + Q_w \tag{2-1}$$

where

$$Q_r = A \cdot h \cdot [\rho_r \cdot C_r \cdot (1 - \phi) \cdot (T_r - T_a)] \tag{2-2}$$

and

$$Q_w = A \cdot h \cdot [\rho_w \cdot C_w \cdot \phi \cdot (T_r - T_a)] \tag{2-3}$$

with parameters defined in Table 2-1.

Table 2-1. Thermodynamic parameters of the reservoir required for calculating total thermal energy.

Symbol	Description	Units
Q_T	Total thermal energy	kJ
Q_r	Heat in rock	kJ
Q_w	Heat in fluid	kJ
A	Area of the reservoir	km^2
h	The average thickness of the reservoir	m
ρ_r	Rock density	kg/m^3
ρ_w	Fluid density	kg/m^3
C_r	Rock specific heat at reservoir conditions	kJ/kg-°C
C_w	Fluid specific heat at reservoir conditions	kJ/kg-°C
ϕ	Porosity	%
T_r	The average temperature of the reservoir	°C
T_a	Final or abandon temperature	°C

2.3 Power plant sizing

Solutions to Equation 2-1 provide only the total thermal energy in the reservoir, while the size of the power plant that could be supported by the resource is calculated by combining the previous into Equation 2-5 as follows:

$$P = \frac{Q_T \cdot RF \cdot C_e}{PF \cdot t} \tag{2-4}$$

$$P = C\left[A \cdot h \cdot (T_r - T_a) \cdot [\rho_r C_r (1-\phi) + \rho_w C_w \phi] \cdot \frac{RF \cdot C_e}{PF \cdot t}\right] \tag{2-5}$$

Parameters are listed in Table 2-2.

Table 2-2. Power plant sizing parameters.

Symbol	Description	Units
P	Geothermal power potential	We
Q_T	Total thermal energy	kJ
RF	Recovery factor	%
C_e	Conversion efficiency	%
PF	Plant net capacity factor or plant factor	%
t	Lifespan (economic life)	years
C	Unite conversion factor	31.6880878

2.3.1 Power plant parameters

The recovery factor refers to the fraction of heat stored in the reservoir that could be extracted to the surface (Zaher, 2011; Sanyal & Sarmiento, 2005). This term depends on the reservoir fraction that is considered permeable and the efficiency by which heat can be withdrawn from such permeable channels. The conversion efficiency accounts for the conversion of recoverable thermal energy into electricity. The economic life of the project is the period required for the full investment to be recovered within its target internal rate of return, which is usually 25 to 30 years. The plant factor refers to the plant availability throughout the year, taking into consideration the period when the plant is scheduled for maintenance, or whether the plant is operated as a base-load or peaking plant. A good performance for many geothermal plants around the world is about 90 to 97 % (DiPippo, 2015; Zarrouk & Moon, 2014).

2.4 Guidelines for determination of the reservoir parameters

Recent developments in the geothermal industry require the establishment of guidelines on how reserve estimation is to be approached and reported in corporate annual reporting or financial statements. Sanyal and Sarmiento (2005) proposed three categories for reserve classification: proven, probable and possible, all of which are more appropriately estimated using volumetric methods. The need for an industry standard is now imminent to create consistency in declarations of estimated reserves for a given project.

Sanyal and Sarmiento (2005) used results from Monte Carlo simulations to determine the proven, probable, and possible or inferred reserves based on the resulting percentiles obtained from the cumulative frequency distribution. The percentile value indicates the probability that the reserve quantities to be recovered will equal or exceed estimates. The following terms are defined in this study such that the proven reserves will have a 90 % probability, and 5 % for the proven + probable + possible reserves or the maximum reserves. Histograms of geothermal reserves calculated by Monte Carlo simulations are often highly skewed; hence, the proven + probable is better represented by the most likely value instead of the 50th percentile (Aravena et al., 2016; SPE, 2001).

2.4.1 Resource

A resource is the energy that can be economically and legally extracted at some specified time in the future (less than 100 years).

2.4.2 Reserves

Reserves are defined as quantities of thermal energy that are anticipated to be recovered from known reservoirs from a given start date. A reserve is a part of the resource, which can be presently economically and legally extracted, and is known and characterized by drilling or geochemical, geophysical, and geological evidence (Muffler & Cataldi, 1978).

2.4.3 Proven

Proven reserves are quantities of heat that can be estimated within reasonable certainty, based on geoscientific and engineering data, to be commercially recoverable from known reservoirs under current economic conditions, operating methods, and government regulation. The definition by Clotworthy et al. (2006) gives a more specific description, stating that a proven reserve is the portion of the resource sampled by wells that demonstrate reservoir conditions and significant fluid deliverability from the reservoir.

2.4.4 Probable

Probable reserves are unproven reserves that are most likely recoverable, but less reliably defined than proven reserves, with sufficient reservoir temperature indicators from either nearby wells or geothermometers along natural surface discharges that characterize the resource temperature and chemistry.

2.4.5 Possible or inferred

Possible reserves have a slightly smaller recovery chance than probable reserves, but have a sound basis from surface exploration (e.g., springs, fumaroles, resistivity anomalies) to declare that a reservoir may exist. Clotworthy et al. (2006) adopted inferred resources from what could cover possible reserves.

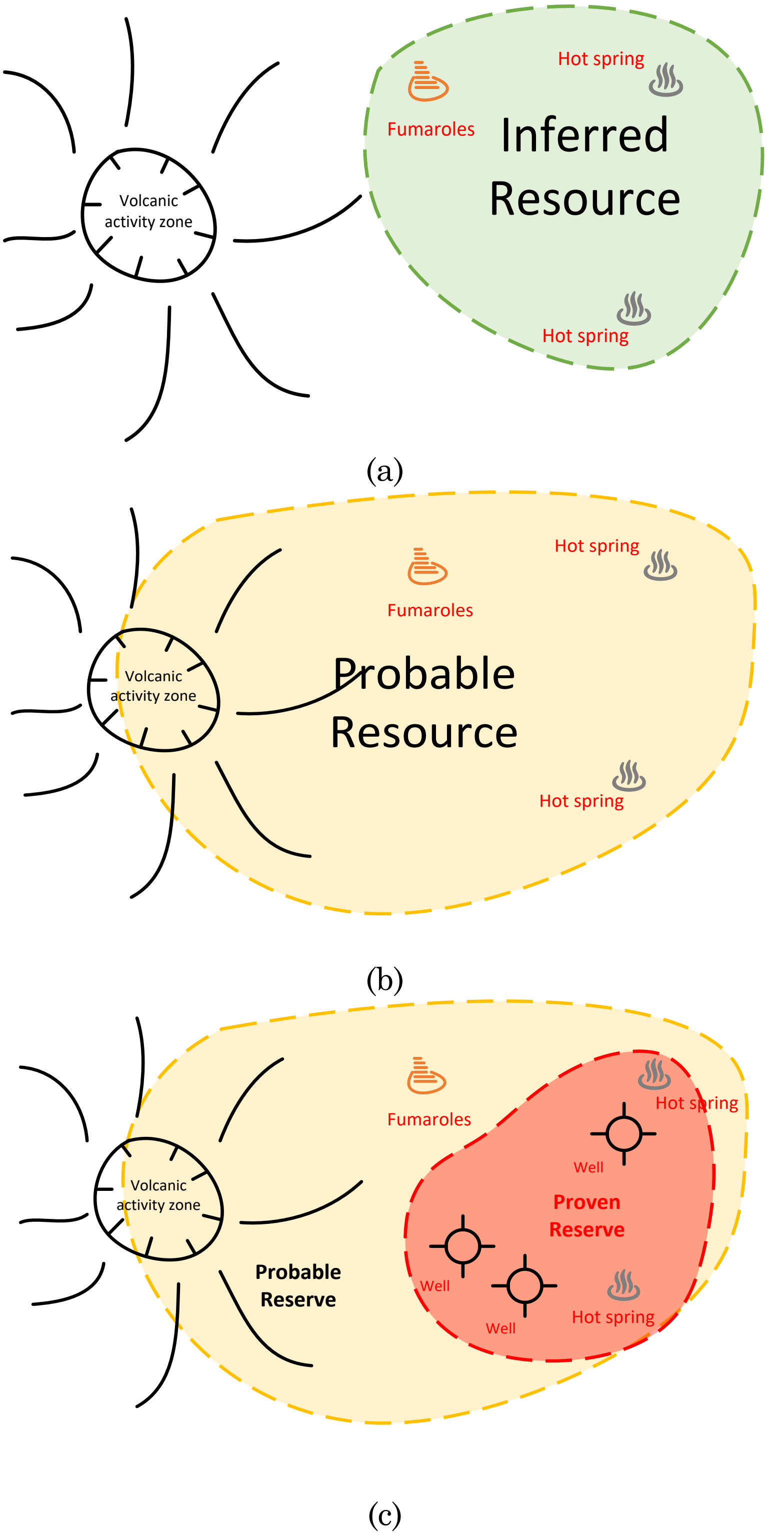

Figure 2-2. Applied examples of proposed classifications. a) Inferred resource based on surface thermal features and geological setting. b) Probable resource based on (a) with additional comprehensive geophysical information that better defines the depth and extent of the geothermal system. c) Proven and probable reserves based on (b) after the drilling of successful exploration wells (Clotworthy et al., 2006).

Proven, probable, and possible reserves are illustrated in Figure 2-2 with hypothetical examples shown during various developmental stages of a hydrothermal system generated by volcanic activity. Such examples might be used in areas where hydrothermal manifestations are due to regional activity (e.g., faults movement, lithologic pressure) instead of volcanic activity. Because the assessment of geothermal power potential following the volumetric method is based on the heat stored in the rocks and fluid exchange, it does not take into account the heat source type.

2.5 Uncertainty distribution

The accuracy of methods used in geothermal reserve estimation depends on the type, amount, and quality of geoscientific and engineering data, which are also dependent on the stage of development and maturity of a given field. Accuracy generally increases once the geothermal field is drilled and more wells and production data become available (Sarmiento & Steingrímsson, 2011). Volumetric estimation is most commonly applied during the early stages of field development to justify drilling and commitment for a specified power plant size. This method is therefore better applied during the early stage than numerical modeling, which requires a significant number of wells and production history to be considered reliable. Assessment of geothermal reserves can be performed during the maturity of the field for use in annual company reporting and to enhance corporate assets for valuation. Some degree of caution and conservatism must be used, however, because of the limited data and uncertainty on the assumptions of reservoir parameters. This approach, which accounts for the risk factor in decision-making, can be quantified with reasonable approximation using a Monte Carlo simulation. Unlike a deterministic approach, where a single value is used representing the best guess, a probabilistic method of calculation is considered to account for the uncertainty on several variables in a geothermal reserve estimation. A Monte Carlo simulation calculates the frequency distribution of the random variables, which are dependent on the number of times a value is extracted from the uncertainty models of the input parameters following frequency distribution previously defined, e.g., Normal, Triangular, Log-Normal, Uniform (Sarmiento & Steingrímsson, 2011; Wakeyama & Ehara, 2009).

As seen in Table 2-3, a range of possible reserve estimates can be obtained depending on the assumptions included in the calculation. In general, the proven, probable, and possible or inferred reserves refer to the minimum, most likely or intermediate, and maximum estimates, respectively.

The reservoir area and thickness are usually assigned by triangular distribution because these parameters are obtained directly from drilling and well measurements. A reasonable approximation of the resource area can be made based on temperature contours and electrical resistivity measurements, while permeability, porosity, and temperature values are directly measured from the well.

Other parameters such as fluid densities and specific heat are dependent on the reservoir and abandon temperatures.

The recovery factor depends on the permeability structure (e.g., fracture vs. matrix, permeability anisotropy, faulting), production and injection well depths and patterns, and the thermal (i.e., heat and fluid recharge from depth) and hydraulic boundary conditions (i.e., recharge/discharge along the ground surface and assumed lateral boundaries of the geothermal reservoir). Because many reservoir properties that affect the thermal recovery factor are likely to be poorly known until the reservoir has been producing for several years, specification of the thermal recovery factor for a given reservoir is often a matter of conjecture. Some estimations of the thermal recovery factor based on both theoretical grounds and data from operating hydrothermal fields suggest that the appropriate range for fracture-dominated geothermal reservoirs is 0.08–0.20 and for sediment-hosted reservoirs the suggested range is slightly higher: 0.10–0.25 (Williams, 2014).

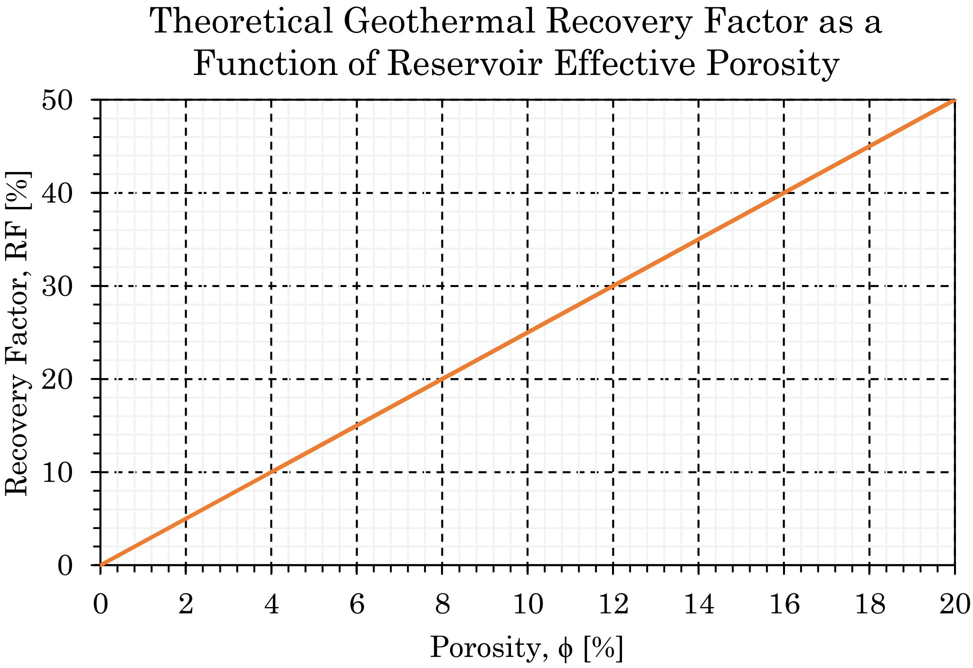

Figure 2-3. A possible variation of geothermal recovery factor as a function of effective porosity for reservoirs producing by a mechanism of intergranular flow. RF is taken to be 50 % for an ideally permeable reservoir in which total porosity is equal to the effective porosity. In the ideal situation, porosity can be assumed to be 20 % (Nathenson, 1975).

The porosity in a geothermal reservoir which produces water or a water-steam mixture through intergranular flow[10] could be reasonably assumed that is a direct linear function of the recovery factor, at least as a conservative approximation (Bodvarsson, 1974; Nathenson, 1975). Figure 2-3 shows the correlation between the recovery factor (RF) and porosity (ϕ) assuming the geothermal recovery factor to be independent of reservoir temperature under an intergranular flow model. This curve is likely to be conservative, with the true relation falling more towards

---

[10] The intergranular flow of water assumes an ideal, porous reservoir where the fluid has a very large contact area with the rock mass and the thermal contact can, therefore, be almost perfect, and the exchange of heat between the rock and the fluid can be practically complete (Muffler & Cataldi, 1978).

the upper left of Figure 2-3, also does not take into account loss in enthalpy as the fluid flows to the earth's surface. For an ideally permeable geothermal reservoir, the RF theoretically could be as much as 50 %, and the effective porosity can be assumed to be 20 %. This assumption points up the immediate need of field and model studies of recoverability of the thermal energy from hot-water systems (Muffler & Cataldi, 1978).

The conversion efficiency is the amount of geothermal energy that can be converted into electricity. This parameter is limited by the second law of thermodynamics, and it is also a function of the optimum plant design and the efficiency of different components, i.e., the conversion efficiency depends on each geothermal power plant. For example, the First Law thermal efficiency of a real thermal water engine based on a single flash steam cycle at 40 °C is less than ~12 % for temperatures between 150 and 250 °C and liquid-dominated reservoirs (Bodvarsson, 1974; Zarrouk & Moon, 2014). In the case of low-enthalpy applications, the conversion efficiency for several operating Organic Rankine Cycle (ORC) power plants is analyzed by applying an exergy efficiency analysis or so-called second law efficiencies. Most operating ORC power plants have relatively low (< 25 %) second law efficiencies (DiPippo, 2004). However, the California Energy Commission has suggested a conversion efficiency of 0.45 in a resource assessment of several low-temperature geothermal fields. Although the previous factor is theoretically possible, resource characteristics (e.g., change in resource temperature an pressure over time) and economic considerations usually dictate a much lower value (Garg & Combs, 2015; Klein et al., 2004).

Table 2-3. Guidelines followed in determining the various parameters for reserve estimation.[11]

Parameter	Proven reserve	Probable resource	Possible resource
Area	Defined by drilled wells with at least 500 meters beyond the drainage of the outermost wells bounded by an extrapolated production temperatures of >100 °C for binary and 180 °C for the flash-type cycle. Enclosed by good permeability and demonstrated commercial production from wells. Acidic blocks excluded until demonstrability for utilization is achieved.	Defined by wells with temperature contours that would extrapolate to >100 °C for binary and 180 °C for the flash-type cycle. Acidic or reinjection blocks earlier delineated could be included. Areas currently inaccessible because of limited rig capacity and restriction imposed within the boundaries of national parks. Areas with wells which could be enhanced by stimulation like acidizing and hydro-fracturing. Areas with surface manifestations where geothermometers indicate temperatures.	Areas include those not yet drilled but enclosed by geophysical measurements like Schlumberger electrical resistivity and magneto-telluric surveys. Defined by areas with thermal surface manifestations, outflow zones, and temperatures based on geothermometers that are suitable for either binary or flash-type power plant.
Thickness	Depth between the 100 °C for binary or 180 °C for the flash-type cycle and the maximum drillable depth of the rig that has demonstrated commercial production. Maximum depth should warrant economic output of the well.	Defined by demonstrated productivity in nearby areas or adjacent wells. Depth beyond the deepest well drilled in the area +500 meters provided projected temperatures reached at least 100 °C for binary or 180 °C for the flash-type cycle.	Defined by demonstrated productivity in nearby areas or adjacent wells. Also, electrical measurements like Schlumberger electrical resistivity and magneto-telluric surveys.
Reservoir temperature	Taken from direct measurement in production wells, supplemented by enthalpy and chemical geothermometers.	Extrapolated from temperature gradients and temperature distribution across the field or results of geothermometers using water, steam, and gas from hot springs and fumaroles	Results of geothermometers using water, steam, and gas from hot springs and fumaroles. Resistivity anomaly where high resistivity anomaly is seen conductive blow cap, indicating chlorite-epidote alteration at depth.
Reference temperature	Use the abandon temperature as a reference temperature. Thus, for a flash-type power plant, the abandon temperature is given by the saturation temperature corresponding to the separator pressure, and for a binary power plant, it equals the so-called pinch point temperature.		

---

[11] These guidelines use suggestions based on a possible classification for geothermal resources (Sanyal, 2005; Sarmiento & Steingrímsson, 2011).

2.6 Monte Carlo simulations using a python stochastic module

The basic premise of a Monte Carlo simulation is to test various outcome possibilities. In reality, only one outcome possibility will play out, but, regarding risk assessment, any of the options could have occurred. A Monte Carlo simulator can help to visualize most or all of the potential outcomes to provide a better idea regarding the risks of a given decision (Harrison, 2018). In terms of programming area, Monte Carlo methods are a broad class of computational algorithms that depend on repeated random sampling to obtain numerical results. The essential concept is to repeat the experiment many times (or use a sufficiently long simulation run) to obtain many quantities of interest using the law of large numbers and other statistical inference methods (Kroese et al., 2014).

Many licensed software are presently available for carrying out this task but in this case, the stochastic Monte Carlo simulation algorithm was programmed using Python (Brueck & Tanner, 2001; Python Software Foundation, 2016) and the Monte Carlo Error Propagation library (Lee, 2014). Python was chosen for the following reasons: 1) simplicity as a pseudo-natural code; 2) the algorithms work either locally (stand-alone) or in web-based applications; 3) Python is open source and is therefore free of charge, and any user can utilize, copy, modify, merge, publish, and distribute it; 4) the Python package can be used in most available operating systems (e.g., Linux-like, Microsoft Windows, MacOS); and 5) the developed stochastic library can be distributed as is without charge.

2.6.1 Object-oriented programming and structure of the library

Object-oriented programming is a programming paradigm based on the concept of objects, which may contain data in the form of fields (often known as attributes or properties), and code, in the form of procedures (often known as methods). The use of classes (i.e., the base form of an object) organizes programs around modules and data abstractions. The key to object-oriented programming is thinking about objects as collections of both data and methods that operate on that data (Guttag, 2015). A generalized flowchart of the several independent steps required for running a Monte Carlo simulation is represented in Figure 2-4.

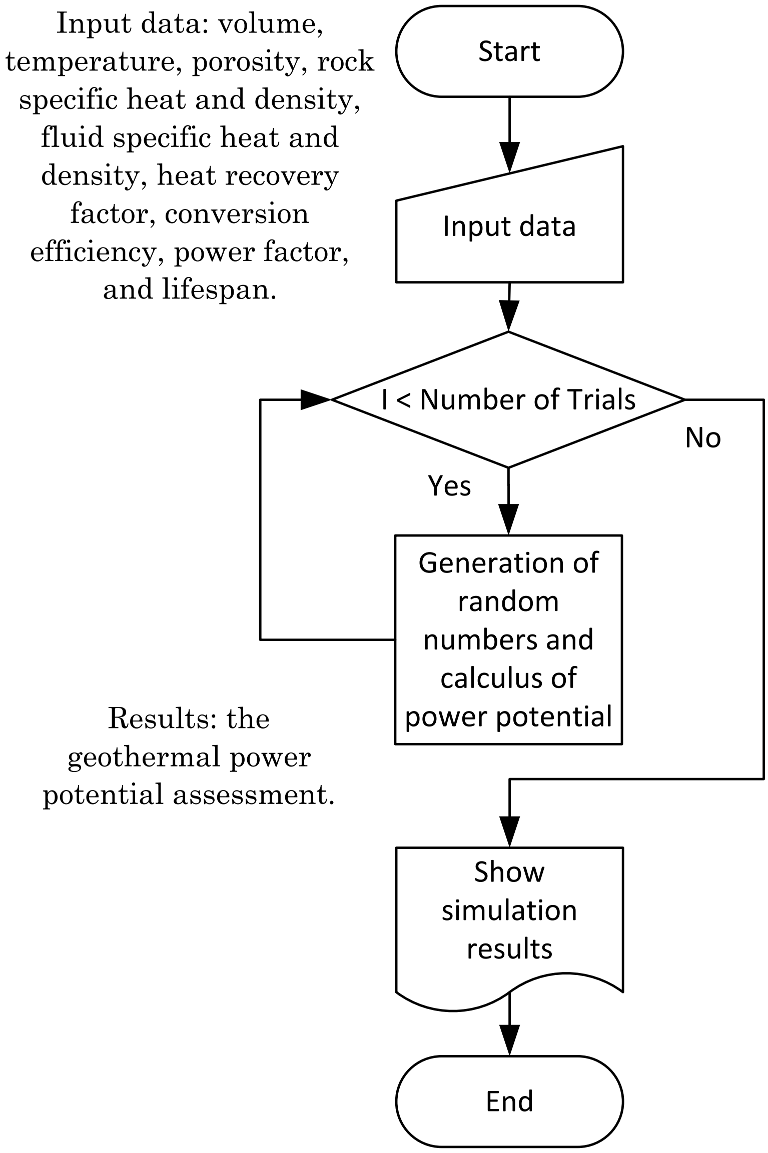

Figure 2-4. Structural flowchart showing the general simulation steps of a Monte Carlo simulation used by the Python-based stochastic library.

The simulation flowchart (Figure 2-4) has three general stages. First, the required geothermal reservoir information, such as those described in Section 2.2, is collected and organized in an input file. The simulation is then run several times, and the amount of trials is customizable to meet the required demands. Controlling the number of trials reduces the root mean square (RMS) of the calculations.

Finally, command line text is used to graphically show the results (i.e., frequency bar, cumulative plot).

Reservoir parameters can be prepared by either using an external CSV file or by manually typing the values during the simulation process. An example of a CSV file is shown in Figure 2-5 which could be edited using either spreadsheet software or a simple ASCII editor. The first two lines are comments and ignored by the reading method. The third line is the first to be imported by the reading method and includes general information related to geothermal reservoir (e.g., name, geographic coordinates, and reservoir surface area). Lines four through fifteen are the remnant parameters required for the simulation.

```
1.      #Input file for the Assessment of Power Energy Generation,,,,,,,,,,,,
2.      #Item,Name_Place,Lat,Lon,Properties,Symbol,Unit,Min,Most_Likely,Max,Mean,SD,PDF
3.      0,Name of place,14.00061,-88.73744,area,A,km2,5,6,7,0,0,T
4.      1,,,,thickness,h,m,450,500,600,0,0,T
5.      2,,,,Volume,v,km3,0.01,0.5,1.193,0,0,None
6.      3,,,,ReservoirTemperature,Tr,oC,110.0,110.0,125.0,0.0,0.0,T
7.      4,,,,AbandonTemperature,Ta,oC,0.0,106.7,0.0,0.0,0.0,C
8.      5,,,,Porosity,Phi,%,0.028,0.1,0.166,0.0,0.0,T
9.      6,,,,RockSpecificHeat,Cr,kJ/kg-oC,0.775,0.7925,0.81,0.0,0.0,T
10.     7,,,,WaterSpecificHeat ,Cf,kJ/kg-oC,4.2479,4.2838,4.3164,0.0,0.0,T
11.     8,,,,RockDensity,rho_r,kg/m3,2330.0,2485.0,2640.0,0.0,0.0,T
12.     9,,,,WaterDensity,rho_f,kg/m3,915.37,928.12,944.95,0.0,0.0,T
13.     10,,,,RecoveryFactor,Rf,%,0.08,0.14,0.2,0.0,0.0,T
14.     11,,,,ConversionEfficiency,Ce,%,0.1,0.175,0.25,0.0,0.0,T
15.     12,,,,PowerFactor,Pf,%,0.9,0.95,1.0,0.0,0.0,T
16.     13,,,,LifeSpan,t,years,0.0,20.0,0.0,0.0,0.0,C
```

Figure 2-5. Code line fragment of a typical comma-separated input file with geothermal reservoir information.

2.7 Python stochastic modules

The Python-based stochastic library, GPPeval, is structured as three essential objects including a geothermal power plant module, a Monte Carlo simulation module, and a tools module, shown schematically in Figure 2-6. These three objects provide basic functionalities in the utility of classes and functions, as well as command line scripts. Incorporation of this modular structure not only enables possible adaption to local setups and configurations, but also conveniently extends the toolbox (Krieger & Peacock, 2014). The GPPeval must be installed, along with all dependencies (Numpy, Matplotlib, Scipy, Mcerp, and Beautifultable)[12] prior to running any simulation. The installation process using the Python command is shown in Figure 2-7. The library can be downloaded as a compressed tar.gz file from https://github.com/cpocasangre/gppeval.

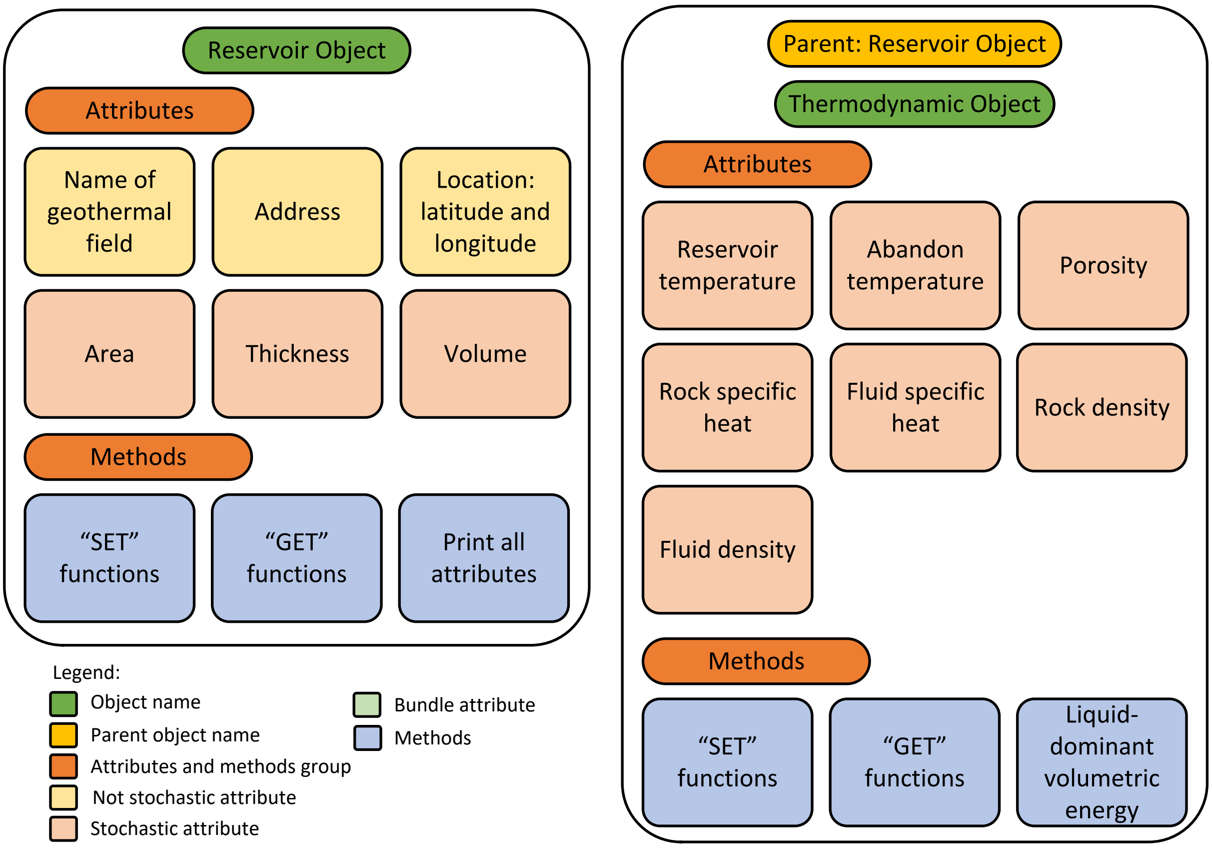

(a)

---

[12]

NumPy:	Numeric Python	http://www.numpy.org/
SciPy:	Scientific Python	http://scipy.org/
Matplotlib:	Python plotting library	http://matplotlib.org/
Mcerp:	Monte Carlo Error Propagation	http://github.com/tisimst/mcerp
Beautifultable:	Utility package to print visually appealing ASCII terminal table	https://github.com/pri22296/beautifultable

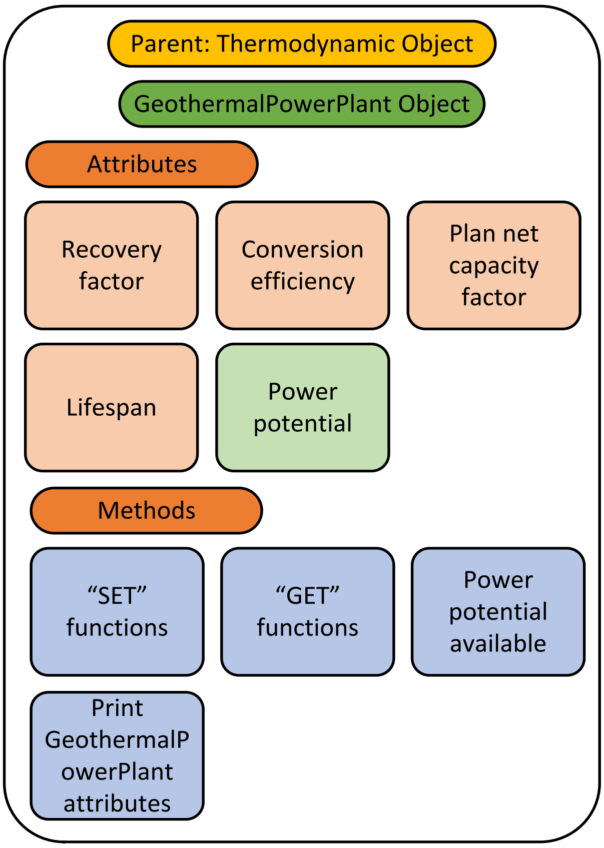

(b)

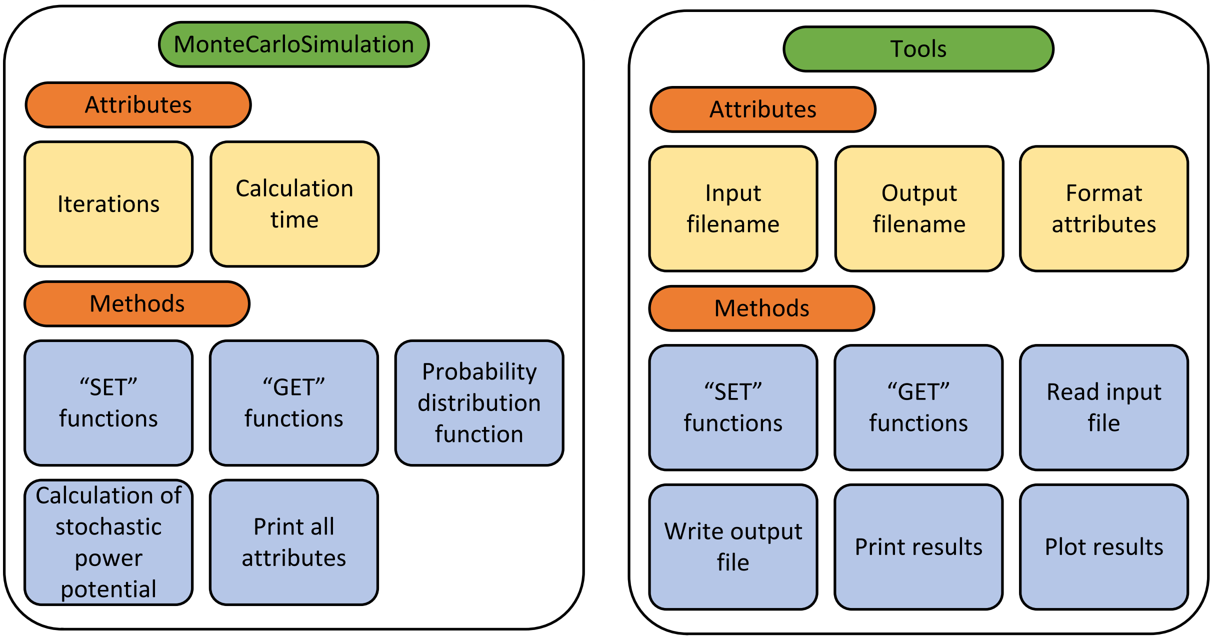

(c)

Figure 2-6. Overview of the objects used in the Python-based stochastic library. (a) & (b) Geothermal power plant module, which inherits properties and methods from parent objects (i.e., thermodynamic and reservoir objects). (c) Monte Carlo and tools modules.

```
user@host:~$ [sudo] pip install numpy matplotlib scipy beautifultable
user@host:~$ [sudo] pip install mcerp
user@host:~$ [sudo] pip install gppeval
user@host:~$ ipython
Python 2.7.12 (default, Dec  4 2017, 14:50:18)
Type "copyright", "credits" or "license" for more information.
IPython 5.4.1 -- An enhanced Interactive Python.
?         -> Introduction and overview of IPython's features.
%quickref -> Quick reference.
help      -> Python's own help system.
object?   -> Details about 'object', use 'object??' for extra details.
In [1]: import gppeval
In [2]: gppeval.__version__
Out[2]: '2019.4.17.0.3.dev1'
```

Figure 2-7. Code line fragment of the GPPeval installation process on a Linux-like operating system showing the installation of Numpy, Matplotlib, Scipy, Beautifultable, Mcerp, and GPPeval libraries.

2.7.1 Reservoir, thermodynamic, and geothermal power plant objects

The reservoir, thermodynamic, and geothermal power plant objects are described below:

1. The geothermal reservoir abstraction or object has characteristic properties and methods for generally describing a geothermal reservoir (Figure 2-6a). The object has the following properties: reservoir name; address; geographic coordinates (latitude and longitude); reservoir surface area; reservoir thickness; and reservoir volume[13]. Each object property is classified as a Python data type. For example, name and address are strings, and location is a dictionary that includes latitude and longitude as floating-point numbers. Because reservoir area and thickness are stochastic properties, they are classified as a dictionary consisting of minimum, most likely, maximum, mean, standard deviation, and probability distribution function values, with input in units of km^2 and m,

---

[13] Reservoir volume is an independent attribute; i.e., it does not have any relationship with both reservoir area and reservoir thickness during the simulation. It must be calculated separately using geoscience methods.

respectively. The geothermal reservoir object also has several methods for setting and obtaining values for every object property.

2. The thermodynamic abstraction or object has the essential thermodynamic properties and methods for describing the geothermal reservoir (Figure 2-6a). The object has the following properties: Tr and Ta in units of °C, ϕ, Cr and Cf in units of kJ/kg, and ρr and ρf in units of kg/m^3. Because all properties of this object are stochastic, they are classified as a Python dictionary with minimum, most likely, maximum, mean, standard deviation, and probability distribution function values. Several methods are available for setting and obtaining values for every object property. Moreover, the volumetric energy (Equation 2-1 in Section 2.2) is calculated by the liquid-dominant volumetric energy method.

3. The geothermal power plant abstraction or object has the remnant properties and methods for running the Monte Carlo simulation and obtaining the geothermal power potential (Figure 2-6b). This object has the following reservoir and geothermal power plant properties: RF, ηe, PF, and t. Because all properties of this object are stochastic, they are classified as a Python dictionary with minimum, most likely, maximum, mean, standard deviation, and probability distribution function values. This object also includes a power potential attribute, which contains all results upon completion of the Monte Carlo simulation. The attributes are the power potential base, frequency distribution, cumulative frequency distribution, trials or iterations, and basic statistics (mean, standard deviation, skew, kurtosis, minimum and maximum value, and percentiles).

2.7.2 Monte Carlo simulation object

The Monte Carlo abstraction or object has the essential properties and methods for running the Monte Carlo simulation and obtaining the geothermal power potential (Figure 2-6c). The object has the following properties: number of trials or iterations and the final calculation time. Additionally, it includes a set of the most common probability distribution functions on the geothermal exploration area (i.e., triangular, uniform, normal, lognormal), and a method for calculating the stochastic power potential.

2.7.3 Tool object

The tool abstraction or object has the essential properties and methods for displaying the simulation results (Figure 2-6c). The object has the following properties: input and output file name and several attributes for designing the presentation. File reading and the saving of reservoir parameters can be executed by using this object. Additionally, the frequency distribution (FD) and cumulative frequency distribution (CFD) are available as a histogram, which includes information including title, 5th, 10th, and 95th percentiles, and the most likely value. Moreover, the print method is available for displaying the statistical analysis on the command line interface. The printed parameters are the most likely power potential and its occurrence probability, the calculated power potential, number of iterations, mean, median, standard deviation, histogram skew and kurtosis, minimum and maximum values, and percentiles.

2.8 Geothermal power potential assessment case study: El Salvador

El Salvador is a small country located in Central America between 13.15°N to 14.46°N and 90.13°W to 87.7°W, surrounded by the Pacific Ocean, Guatemala, and Honduras. Because it is located close to the Ring of Fire, there exists a vast geothermal resource potential. The government of El Salvador has made plans to improve electricity generation in the period between 2014 and 2024 using renewable energy, such as geothermal energy (Consejo Nacional de Energía Gobierno de El Salvador, 2014). The government will include two more geothermal power plants, Chinameca and San Vicente (Santos & Rivas, 2009), as well as new studies from low-enthalpy areas, which are the primary purposes of this research. Vast geothermal energy potential can be found throughout the territory, and there are many hydrothermal manifestations of both high and low enthalpy. Many previous studies have been conducted by the government and demonstrated the available geothermal potential. As a result, there are two high-enthalpy hydrothermal fields in operation, Ahuachapán and Berlín. The temperature is higher than 200 °C, and the total power generation is 204.4 MWe, i.e., 95 MWe and 109.4 MWe from Ahuachapán and Berlin power plant respectively (Consejo Nacional de Energía Gobierno de El Salvador, 2010; Gobierno de El Salvador et al., 2012). The low- and high-enthalpy hydrothermal areas of El Salvador are shown in Figure 2-8 with a red rectangle indicating the working area in the northern zone of El Salvador, which includes the Municipality of Nombre de Jesus, because this region has the highest available potential. The points selected as energy potential sites are as a result of several studies by the government agency called the Hydroelectric Commission of the Lempa River, CEL (Campos, 1988). Two significant areas are identified on the map in Figure 2-8: the northern and central mountain ranges. The central mountain range is made of young rocks, Quaternary geological structures with ongoing volcanic activity, and high enthalpy points such as Ahuachapán and Usulután. The northern ridge is formed by the oldest, tertiary, or additional geological structures. Hydrothermal manifestations are mostly low enthalpy and are caused by remnants of volcanic or regional activity.

The specific boundaries of the municipality of Nombre de Jesus is shown in Figure 2-9. All the hydrothermal manifestations in this area are considered low-enthalpy fluids. According to government surveys, the inferred resource has an area of 6 km^2 with an average temperature of 160 °C, as calculated by geothermometers (Campos, 1988). The geologic map also displays a hydrothermal alteration zone on extrusive volcanic rocks or rhyolites due to regional influences. Volcanic activity in this zone is not considered to be recent, so that the heat source might be a fossilized magmatic intrusion such that the temperature is only a remnant of the volcanic effect.

An example of a conventional geothermal power potential assessment is presented below to demonstrate the implementation of the GPPeval (Pocasangre & Fujimitsu, 2018).

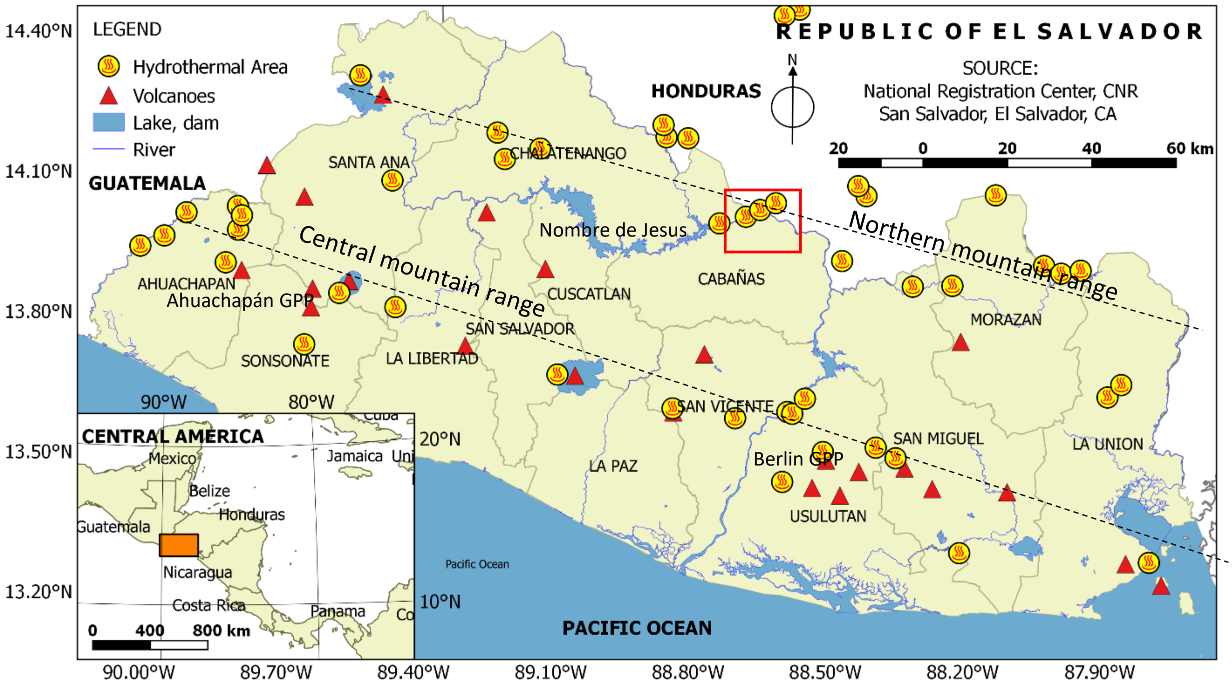

Figure 2-8. Hydrothermal areas in El Salvador, Central America. Volcanoes are represented as red triangles, lakes, dams, and rivers are in blue, and hydrothermal manifestation areas are represented by yellow-red circles. The red rectangle encloses the hydrothermal manifestations of low-enthalpy fluids in the Municipality of Nombre de Jesus, which are the case study presented here. The study area is located at 14°N and 88.73°W. The figure is a modified map (National Registration Center CNR, 2015) and composed using Geographic Information System software (QGIS Development Team, 2017).

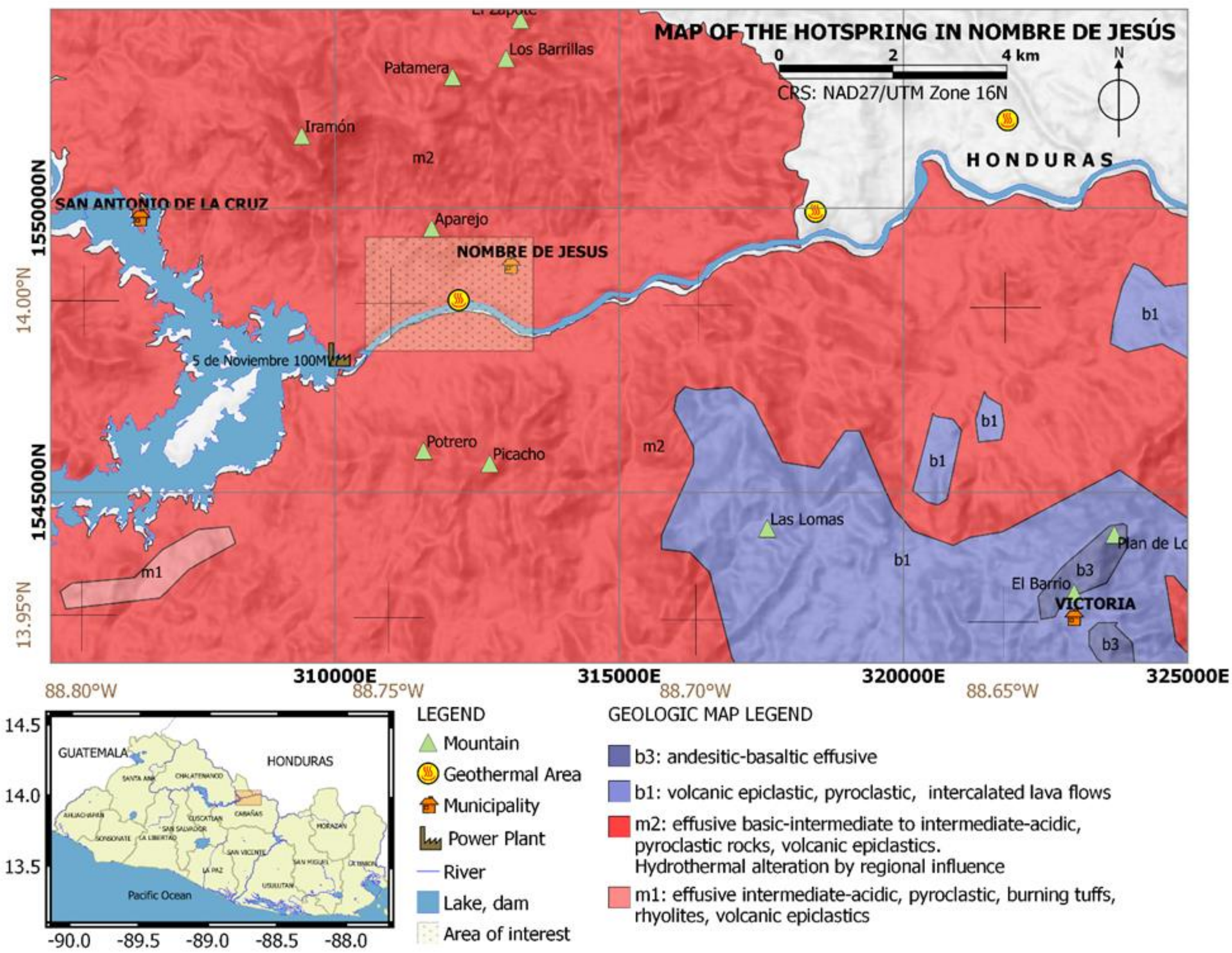

Figure 2-9. Map of the hot springs in the municipality of Nombre de Jesus. The dotted rectangle encloses the 6 km^2 area of interest. The regional geology provides evidence of hydrothermal alteration on extrusive volcanic rocks or rhyolites (National Registration Center CNR, 2015).

2.8.1 Input file preparation

The input file must be formatted as a CSV file, as shown in Section 2.6.1. The reservoir parameters are listed in Table 2-4 (Campos, 1988; Monterrosa & La Geo, 2007). For this example, a low-enthalpy fluid that heats a secondary working fluid (isobutane) with an assumed pressure of 20 bar is used and saturation temperature of 100.36 °C. Therefore, a temperature difference of 5 °C at the pinch point, and an abandon temperature of 105.36 °C and a conversion efficiency of less than 0.25 are considered (DiPippo, 2004).

Table 2-4. Typical worksheet and input reservoir parameters for assessing the geothermal power potential in Nombre de Jesús (Campos, 1988; Monterrosa & La Geo, 2007).

Reservoir Properties	Min	Most Likely	Max	Distribution
Reservoir Area, A[km^2]	5	6	7	Triangular
Thickness, h[m]	450	500	600	Triangular
Reservoir Temp., Tr[°C]	130	160	163	Triangular
Abandon Temp., Ta[°C]		105.36		Constant
Porosity, ϕ		0.06/0.02		Log-Normal
Rock SH C_r[kJ/kg °C]	0.85	0.85	0.9	Triangular
Water SH, C_f[kJ/kg °C]		5.18		Constant
Rock Density ρ_r[kg/m^3]		2500		Constant
Water Density, ρ_f[kg/m^3]		764.45		Constant
Recovery Factor, RF	0.08		0.2	Uniform
Conversion Efficiency, η_e		0.25		Constant
Power Factor, PF	0.9	0.95	1	Triangular
Lifespan, t[years]		25		Constant

The following example uses the IPython command line interface for running the Monte Carlo simulation and result processing (Golman, 2016; Perez & Granger, 2007). The tool object is used for importing data from the file that has been prepared as a CSV file.

```
user@host:~$ ipython
In [1]: import gppeval # geothermal power potential evaluation library
In [2]: tool = gppeval.Tools()
In [3]: sim = gppeval.MonteCarloSimulation()
In [4]: nj = tool.read_file_csv('reservoir_properties_list.csv')
READ FILE ... OK
In [5]: print nj # show the information that was read before
```

Figure 2-10. Commands for starting the simulation: 1) import the GPPeval library; 2) create two helping variables, (tool and sim); and 3) create the variable that represents the characteristics of the reservoir.

2.8.2 Running the Monte Carlo simulation

In this stage, the Monte Carlo simulation object is used.

```
In [6]: nj = sim.calc_energy_potential(nj)
SIMULATION ... DONE
```

Figure 2-11. Command for running the Monte Carlo simulation.

2.8.3 Displaying simulation results

There are several ways for presenting the results (FD, Figure 2-13; CFD, Figure 2-15) and command line text (Figure 2-16).

1. Frequency distribution (FD) as a histogram

```
In [7]: tool.plot_pdf(nj, show=True)
```

Figure 2-12. Command for plotting the results as a frequency distribution histogram and the empirical density estimation curve.

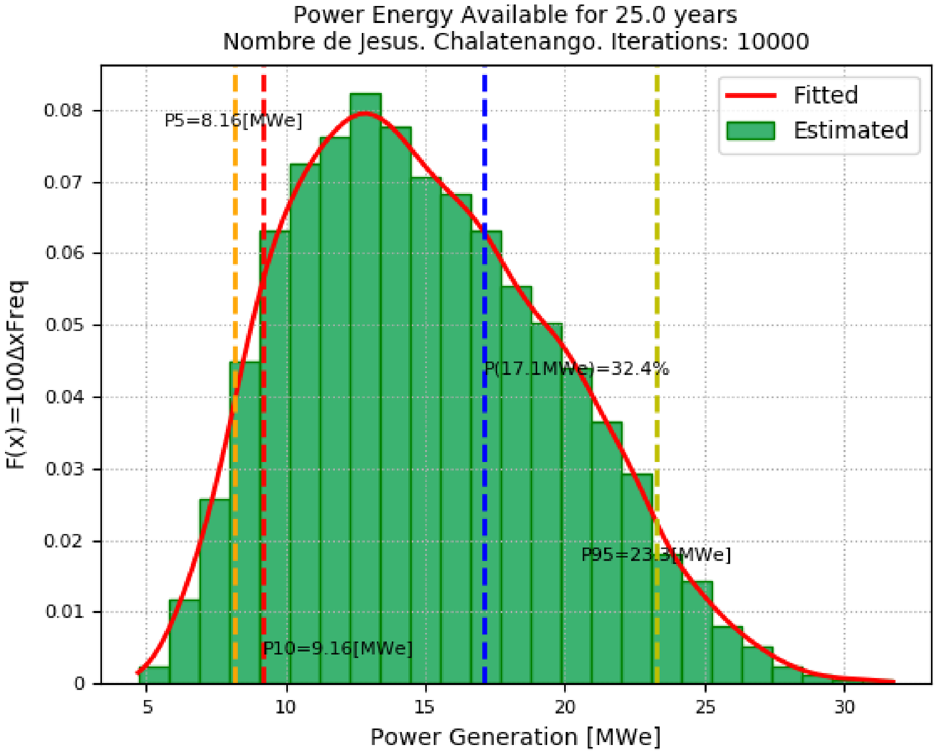

Figure 2-13. Frequency distribution (FD) of Nombre de Jesus, El Salvador. This simulation was run for 25 years.

2. Cumulative frequency distribution (CFD)

```
In [8]: tool.plot_pdf(nj, type_graph='higher', show=True)
```

Figure 2-14. Command for plotting the results as a cumulative frequency distribution.

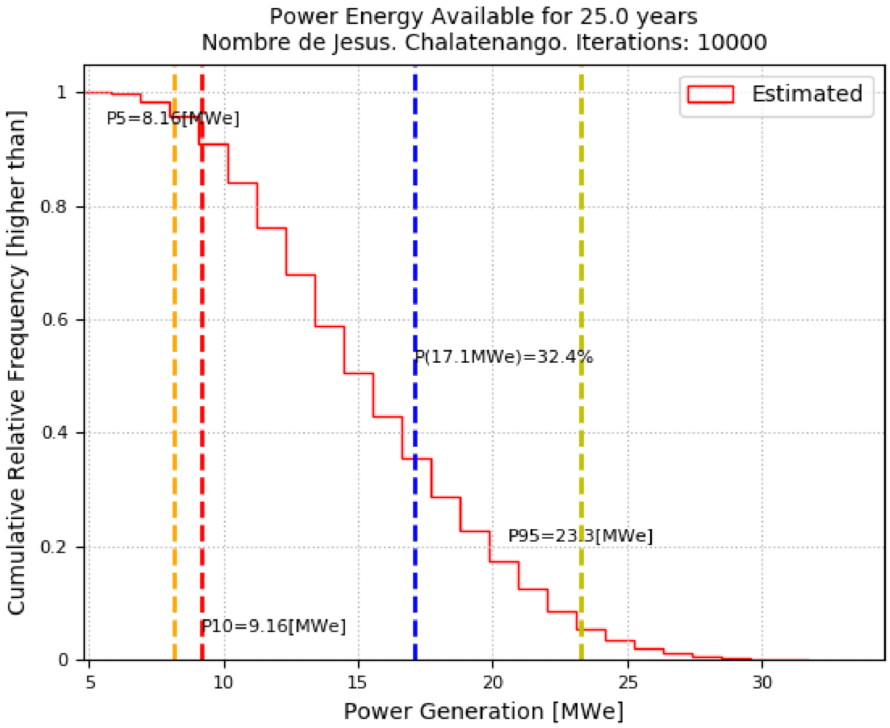
Power Energy Available for 25.0 years
Nombre de Jesus. Chalatenango. Iterations: 10000

Figure 2-15. Cumulative frequency distribution (CFD) of Nombre de Jesús, El Salvador. This simulation was run for 25 years.

3. Command line text

This tool, "`tool.print_results(nj)`", shows the statistical results after the Monte Carlo simulation has finished, such as percentiles, mean, median, standard deviation, skew, kurtosis, and values minimum and maximum.

```
In [9]: tool.print_results(nj)
MAIN INFORMATION:
Most Likely PowerGeneration [MWe]= 17.1091
Probability of  17.1091 [MWe]= 0.3241
P10% [MWe]= 9.15509

STATISTICAL ANALYSIS:
Iterations= 10000
Mean= 15.026 [MWe]
Median= 14.5297 [MWe]
```

```
Standard Deviation= 4.71778 [MWe]
Skew= 0.38715
Kurt= 2.55956
Minimum= 4.70277 [MWe]
Maximum= 31.76 [MWe]
P5%= 8.1645 [MWe]
P10%= 9.15509 [MWe]
...
P95%= 23.2853 [MWe]
END
```

Figure 2-16. Command for displaying the results as a text list.

4. Linear figure

```
In [10]: tool.plot_pdf(nj, type_graph='linear', show=True)
```

Figure 2-17. Command for plotting the results summary as a linear bar.

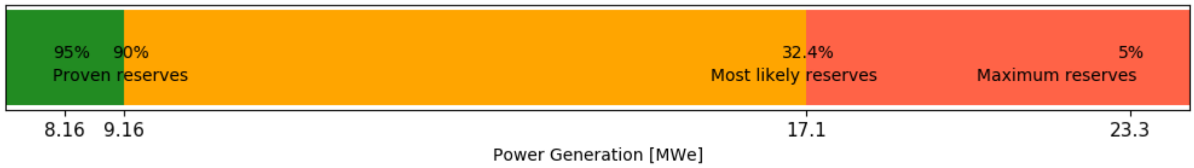

Figure 2-18. Linear representation of hot spring data from Nombre de Jesus, El Salvador. This simulation was run for 25 years.

In Figure 2-18, the model reserves are 9.16 MWe with a possible expansion of the geothermal power plant up to 17.1 MWe. Finally, the maximum and less probable geothermal power potentials reach around 23.3 MWe.

2.8.4 Manual set up of reservoir parameters

Changes to a given reservoir parameter sometimes need to be made to run a simulation and to create several outcome scenarios. For instance, the simulation requires two hypothetical power plants to be operating for 25 and 30 years, respectively. The GPPeval library therefore has several methods for modifying object attributes and for using an external package to create a new scenario from the original one. Figure 2-19 demonstrates how to edit the original case (lines 1–15) and how to create a new one (lines 16–21).

```
In [11]: nj. set_name('new_name')
In [12]: nj.set_location(lat=14.12, lon=31.5)
In [13]: nj.set_area(min=5.0, most_likely=6.0, max=7.0, pdf='T')
In [14]: nj.set_thickness(min=450, most_likely=500, max=600, pdf='T')
In [15]: nj.set_reservoir_temp(min=130, most_likely=160, max=163, pdf='T')
In [16]: nj.set_abandon_temp(most_likely=80.0, pdf='C')
In [17]: nj.set_porosity(most_likely=0.06, mean=0.06, sd=0.02, pdf='L')
In [18]: nj.set_rock_specific_heat(min=0.85, most_likely=0.85, max=0.9, df='T')
In [19]: nj.set_fluid_specific_heat(min=0.0, most_likely=5.18, max=0, pdf='C')
In [20]: nj.set_rock_density(most_likely=2500, pdf='C')
In [21]: nj.set_fluid_density(most_likely=764.45, pdf='C')
In [22]: nj.set_recovery_factor(min=0.08, most_likely=0.14, max=0.2, pdf='U')
In [23]: nj.set_conversion_efficiency(most_likely=0.25, pdf='C')
In [24]: nj.set_plant_net_capacity_factor(most_likely=764.45, pdf='C')
In [25]: nj.set_lifespan(min=0.0, most_likely=25.0, max=0.0, pdf='C')
In [26]: import copy
In [27]: nj_new = copy.deepcopy(nj) # new instance from original instance ‘nj’
In [28]: nj_new.set_lifespan(most_likely=30.0)
In [29]: nj_new = sim.calc_energy_potential(nj_new)
SIMULATION ... DONE
In [30]: tool.print_results(nj)
```

Figure 2-19. Commands for manually setting up the reservoir parameters and creating new scenarios

2.8.5 Interpretation of Monte Carlo simulation results

Figure 2-13, Figure 2-15, and Figure 2-18 show possible inference when the output greater than or equal to 9.16 MWe is 90 % (i.e., proven reserves), and when the capacity greater than or equal to 17.1 MWe is 32.4 % (i.e., proven + probable reserves). Additionally, the probability that the output is greater than or equal to 23.3 MWe is only 5 % (i.e., proven + probable + possible or maximum reserves), after which, the preliminary power potential assessment is 1.53 MWe/km^2 for a maximum of 25 years. These results imply that the field could initially support a 9.16 MWe geothermal power plant for 25 years maximum with a possible expansion to 17.1 MWe, subject to further delineation drilling and availability of field performance data. Finally, the risk that the field could not sustain 9.16 MWe is equal to or less than 10 % can be affirmed. However, this interpretation will be subject to further investigations for obtaining and validating the new data. Alternatively, it has been observed that the reservoir volume (i.e., A and h) has a direct influence over the geothermal potential.

2.9 Conclusion

The primary purposes of this study are to use the volumetric method to estimate the electrical energy production ability from a geothermal liquid-dominated reservoir, and to code a Python-based stochastic library with suitable methods for running the simulation. The calculation of geothermal energy stored in a volume is based on the range of reservoir parameters and carried out using a stochastic Monte Carlo simulation. During early exploration, estimates of essential reservoir parameters are poorly constrained, but application of the USGS “heat in place” evaluation method along with Monte Carlo simulations produces a wide distribution for the probable power potential. The USGS volumetric “heat in place” method, together with Monte Carlo simulations, are a useful tool for assessing the electrical capacity of a geothermal reservoir.

Although licensed software is available for carrying out these simulations, an open-source programming language was selected, Python. The resulting stochastic library is called the Geothermal Power Potential Evaluation, GPPeval. The new library utilizes the standard numerical modules, Numpy and Scipy, but also the Matplotlib module for graphical visualization, and the Mcerp module for performing non-order specific error propagation or uncertainty analysis. The GPPeval is structured as three essential objects including a geothermal power plant module, a Monte Carlo simulation module, and a tools module.

Finally, to demonstrate how the Python-based stochastic library can be used for assessing the geothermal power potential, an assessment of hot spring data in the municipality of Nombre de Jesus, El Salvador is presented. After running the stochastic simulation, the frequency distribution shows that the field could initially support a 9.16 MWe power plant for 25 years and a possible expansion to 17.1 MWe. However, the geothermal power potential must be investigated further to obtain and validate the new data.

Chapter 3

Field Characteristics of Isa, Kagoshima

3.1 Overview

The regional geology and structural setting of the study area in the eastern part of Isa, Kagoshima, have attracted much researches, and some review papers have been written because of the importance of gold mine exploitation. This chapter describes the geology and structural makeup of the Isa area both regional and local.

3.2 General geology and structural setting

The area is an ancient volcanic region, and one of the most important gold mines in Japan is located in this area. Hishikari mine is an epithermal gold mine and has a very high ore grade (Izawa et al., 1990). In the neighborhood of Hishikari region, specifically in the eastern part of Isa City, the fundamental structure in the most profound element is controlled by Cretaceous Shimanto Supergroup. This arrangement is typically composed of sandstone, shale, acid tuff with subordinate conglomerates, and their alternations, also Pliocene volcanic rocks and alluvial deposits. The total area is divided into two regions, Yamada and Sendai Rivers and Honko-Sanjin area.

The Honko-Sanjin area, which is located in the eastern part of the Hishikari deposit, rises to 500 m A.S.L and it is formed mainly of dacite and rhyolite rocks. The volcanic rocks, which cover the Shimanto Supergroup, are Hishikari Lower Andesite, Welded Tuff, and Pyroclastic Flow Deposits, in ascending order; and the second group corresponds to alluviums, Pumice, volcanic ash, and sediment deposits. The latter rocks were put down by Yamada River, Sendai River, and ancient volcanic eruptions at Okuchi basin in the western part of Hishikari area. According to the geological map, it is possible to find three main group of rocks. First, Andesite and basaltic rocks are in the northern part of Hishikari hot spring; second, dacite and rhyolite rocks in the southern part; and third, pumice, volcanic ash, alluvial fan, and sediments overlay Yamada and Sendai River banks. Besides, there are many hot springs in Kakuto Basin due to volcanic activity in the late Pleistocene. On the contrary, Okuchi Basin is an old volcanic region that is why the hot spring temperature is quite low (Saito et al., 2010). Apart from the caldera, such as Okuchi and Kakuto basin, geologists have identified two geological faults aligned with northeast to southwest trending and situated along the Yamada River in the direction of the Kakuto Caldera. Figure 3-1 shows the geological map of the eastern part of Isa area. The dotted red square indicates the selected research area of 10 x 10 km at 31.97°N to 32.06°N and 130.64°E to 130.75°E and indicates the area used for the Three-Dimensional gravity modeling. Lithologic structure age legends are: Holocene (H), reclaimed land (rl), fan deposits (fn), marine and non-marine sediments (sr), Quaternary or Pleistocene (Q), lower terrace (tl), non-alkaline mafic volcanic rocks or Andesite and basaltic type (vb), non-alkaline pyroclastic flow volcanic rock or Pumice and volcanic ash (vp), non-alkaline felsic volcanic rock or Dacite end Rhyolite (vf), and Neogene or Miocene to Pliocene (N) (Sakaguchi et al., 1997).

3.3 Local schematic description about Hishikari gold deposits

Among several epochs of gold-silver mineralization in the Japanese Islands, the late Cenozoic has been most productive in so-called Green Tuff region (Nishikawaki et al., 1971; Saga et al., 1955) where late Cenozoic magnetite-series igneous rocks occur extensively. Gold occurs, together with silver, mostly in epithermal quartz veins but subordinate amounts of the metals are extracted from base metal veins (Ishihara et al., 1986).

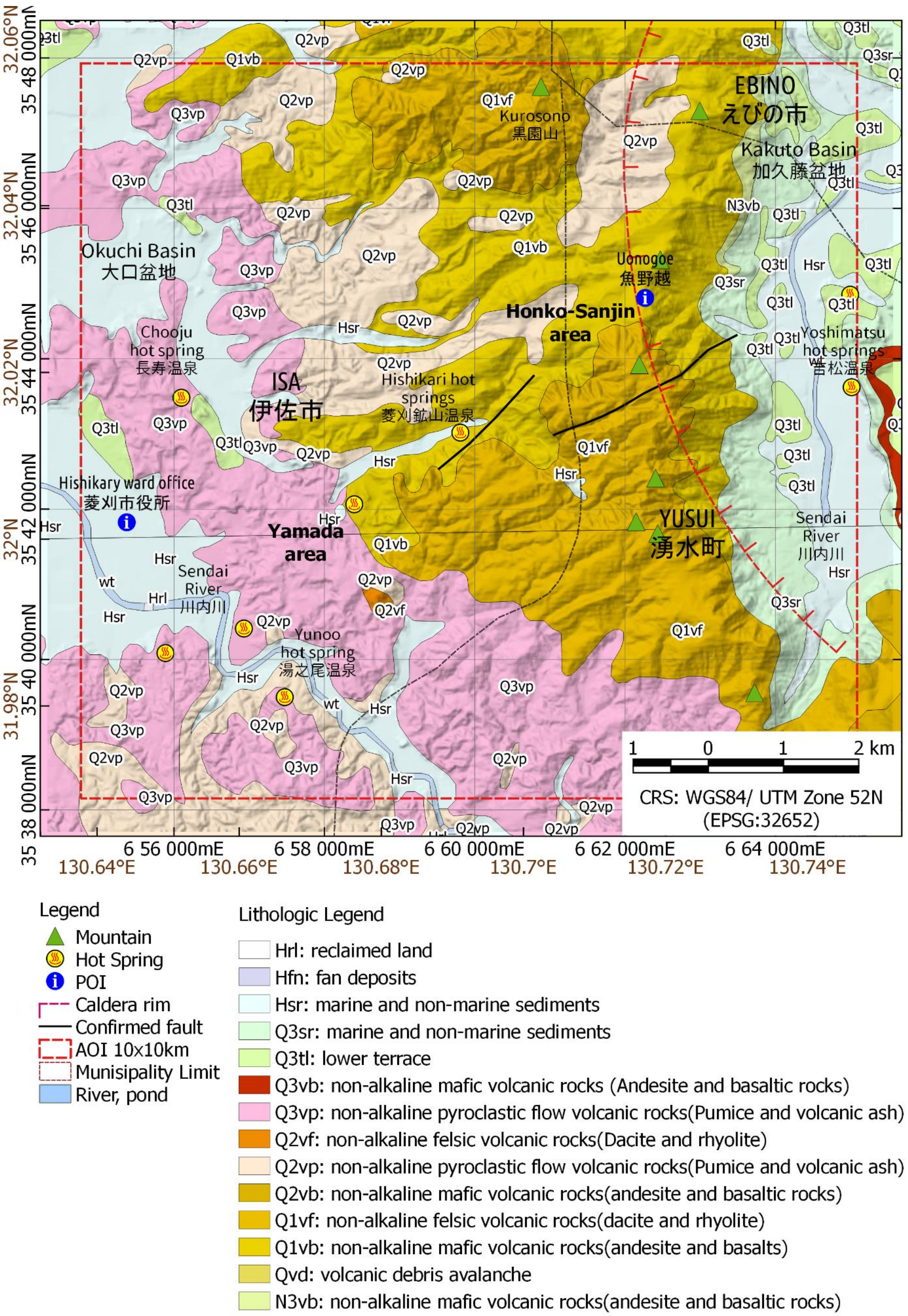

Figure 3-1. Geological Map of the eastern part of Isa, Kagoshima Prefecture (Sakaguchi et al., 1997).

The gold-quartz vein deposits occur in late Cenozoic volcanic rocks extruded onto diverse basement settings. Three possible sources can be considered for the provenance of gold as follows:

i. Magmatic source, either from upper mantle or lower continental crust, brought up with magmatic fluid,
ii. Basement rocks, either sedimentary or igneous, concentrated by meteoric hydrothermal water convection system, and
iii. Host andesitic rocks, concentrated by lateral secretion or by meteoric hydrothermal circulation.

The Hishikari gold mine is located in the northern part of Kagoshima Prefecture, about 60 km north of the Kagoshima city (32°00' N, 130°41' E). The area is immediately west of the Kakuto caldera, part of the Kagoshima Graben in which the active Kirishima volcano is located, see Figure 1-10. The portal of the mine is at 265 m above sea level. The topography, ranging from 200 to 600 m in elevation, comprises densely timbered, hilly terrain separated by small valleys cultivated mainly with rice. The atmospheric temperatures range from a low of -7 ºC to a high of 35 °C. Rainfall is rather high, averaging 2500 mm per annum (Izawa et al., 1990; Izawa & Urashima, 1987; Yasuhara et al., 2003). The first prospecting record in the Hishikari mine area dates back to 1750 (Kondoh, 1986). Since then, exploration and small-scale mining (limited to above 230 m elevation) has been intermittent. In 1903, near-surface exploitation began on three gold-bearing quartz-calcite-clay veins. The veins are located 100 m directly above the top of the present Hishikari veins (Honko veins), and are now interpreted to be an upper manifestation of mineralization at Hishikari. A crosscut was driven in 1933 about 180 m in length at an elevation of 230 m, using explosives and dewatering pumps. Ore was shipped to the Saganoseki copper smelter 170 km from the mine. The maximum grade of this ore was as high as 130 g/metric ton gold. In 1943 a plan of downward development was suspended owing to intensification of World War II. The crosscut of the 230 m level was re-opened in 1952, with about 40 m of drifting on the No. 3 vein; however, the results were discouraging (Nishizawa & Ibaraki, 1985). In 1973 the Taio Mining Co., a subsidiary of the Sumitomo Metal Mining Co., Ltd. (SMM), acquired the mineral rights.

It was rediscovered underneath old passages by the Metal Mining Agency of Japan (MMAJ) in 1981 and subsequent development by the property owner, the Sumitomo Metal Mining Co., Ltd. (SMM), has shown Hishikari (the Main or Honko deposit) to be one of the richest gold veins in the world. In 1988, the second deposit, called the Yamada deposit which is located 1.2 km southwest of the Main deposit, was discovered as the result of integrated geological, geochemical and geophysical study conducted by SMM. The Sanjin deposit, the third one, was discovered 0.5 km southeast of the Main deposit in 1990. The underground exploration and development work have continued in the latter two deposits (Ibaraki et al., 1992; Ibaraki & Suzuki, 1993; Sumitomo Metal Mining Co. LTD, 2017).

The recent discovery of very high-grade ores at Hishikari occurring in the basement rocks leads us to examine the bearing of sedimentary basement for the genesis of the gold mineralization. Certainly, Izawa et al. (1990) considers the ore gold is derived from the sedimentary rocks of the Shimanto Supergroup. This hypothesis may be reasonable, because the gold deposits occur mostly in the Shimanto sedimentary terrane and hydrothermal solutions responsible for formation of the gold veins are generally known to be meteoric in origin e.g., Kushikino mine, Kagoshima (Matsuhisa et al., 1985).

3.3.1 Geology of the Hishikari Deposit

The geology of the Hishikari mine area is composed of basement sedimentary rocks of pre-Neogene Shimanto Supergroup, volcanic rocks of Quaternary age and alluvial deposits. The Shimanto Supergroup is not exposed in the vicinity of the mine but is recognized 100 m below surface (120 m elevation) in the central part of the Main deposit, see Figure 3-2. It is generally present at an elevation less than -400 m in the surrounding area and was intersected at a depth of 100 m below sea level by only two drill holes at the northeastern part of the Yamada area.

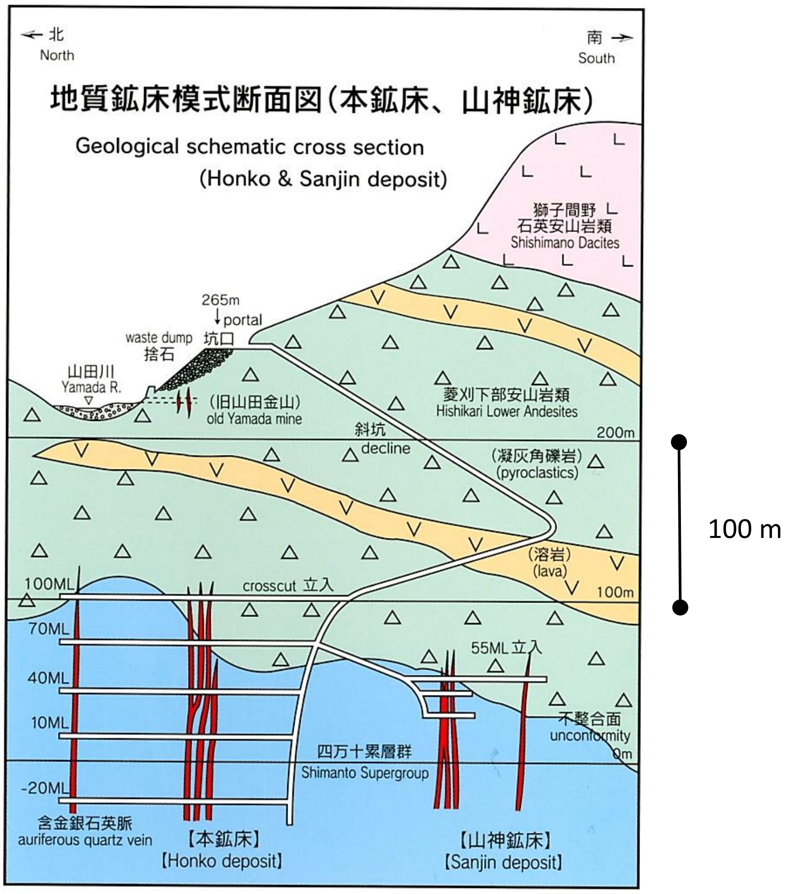

Figure 3-2. Schematic north-south section across the Main or Honko and the Sanjin gold deposits. Courtesy of Sumitomo Metal Mining Co. LTD (2017).

Exposed rock units are andesitic lavas and tuffs of so-called Hokusatsu andesite, Kurosonsan rhyolites and Ito ignimbrites. Radiometric ages dated to date (Abe et al., 1986; Izawa et al., 1990) can be summarized as follows:

- Ore vein: K-Ar method, adularia: 0.97±0.04 Ma, 0.98±0.04 Ma
- Kurosonsan rhyolite: ditto, whole rock; 1.0±0.1 Ma, 1.1±0.1 Ma
- Hokusatsu Younger andesite: ditto, whole rock: 1.3±0.1 Ma, 1.6±0.1 Ma
- Hokusatsu Older andesite: ditto, whole rock 1.7±0.6 Ma

Hence, all the volcanic rocks listed above are young in age (latest Neogene to Quaternary) and have the possibility to host the Hishikari gold deposit, except for the Ito ignimbrite located at west of the gold deposits. The Hishikari gold deposit is the first large gold concentration discovered in the sedimentary basements in

Japan. This indicates, however, that the basement did not play any important role as the source material for the ore constituents. The ores may be of magmatic origin. The assumed rhyolitic plug underneath the ore deposit was significant serving as the conduit (vertical fracture system) for the rising ore solution and the related magmatic ore solution was a main source for sulfur and possibly gold. The unusually high grade ores of the Hishikari deposit can be explained by strong magmatic concentration of gold in the primary magmatic hydrothermal solution. The Hishikari mineralization model is illustrated in Figure 3-3. The unconformity plane acted as passage for meteoric groundwater which cooled down the ascending magmatic ore solution to precipitate the ore minerals (Ishihara et al., 1986). Thus the Hishikari deposit is the second example of unconformity controlled type after the Bajo gold deposit in northern Kyushu, Oita, and this suitable environment for the gold deposition may be the second reasoning for the high grade ores (Sawai et al., 2002; Watanabe, 2005).

3.3.2 Ore deposit in Hishikari area

The vein system can be classified as an epithermal gold-silver-bearing quartz-adularia vein deposit. At present, development has focused on the Honko vein system. A separate vein system was recently discovered in the Yamada area 1 km southwest of the Honko deposit; it is hosted by the Hishikari Lower Andesite and consists of several major veins with numerous parallel veins. The Honko vein system is composed of 3 major vein groups and numerous veinlets in an area 1,100 m by 200 m. They occur in both the Shimanto Supergroup and the Hishikari Lower Andesite (Figure 3-2).

Vein minerals are composed mainly of quartz, adularia and clay minerals. More than 90 % of the clay minerals are smectite, with minor amounts of sericite, chlorite and kaolinite. The principal metallic minerals are electrum, naumannite-aguilarite, pyrargyrite, chalcopyrite, pyrite and marcasite, with minor amounts of sphalerite, galena, stibnite, tetrahedrite, miargyrite, hessite, Ag-Au selenide, acanthite, Cd-sulfide (greenockite or hawleyite), and hematite (Izawa & Urashima, 1987; Urashima & Izawa, 1983). Lamellar quartz is common and, in some places, there are minor amounts of carbonates (calcite and Mn-Fe-Ca carbonate), gypsum, truscottite (alkali-free and alkali-rich varieties), xonotlite, wairakite and laumontite (Izawa & Nakae, 1983; Urashima & Izawa, 1982).

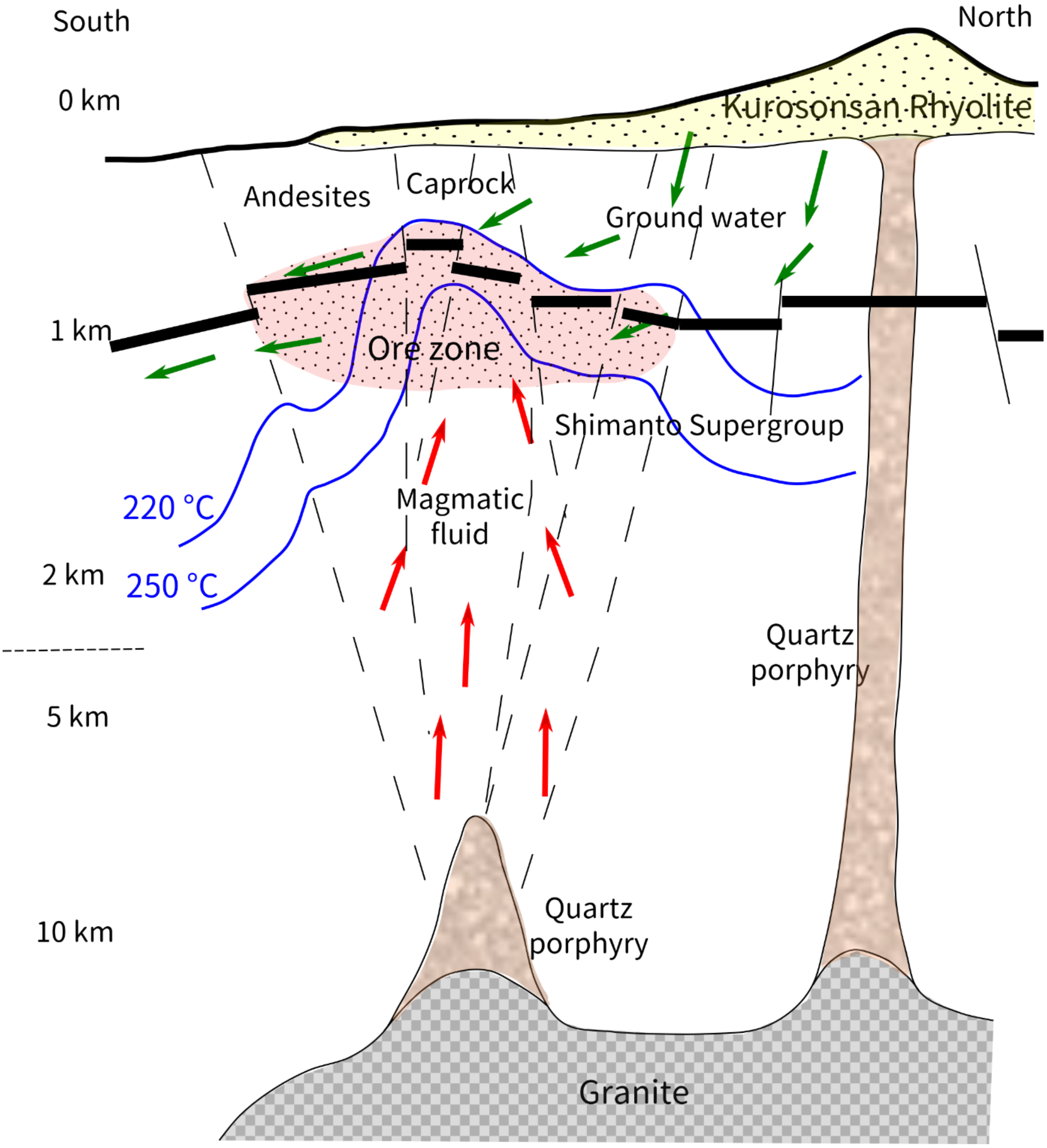

Figure 3-3. Schematic model for the formation of the Hishikari gold deposit emphasizing magmatic origin of gold and sulfur related to felsic subvolcanic intrusive body and significant role of the unconformity for the gold deposition (Ishihara et al., 1986). The Figure was generated using professional quality vector graphics software (Inkscape Project, 2019).

3.4 Lineaments studies

A quantitative study of lineaments was carried out to determine the length and directional patterns of lineament sets about geological structures. In this study, a band combination of cloud-free Landsat 7 Enhanced Thematic Mapper Plus (ETM+) of path/row 169/60 acquired on May 10, 2016, was integrated with the geological map and analyzed alongside a shaded relief map created from Digital Elevation Model (DEM). The DEM was extracted from Shuttle Radar Topography Mission (SRTM) data retrieved from the online Data Pool, courtesy of the NASA Land Processes Distributed Active Archive Center (LP DAAC), USGS/Earth Resources Observation and Science (EROS) Center. The preprocessing of Landsat image included conversion from a calibrated digital numbers (DNs) to physical units, such as sensor radiance and surface reflectance (SR), using Landsat calibration and FLAASH (Fast Line-of-Sight Atmospheric Analysis of Spectral Hypercubes) algorithm of ENVI software (Gawad et al., 2016; Kanda et al., 2019; Matthew et al., 2002).

The edge detection algorithm of Canny (1986) was used to retrieve the lineaments. This algorithm is famously known for its suitability based on the three criteria of proper localization, good detection and single response to an edge (Ding & Goshtasby, 2001; Heath et al., 1996). The Canny algorithm uses a filter based on the first derivative of a Gaussian for the reason that it is prone to noise present on the unprocessed image data (Marghany & Hashim, 2010). The operation of retrieving lineaments was carried out using arguably the most widely used software for the automatic lineament extraction, the LINE module of the PCI Geomatica (PCI Geomatics, 2015). The linear density of lineaments was then calculated as their total length per unit of the area using Line Density tool built in ESRI ArcGIS © software which computes the density (in units of length per unit of area) of linear features in the neighborhood of each output raster cell. Spatial properties of lineaments related to geological displacement have played an essential role in tectonic studies for the delineation of structural units as well as in identification of geological boundaries (Abebe et al., 1993; Ekneligoda & Henkel, 2010; Hashim et al., 2013; Kageyama et al., 2000; Marghany & Hashim, 2010; Mountrakis & Luo, 2011; Noltimier et al., 1998; Salati et al., 2011). Analysis of these structures (fractures, faults, dikes, and lithological contacts), from remotely sensed Satellite data is widely used as the basis of information for geologists to map lineaments at local and regional scales and provides useful information for energy and mineral exploration.

Lineaments in the present work are analyzed using rose diagrams, which are some of the conventional methods generally used (Hung et al., 2005; Karnieli et al., 1996; Zakir et al., 1999). In this study area, in the municipality of Isa, a total of 277 lineaments (with total length of 157,691 m) were extracted with lengths, comprising of both natural features owing to geology-related structures and artificial lineaments that arise due to human-made features such as roads, farm boundaries, among others. Lineaments considered as products of human activities were excluded by use of DEM map with multiple sun azimuth directions in addition to field observations.

Figure 3-4 shows a quantitative study of lineaments conducted to determine the length and directional patterns of lineament sets. In the present study, the lineaments map was used to find the link between the distributions of existing geological faults. Lineaments has been widely used as a tool in the delineation of fracture zones based on lineament indices extracted from satellite imagery (Hung et al., 2005). The geological map was used to corroborate the density concentrations and known lithological units in the study area. The Rose diagrams, Figure 3-4, show the azimuths direction of the local distribution of lineaments trending ENE-WSW, with radial coordinate indicating the distribution percent of lineament. Analysis of the orientation of structures completed using rose diagrams helps in ascertaining the most common directions of the lineaments, which then can be compared with directions of existing faults. This angular tendency corresponds pretty much to that of the faults, the general trend from lineaments matched with the regional trend of Kagoshima Graben, which is shown in Figure 1-10a (Faye et al., 2018; Izawa et al., 1990; Tsuyuki, 1969).

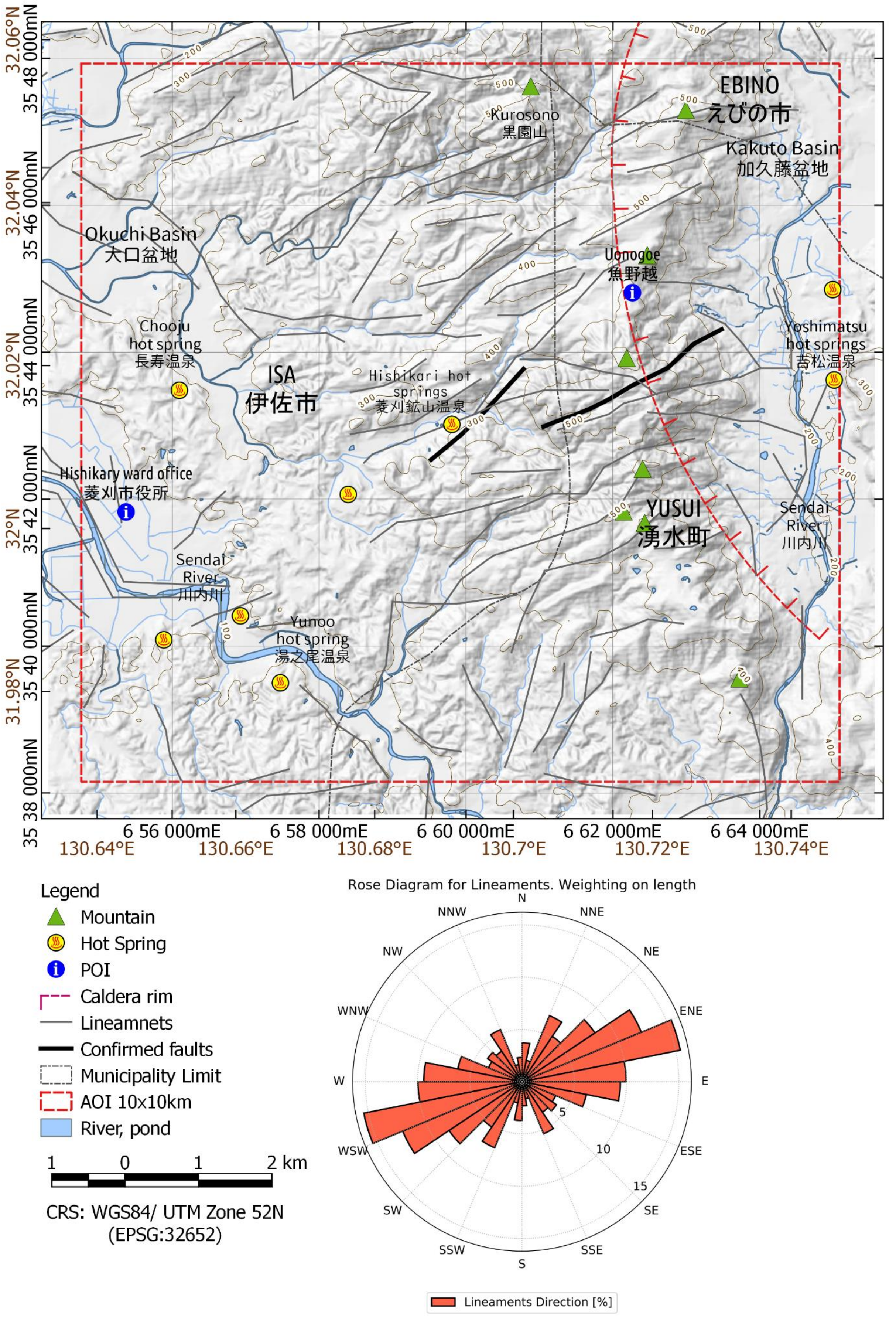

Figure 3-4. Lineament map of the study area in the eastern part of Isa, Kagoshima.

Using the QGIS line direction histogram Plugin, the rose diagram was obtained (QGIS Development Team, 2017; Tveite, 2015). The main functionalities of the plugin are: 1) it creates a rose diagram that can be used to investigate the distribution of the directions of line segments of a line or polygon vector dataset; 2) the accumulated lengths of the line segments for each direction bin determines the shape of the histogram. Alternatively, the number of segments can be used (no weighting on line segment length); 3) Line and Polygon vector layers are supported, including multigeometries; 4) Feature selections are supported; 3) the number of direction bins for the histogram can be specified; 5) All the direction bin sectors will have the same size (same number of degrees covered). This type of angle histogram is also called a “rose diagram” or “rose plot”; 6) an angle offset (positive or negative - clockwise or counter clockwise) for the direction bins can be specified; 7) the positions of the direction bins are shown graphically; 8) the user can choose if the histograms shall be “orientation” neutral (0-180 degrees instead of 0-360 degrees); 9) the histogram can be saved to a either CSV, PDF file, or copied to the clipboard. Table 3-1 shows the line direction histogram results. The angle is quantified from north to south. The table shows that the predominant directions are angles 56.25°-67.5°, 67.5°-78.75°, and 78.75°-90° which correspond NE, ENE, and E respectively.

Table 3-1. Rose diagram data for lineament in the study area.

Start Angle	End Angle	Length [m]	Number	Percent
0	11.25	5869.9308	9	3.7%
11.25	22.5	3268.90715	7	2.1%
22.5	33.75	10786.1111	23	6.8%
33.75	45	8222.44358	11	5.2%
45	56.25	13238.1972	25	8.4%
56.25	67.5	19488.9494	30	12.4%
67.5	78.75	24342.8671	36	15.4%
78.75	90	15708.7047	24	10.0%
90	101.25	14831.2609	30	9.4%
101.25	112.5	9881.70458	21	6.3%
112.5	123.75	5473.81227	9	3.5%
123.75	135	6251.17008	11	4.0%
135	146.25	5538.96573	15	3.5%
146.25	157.5	8498.55145	13	5.4%
157.5	168.75	2632.24385	6	1.7%
168.75	180	3657.50488	7	2.3%

3.5 Well temperature logging in the study area

The Government of Japan did the excavation work or drilled up to 10 exploration wells for understanding the geology, geochemistry, and heat flow using temperature logging, of the zone (NEDO New Energy and Industrial Technology Development Organization, 1991). The Table 3-2 lists the exploration wells drilled in the eastern part of Isa.

Table 3-2. List of well showing the primary characteristics (NEDO, 1991).

Name	Lon [°]	Lat [°]	Depth [m]	Max temp. [°C]	Elevation [m.a.s.l]	Water table [m]
HK-T-1	130.68948	32.05842	400	42.1	317	2 (315 m.a.s.l)
HK-T-2	130.66629	32.04108	400	29.5	237	54 (183 m.a.s.l)
HK-T-3	130.68813	31.9938	400	49.7	236	31 (205 m.a.s.l)
N1-HK-6	130.71502	32.01125	1500	118.2	470	327.5 (142 m.a.s.l)
N1-HK-7	130.68147	32.00215	1503	106.7	228	93.7 (134 m.a.s.l)
N62-HK-1	130.66635	32.02201	1000	73.3	197	23.1 (174 m.a.s.l)
N62-HK-2	130.70193	32.01149	1000	99	295	207 (88 m.a.s.l)
N63-HK-3	130.6983	32.02368	1000	67	355	262 (93 m.a.s.l)
N63-HK-4	130.71007	32.00498	1500	113.6	450	370 (80 m.a.s.l)
N63-HK-5	130.67962	31.99646	1200	102.2	240	1.6 (238 m.a.s.l)

The wells are located in a variety of places from areas whose elevation is from 200 m a.s.l to 500 m a.s.l. This shows a lithological and geological variety such as Goshiki Andesite, Hannyaji welded tuff, Ichiyamagawa upstream andesite, Kirishima Welded tuff, Kusumoto Andesite, Nagano Formation, Shimanto Supergroup, Shinkawa andesite, Shinkawa conglomerate, ShishiMano Dacite, Tataraishi andesite, Weathered rock, Yamadagawa Andesite, and Yotsueda andesite (Figure 3-7); also, the rock properties are described in detail in the Table 3-3 (Faye et al., 2018).

The wells were drilled for different purposes, for example, HK-T1, HK-T2, and HK-T3 are exploratory; the others besides being experimental, but also have the intention of looking for a possible geothermal reservoir. The depths vary from 400 m to 1500 m deep. The wells that have the highest depths also show the maximum temperatures of 118.2, 106.7, 113.6 °C which are N1-HK-6, N1-HK-7, and N63-HK-

4 respectively. These wells can be used for the installation of a small geothermal plant just in case somebody decided to utilize them.

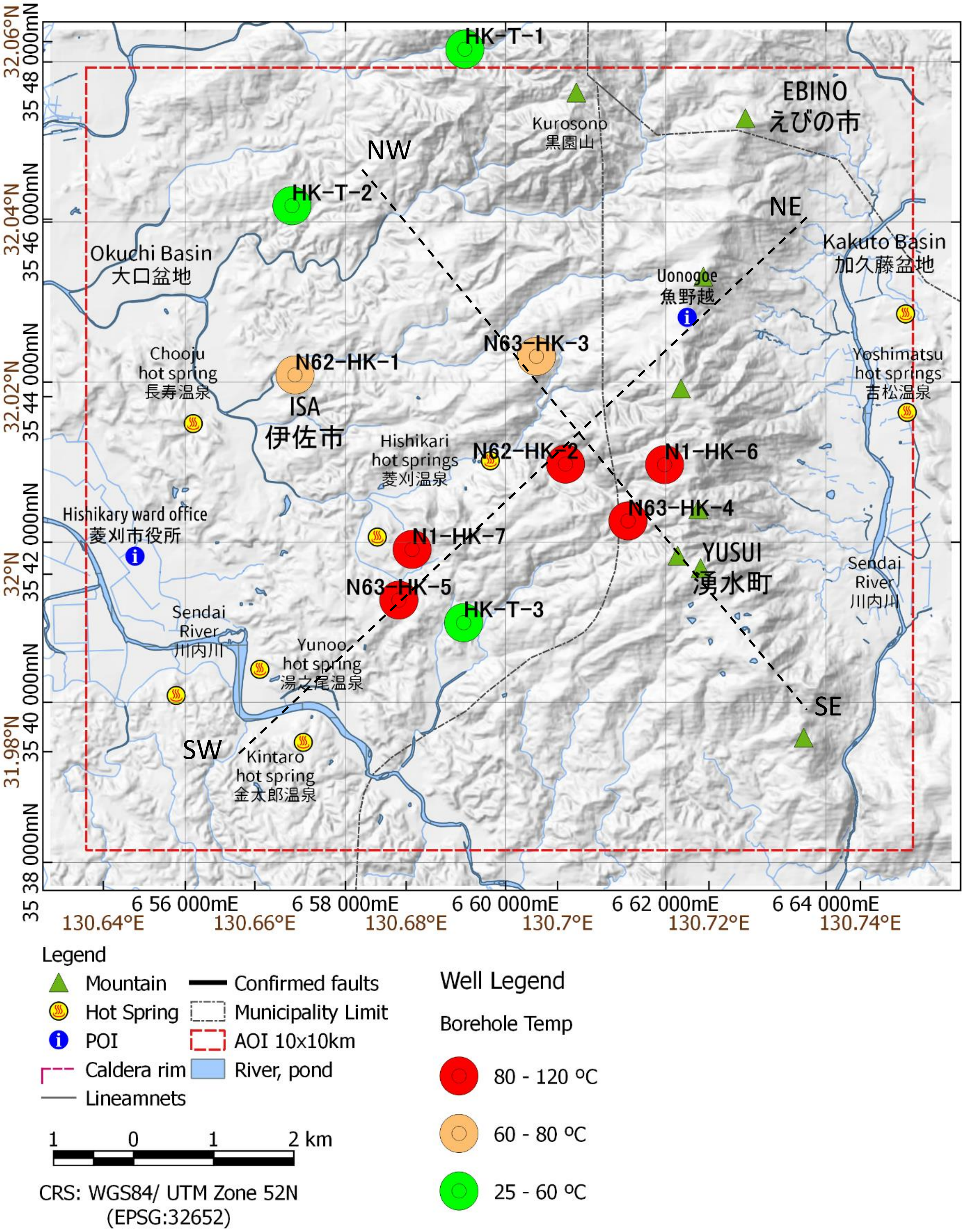

Figure 3-5. Location of the wells in the eastern part of Isa. Also, the bottom temperature is highlighted using color range such as red, orange, and green for 80-120 °C, 60-80 °C, and 25-60 °C respectively (NEDO, 1991).

Table 3-3. Rock properties of the geology structures in the study area (Faye et al., 2018; NEDO, 1991).

Age		Geologic formation			Rock type	Density (g.cm^{-3})									Effective Porosity (%)			Magnetic susceptibility (*10E^{6} emu.cc^{-1})			Elastic wave speed									Thermal conductivity (*10E^{-3} cal.cm^{-1}.sec^{-1}.°C^{-1})		
						natural			dried			wet									natural			dried			wet					
						max	min	Average	max	min	Average	max	min	Average	max	min	Average	max	min	Average	max	min	Average	max	min	Average	max	min	Average	max	min	Average
Pleistocene	Middle	Hannyaji welded tuff			Tuff	*	*	*	*	*	*	*	*	*	*	*	*	66	66	66	1.24	1.24	1.24	1.89	1.89	1.89	*	*	*	2.52	1.75	2.135
					lapilli tuff	-	-	-	-	-	-	-	-	-	-	-	-	-	-	-	-	-	-	-	-	-	-	-	-	1.006	1.006	1.006
					welded tuff	2.18	2.18	2.18	2.16	2.16	2.16	2.28	2.28	2.28	11.4	11.4	11.4	1701	1701	1701	3.28	3.28	3.28	3.37	3.37	3.37	3.46	3.46	3.46	2.614	2.27	2.412
					Total	2.18	2.18	2.18	2.16	2.16	2.16	2.28	2.28	2.28	11.4	11.4	11.4	1701	66	884	3.28	1.24	2.26	3.37	1.89	5.26	3.46	3.46	3.46	2.614	1.006	2.02
	Early	Shishimano Dacite			Pumice (tuff)	*	*	*	*	*	*	*	*	*	*	*	*	661	661	661	0.77	0.77	0.77	0.86	0.86	0.86	0.56	0.56	0.56	0.811	0.811	0.811
					lava	2.41	2.28	2.33	2.4	2.26	2.32	2.44	2.34	2.38	8.2	3.6	6.4	741	532	627	4.12	3.02	3.44	4.19	2.91	3.43	4.26	3.13	3.61	4.506	2.667	3.675
					Total Strata	2.41	2.28	2.33	2.4	2.26	2.32	2.44	2.34	2.38	8.2	3.6	6.4	741	532	636	4.12	0.77	2.77	4.19	0.86	2.78	4.26	0.56	2.85	4.506	0.811	2.959
		Shishimano Volcanic rocks	Hishikari Middle andesites	Yotsueda Andesite	tuff breccia	-	-	-	-	-	-	-	-	-	-	-	-	-	-	-	-	-	-	-	-	-	-	-	-	2.578	2.47	2.524
					Volcanic (pyroclastic) breccia	-	-	-	-	-	-	-	-	-	-	-	-	-	-	-	-	-	-	-	-	-	-	-	-	3.303	3.303	3.303
					lava	2.76	2.36	2.6	2.74	2.32	2.57	2.76	2.43	2.62	11.1	2	4.8	3602	1692	2186	5.6	3.9	4.84	5.37	3.96	4.74	5.6	4.09	4.85	4.753	3.456	4.649
					Volcanic breccia	2.05	2.05	2.05	1.89	1.89	1.89	2.19	2.19	2.19	30.3	30.3	30.3	2500	2500	2500	2.33	2.33	2.23	1.48	1.48	1.48	1.62	1.62	1.62	2.542	2.542	2.542
					Total Strata	2.76	2.05	2.49	2.74	1.89	2.44	2.76	2.19	2.53	30.3	2	9.9	3062	1692	2249	5.6	2.33	4.34	5.37	1.48	4.08	5.6	1.62	4.2	4.753	2.47	3.277
			Hishikari Lower andesites	Goshiki Andesite	Tuff breccia	1.68	1.68	1.68	1.64	1.64	1.64	2.02	2.02	2.02	37.9	37.9	37.9	749	749	749	1.4	1.4	1.4	1.32	1.32	1.32	1.42	1.42	1.42	1.32	1.32	1.32
				Shinkawa Andesite	Tuff breccia	2.1	2.1	2.1	2.05	2.05	2.05	2.25	2.25	2.25	20.7	20.7	20.7	2362	2362	2362	3.66	3.66	3.66	3.41	3.41	3.41	3.32	3.32	3.32	2.781	2.781	2.781
					lava	2.38	2.38	2.38	2.31	2.31	2.31	2.39	2.39	2.39	8	8	8	1800	1800	1800	4.66	4.66	4.66	4.5	4.5	4.5	4.84	4.84	4.84	3.12	3.12	3.12
					Total Strata	2.38	2.1	2.24	2.31	2.05	2.18	2.39	2.25	2.32	20.7	8	14.4	2362	1800	2081	4.66	3.66	4.16	4.5	3.41	3.96	4.84	3.32	4.08	3.12	2.781	2.951
				Yamadagawa Andesite	tuff	2.16	2.16	2.16	2.13	2.13	2.13	2.39	2.39	2.39	25.6	25.6	25.6	13999	13999	13999	2.16	2.16	2.16	2.69	2.69	2.69	2.29	2.29	2.29	3.956	3.584	3.77
					lapilli tuff	2.1	1.82	1.98	2.06	1.69	1.91	2.27	2.03	2.17	33.8	21	25.7	400	30	249	3.23	2.01	2.82	3.49	2.45	3.02	3	1.99	2.65	4.167	3.828	3.994
					tuff breccia	2.43	1.3	2.09	2.37	1.17	2.01	2.5	1.87	2.24	70.3	5.9	23.9	2880	18	750	4.44	1.57	2.78	4.36	1.61	2.77	4.52	1.65	2.76	7.142	2.109	4.591
					lava	2.8	2.33	2.6	2.79	2.26	2.58	2.8	2.44	2.62	18.5	0.7	4.5	4770	91	1939	5.64	2.83	4.81	5.52	3.19	4.71	5.77	2.86	4.85	6.503	3.631	4.989
					Volcanic conglomerate	2.16	1.8	2	2.12	1.61	1.89	2.31	1.76	2.13	30.1	15.1	23.2	1968	102	1234	3.15	2.31	2.72	3.84	2.03	2.98	3.46	2.39	2.81	4.623	2.453	3.56
					Total Strata	2.8	1.3	2.27	2.79	1.17	2.21	2.8	1.76	2.37	70.3	0.7	16.6	13999	18	1623	5.64	1.57	3.53	5.52	1.61	3.56	5.77	1.65	3.55	7.142	2.109	4.591
		Kurozonsan Volcanic rocks	Hishikari Lower andesites	Kusumoto Andesite	Volcanic breccia	-	-	-	-	-	-	-	-	-	-	-	-	-	-	-	-	-	-	-	-	-	-	-	-	1.881	1.881	1.881
					lava	2.67	2.58	2.62	2.66	2.56	2.6	2.67	2.6	2.63	5.4	1.6	3.5	2224	1374	1752	5.18	4.1	4.58	5.18	4.16	4.68	5.08	4.23	4.68	5.343	4.27	4.867
					Total Strata	2.67	2.58	2.62	2.66	2.56	2.6	2.67	2.6	2.63	5.4	1.6	3.5	2224	1374	1752	5.18	4.1	4.58	5.18	4.16	4.68	5.08	4.23	4.68	5.343	1.881	4.701
				Shinkawa Conglomerate	tuff	-	-	-		-	-	-	-	-	-	-	-	-	-	-	-	-	-	-	-	-	-	-	-	1.658	1.658	1.658
					Pumice tuff	1.69	1.44	1.57	1.46	1.37	1.42	1.87	1.66	1.77	40.9	28.5	34.7	1154	261	708	1.8	1.63	1.72	2.08	1.17	1.63	1.84	1.49	1.67	2.439	0.606	1.731
					tuff breccia	1.82	1.75	1.79	1.69	1.66	1.68	2.01	1.98	2	31.6	3.2	17.4	2096	1230	1616	2.24	1.58	1.91	2.45	1.63	1.92	2.71	1.26	1.99	2.853	1.356	2.19
					Volcanic conglomerate	-	-	-	-	-	-	-	-	-	-	-	-	-	-	-	-	-	-	-	-	-	-	-	-	2.428	2.042	2.235
					Total Strata	1.82	1.44	1.68	1.69	1.37	1.55	2.01	1.66	1.89	40.9	3.2	26.1	2096	261	1162	2.24	1.58	1.85	2.45	1.17	1.8	2.71	1.26	1.83	2.853	0.606	1.988
				Tataraishi andesite	Tuff breccia	1.84	1.43	1.84	1.78	1.09	1.78	2.06	1.7	2.06	60.8	2.85	28.5	740	341	541	2.14	2.14	2.14	2.12	2.12	2.12	1.94	1.94	1.94	2.625	2.139	2.412
					Volcanic breccia	-	-	-	-	-	-	-	-	-	-	-	-	-	-	-	-	-	-	-	-	-	-	-	-	3.378	1.403	2.109
					lava	-	-	-	-	-	-	-	-	-	-	-	-	-	-	-	-	-	-	-	-	-	-	-	-	5.634	4.678	5.126
					Tuffaceous sandstone	2.03	2.03	2.03	2.02	2.02	2.02	2.1	2.1	2.1	8.2	8.2	8.2	238	238	238	1.43	1.43	1.43	1.33	1.33	1.33	*	*	*	3.256	3.256	3.256
					Total Strata	2.03	1.84	1.94	2.02	1.78	1.9	2.1	2.06	2.08	28.5	8.2	18.4	740	238	440	2.14	1.43	1.79	2.12	2.12	1.73	1.94	1.94	1.94	5.634	1.403	3.119
				Ichiyamagawa upstream andesite	lapilli tuff	1.61	1.16	1.39	1.31	1.07	1.19	1.8	1.63	1.72	56.5	49.4	53	2133	218	1176	0.75	0.75	0.75	0.88	0.88	0.88	*	*	*	4.45	2.264	3.768
					tuff breccia	1.65	1.65	1.65	1.59	1.59	1.59	1.95	1.95	1.95	35.3	35.3	35.3	247	247	247	2.28	2.28	2.28	2.39	2.39	2.39	2.13	2.13	2.13	3.306	2.259	2.744
					lava	2.67	2.67	2.67	2.67	2.67	2.67	2.67	2.67	2.67	0.3	0.3	0.3	1606	1606	1606	5.46	5.46	5.46	5.46	5.46	5.46	5.34	5.34	5.34	5.359	4.042	4.323
					Total Strata	2.67	1.65	2.16	2.67	1.59	2.13	2.67	1.95	2.31	35.3	0.3	17.8	2133	218	1051	5.46	0.75	2.83	5.46	0.88	2.91	5.34	2.13	3.74	5.359	2.259	3.51
Pliocene?		Kirishima welded tuff			welded tuff	2.27	2.27	2.27	2.23	2.23	2.23	2.39	2.39	2.39	15.3	15.3	15.3	957	957	957	4.01	4.01	4.01	3.95	3.95	3.95	3.28	3.88	3.88	4.398	4.398	4.398
		Nagano formation			Tuffaceous sandstone	2.26	2.26	2.26	2.16	2.16	2.16	2.42	2.42	2.42	26.6	26.6	26.6	189	189	189	3.04	3.04	3.04	2.97	2.97	2.97	3.28	3.28	3.28	4.392	4.392	4.392
Cretaceous		Shimanto supergroup			Mudstone	2.7	2.38	2.61	2.69	2.36	2.59	2.7	2.43	2.63	12.6	1.7	4.3	204	32	58	5.02	3.11	4.27	5.6	2.11	3.93	4.83	3.4	4.28	9.309	5.073	7.003
					Siltstone	2.63	2.63	2.63	2.63	2.63	2.63	2.66	2.66	2.66	3.4	3.4	3.4	62	62	62	4.75	4.75	4.75	4.42	4.42	4.42	4.34	4.34	4.34	8.94	8.94	8.94
					Sandstone mudstone interlayer	2.85	2.43	2.65	2.82	2.42	2.63	2.84	2.52	2.66	10.2	0.3	3.5	108	37	60	5.13	3.23	4.25	5.35	2.53	3.88	5.35	3.41	4.31	9,406	5.773	7.293
					Sandstone	2.68	2.54	2.64	2.68	2.52	2.64	2.68	2.56	2.65	4	0	1.1	148	36	87	5.73	4.1	5.16	6.3	3.8	5.04	5.59	1.25	5.15	10.856	6.945	8.625
					Total Strata	2.85	2.38	2.64	2.82	2.36	2.62	2.84	2.43	2.65	12.6	0	2.8	204	32	70	5.73	3.11	4.62	6.3	2.11	4.37	5.59	3.4	4.64	10.856	5.073	7.723

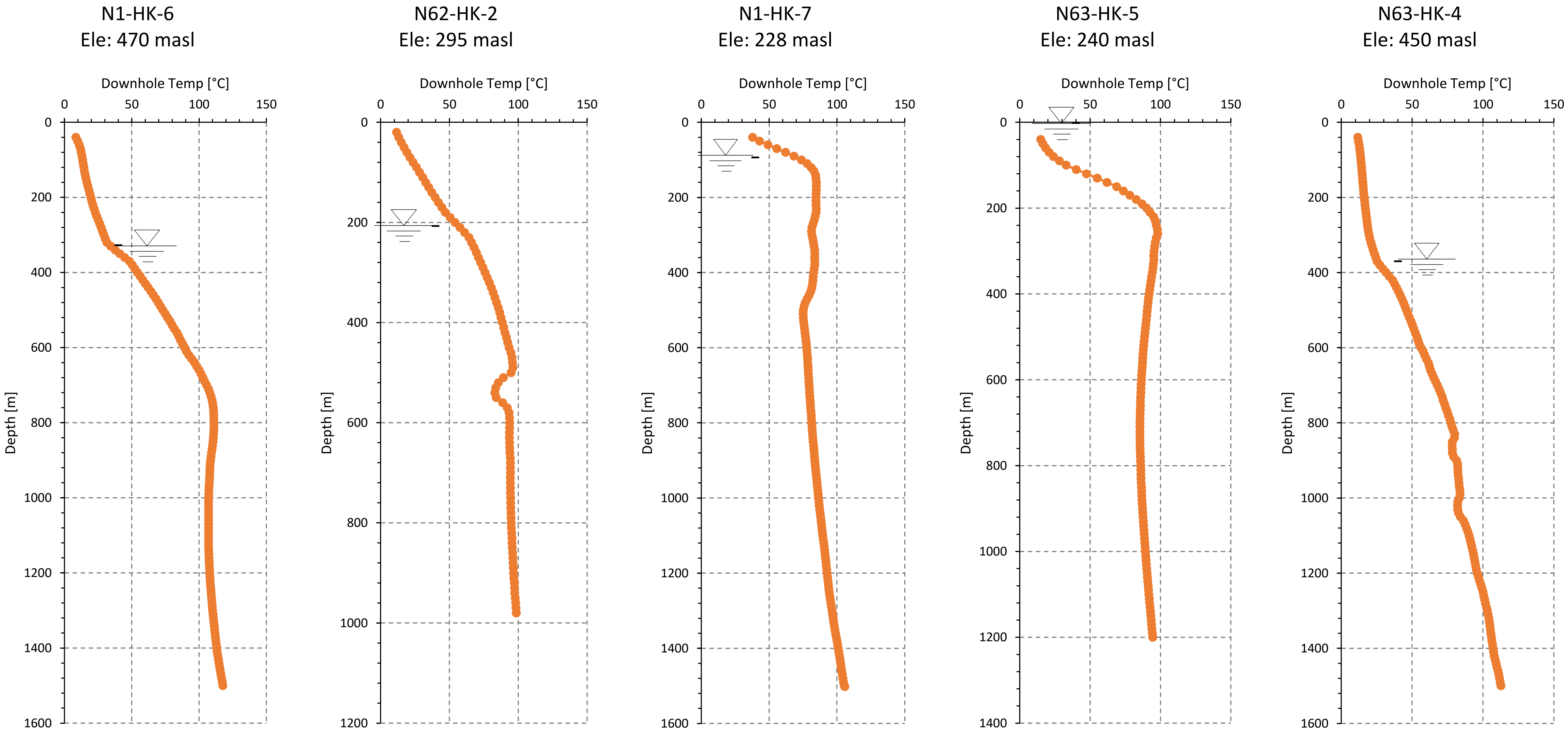

(a)

(b)

(c)

(d)

(e)

Figure 3-6. Downhole temperature of N1-HK-6, N62-HK-2, N1-HK-7, N63-HK-5, N63-HK-4 (NEDO, 1991).

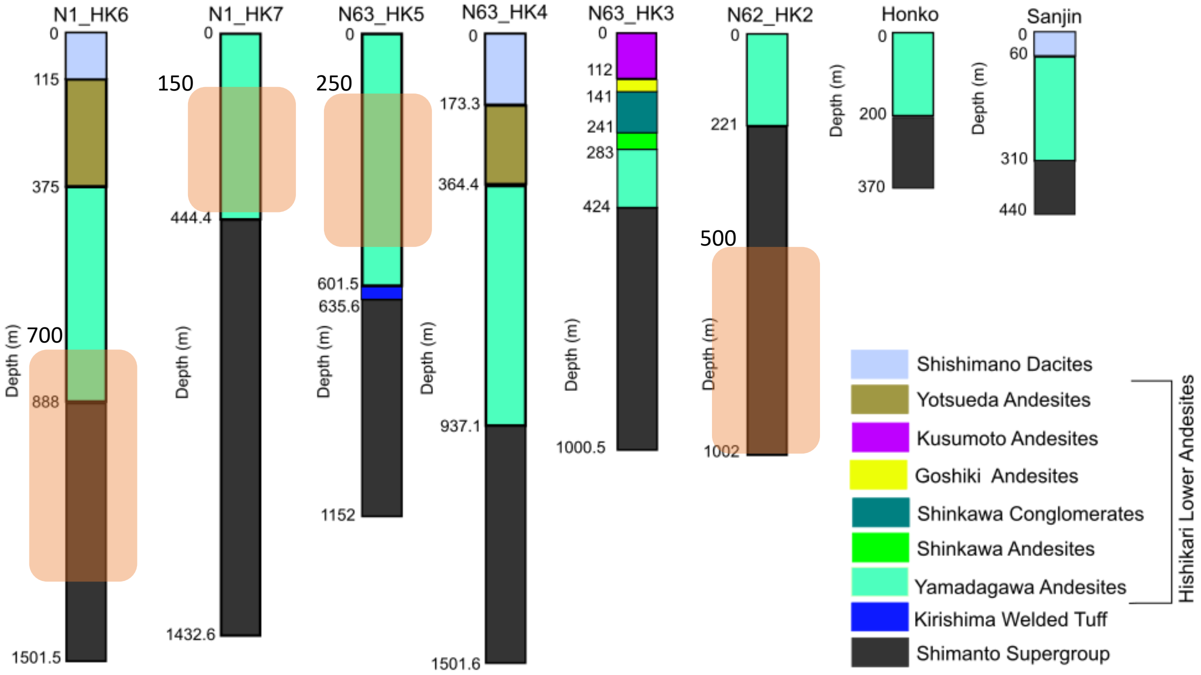

Figure 3-7. General representation of the geology well logging in Isa area. The orange rectangles highlight the location of geothermal reservoir (Faye et al., 2018; NEDO, 1991).

Analyzing the temperature logging, the possible geothermal reservoir location could be estimated (Figure 3-6 and Figure 3-7). The hydrothermal zone is located 500 m and 700 m deep into wells N62-HK-2 and N1-HK-6 respectively in Uonogoe place. Furthermore, at 150 m and 250 m depth into wells N1-HK-7 and N63-HK-5 respectively, i.e., the reservoir possibly extends from NE to an altitude of -250 m a.s.l and rises following the NE-SW line to the 80 m a.s.l. Finally, it finishes around the well N63-HK-5 at -10 m a.s.l depth. The geothermal reservoir can be clearly observed in the conceptual model presented by NEDO (1991) and shown in Figure 3-8.

3.6 Conceptual Model of the geothermal reservoir in Isa region

The geothermal structure or conceptual model in and around the Hishikari area has the following considerations:

1. The reservoir formation is a fractured system and dike filled with stone and calcite in the Yamada River andesite where lava of the Shimanto Supergroup and its upper elevation is predominant.
2. Hot water supplied to the reservoir mainly is sourced from the rain. The supply of rain to the deep ground is primarily conducted through the Shimanto Supergroup, which has developed a highly effective quaternary system with high effective porosity, and the fracture system.
3. Scientists think that there is a countercurrent of shallow underground water in the quaternary structure with high effective porosity, and this countercurrent supplies to the deep underground rainwater.
4. The Shimanto Supergroup supplies the heat to the deep groundwater because the rock has a high heat transfer coefficient. Also, the direct contribution of the volcanic heat transfer body is almost negligible. The heat source that supplies heat to the basement rock is a magma reservoir which might be solidified.
5. The hydrothermal fluid that flows up reacts with the host rock to change the chemical composition, and passes through the altered zone and ascends.
6. The upwelling hydrothermal fluid is led to the formed extensional fissure system or the dike system in which the dike has penetrated in the shallow basement area. At the same time as calcite veins are deposited, it forms a strong-clumping zone in the Quaternary group consisting of volcanic rocks in the upper part of the calcite vein, and a reservoir layer was formed, with the underground area as the cap lock.
7. The hot water contained in the reservoir layer acts as a moving water gradient in the reservoir. It is released as a hot spring at the point where the groundwater appears on the surface.
8. The hydrothermal fluid contained in the geothermal reservoir will be treated chemically depending on the condition of the soil and the formation of rock.

Based on the previous paragraphs, NEDO (1991) presents the conceptual model that is shown in Figure 3-8. Two profiles are presented: SW-NE and NW-SE. These profiles illustrate the orientation of the possible geothermal reservoir. Using this information in the following chapter, the electric energy potential will be calculated.

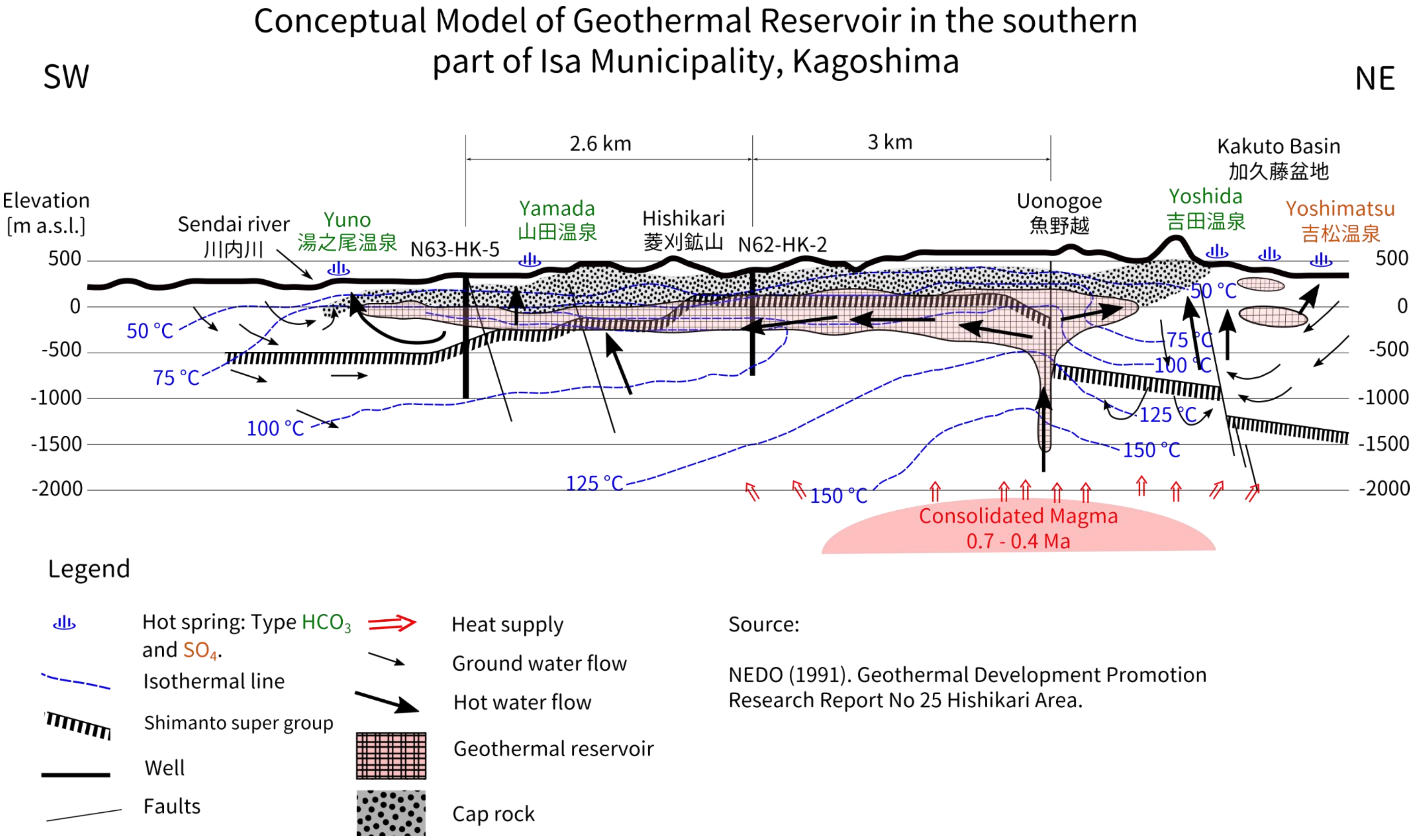

Source:

NEDO (1991). Geothermal Development Promotion Research Report No 25 Hishikari Area.

(a)

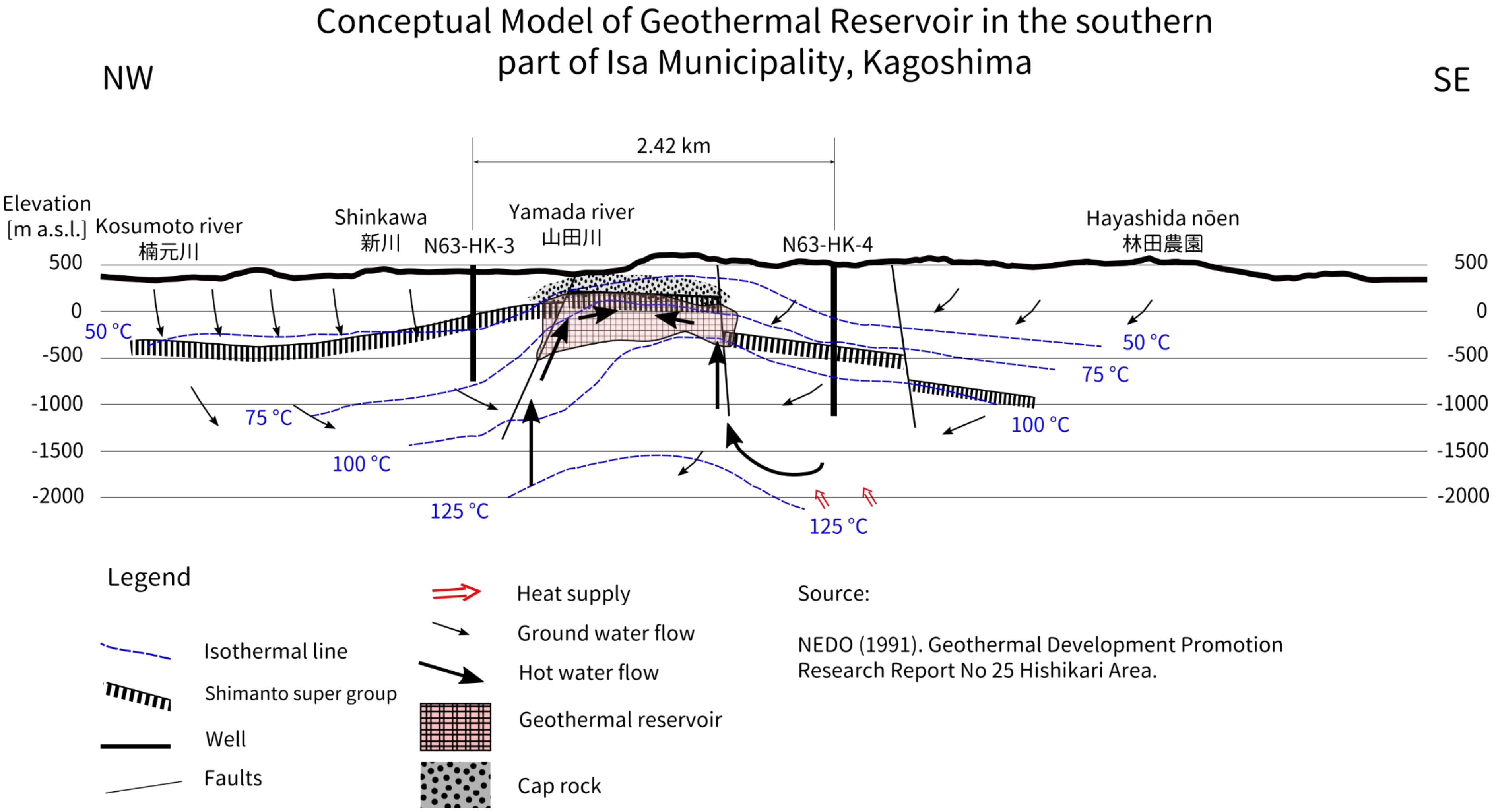

Source:

NEDO (1991). Geothermal Development Promotion Research Report No 25 Hishikari Area.

(b)

Figure 3-8. Conceptual Model of Geothermal reservoir at east of Hishikari gold mine; (a) NE-SW geothermal reservoir profile; (b) NW-SE geothermal reservoir profile. The location of the sections (a) and (b) is shown in Figure 3-5. Courtesy of NEDO (1991).

In the Hishikari area, scientists consider that several types of geothermal systems have been formed in the past as a result of the change in the volcanic activity in this region. They inferred that the most superior geothermal system of this type was formed around 0.91 to 1.15 Ma close to Mount Kurozono (黒園山) site. The fluid inclusion temperature of the veins indicates that the high temperature and dominant hydrothermal activity reached a maximum of 240 °C. The large-scaled deformation zone accompanied by the mineralization of gold and silver were also formed at this time. Considering the distribution of the land temperature and the temperature of the reservoir, the center of the hydrothermal activity is the one near the Uonogoe (魚野越) field in the eastern end of this area. It indicates the possibility that there is a deep underground geothermal potential where the Hishikari upper part andesite was volcanically active. The extrapolated temperature using well logging shows a value of 144 °C.

3.7 Conclusion

The regional geology and structural setting of the study area in the eastern part of Isa, Kagoshima, have attracted much researches, and some review papers have been written due to the importance of gold mine exploitation. The area is an ancient volcanic region, and one of the most important gold mines in Japan is located in this area, Hishikari gold mine. In 1973 the Taio Mining Co., a subsidiary of the Sumitomo Metal Mining Co., Ltd. (SMM), acquired the mineral rights. In the neighborhood of Hishikari region, specifically in the eastern part of Isa City, the fundamental structure in the most profound element is controlled by Cretaceous Shimanto Supergroup; additionally Quaternary volcanic rocks. The topography, ranging from 200 to 600 m in elevation, comprises densely timbered, hilly terrain separated by small valleys cultivated mainly with rice. The atmospheric temperatures range from a low of -7 ℃ to a high of 35 °C. The vein system can be classified as an epithermal gold-silver-bearing quartz-adularia vein deposit. Analysis of the orientation of structures completed using rose diagrams, the angular tendency corresponds pretty well to that of the faults, the general trend from lineaments matched with the regional trend of Kagoshima Graben. Finally, it inferred that the most superior geothermal system was formed around 0.91 to 1.15 Ma close to Mount Kurozono site, and the center of the hydrothermal activity is near the Uonogoe field with an extrapolated temperature of 144 °C using well logging.

Chapter 4

Gravity Data Analysis and Interpretation

4.1 Overview

A local change in a gravity field is interpreted as arising from density variations in the basic model. The genesis of these variations could be structure related such as fault zones, crack density, rock porosity or perhaps associated with a temperature field. Gravity is commonly employed geophysical tool for prospecting unknown geothermal reservoirs and for monitoring reservoir changes during exploitation. During the exploration stage of geothermal development, gravity results are beneficial in delineating geological structures. In this chapter, the gravity method is utilized in understanding the subsurface structures that are controlling the placement of heat sources and thermal fluid flow in the case of the eastern part of the Municipality of Isa.

4.2 Gravity method: theory and application

The Newton's law of gravitation states that the force (N) between two point masses m_1, m_2 (kg) is equal to the product of the two masses and the inverse of the distance square, Equation (4-1); where r (m) is the distance between the masses (Hinze et al., 2013b).

$$F = \frac{G m_1 m_2}{r^2}; \quad G = 6.67 \times \ 10^{-11} m^3 kg^{-1} s^{-2} \tag{4-1}$$

The force is one of the attraction, which acts along the line joining m_1 and m_2 within a gravitation field. The force acting on the point mass m_1 in the gravitation field of m_2 is also given by $'Force(N) = Mass(kg) \times Acceleration\ (m/s^2)'$. A body will experience an acceleration if placed in the vicinity of a point mass of another body's gravitational field, and thus the total force on the mass due to the body in any given direction can be obtained by applying Newton's law to infinitesimal, point mass components of the body and integrating over the entire volume (Parasnis, 1986).

The gravitation potential (Jkg^{-1}) due to a point mass m at a distance r from itself is given by

$$V = \frac{Gm}{r} \tag{4-2}$$

The acceleration a of any point mass towards m is given by differentiating equation (4-2) with respect to r.

$$a = -\frac{Gm}{r^2} \tag{4-3}$$

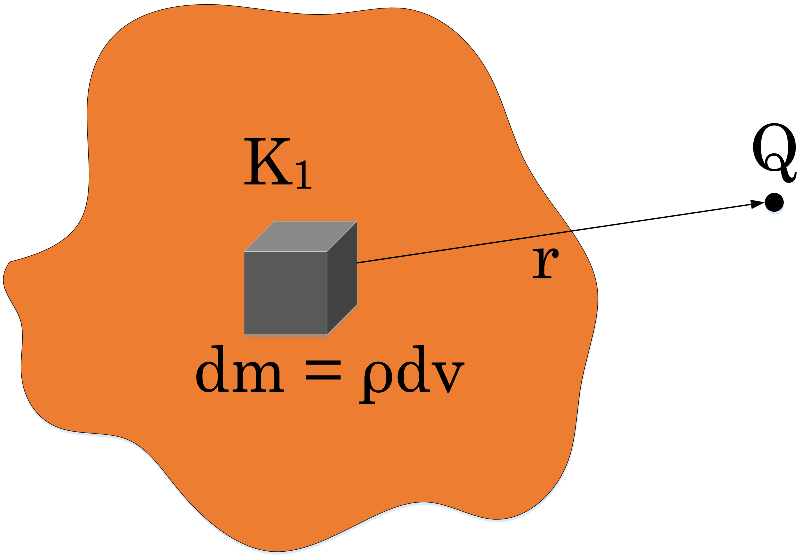

Figure 4-1. Geometry representation of the points K and Q and distance r between them; notations of Equation (4-4).

In general, the acceleration of a point mass in a particular direction is given by the derivative of V in that direction. For an arbitrarily shaped body at a point K, the gravitational potential anywhere in the body is

$$V = \int \frac{G\rho}{r}\, dv \tag{4-4}$$

where ρdv is the mass of an infinitesimal volume element dv positioned at point Q of the body, ρ is the density at Q, **r** is the distance KQ and the integral is taken over the entire volume of the body (Figure 4-1).

Gravity is a geophysical method which has been extensively used to examine density irregularity of deeper subsurface bodies and has successfully been used in exploring geological structures (Nishijima & Naritomi, 2017), groundwater (Carmichael & Henry, 1977; Chen et al., 2014; Feng et al., 2013; Tiwari et al., 2009), magma chambers (Battaglia et al., 1999; Fedi et al., 2018; MacQueen et al., 2016), and geothermal resource (Guglielmetti et al., 2013; Hunt, 1970; Mariita, 2012; Tontini et al., 2015). The interpretation of lateral structures suffers from an inherent non-uniqueness. That is, an infinite number of mass distributions may give rise to the same potential on the surface (Phillips & Lambeck, 1980). Nonetheless, a good model should be more sensible and comparable to other available geophysical and geological data.

4.3 The gravity survey analysis

As part of the main objective of this study, which is to analyze the gravity data for figuring out geothermal reservoir border and calculating the geothermal power energy, an area of 10 x 10 km was selected (31.97°N to 32.06°N and 130.64°E to 130.75°E) as well as the analysis of available gravity data comprising of 175 stations (Geological Survey of Japan, 2013; Pocasangre & Fujimitsu, 2017) and Bureau Gravimétrique International BGI (Drewes et al., 2016). Measurement stations were insufficient and therefore further survey is needed for better understanding of the area. During the testing survey, measurements were carried out using a Scintrex CG-5 which has a reading resolution of 0.001 mGal, and repeatability accuracy of 0.005 mGal (Scintrex, 2012). The stations were positioned by using a Differential Global Positioning System (DGPS), whose vertical uncertainty is lower than 0.03 m. This form of Global Positioning System, GPS uses a static base station as the reference position to adjust real-time GPS signals in order to eliminate pseudo-range errors. DGPS data provided accurate relative positions for all the gravity stations measured during the survey.

Usually, the readings of gravimeters drift with time due to elastic change in the springs causing an apparent change in the gravity at any given station. These fluctuations may vary from as low as 0.01 mGal to about 1 mGal per hour (Hinze et al., 2013a, 2013b; Parasnis, 1986). Measurements were done at the beginning of the survey of any given day at a designated station (reference station), repeated at the close of the daily survey. The differences obtained were plotted against the time between the two readings at a station in order to correct the drift problem. The corrections were then obtained from a 'drift curve' since most gravimeters drift linearly with time.

4.4 Gravity data reduction and Bouguer density estimation

4.4.1 Gravity data correction

Gravity measurements are usually not made on the Earth's ellipsoid in actual practice. Hence, appropriate corrections must be applied to the measured gravity to reduce it to sea-level equivalent. These corrections allow the determination of an anomaly by subtracting the normal gravity value from the actual measured value. Several corrections which include latitude correction, free-air correction, Bouguer correction and terrain correction, were done to the observed gravity to obtain the Bouguer anomaly. This is the local irregularities in the topography, and earth variables around a gravity station may give rise to significant effect, e.g., hills rising above the stations will cause a reduction in gravity or upward pull while valleys falling below the stations will cause a reduction in gravity due to the deficit of mass that would be included in the Bouguer assumption of an infinite slab (Saibi et al., 2007). The Bouguer anomaly is calculated at gravity ellipsoid by adding Free-Air correction, Bouguer effect, and terrain effect, see Equation (4-5) and Figure 4-2.

Bouguer anomaly (BA) in $mGal$ can be loosely defined as the measured gravity corrected for the known or modeled gravity effects at a planetary scale (Karcol et al., 2017), and written in the form of a simplified equation (Yamamoto, 1999a), see Equation (4-5).

$$BA = g - \gamma + \beta h - 2\pi G\rho h + \rho T \tag{4-5}$$

where g $(mGal)$ is the observed absolute gravity, γ $(mGal)$ is the normal gravity value, $\beta(mGal/m)$ is the elevation-dependent free-air term, and T is the terrain correction per unit density. G $(m^3.kg^{-1}.s^{-2}), \rho$ $(kg\ m^{-3})$and $h(m)$, are the universal gravitational constant, density and elevation terms, respectively.

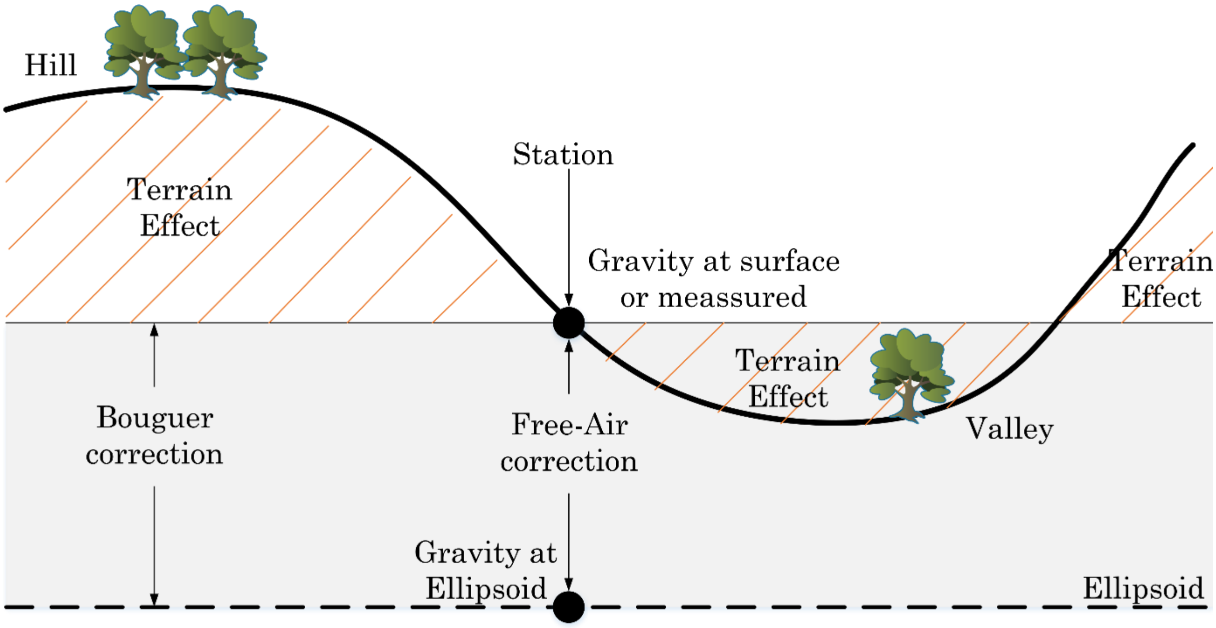

Figure 4-2. Bouguer anomaly calculated at gravity ellipsoid adding Free-Air correction, Bouguer effect, and Terrain correction (Saibi et al., 2007).

1. Latitude correction (normal gravity)

Latitude correction γ, deals with the shape of the earth where the radius of the earth's poles is smaller than the radius along earth's equator. However, there is an opposing centrifugal acceleration at the equator and more mass under the equator. The net effect is that gravity at the poles is greater than the equator. The gravity effect of a reference ellipsoid is represented by normal gravity as a geometry, which can be defined to represent the shape of the Earth. The computation of the gravity effect is straightforward since the ellipsoid can be defined mathematically. The Somigliana–Pizetti formula (Götze, 2011; Hofmann-Wellenhof & Moritz, 2006) expresses a closed-form expression for calculating the normal gravity on the surface of a geocentric reference ellipsoid, and is expressed by

$$\gamma = \gamma_e \frac{1 + k\sin^2\phi}{\sqrt{1 - e^2 k\sin^2\phi}} \tag{4-6}$$

where k is the normal gravity constant (0.00193185265241), γ_e is the normal gravitational acceleration at the equator (9.7803253359 m s^{-2}), ϕ is the geodetic latitude, and e^2 is the square of the first numerical eccentricity of the ellipsoid (6.69437999014 × 10^{-2}). The values k, γ_e and e^2 are WGS 84 reference ellipsoid derived constants (NIMA, 1984).

2. Free-air correction

The free-air correction β, accounts for gravity disparities caused by elevation changes in the measurements point, p, which is almost never located precisely on the surface of the reference ellipsoid. This implies that the model value at p above the reference ellipsoid will be less than γ, and this is accounted by free-air correction, which uses the rate of change in gravity above the Earth surface to correct for the drop in gravity with elevation. The value of the free-air correction was traditionally approximated as 0.3086 mGal/m, the gradient above a spherical Earth, and can be expressed as

$$\beta = \frac{\partial g}{\partial h} h \tag{4-7}$$

3. Bouguer correction

The Bouguer correction, BGC, is a first-order reduction to account for the excess mass underlying measurement point located at elevations higher than the reference ellipsoid, and also for a mass deficiency at measurement point positioned below the reference ellipsoid. The Bouguer correction is computed by representing the body of rock between the observation point and surface of the reference ellipsoid as a slab that extends horizontally to infinity. The most sophisticated illustrations of the rock mass below the measurement station accounts for the curvature of the Earth's surface, and the common representation is the spherical cap, ${\delta_{gB}}^{cap}$, the gravity effect given by LaFehr (1991a):

$${\delta_{gB}}^{cap} = 2\pi G\rho[\mu t - \lambda(R_E + t)] \tag{4-8}$$

where ρ is the assumed density of the slab, t is the thickness of the cap which is generally equivalent to h, and G is the universal gravitational constant, $6.67 \times 10^{-11}\ m^3.kg^{-1}.s^{-2}$. R_E is the mean radius of the reference ellipsoid, μ and λ are dimensionless coefficients connected to R_E, and whose angle is subtended by the spherical cap at the center of the Earth. Bullard (1936) originally selected a spherical cap that extends to a distance of 166.735 km from the observation point in order to minimize the difference between the infinite slab and the gravity effect of the spherical cap for a range of elevations (LaFehr, 1991b).

4. Terrain correction

The terrain correction, T, accounts for disparities in the observed gravitational acceleration caused by the differences in topography of areas surrounding the measurement point. Terrain correction is positive irrespective of whether the local topography is mountains or a valley due to the assumptions made during the Bouguer correction. In general, computation of terrain corrections is divided into two segments which independently consider the near and far topography (Hinze et al., 2013a). A number of methods used in terrain correction have been proposed and reviewed in previous works (Banerjee & Das Gupta, 1977; Hammer, 1939; Nagy, 1966; Nishijima, 2009; Nowell, 1999; Saadi et al., 2008; Yamamoto, 2002). In this study, a code written by Nishijima (2009) is used to compute spherical terrain corrections for gravity data using ASTER GDEM v2 Worldwide Elevation Data (1-arc-second resolution) obtained from the NASA Land Processes Distributed Active Archive Center (LP DAAC), USGS/Earth Resources Observation and Science (EROS) Center. This method is based on a standard right rectangular prism model in a distant zone of a given gravity station. The vertical elements of the gravitational attraction at the origin due to a right rectangular prism bounded by planes $x = x_1$, $x = x_2 (x_2 > x_1)$; $y = y_1$, $y = y_2 (y_2 > y_1)$; and $z = h > 0$; is given by

$$g_p = G\rho[F(x_2, y_2, h) - F(x_1, y_2, h) - F(x_2, y_1, h) + F(x_1, y_1, h)] \tag{4-9}$$

where G is the universal gravitational constant and ρ is the density of the prism (Banerjee & Das Gupta, 1977; Nagy, 1966), and the function F is given by

$$F(x, y, h) = x \ln\left(\frac{y + \sqrt{x^2 + y^2}}{y + \sqrt{x^2 + y^2 + h^2}}\right) + y\, ln\left(\frac{x + \sqrt{x^2 + y^2}}{x + \sqrt{x^2 + y^2 + h^2}}\right) \tag{4-10}$$

$$+h \tan^{-1}\left(\frac{xy}{h\sqrt{x^2 + y^2 + h^2}}\right)$$

4.4.2 Bouguer density estimation methods

To evaluate the Bouguer anomaly, a *priori* knowledge about gravity reductions is necessary. Performing a complete Bouguer reduction demands proper selection of the reduction density. The commonly accepted density value of 2.67×10^3 kg m^{-3} is a reasonable compromise for a specific group of geological rocks (Bowie, 1912), which assumes that the mean density of continental surface rocks is crystalline and of granitic in composition (Hinze, 2003). A quantitative study of gravity anomalies demands an accurate Bouguer reduction density and considering the geology of Isa area that predominantly consists of volcanic rocks (Andesite), sedimentary basement and quaternary sediments, this standard value may not give the optimum value required. Estimation of Bouguer density from the gravity data is deemed the best way to calculate the optimum Bouguer density (Murata, 1993). Following is described several methods for calculating the Bouguer density (Yamamoto, 1999b).

1. Simple G-H method

Bouguer anomalies are described as a function of altitude and the density is estimated by the procedure based on a linear fitting scheme. The optimum density is determined from the slope of a best fitting straight line. The Simple G-H method generally does not consider terrain corrections. Rearranging equation (4-5), the new expression is

$$BA = \left(g_{obs} - \gamma + \rho T\right) + (\beta - 2\pi G\rho)h \tag{4-11}$$

Substituting the first term of the right-hand side with Q and the coefficient of h in the second term with α of Equation (4-11), then the equation becomes

$$BA = Q + \alpha h \tag{4-12}$$

The optimum density can then be obtained either from the slope of the plot of Q ($= g - \gamma$) against h or using the statistic solution in Equation (4-13) which is coded on Python language (Figure 4-3).

$$\rho_{GH} = \frac{\sum_{i=1}^{N}(h_i - \bar{h})(F_i - \bar{F})}{2\pi G \sum_{i=1}^{N}(h_i - \bar{h})^2} \tag{4-13}$$

where

$$F_i = g_i - \gamma_i + \beta h_i$$

```
# -*- coding: utf-8 -*-
"""
@author: Carlos Pocasangre
Description: script for calculation Bouguer Density by using G-H method
input file "input.csv": [station, lon, lat, elevation, gravObs]
use: python input.csv
"""
import numpy as np
from sys import argv
import matplotlib.pyplot as plt
beta = 0.3086; G = 6.673e-11
TextUsed = ['STA','LON','LAT','ELEV','GRAVOBS']
FileTypeCSV=np.dtype([
                         (TextUsed[0],str,10),
                         (TextUsed[1],float),
                         (TextUsed[2],float),
                         (TextUsed[3],float),
                         (TextUsed[4],float)])

def ReadFile(InputFileName):
    return np.genfromtxt(InputFileName,delimiter=',',comments='#',skip_header
            = 1,dtype=FileTypeCSV)

def NormalGravC(Lat):
    "Calculate the Normal Gravity Correction, return value [mgal]"
    a = 6378137.0
    b = 6356752.3141
    gamma_a = 978032.67715
    gamma_b = 983218.63685
    Lat = Lat * np.pi / 180.0
    return (a * gamma_a * np.cos(Lat) ** 2 + b * gamma_b * np.sin(Lat) ** 2) /
           np.sqrt((a * np.cos(Lat)) ** 2 + (b * np.sin(Lat)) ** 2)

def GraphXY(x,y,SetTitle,SetTextX,SetTextY,legendText,AxisXY,LocationLegend,
            LegendTextPositions):
      fig = plt.figure()
      ax1 = fig.add_subplot(111)
      ax1.plot(x,y,'ob',markersize=4)
      ax1.grid()
      ax1.set_title(SetTitle,fontsize=16)
      ax1.set_xlabel(SetTextX,fontsize=14)
      ax1.set_ylabel(SetTextY,fontsize=14)
```

```
        return ax1

def linefunc(A,B,x):
    return A * x + B

def FiguresToPresent(value=1,figures=1):
        fi = '%.'+str(figures)+'g'
        value = fi%value
        return value

if __name__ == "__main__":
        script, InputFileName = argv
        DATA = ReadFile(InputFileName)
        n = len(DATA)
        X = DATA[TextUsed[3]][:]
        Y = DATA[TextUsed[4]][:] - NormalGravC(DATA[TextUsed[2]][:])
        XY = X * Y
        sumXY = np.sum(XY)
        X2 = X ** 2
        sumX2 = np.sum(X2)
        sumX = np.sum(X); sumY = np.sum(Y)
        A = (n * sumXY - sumX * sumY)/(n * sumX2 - sumX ** 2)
        B = (sumY - A * sumX)/n
        rho = (beta - np.abs(A))/(2e5*np.pi*G)
        print "rho [kg/m3]: ",rho
        print "rho [g/cm3]: ",rho/1000
        fitY = linefunc(A,B,X)
        g1 = GraphXY(X,Y,"Bouguer Density G-H","Elevation [m]","Q
              [mGal]",["1h","12h","24h"],[min(X)-
              10,max(X)+10,min(Y),max(Y)],1,[4,0.5e7,11,0.5e7,17,0.5e7])
        g1.plot(X,fitY,'r',linewidth=1)
        rhoS = FiguresToPresent(rho/1000,3)
        rhoS = r"$\rho = " + rhoS + r"\left( \frac{g}{cm^3} \right)$"
        textX = min(X) + 0.5 * (max(X) - min(X))
        textY = min(Y) + 0.75 * (max(Y) - min(Y))
        g1.text(textX,textY,rhoS,fontsize=16)
        plt.show()
```

Figure 4-3. Script for calculation Bouguer density using G-H method.

2. F-H method

F - H relationship method or simple F - H method (Parasnis, 1986; Parasnis et al., 1978; Parasnis & Cook, 1952). Bouguer anomalies are described as a function of assumed density itself. The optimum density is estimated by minimizing the summations of the difference between the Bouguer anomaly averaged in whole area and each Bouguer anomaly. This technique was initially proposed by Parasnis (1986). In this method the Equation (4-5) is rearranged as

$$B = (g_{obs} - \gamma + \beta h) - (2\pi G h + T)\rho \tag{4-14}$$

From Equation (4-14), the second term is plotted against the coefficient of ρ, and the gradient of the straight line is then determined by least squares technique and the value is taken as the optimum reduction density. The gradient is equivalent to assuming Bouguer anomaly to be a random error. This method minimizes the summation of the difference between each Bouguer anomaly value and the representative $\overline{B}$ of the smoothed profile of Bouguer anomaly, which is averaged over the area of interest.

Equation (4-14) can be modified and reduced to

$$B = F - H\rho$$

where

$$F_i = g_i - \gamma_i + \beta h_i$$
$$H_i = 2\pi G h_i - T_i \qquad (4\text{-}15)$$

where F is a free-air anomaly and H is a topography term.
Also, the system can be solved using statistic as shown in Equation (4-16) and the code is shown in Figure 4-4.

$$\rho_{FH} = \frac{\sum_{i=1}^{N}(H_i - \bar{H})(F_i - \bar{F})}{\sum_{i=1}^{N}(H_i - \bar{H})^2} \qquad (4\text{-}16)$$

```
"""
Created on Tue May 02 14:54:54 2017
@author: Carlos Pocasangre
Description: script for calculation Bouguer Density by using simple F-H method
input file "input.csv": [station,lon,lat,elevation,gravObs,TC_1g_cc]
use: python input.csv
"""
import numpy as np
from sys import argv
import time
import matplotlib.pyplot as plt

if __name__ == "__main__":
        script, InputFileName = argv
        DATA = ReadFile(InputFileName)
        n = len(DATA)
        X = 2e8*np.pi*G*DATA[TextUsed[3]][:] - DATA[TextUsed[5]][:]/1e0
        Y = DATA[TextUsed[4]][:] - NormalGravC(DATA[TextUsed[2]][:]) + beta *
            DATA[TextUsed[3]][:]
```

```
        XY = X * Y
        sumXY = np.sum(XY)
        X2 = X ** 2
        sumX2 = np.sum(X2)
        sumX = np.sum(X)
        sumY = np.sum(Y)
        A = (n * sumXY - sumX * sumY)/(n * sumX2 - sumX ** 2)
        B = (sumY - A * sumX)/n
        rho = A
        print "rho [kg/m3]: ",rho * 1000
        print "rho [g/cm3]: ",rho
        #--------------------------------
        g1 = GraphXY(X,Y,"Bouguer Density simple F-H","H [mGal/g/cm3]","F
              [mGal]")
        fitY = linefunc(A,B,X)
        g1.plot(X,fitY,'r',linewidth=1)
        rhoS = FiguresToPresent(rho,3)
        rhoS = r"$\rho = " + rhoS + r"\left( \frac{g}{cm^3} \right)$"
        textX = min(X) + 0.1 * (max(X) - min(X))
        textY = min(Y) + 0.85 * (max(Y) - min(Y))
        g1.text(textX,textY,rhoS,fontsize=16)
        plt.show()
        H = X
        F = Y
        num = (H - np.average(H) ) * (F - np.average(F) )
        sumNum = np.sum(num)
        den = (H - np.average(H) ) ** 2
        sumDen = np.sum(den)
        #rho g/cc
        rho2 = sumNum / sumDen
```

Figure 4-4. Script for calculating Bouguer density using F-H method.

3. Extended F-H

This method uses F-H method over subdivided mesh areas of equal size and estimates a reduction density corresponding to each mesh size. Finally the density is calculated as a function of mesh size and the optimum density is determined such that the calculated density becomes an approximately constant value over various mesh sizes. This technique, which considers a smooth Bouguer anomaly profile, was proposed by Fukao et al. (1981) obtained by dividing the area under consideration into a series of grids of equal size. The method is based on F-H method in which the estimation of Bouguer anomalies is made by a piecewise step function in a 2-D space. It takes into account the correlation between the long-wavelength elements of Bouguer anomalies and the fact that topography tends to be supported by dynamic force or in isostatic equilibrium within the earth in a larger area. Rewriting Equation (4-5) in a 2-D space, it is obtained the Equation (4-17):

$$\begin{aligned} B_{ij} &= g_{ij} - \gamma_{ij} + \beta h_{ij} - 2\pi G\rho h_{ij} + \rho T_{ij} \\ &= (g_{ij} - \gamma_{ij} + \beta h_{ij}) - (2\pi G h_{ij} - T_{ij})\rho \\ B_{ij} &= F_{ij} - H_{ij}\rho \end{aligned} \tag{4-17}$$

moreover, if it is assumed the number of grids to be M and the number of stations to be N_j within the Jth grid, the minimization condition can be obtained as follows

$$\begin{gathered} S = \sum_{j=1}^{M}\sum_{i=1}^{N_j}\left\{F_{ij} - H_{ij}\rho - \overline{B}_j\right\}^2 \Rightarrow minimum\left(\overline{B}_j = \frac{\sum_{k=1}^{N_j} B_{jk}}{N_j}\right) \\ \frac{\partial S}{\partial \overline{B}_j} = \frac{\partial S}{\partial \rho} = 0 \Rightarrow solution \end{gathered} \tag{4-18}$$

This minimization condition yields the estimated density, ρ_{EF}

$$\rho_{EF} = \frac{\sum_{j=1}^{M}\sum_{i=1}^{Nj}(H_{ij} - \overline{H}_j)(F_{ij} - \overline{F}_j)}{\sum_{j=1}^{M}\sum_{i=1}^{Nj}(H_{ij} - \overline{H}_j)^2} \tag{4-19}$$

In general, the resulting estimated Bouguer density depends on the size of the grid. The code for solving Equation (4-19) is shown in Figure 4-5; this code has been adapted for running as Multi processing technique for accelerating the calculation and reducing time.

```
#!/usr/bin/env python
# -*- coding: utf-8 -*-
"""
Created on Tue May 02 14:54:54 2017
@author: Carlos Pocasangre
Description: script for calculation Bouguer Density using Extended F-H method
input file "input.csv": [station,lon,lat,elevation,gravObs,TC_1g_cc]
```

```
use: python input.csv
"""
import numpy as np
from multiprocessing import Pool

def multi_run_wrapper(args):
   return ExtendedFH(*args)

def ExtendedFH(DATA,J):
    "Calculate Bouguer density by Extended FH. J is mesh in meters"
    beta = 0.3086 #Vertical Gradient [mGal/m]
    G = 6.673e-11 # Gravity constant [m3/kg/s2]
    TextUsed = ['STA','LON','LAT','ELEV','GRAVOBS','TC1g_cc','X','Y']
    DataVectorSize = len(DATA);X = DATA[TextUsed[6]][:];Y =
        DATA[TextUsed[7]][:]
    Xmin = np.floor(min(X));Xmax = np.ceil(max(X));Ymin =
        np.floor(min(Y));Ymax = np.ceil(max(Y));
    deltaX = Xmax-Xmin;deltaY = Ymax-Ymin;
    N = int(deltaX // J)
    M = int(deltaY // J)
    PointsSelected = 0
    MeshCounter = 0
    sumNumJ = 0
    sumDenJ = 0
    for m in range(M+1):
        yl = Ymin + m * J
        yu = Ymin + (m+1) * J
        for n in range(N+1):
            xl = Xmin + n * J
            xu = Xmin + (n+1) * J
            MeshCounter = MeshCounter + 1
            F = [];H = []
            for k in range(DataVectorSize):
                if xl <= X[k] and X[k] <= xu and yl <= Y[k] and Y[k] <= yu:
                    PointsSelected = PointsSelected + 1
                    F.append(DATA[TextUsed[4]][k] -
                      NormalGravC(DATA[TextUsed[2]][k]) + beta *
                                DATA[TextUsed[3]][k])
                    H.append(2e8*np.pi*G*DATA[TextUsed[3]][k] -
                             DATA[TextUsed[5]][k])
            if len(F) and len(H):
                num = (H - np.average(H) ) * (F - np.average(F) )
                sumNumJ = sumNumJ + np.sum(num)
                den = (H - np.average(H) ) ** 2
                sumDenJ = sumDenJ + np.sum(den)
    return [sumNumJ / sumDenJ, PointsSelected, MeshCounter]

if __name__ == "__main__":
    p = Pool(processes=8)
    try:
        script, InputFileName = argv
        DATA = ReadFile(InputFileName)
    except ValueError:
        print "ERROR: Syntax no valid\ntry: >python name.py input.csv"
    try:
        Increment = 50
        MeshMin = 50
        MeshMax = 10000
        #MeshMin/Increment = integer
```

```
        #(MeshMax - Increment)/Increment+1 = integer
        mesh = [i*Increment + Increment for i in
                range(MeshMin/Increment,(MeshMax -
              Increment)/Increment+1)]
        results = p.map(multi_run_wrapper, [(DATA, mesh_i) for mesh_i in
                           mesh])
        p.terminate()
        rho = [val[0] for val in results]
        print('Calculation time of Calculus: ' + str('%.4g' % time2) + 'sec')
        #--------
        #statistical Analysis
        mean = np.average(rho)
        std = np.std(rho)
        stderr = std / len(rho)**0.5
        conf_interv = 1.96 * stderr
        print "rho [g/cm3]: "+ FiguresToPresent(mean,4)+" ±
                     "+FiguresToPresent(conf_interv,4)
        print "Std: ",FiguresToPresent(std,4)
        print "Interval: "+FiguresToPresent(mean - conf_interv,4)+" < rho <
              "+FiguresToPresent(mean + conf_interv,4)
        print "Mesh [m]: "+str(MeshMin)+"-"+str(MeshMax)+", dx =
                   "+str(Increment)
        [g1,graph1] = GraphXY(1e-3* np.array(mesh),rho,"Extended FH","mesh
                     [km]","Bouguer Density [g/m3]")
        Parameters, covariance_matrix = curve_fit(func, 1e-3* np.array(mesh),
                     rho)
        g1.plot(1e-3* np.array(mesh), func(1e-3* np.array(mesh), *Parameters),
                        'r-', label='fit')
        g1.legend(handler_map={graph1:
                   HandlerLine2D(numpoints=3)},fontsize=8,loc=4)
        PlotProbabilityDistribution(rho,False)
        plt.show(block=True)
    except ValueError:
        print "ERROR: ValueError __main__ "
    except TypeError:
        print "ERROR: TypeError __main__ "
```

Figure 4-5. Script for calculating Bouguer density using Extended F-H method.

4. Akaike's Bayesian Information Criterion (ABIC)

Based on the assumption that the Bouguer anomaly varies smoothly with topography, Murata (1990, 1993) proposed the ABIC method, approximating the Bouguer anomaly by a smooth function. In his method, the optimum terrain density is obtained by minimizing the function

$$\sum_{i=1}^{N}\{F_i - \rho H_i - f(x_i, y_i|\mathbb{s})\}^2 + \sum_{k=1}^{2}\omega_k \int_v \int_v \|\nabla^k f\|^2 \, dx\, dy \Rightarrow min \qquad (4\text{-}20)$$

where f is the cubic B spline function that is fitted to the observed Bouguer anomalies, $F_i - \rho H_i$, $\nabla^k f$ is the k-th differentiation of the function f, $\mathbb{s}$ is a vector of spline parameters, and ω_k is the trade-off parameters. The roughness of the first-order gradient of f and second-order curvature of f, of the Bouguer anomaly surface are controlled, by the trade-off parameters ω_1 and ω_2, respectively, and a fitting choice of these parameters is made by minimizing ABIC (Akaike, 1998). Equation (4-20) above can be reduced in form of a matrix as

$$\|F - \rho H - E\mathbb{s}\|^2 + \|D_\omega \mathbb{s}\|^2 0 \Rightarrow min \tag{4-21}$$

where F and H are vectors that represents free-air anomalies and terrain-Bouguer corrections per unit density, respectively. The term $\mathbb{s}$ is the M parameters of the function f whereas D_ω and E are an $N \times M$ matrices containing ω_1 and ω_2 parameters and spline values at the stations, in that order.

For solving Equation (4-20), a Fortran code, BayRho: Bayesian Bouguer Density Estimation Program, was used (Murata, 1990, 1993; Murata & Noro, 1993). This code is a Modified-Cholesky decomposition version for UNIX machine (Original code was written in May 1990).

5. Comparison with the Variance of the Upward-Continuation (CVUR)

The CVUR method was proposed by Komazawa (1995). The method assumes that the surface layer produces shorter wavelength elements of Bouguer anomalies, and in the case where the density corresponds with the surface layer density, the first layer will then appear transparent and the short wavelength elements caused by the surface topography will have to be attenuated. The more natural way is to compare the variances obtained from band-pass or high-pass filtered residuals and to determine the appropriate density as the one giving the minimum variance. These variances are taken to be a measure of roughness or randomness resulting from the skin effects. The method is applied to the meshed dataset, and the grid at a point $p\,(i,j)$ is interpolated from the Bouguer anomalies. Assuming the correction is made with an estimated density ρ followed by an upward-continuation to a height h, the Bouguer anomaly at point p can be defined as $g_p(\rho, h)$, and the variance $a_p{}^M(\rho; h_1 h_2)$ is then defined by the differences between the two upward-continued anomalies and given by

$$\begin{aligned} a_p{}^M(\rho; h_1 h_2) &= \sum_q^M W_q \left\{g_{p-q}(\rho, h_1) - g_{p-q}(\rho, h_2) - \left(g_p{}^M\right)\right\}^2 / \sum_q^M W_q \\ &= \sum_q^M W_q \left\{\nabla g_{p-q}((\rho; h_1 h_2) - \left(g_p{}^M\right)\right\}^2 / \sum_q^M W_q \end{aligned} \tag{4-22}$$

where M is the number of range of sampling, q is the convolution parameter of grid point p, h_1 and h_2 are continuation heights, $\sum_q^M i$ denotes the summation with respect to q within a circular region ($|q| \leqq M$). The term $g_p{}^M$ is the weighted mean value and W_q is the weight adopted for smoothing.

For solving Equation (4-22), a Python code which was coded by Prof. Nishijima J., Kyushu University was used. The script is shown in Figure 4-6.

```
# -*- coding: utf-8 -*-
"""
Created on Tue May 02 14:54:54 2017
@author: Jun Nishijima, Geothermics Laboratory, Kyushu University
Description: Comparison with the Variance of the Upward-Continuation (CVUR)
"""
import numpy as np
# Sampling radius and center of circumference
R=4600
AX = 660000
AY = 3543000
# Load X, Y, Upward residual data
UCD = np.loadtxt('UCD.txt', delimiter = None)
X = UCD[:, 0]
Y = UCD[:, 1]
BA18 = UCD[:, 2]
BA19 = UCD[:, 3]
BA20 = UCD[:, 4]
BA21 = UCD[:, 5]
BA22 = UCD[:, 6]
BA23 = UCD[:, 7]
BA24 = UCD[:, 8]
BA25 = UCD[:, 9]
BA26 = UCD[:, 10]
BA27 = UCD[:, 11]
```

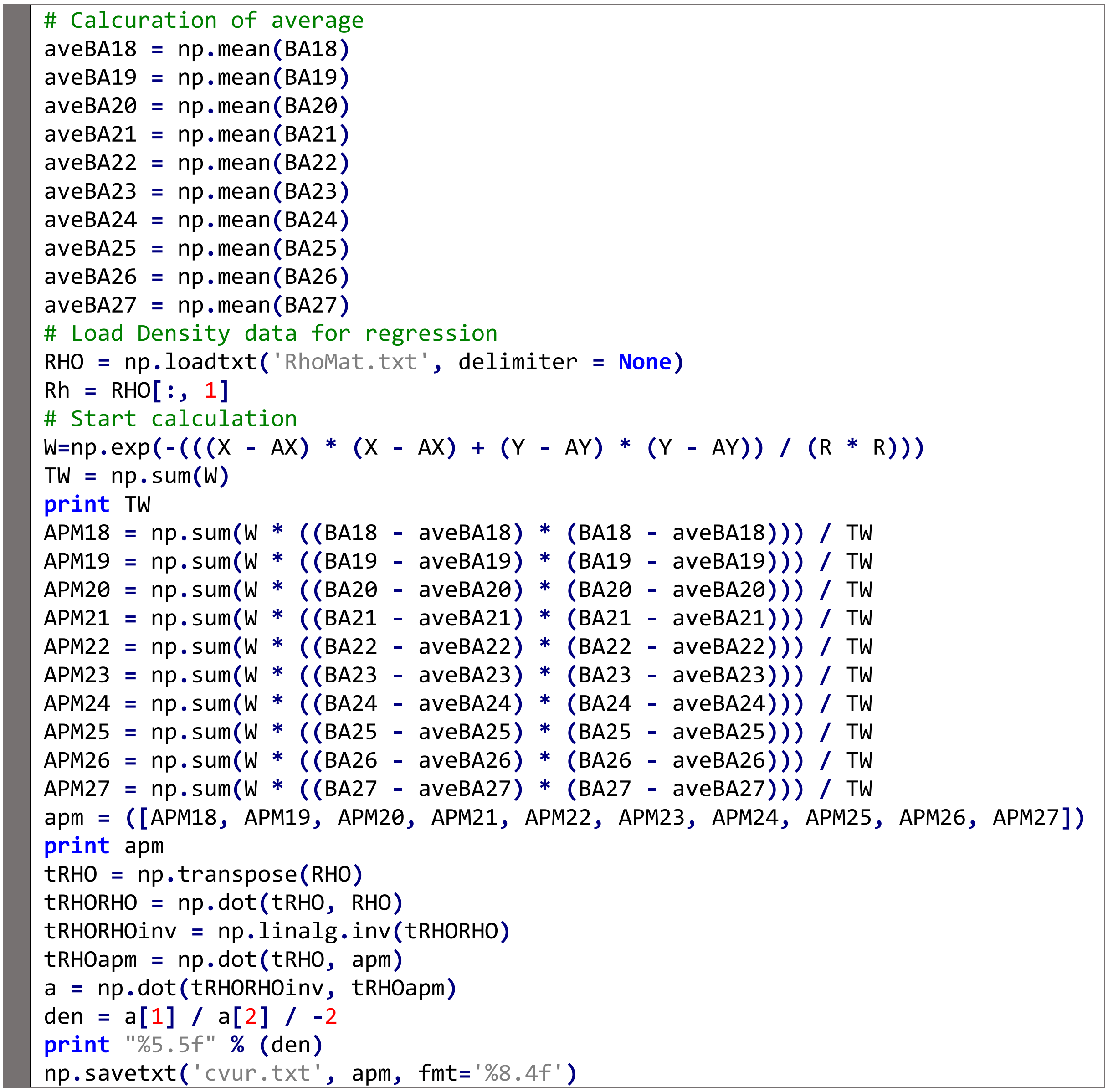

```
# Calcuration of average
aveBA18 = np.mean(BA18)
aveBA19 = np.mean(BA19)
aveBA20 = np.mean(BA20)
aveBA21 = np.mean(BA21)
aveBA22 = np.mean(BA22)
aveBA23 = np.mean(BA23)
aveBA24 = np.mean(BA24)
aveBA25 = np.mean(BA25)
aveBA26 = np.mean(BA26)
aveBA27 = np.mean(BA27)
# Load Density data for regression
RHO = np.loadtxt('RhoMat.txt', delimiter = None)
Rh = RHO[:, 1]
# Start calculation
W=np.exp(-(((X - AX) * (X - AX) + (Y - AY) * (Y - AY)) / (R * R)))
TW = np.sum(W)
print TW
APM18 = np.sum(W * ((BA18 - aveBA18) * (BA18 - aveBA18))) / TW
APM19 = np.sum(W * ((BA19 - aveBA19) * (BA19 - aveBA19))) / TW
APM20 = np.sum(W * ((BA20 - aveBA20) * (BA20 - aveBA20))) / TW
APM21 = np.sum(W * ((BA21 - aveBA21) * (BA21 - aveBA21))) / TW
APM22 = np.sum(W * ((BA22 - aveBA22) * (BA22 - aveBA22))) / TW
APM23 = np.sum(W * ((BA23 - aveBA23) * (BA23 - aveBA23))) / TW
APM24 = np.sum(W * ((BA24 - aveBA24) * (BA24 - aveBA24))) / TW
APM25 = np.sum(W * ((BA25 - aveBA25) * (BA25 - aveBA25))) / TW
APM26 = np.sum(W * ((BA26 - aveBA26) * (BA26 - aveBA26))) / TW
APM27 = np.sum(W * ((BA27 - aveBA27) * (BA27 - aveBA27))) / TW
apm = ([APM18, APM19, APM20, APM21, APM22, APM23, APM24, APM25, APM26, APM27])
print apm
tRHO = np.transpose(RHO)
tRHORHO = np.dot(tRHO, RHO)
tRHORHOinv = np.linalg.inv(tRHORHO)
tRHOapm = np.dot(tRHO, apm)
a = np.dot(tRHORHOinv, tRHOapm)
den = a[1] / a[2] / -2
print "%5.5f" % (den)
np.savetxt('cvur.txt', apm, fmt='%8.4f')
```

Figure 4-6. Comparison with the Variance of the Upward-Continuation script.

4.4.3 Bouguer density estimation in the eastern part of Isa

For the Bouguer Correction and terrain effect, it is very important to have a good regional density value or Bouguer density, which includes an average of principal existent rocks in the selected area.

According to NEDO (1991), the Hishikari area consists of approximately 100 - 1500 m thick of quaternary volcanic rock and sediments with a density range of 2.36 –

2.54×10^3 kg m^{-3}, and a sedimentary tertiary basement, Shimanto Supergroup, of $2.57 – 2.62 \times 10^3$ kg m^{-3} (Faye et al., 2018); the result was 2.41×10^3 kg m^{-3} using G-H method.

To calculate Bouguer density, there are several mathematical methods listed previously for calculating this value such as Nettleton's or profile method (Nettleton, 1939; Yamamoto, 1999a), relationship Free-air anomaly and Terrain effect or F-H method (Parasnis & Cook, 1952), Extended F-H method (Fukao et al., 1981), the Akaike's Bayesian Information Criterion method (ABIC) (Murata, 1993), and Comparison of Variance of Upward-continuation Residual method (CVUR) (Komazawa, 1995; Murata, 1993). These methods gave comparable Bouguer density of 2.38×10^3 kg m^{-3} (see Figure 4-7), 2.55×10^3 kg m^{-3} (see Figure 4-8), 2.58×10^3 kg m^{-3} (see Figure 4-9), 2.26×10^3 kg m^{-3}, and 2.52×10^3 kg m^{-3} (Figure 4-10), respectively. An average density of 2.458×10^3 kg m^{-3} was selected and deemed enough to produce a smooth anomaly. This average value lies within the range of density values proposed in some previous studies. The Bouguer density results are listed in Table 4-1.

Table 4-1. Calculated Bouguer density by several methods.

Method	Bouguer Density [g/cm^3]
Nettleton's	2.38
F-H	2.55
Extended F-H	2.58
ABIC	2.26
CVUR	2.52
$\bar{\rho}$ average	2.458

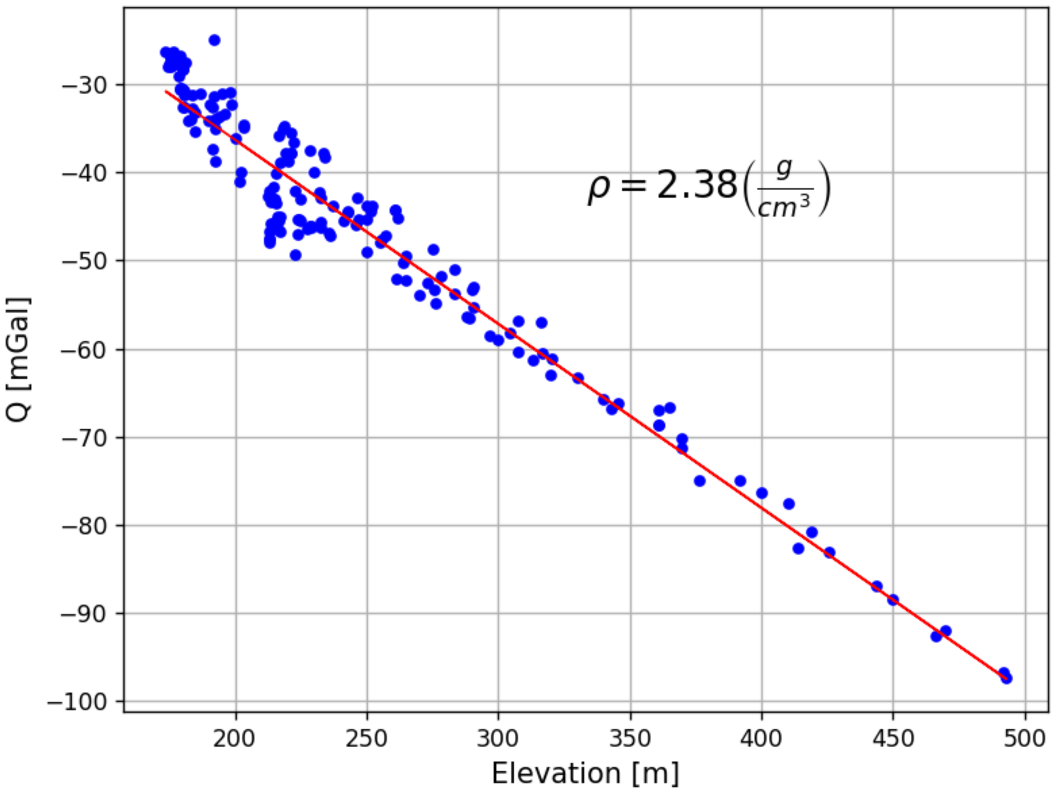

Figure 4-7. Bouguer density by G-H method.

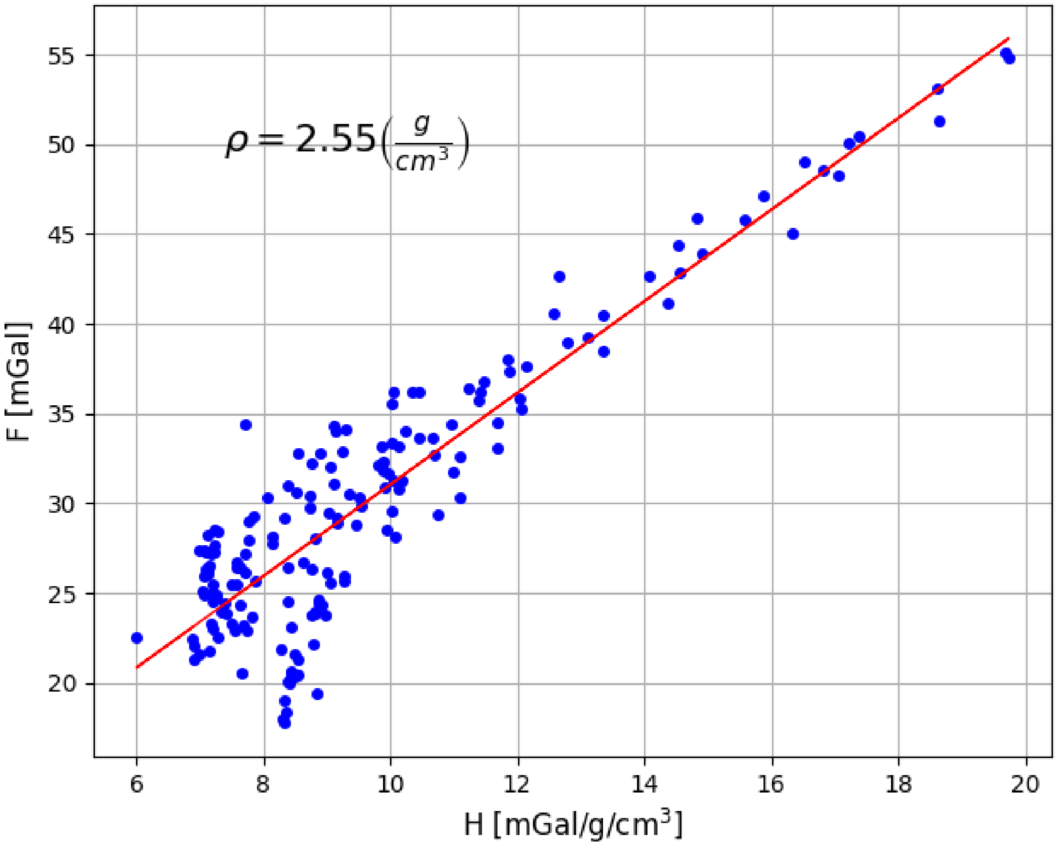

Figure 4-8. Bouguer density by the simple F-H method.

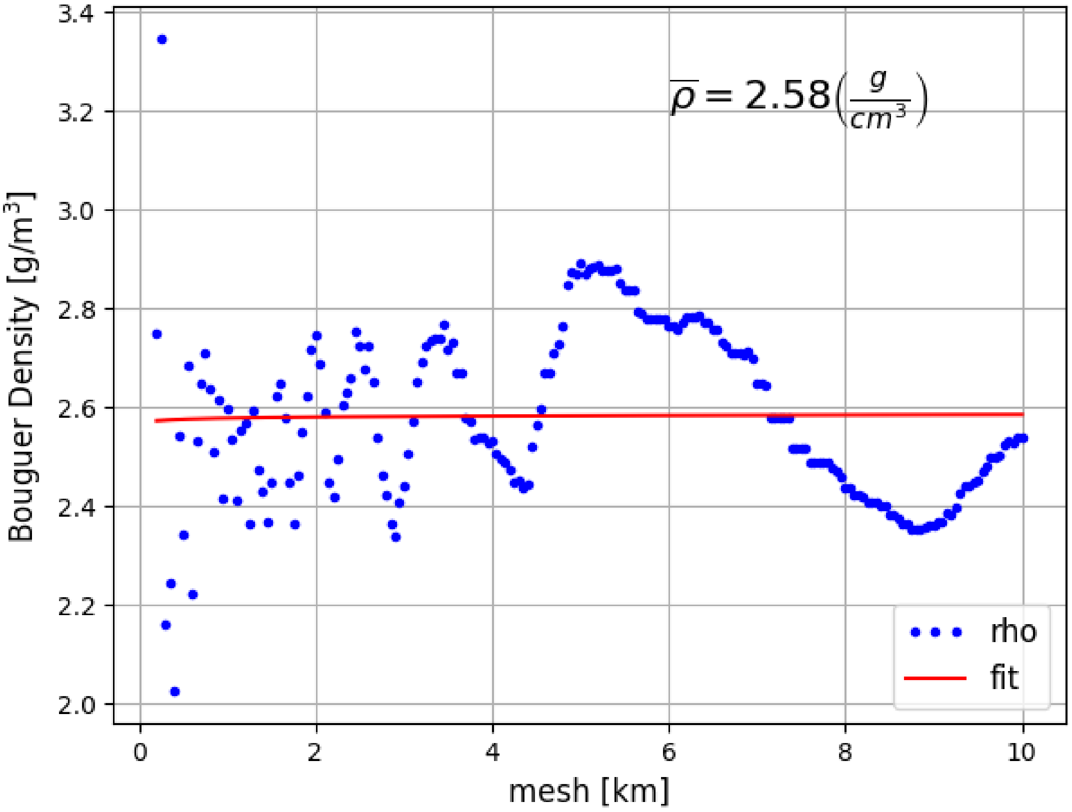

(a)

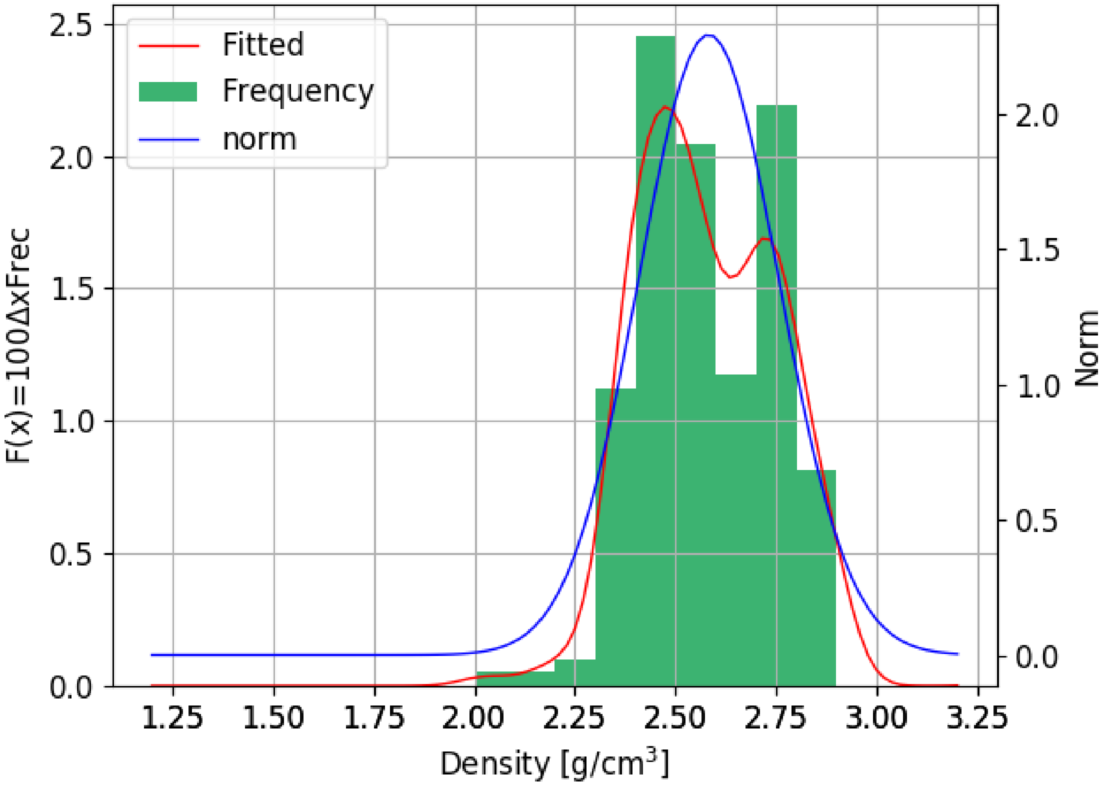

(b)

Figure 4-9. (a) Bouguer density by Extended F-H method, (b) Extended F-H density frequency distribution.

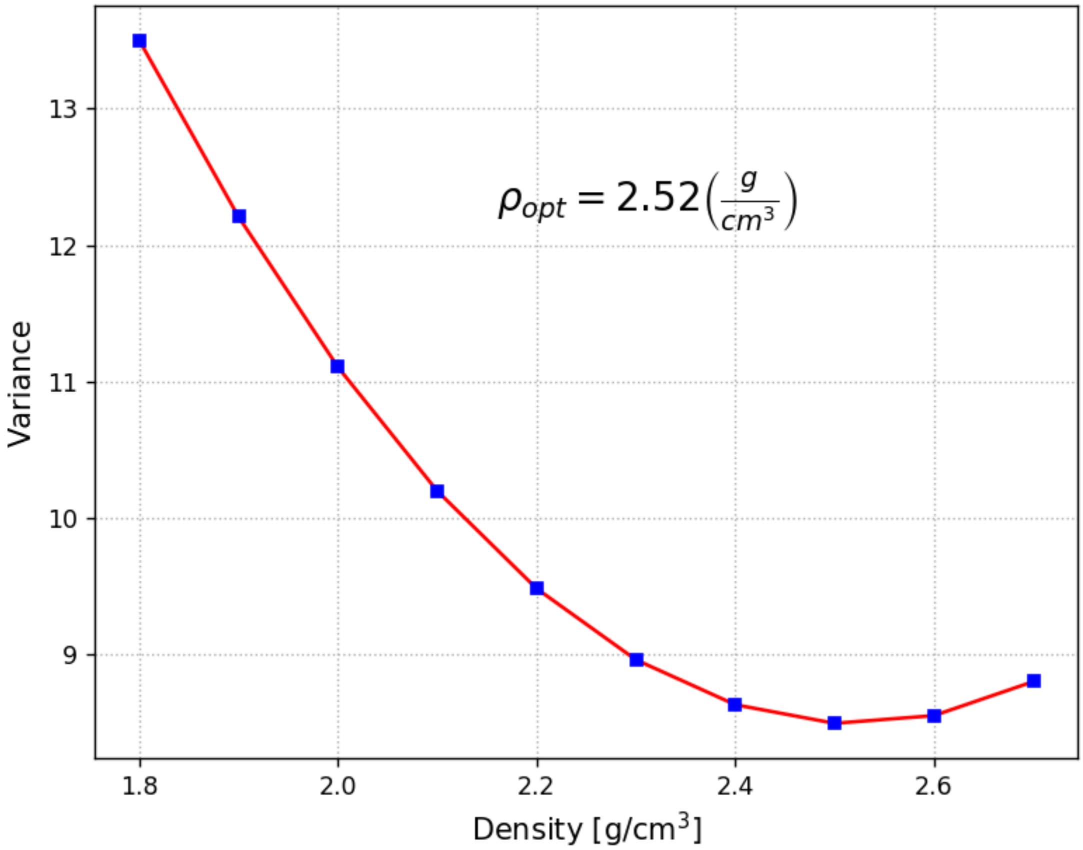

Figure 4-10. Bouguer density by Comparison with Variance of the Upward-Continuation (CVUR).

4.5 Bouguer anomaly

Interpretation of Bouguer anomaly, calculated by using Equation (4-5), was limited to the distribution of survey stations shown in Figure 4-12. Areas with no stations were removed and structures located in areas with sparse stations interpreted with caution, nevertheless, the areas considered relevant to this study appear to be well covered during the survey. The complete Bouguer anomaly was interpolated to a 100 m grid with the minimum curvature method with tension (Smith & Wessel, 1990), using the Surface module implemented in the Generic Mapping Tools system (Wessel et al., 2017). The minimum curvature method is widely used but old principle for constructing smooth surface estimates from irregularly spaced data (Briggs, 1974). The estimated surface of minimum curvature relates to the minimum of the Laplacian differential equation or, in an alternative formulation, satisfies the bi-harmonic differential equation. Gridding with tension is an improvement to the minimum curvature methods as it adds a degree of freedom and relaxes the minimum-curvature constraint by introducing some tension into the surface. This technique tries to force a thin elastic plate to go through randomly-spaced (x,y,z) dataset and generates a binary grid file of gridded values z(x, y) by solving:

$$(1-T)\cdot\nabla^2(\nabla^2 z)+T\cdot\nabla^2 z=0 \tag{4-23}$$

where $\boldsymbol{T}$ is a tension factor between 0 and 1, $\boldsymbol{\nabla^2}$ indicates the Laplacian operator, and $\boldsymbol{z}$ represents the small displacements of a thin elastic plate of constant flexural rigidity, subject to a vertical normal stress and constant horizontal forces per unit vertical length (Smith & Wessel, 1990).

The GMT SURFACE module achieves this by finding a function that satisfies the following constraints (Smith & Wessel, 1990; Wessel et al., 2017):

$$\begin{gathered} Z(x_k, y_k) = z_k, \text{ for all data } (x_k, y_k, z_k), k = 1, n \\ (1-t)\nabla^4 z - t\nabla^2 z = 0 \text{ elsewhere} \end{gathered} \tag{4-24}$$

where $\boldsymbol{t}$ is the tension, $\boldsymbol{0 \leq t < 1}$.

In the case of terrain correction, the 50 m mesh digital elevation map of Japan was used (Nishijima, 2009). The script for calculating the minimum curvature method with tension, Trend removal, and filtering is shown in Figure 4-11 which uses Linux BASH and GMT 5.0.

```
#!/bin/bash
# GMT script. Last modified Wed Jan 10 13:58:43 JST 2018
echo 'Start variables           [###.........................]10%'
## DECLARATION OF VARIABLES ##
  LATMIN=3538051.462
  LATMAX=3548027.027
  LONMIN=654985.8989
  LONMAX=665125.0278
  CBADATA=data.csv
  CELL=100e
  CBAGRID=BA.nc
```

```
  LBAGRID=LOCAL.nc
  RBAGRID=REGIONAL.nc
  HDBAGRID=HD.nc
  INHTBAGRID=INH.nc
#----Create the Interpolating Surface by Minimum Curvature Method ------------
gmt surface $CBADATA -G$CBAGRID -I$CELL -T0.2
           -Re$LONMIN/$LONMAX/$LATMIN/$LATMAX -V
echo 'Anomaly                  [##########..................]20%'
#-----Remove a planar trend: Regional-Local separation------
gmt grdtrend $CBAGRID -N3 -D$LBAGRID -T$RBAGRID -V
echo 'Local Anomaly            [##########..................]40%'
#------ Edge detection filter HD --------
gmt grdmath $LBAGRID 1000 MUL = TEMP.nc
gmt grdfft TEMP.nc -A0 -GTEMP_dg_dx.nc
gmt grdfft TEMP.nc -A90 -GTEMP_dg_dy.nc
gmt grdmath TEMP_dg_dx.nc TEMP_dg_dy.nc R2 = TEMP.nc
gmt grdmath TEMP.nc SQRT = $HDBAGRID
echo 'Horizontal Derivative     [##########..................]60%'
#------ Edge detection filter INHT --------
gmt grdmath $LBAGRID 1000 MUL = TEMP.nc
gmt grdfft TEMP.nc -A0 -GTEMP_dg_dx.nc
gmt grdfft TEMP.nc -A90 -GTEMP_dg_dy.nc
gmt grdfft TEMP.nc -D -GTEMP_dg_dz.nc
gmt grdmath TEMP_dg_dz.nc ABS = TEMP_dg_dz.nc
gmt grdmath TEMP_dg_dz.nc 0.005 ADD = TEMP_dg_dz.nc
gmt grdmath TEMP_dg_dx.nc TEMP_dg_dy.nc R2 = TEMP.nc
gmt grdmath TEMP.nc SQRT = TEMP.nc
gmt grdmath TEMP.nc TEMP_dg_dz.nc DIV = TEMP.nc
gmt grdmath TEMP.nc ATAN = $INHTBAGRID
echo 'Improved Normalized Horizontal Tilt'
echo 'END                       [############################]100%'
exit 0
```

Figure 4-11. Linux BASH script "*bouguer.sh*" using GMT 5.0 for interpolating and filtering the Bouguer Anomaly.

Figure 4-12 represents the Bouguer anomaly map. The anomaly map shows values ranging from -2.6 mGal to 11.5 mGal. In particular, in the center of the map, the highest gravity anomaly, which is between 8.5 mGal and 11.5 mGal is observed. This particular area could represent the propylitic alteration or hydrothermal activity that is rich in minerals and where the Hishikari gold mine is set up; likewise, the anomaly has a trend NE-SW, i.e., the anomaly is aligned along with the regional trending shown by lineaments map in Figure 3-4, and it corresponds with the Kagoshima graben. Additionally, the Kakuto basin is evident in the eastern part of Isa with the lowest gravity anomaly from -2.6 mGal to 3.8 mGal, as well, the Okuchi basin at the western part of the study area.

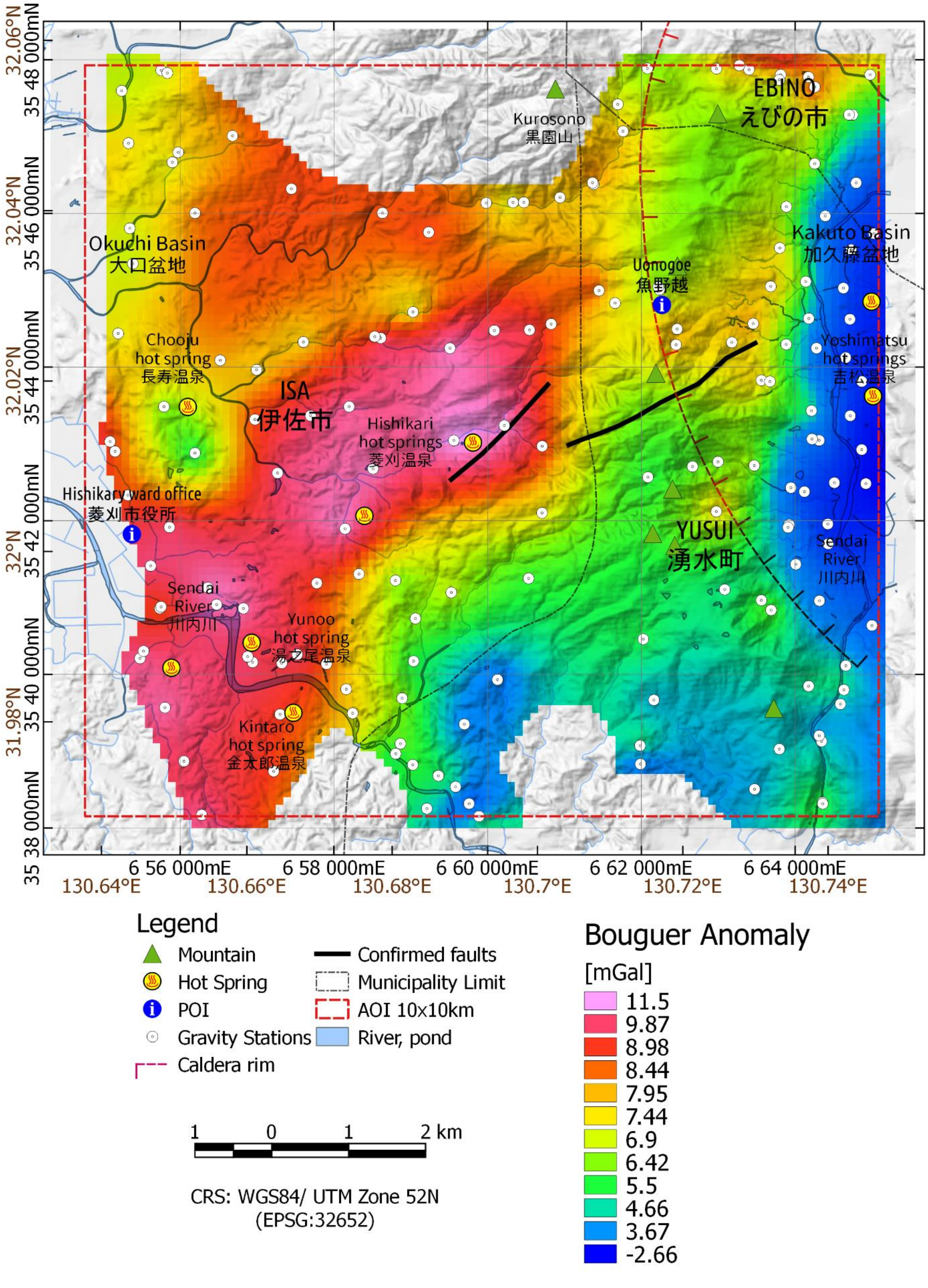

Figure 4-12. Bouguer anomaly map with Bouguer density of 2.458 g/cm^3.

4.5.1 Trend separation: Regional and local Bouguer anomaly

The next step of the gravity processing is the regional and local anomaly separation because Bouguer anomaly includes the effect of a regional trend caused by the profound and vast structure. The script is shown in Figure 4-11. The separation of the complete Bouguer anomaly, Equation (4-5), is done using GMT GRDTREND tool which fits trend surface to grids and compute residuals (Wessel et al., 2017). The algorithm reads a 2-D grid file and fits a low-order polynomial trend to these data by least-squares. In the case of this dissertation, a bilinear trend surface, i.e., $m_1 + m_2x + m_3y$ was fitted. The trend surface expression is defined by

$$m_1 + m_2x + m_3y + m_4xy + m_5x^2 + m_6y^2 + m_7x^3 + m_8x^2y + m_9xy^2 + m_{10}y^3 \quad (4\text{-}25)$$

Because this study targets to reveal the shallow gravity basement structure, the regional anomaly was isolated by using the bilinear polynomial trend which is considered to represent the andesite and Shimanto Supergroup structures (Naritomi et al., 2015; Nishijima & Naritomi, 2017). Typically, a residual anomaly shows local structure characteristics of the study area differentiated by positive and negative gravimetric values, i.e., high and low rock density. Figure 4-13 shows the residual Bouguer anomaly map that clarifies the existence of altered rock in the center of the study area by obtaining positive gravity values. Those values are associated with very-well consolidated rocks due to mineralization, compaction, and type of rock (Renderos et al., 2013). Also, the dotted red lines, with zero values, evidence the gravity anomaly change (from low to high density) of the shallow structures, i.e., they show the edge of those structures. The area with maximum gravity anomaly is approximately 5.61 km^2, which could be used as the maximum most-likely area of the geothermal reservoir for power generation assessment. Alternatively, Kakuto basin is highlighted in the eastern part of the map showing negative gravity values. The basin rim is clearly revealed with red anomalies which follow the basin's trend. Similarly, Okuchi basin is emphasized at the west; however, because the structure is an ancient caldera and has been covered by a lot of sediments, tuff, etc., the gravity values are not as low as in Kakuto basin.

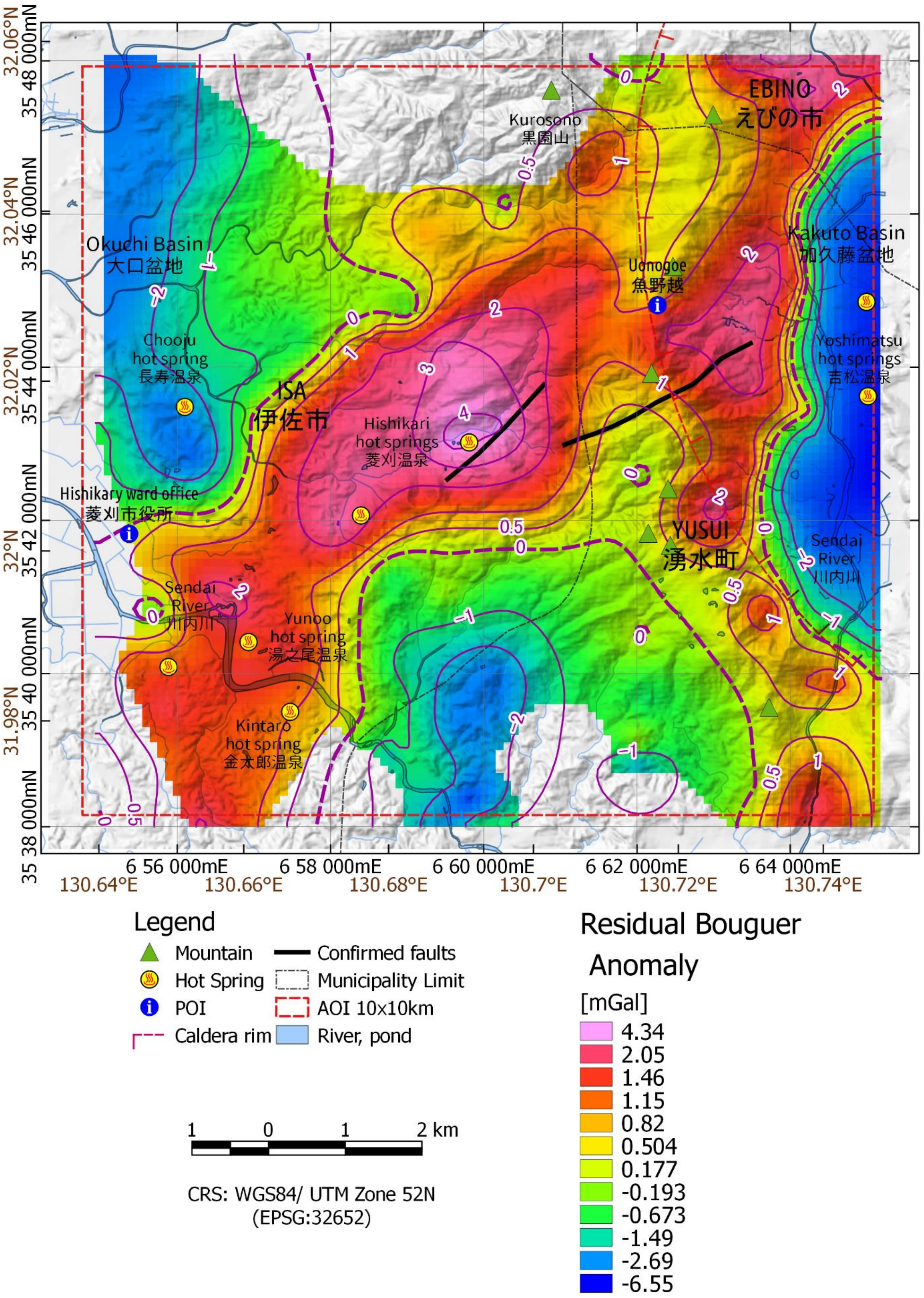

Figure 4-13. Residual Bouguer anomaly map with Bouguer density of 2.458 g/cm^3.

4.5.2 Edge detection filter

There exist several types of high-pass filters which enhance subtle detail in potential field data, such as downward continuation, horizontal and vertical derivatives. The horizontal location of the edges of causative sources is a commonly requested task in the interpretation of geophysical data; many filters are available to accomplish this task (Askari, 2014). The vertical derivative has been used for many years to delineate edges in gravity and magnetic field data. Grauch and Cordell (1987) have investigated the effect of a sloping side on the location of the maximum horizontal gradient. Telford et al. (1990) explained that the location of the maximum horizontal gradient may be used as an indicator of the location of the edges of the source. In general, the first vertical derivative is positive over the source, zero over the edge and negative outside of a vertical sided source. The horizontal gradient peaks over the edges and is zero over the body. Consequently, either of these two measures will locate the edges of an isolated anomaly source. The horizontal derivative (HD) maximizes above any abrupt change of density (Cordell & Grauch, 1985; Hosseini et al., 2013; Ma & Li, 2012) and can be given by

$$f(x,y) = \sqrt{\left(\frac{\partial g}{\partial x}\right)^2 + \left(\frac{\partial g}{\partial y}\right)^2} \tag{4-26}$$

where $\partial g/\partial x$ and $\partial g/\partial y$ are the directional derivatives of the gravity anomaly in the x and y directions, respectively. Advantages of the HD are less susceptibility to noise and that it can recognize the edges of both shallow and deep structures clearly (Zaher et al., 2011; Nishijima & Naritomi, 2017). Figure 4-14 represents the amplitude of HD in the study area. The dashed line in the HD map corresponds to the Kakuto basin rim in the eastern part of the municipality of Isa. Besides, two high HD with NE-SW trend were detected in the center of the map which might represent the border of the altered hydrothermal zone where the Hishikari gold mine is set up (Renderos et al., 2013; Uwiduhaye et al., 2018).

The improved normalized horizontal tilt angle (INH) filter, proposed by Li et al. (2014) is an edge-detection filter that is an improvement upon the normalized horizontal tilt angle (TDX) filter developed by Cooper & Cowan (2006), Nasuti & Nasuti (2018) and can be given by

$$f(x,y,z) = \tan^{-1}\left(\frac{\sqrt{\left(\frac{\partial g}{\partial x}\right)^2 + \left(\frac{\partial g}{\partial y}\right)^2}}{p + \left|\frac{\partial g}{\partial z}\right|}\right) \tag{4-27}$$

where p is a positive constant value, and is decided by the interpreter. In general, the value of p is approximately equal to one-tenth or one-twentieth of the maximum of the total horizontal derivative. The INH only adds a constant value to the denominator compared to the TDX, but the INH filter gives maximum values when the total horizontal derivatives reach their maximum values and the vertical derivatives becomes zero (Li et al., 2014). Figure 4-15 shows the INH of the residual gravity anomaly with p of 0.005. The value of p was decided by trial and error by Nishijima & Naritomi (2017) giving a good result for gravity filtering. The high INH values in the eastern and central parts of the area match well with the HD map (Figure 4-14). The dashed two lines in the INH map corresponds to the Kakuto basin rim in the eastern part of the municipality of Isa. Besides, two high INH with NE-SW trend were detected again for the filter in the center of the map which might represent the border of the altered hydrothermal zone. Also, INH confirms the regional trending, NE-SW, shown by geologic faults in the center of the geologic map (Figure 3-1) and lineaments (Figure 3-4). In the northern area, close to Uonogoe and Kurosonoyama place, there are some large, anomalous, high-gradient areas that might be caused by lack of gravity measurement points.

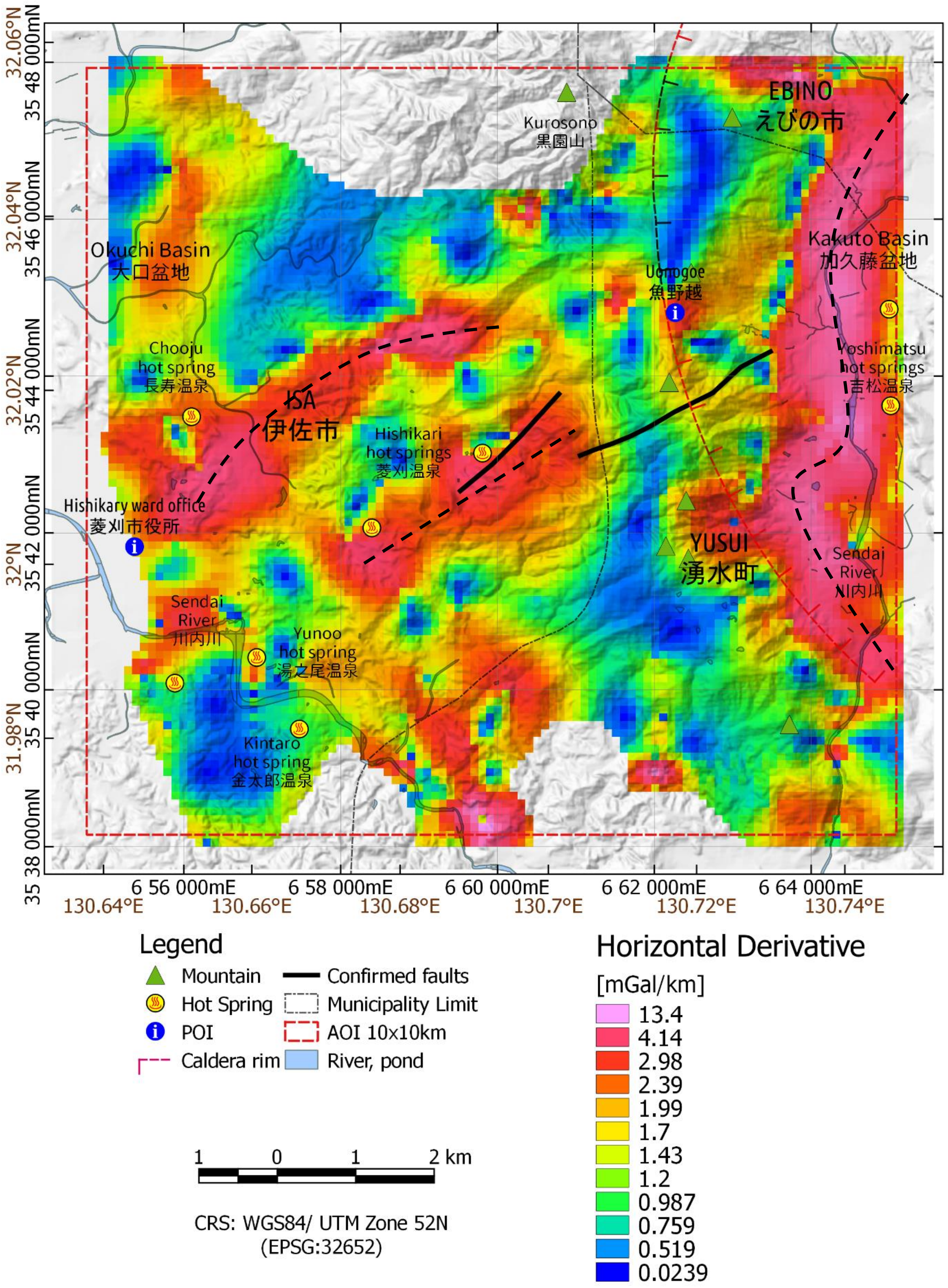

Figure 4-14. Horizontal derivatives (HD) of the Bouguer anomaly. The dashed lines show the discontinuities identified using the HD map.

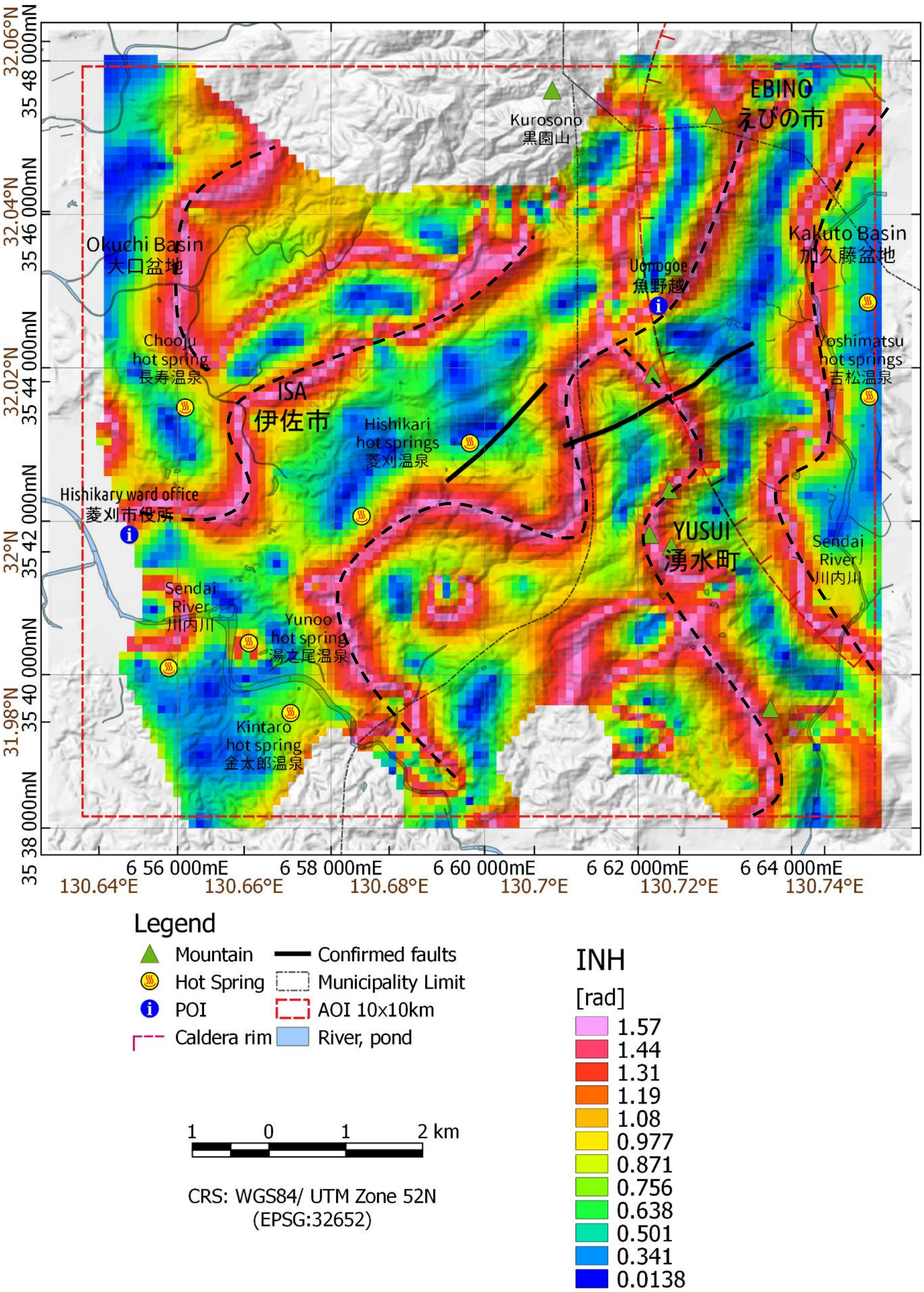

Figure 4-15. Improved normalized horizontal tilt angle (INH) map of the Bouguer anomaly. The dashed lines show the discontinuities identified using the INH map.

4.6 Two-layer 2-D gravity inversion

The previous filtering method can easily detect steep gravity gradients that indicate the location of faults or geological boundaries, but it is impossible to estimate their depths. To determine the depth and detailed shape of the basement rock, a two-layer 2-D gravity modeling was conducted (Pocasangre et al., 2018b). Distribution of 2-D gravity basement structures is usually modeled by approximating them by an aggregation of rectangles whose horizontal dimensions are the same as those of the input Bouguer anomaly grid. The gravity anomaly that is caused by each rectangle can be calculated using a mathematical expression that adjusts the depth of the rectangles that form the gravity basement model until it minimizes the root mean square error RMS, which is determined by the difference between the measured residual and the calculated Bouguer anomaly (Cordell & Henderson, 1968; Nishijima & Fujimitsu, 2015; Rao et al., 1999; Zaher et al., 2012).

The results presented here were obtained with the help of the open-source software Fatiando a Terra (Carlos et al., 2016; Uieda, 2018; Uieda et al., 2013). The Python –base library estimates the relief of a sedimentary basin approximating by a polygon. The top of the basin is straight and fixed at a given height. Polygon vertices are distributed evenly in the x-direction. The inversion is a non-linear and estimates the depths of each vertex. Therefore, the initial estimation must be configured before running the algorithm. For calculating the initial values, an assistant method called "*config*" is given. Finally, it uses the recommended configuration (Levenberg-Marquardt[14] algorithm with initial estimate to the average expected depth of the basin). The Python-based script for calculating the 2-layers 2-D gravity inversion is shown in the Figure 4-16.

---

[14] The Levenberg-Marquardt algorithm was developed in the early 1960's to solve nonlinear least squares problems (Gavin, 2019).

The modeling method requires a contrast in density between the two assumed layers, i.e., the basement and light-density deposit. According to geological maps (Saito et al., 2010), the survey area can be approximated into two geological layers: Quaternary-Pleistocene rocks and sedimentary basement rock. The thicknesses of the rectangles represented the depth from the surface to the basement, and a constant density contrast of 0.4 g/cm^3 was assigned. The horizontal size of the rectangle was 250 m. Figure 4-17 shows the location of the profiles A, B, and C, while Figure 4-18 shows the 2-layer 2-D gravity inversion cross-sections.

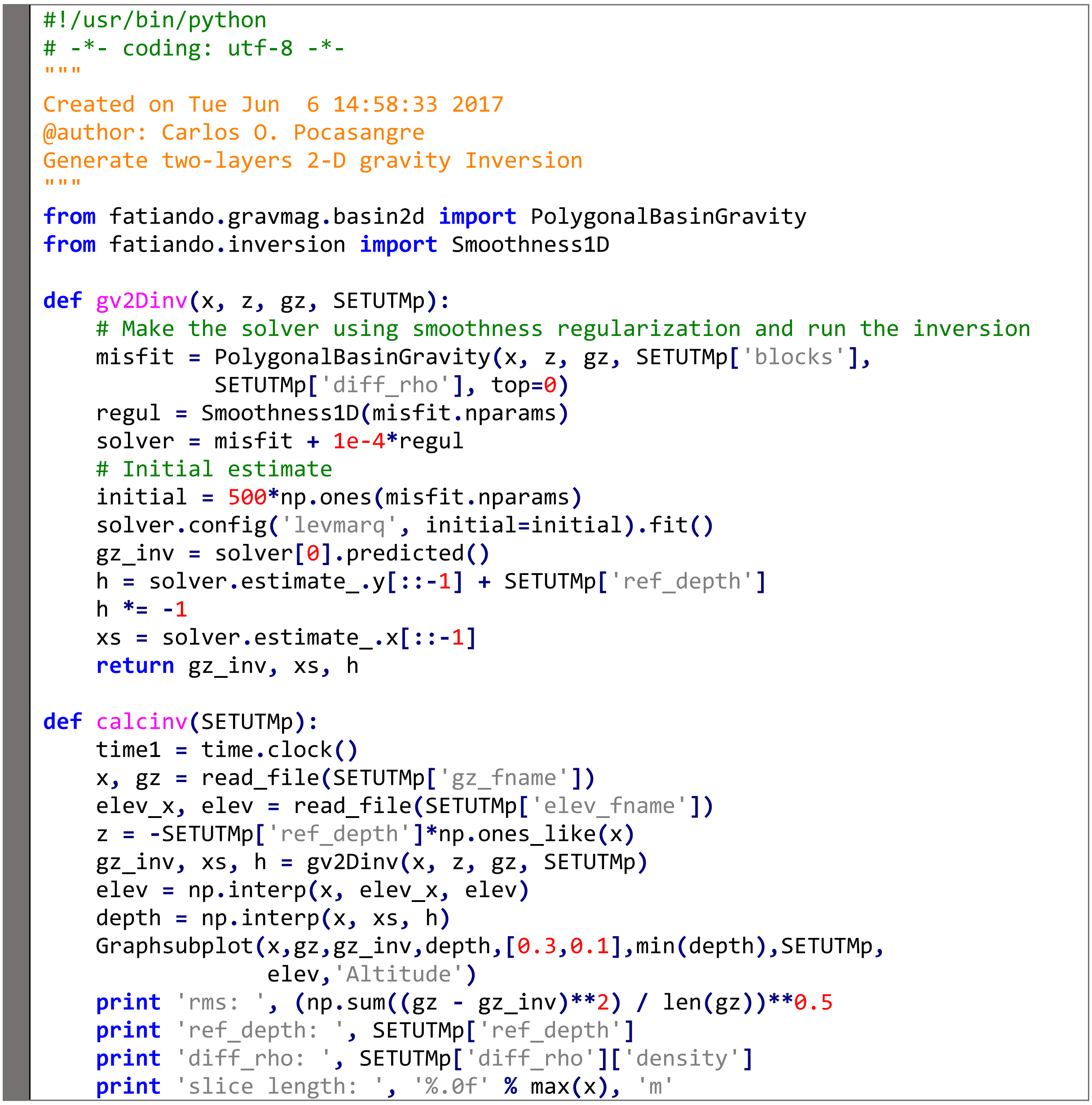

```python
#!/usr/bin/python
# -*- coding: utf-8 -*-
"""
Created on Tue Jun  6 14:58:33 2017
@author: Carlos O. Pocasangre
Generate two-layers 2-D gravity Inversion
"""
from fatiando.gravmag.basin2d import PolygonalBasinGravity
from fatiando.inversion import Smoothness1D

def gv2Dinv(x, z, gz, SETUTMp):
    # Make the solver using smoothness regularization and run the inversion
    misfit = PolygonalBasinGravity(x, z, gz, SETUTMp['blocks'],
             SETUTMp['diff_rho'], top=0)
    regul = Smoothness1D(misfit.nparams)
    solver = misfit + 1e-4*regul
    # Initial estimate
    initial = 500*np.ones(misfit.nparams)
    solver.config('levmarq', initial=initial).fit()
    gz_inv = solver[0].predicted()
    h = solver.estimate_.y[::-1] + SETUTMp['ref_depth']
    h *= -1
    xs = solver.estimate_.x[::-1]
    return gz_inv, xs, h

def calcinv(SETUTMp):
    time1 = time.clock()
    x, gz = read_file(SETUTMp['gz_fname'])
    elev_x, elev = read_file(SETUTMp['elev_fname'])
    z = -SETUTMp['ref_depth']*np.ones_like(x)
    gz_inv, xs, h = gv2Dinv(x, z, gz, SETUTMp)
    elev = np.interp(x, elev_x, elev)
    depth = np.interp(x, xs, h)
    Graphsubplot(x,gz,gz_inv,depth,[0.3,0.1],min(depth),SETUTMp,
                 elev,'Altitude')
    print 'rms: ', (np.sum((gz - gz_inv)**2) / len(gz))**0.5
    print 'ref_depth: ', SETUTMp['ref_depth']
    print 'diff_rho: ', SETUTMp['diff_rho']['density']
    print 'slice length: ', '%.0f' % max(x), 'm'
```

Figure 4-16. Script for modeling the two-layers 2-D gravity inversion.

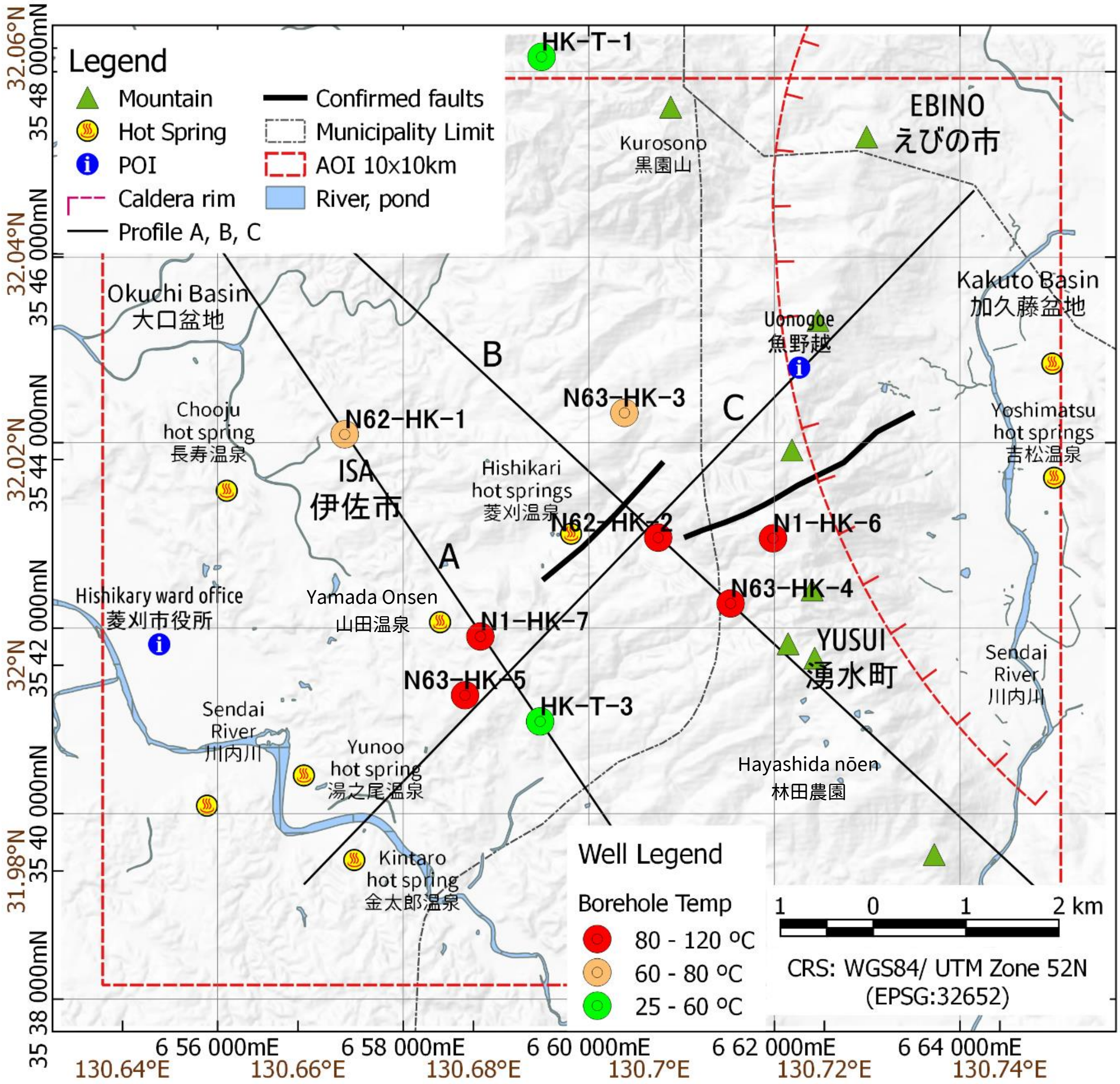

Figure 4-17. Profiles A, B, and C in the study area.

The inversion result relatively shows an effective curve fitting with a root-mean-square of 0.16, 0.14, and 0.07 for profiles A, B, and C respectively. The profile A (Figure 4-18a) which trends to NNW-SSE in the center of the selected area, ISA municipality, indicates that the sedimentary underground structure, Shimanto Supergroup, is found at around 1,400 m, 250 m, and 700 m deep at Okuchi basin, Yamada Onsen, and Sendai River respectively. Also, the inversion profile evidences the borders of the propylitic reservoir which shows high gravity values. The wells N62-HK-1, N1-HK-7, and HK-T3, which are shown in the figure, partially validate the Shimanto Supergroup depth, i.e., NEDO (1991) found that the depth of the basement is around 800 m and 450 m deep for N62-HK-1 and N1-

HK-7 respectively. However, the inversion modeling shows 900 m, 600 m deep for N62-HK-1 and N1-HK-7 respectively.

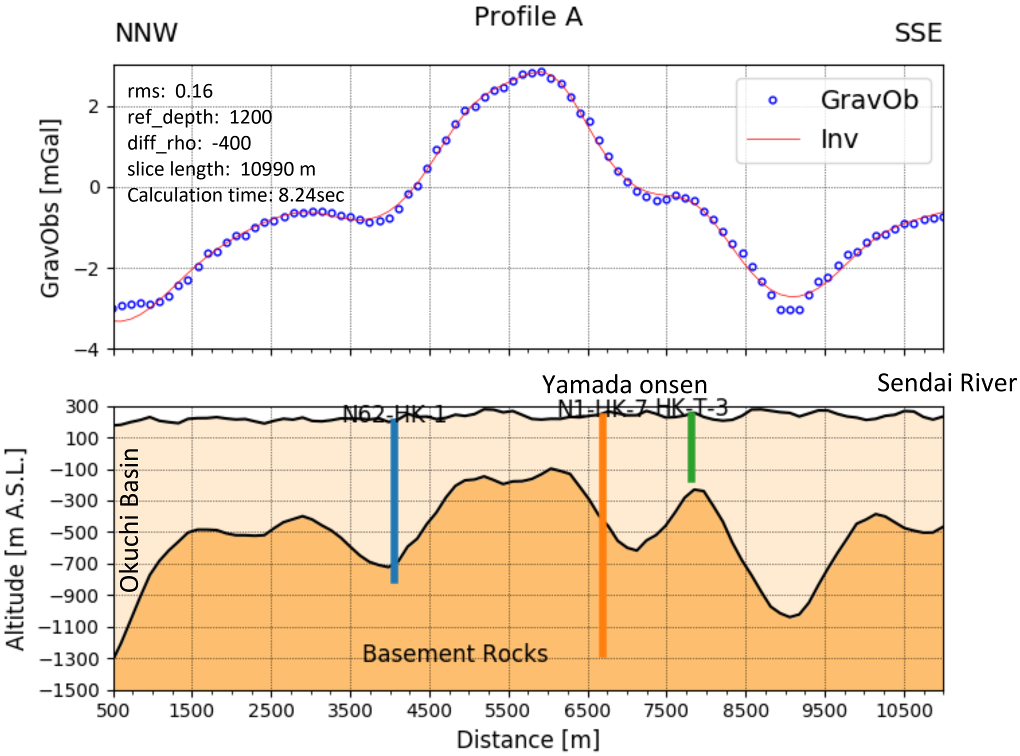

(a)

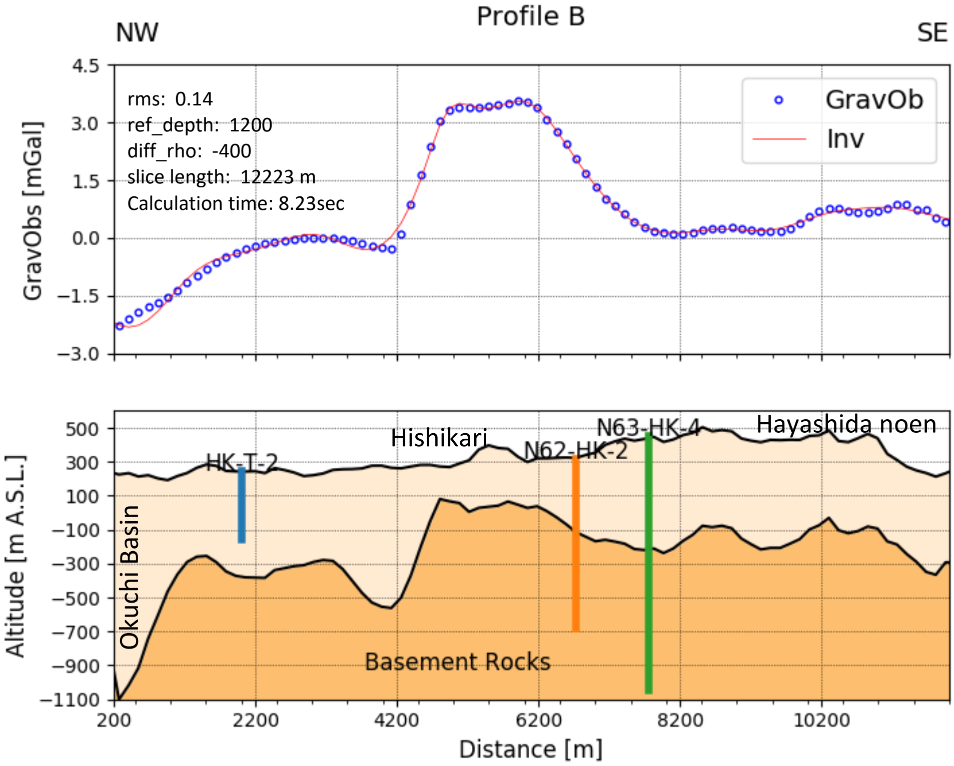

(b)

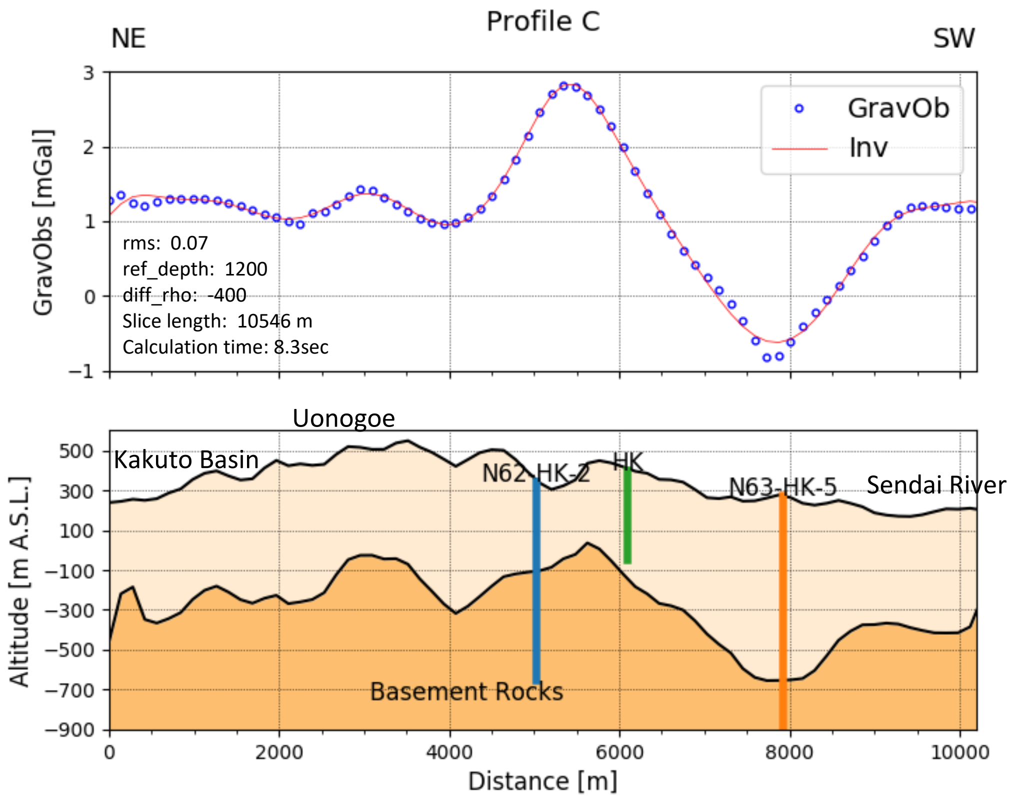

(c)

Figure 4-18. Profiles showing the 2-layers 2-D gravity inversion. (a) Profile A trending NNW-SSE, (b) profile B trending NW-SE, (c) profile C trending NE-SW. The color lines show the borehole depth.

Subsequent, the profile B (Figure 4-18b) which trends to NW-SE in the center of the selected area, ISA municipality, indicates that the sedimentary underground structure, Shimanto Supergroup, is found at around 1,300 m, 200 m, and 400-500 m deep at Okuchi basin, Hishikari gold mine, and Hayashida noen area at the south-east of the region respectively. Also, the inversion profile evidences the borders of the propylitic reservoir which shows high gravity values. The wells N62-HK-2 and N63-HK-4, shown in figure, partially validate the Shimanto Supergroup depth, i.e., NEDO (1991) found that the depth of the basement is around 220 m and 900 m deep for N62-HK-2 and N63-HK-4 respectively. However, the inversion modeling shows 440 m and 680 m deep for N62-HK-2 and N63-HK-4 respectively.

For the last profile presented, the profile C (Figure 4-18c) which trends to NE-SW in the center of the selected area, ISA municipality, indicates that the sedimentary underground structure, Shimanto Supergroup, is located around 600 m, 520 m, 600 m deep at Kakuto basin, Uonogoe, and Sendai river respectively. The wells N62-HK-2, Hishikari mine, and N63-HK-5, which are shown in figure, partially validate the Shimanto Supergroup depth, i.e., NEDO (1991) found that the depth of the basement is around 220 m and 700 m for N62-HK-2 and N63-HK-5 respectively, and the Hishikari mine tunnel at Sanjin area in Figure 3-2 shows the Shimanto Supergroup is found at around 100-250 m deep. However, the inversion modeling shows 450 m, 400-500 m, 950 m deep for N62-HK-2, Hishikari tunnel, and N63-HK-5 respectively.

4.7 3-D gravity modeling

This 3-D modeling is an essential stage of the complete gravity analysis in the region. Because the integrated gradient interpretation techniques for edge detection, i.e., horizontal-derivative (HD) and improved normalized horizontal tilt angle (INH), can quickly detect steep gradients and indicate the location of either faults or geological boundaries, however, they cannot estimate geological structure volume. To determine the geological structure volume, a 3-D gravity inversion modeling was conducted (Arima et al., 2013; Nishijima & Naritomi, 2017; Pocasangre et al., 2018a). The implementation of 3-D modeling of gravity has become an essential tool in the exploration of geological resources (Zaher et al., 2018; Li & Oldenburg, 1998). However, the inversion of the field gravity data is one of the most ambiguous problems in exploration geophysics studies (Oldenburg, 1974). Inversion of gravity data is usually fraught with problems due to data noise and inhomogeneity of geological bodies even with a reasonably accurate gravity measurement and data reduction. Therefore, carrying out gravity inversion of field data and generating geologically realistic results may not be easy because the inverse problem in potential field modeling suffers from ambiguity and non-uniqueness of its solutions. To remedy the non-uniqueness problem and improve the inversion performance, one may choose for regularization or instead addition of a *priori* knowledge as constraints to reduce the ambiguity of the inverse problem. The application of a *priori* data, such as, drilling or geological information to constrain gravity inversions has been increasing in the last two decades (Dahlin et al., 2002; Fullagar et al., 2008; Li & Oldenburg, 2000; Represas et al., 2012).

4.7.1 Lithostratigraphy of the exploration wells

In this dissertation, a *priori* information of borehole geology from the initial ten geothermal wells drilled in the eastern part of the municipality of Isa has been integrated to produce a reasonable source model approximation (Table 4-2). These wells are located close to the highest gravity anomaly, therefore according to the 2-D inversion model, the Shimanto Supergroup is found between 200 – 800 m.

The lithostratigraphy is predominantly composed of Shimanto Supergroup (sedimentary rocks), dacite, and andesite rocks. Close to the surface and as a cap rock, dacite and andesite rocks are the most dominant rock-type. Shimanto Supergroup is the basement which is made of sedimentary rocks with high density values. The lithology of these wells generally shows very close similarity (Faye et al., 2018; NEDO, 1991).

Table 4-2. Different rock types and their depths of occurrence from the 10 exploration wells drilled in Isa (NEDO, 1991).

Hole_ID	From	To	Lithology	Full Lithology's name
HK-T-1	0	9.5	Weathered rock	Weathered rock
	9.5	401.5	HLA	Tataraishi andesite
HK-T-2	0	20.8	Weathered rock	Weathered rock
	20.8	259.3	HLA	Kusumoto andesite
	259.3	401.3	SSG	Shinkawa conglomerate
HK-T-3	0	30.3	Weathered rock	Weathered rock
	30.3	101.3	Hannyaji welded tuff	Hannyaji welded tuff
	101.3	173.15	HMA	Yotsueda andesite
	173.15	401.4	HLA	Yamadagawa andesite
N1-HK-6	0	115	ShishiMano Dacite	Weathered rock
	115	375	HMA	Kusumoto Andesite
	375	888	HLA	Shinkawa conglomerate
	888	1501.5	SSG	Shinkawa andesite
N1-HK-7	0	70.01	Hannyaji welded tuff	Tataraishi andesite
	70.01	514.5	HLA[15]	Ichiyamagawa upstream andesite
	514.5	1502.6	SSG	Nagano Formation

---

[15] HLA: Hishikari Lower Andesite

Hole_ID	From	To	Lithology	Full Lithology's name
N62-HK-1	0	30	Weathered rock	Shimanto Supergroup
	30	180.6	HLA	Weathered rock
	180.6	251.2	HLA	Yamadagawa andesite
	251.2	314.6	HLA	Shimanto Supergroup
	314.6	396.4	HLA	Weathered rock
	396.4	581.1	HLA	Kusumoto Andesite
	581.1	628.3	SSG	Goshiki Andesite
	628.3	1001.5	SSG	Shinkawa conglomerate
N62-HK-2	0	30	Weathered rock	Shinkawa andesite
	30	220.7	HLA	Yamadagawa andesite
	220.7	1002	SSG	Shimanto Supergroup
N63-HK-3	0	30	Weathered rock	Weathered rock
	30	111.8	HLA	Shishimano Dacite
	111.8	141.3	HLA	Yotsueda andesite
	141.3	241.1	HLA	Yamadagawa Andesite
	241.1	283.4	HLA	Shimanto Supergroup
	283.4	423.8	HLA	Weathered rock
	423.8	1000.5	SSG[16]	Hannyaji welded tuff
N63-HK-4	0	30	Weathered rock	Yamadagawa Andesite
	30	173.31	Shishimano Dacite	Kirishima Welded tuff
	173.31	364.41	HMA[17]	Shimanto Supergroup
	364.41	937.1	HLA	ShishiMano Dacite
	937.1	1501.6	SSG	Yotsueda andesite
N63-HK-5	0	30	Weathered rock	Yamadagawa Andesite
	30	49	Hannyaji welded tuff	Shimanto Supergroup
	49	650.5	HLA	Hannyaji welded tuff
	650.5	684.6	SSG	Yamadagawa Andesite
	684.6	1201	SSG	Shimanto Supergroup

The actual measurements of rock densities from these wells (or of surface geology within the study area) were not available openly, and as a result, representative densities were approximated using Table 3-3 (Faye et al., 2018).

The density average for major quaternary volcanic rocks such as andesite (2.135 g/cm^3), dacite (2.33 g/cm^3) appears to control the average density in the region because they exist mainly close to the surface. But also, the Shimanto Supergroup

---

[16] SSG: Shimanto Supergroup

[17] HMA: Hishikari Middle Andesite

which has an average density of 2.65 g/cm^3 might contribute. Regionally, it was estimated a Bouguer density of 2.458 g/cm^3 which is close to the mean rock density computed using rock property table. The approximation using Table 4-3, gave a density contrast of 0.515 g/cm^3 from an average of 2.37 g/cm^3, which is somehow lower than the computed Bouguer density that was used to reduce the gravity data.

Table 4-3. Rock properties of the study area in the municipality of Isa.

Rock Unit	Thermal conductivity [W/m · K]	Heat Capacity [J/kg · K]	Density [kg/m^3]	Effective porosity %
Shishimano Dacite	1.239	810	2330	0.064
Yotsueda Andesite	1.373	810	2490	0.099
Goshiki Andesite	0.553	795	1680	0.379
Shinkawa Andesite	1.236	810	2240	0.144
Yamadagawa Andesite	1.922	810	2270	0.166
Kusumoto Andesite	1.968	815	2620	0.035
Shinkawa Conglomerate	0.832	795	1680	0.261
Tataraishi Andesite	1.306	810	1940	0.184
Ichiyamagawa upstream Andesite	1.469	810	2160	0.178
Kirishima Welded Tuff	1.841	810	2270	0.153
Nagano Formation	1.839	785	2260	0.266
Shimanto Supergroup	3.233	775	2640	0.028

The discrepancy obtained between the mean density rocks and Bouguer density could be attributed to the dominance of the Shimanto Supergroup which tends to control the region, and it rises at the surface in the center of the study area. Despite this, the Bouguer density value was removed for each of the rock types, which corresponds to the removal of a uniform background from the observed data. As a result, a density contrast of between -0.72 g/cm^3 and 0.22 g/cm^3 was obtained ($\Delta\rho = 0.94\ g/cm^3$). The resulting density contrast was then empirically gridded to a distance of 50 m using Kriging method and a tool into Geosoft platform to obtain a reference model or constrain (Geosoft, 2018). The result of the gridding is shown in Figure 4-19.

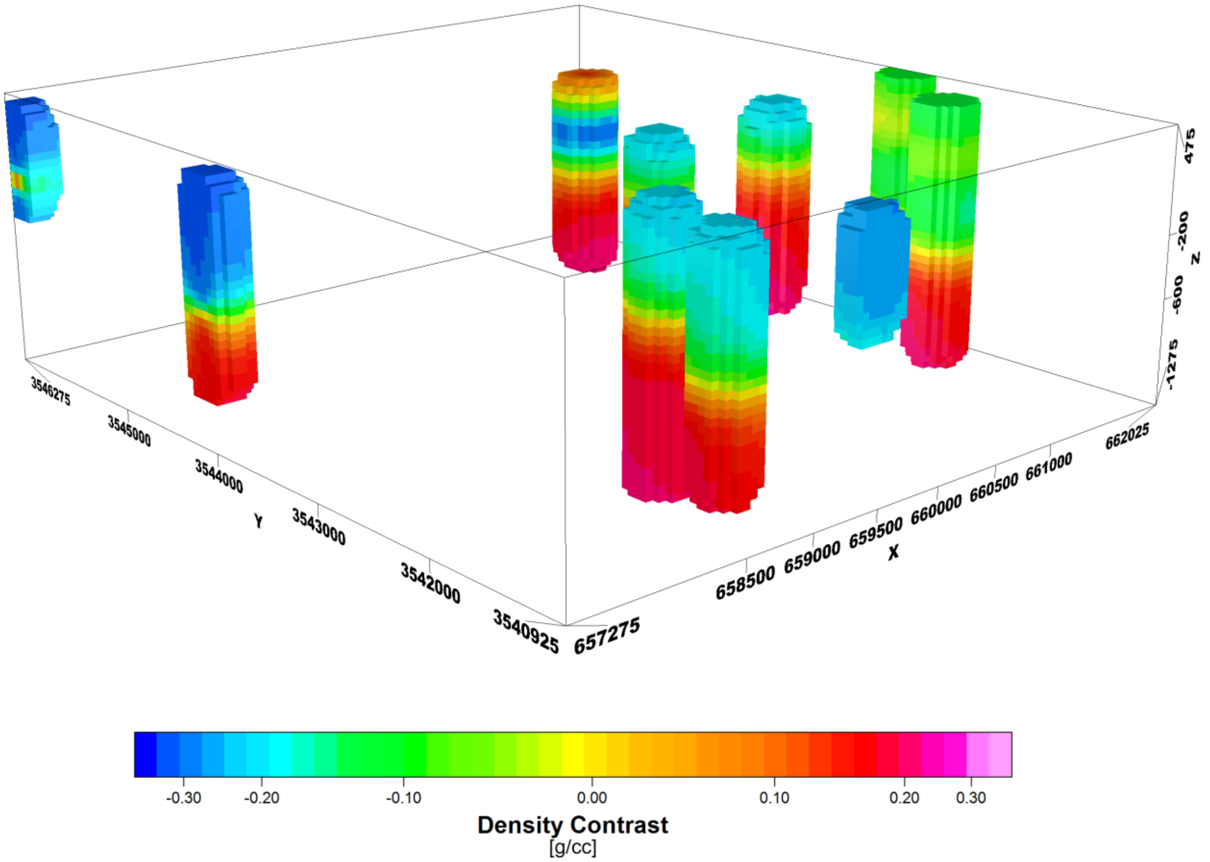

Figure 4-19. Reference model from the gridded density contrast of the downhole density estimated from the initial 10 exploration wells.

4.7.2 The 3-D Voxel-based model

To determine the density distribution of the subsurface structure, a 3-D inversion of the Bouguer gravity anomaly using the VOXI[18] Earth Modeling tool was carried out (Geosoft, 2018), a voxel-based tool that is built within the Geosoft platform. This platform is a cloud-based computing service, and this makes it possible to calculate a large-scale 3-D model at high speed without depending on the local computer specification. It applies a Cartesian Cut Cell method developed by Ingram et al. (2003), which allows accurate geometric representation of geological surfaces (Ellis & MacLeod, 2013). The solution search method uses the iterative re-weighting least squares (IRLS) algorithm initially developed by Lawson (1961).

---

[18] VOXI is a Geosoft Oasis Montaj cloud and clustered computing module that allows the 3-D inversion of geophysical data, e.g., gravity, magnetics.

The IRLS approach solves certain optimization problems using weighted least squares calculations, iteratively. In order to obtain a stable solution, the objective function is regularized by the misfit between observed and calculated values. The reduced chi-squared misfit (Taylor, 1997) is then used to measure the degree which indicates that the predicted response agrees with the observed data. The inversions can be completed as 'unconstrained' or 'constrained' using drill-hole information (e.g., magnetic susceptibility or density logs) or geological information. Gravity and magnetic data (ground or airborne data, total field or gradient measurements) can be inverted using different methods, and sets of constraints or regularizations (Barbosa & Pereira, 2013; Farhi et al., 2016).

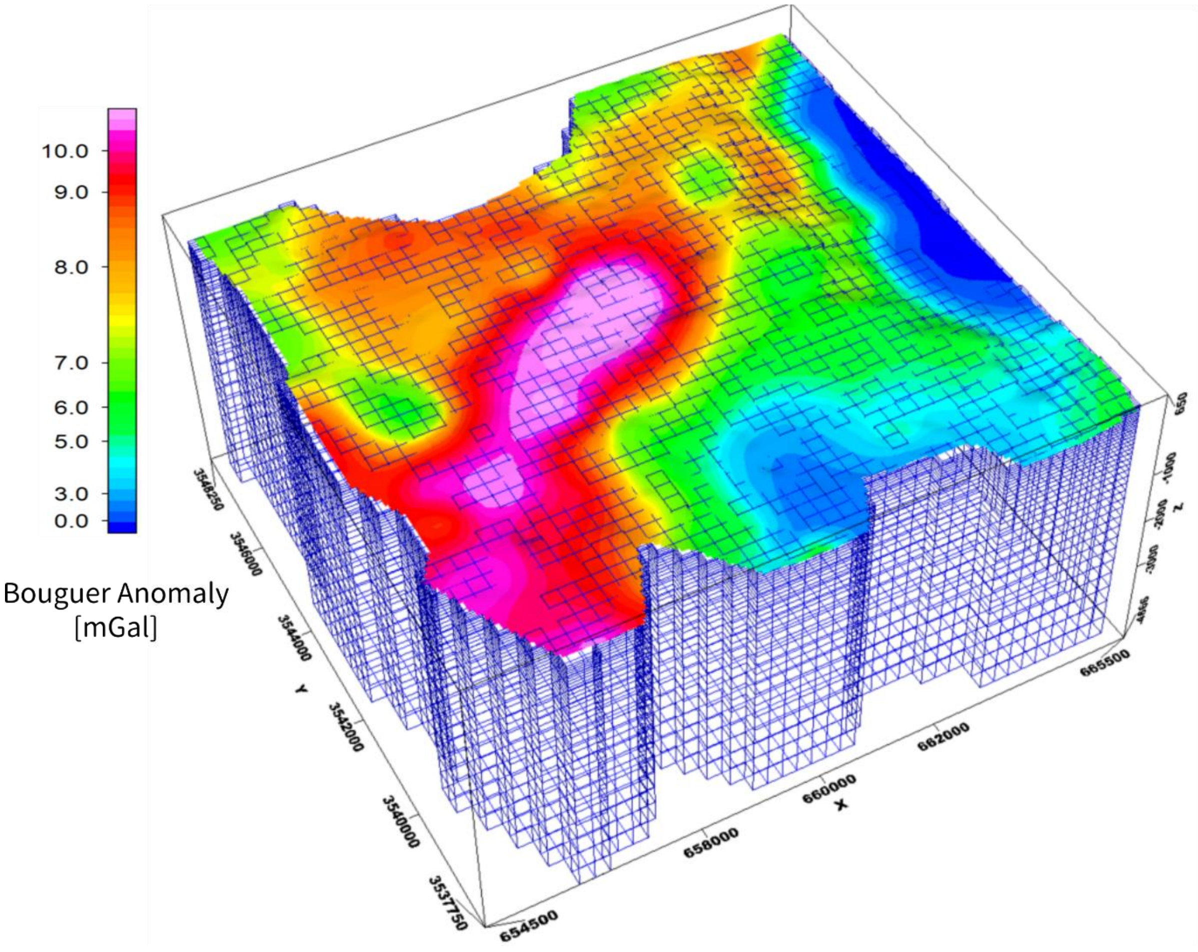

Figure 4-20. A 3-D Gravity inversion grid. The cell size is 250 m × 250 m × 50 m (number of cells *x*, *y*, *z* are 42, 41, 38 respectively). The colored map represents Bouguer anomaly (CBA) with values ranging from -2.9 mGal to 11.7 mGal.

The subsurface of the study area was discretized into 42 × 41 × 38 rectangular cells in the *x*, *y* and *z*-direction, respectively (Figure 4-20). The size of the rectangular cell was set to 250 m and 250 m along respective x and y directions. The height of the cells increases from a top layer of 50 m by a factor of 1.08 for each successive deeper layer. The inversion process involves varying the trade-off regularization parameter in an attempt to fit the data, and the inversion improves the model iteratively until the predicted data satisfy the residual chi-squared criterion to obtain the optimal model.

The reference model generated from the density contrasts was used to constrain the inversion (Figure 4-19). To ensure that the results are within an acceptable range, lower-bound and upper-bound constraints of -0.55 g/cm^3 (tuff, pumice, and sediment formations[19]) and 0.2 g/cm^3 (basement or Shimanto Supergroup formation[20]), respectively, were set. These values are based on the density variation derived from the estimated densities of local geology. Also, an Iterative Reweighting Inversion Focusing (IRIF) constraint was applied to enhance the model and produce a more geologically plausible inversion result (Ellis, 2012). IRIF uses the output of the inversion as a weighting function in successive iterations and this results in a more focused model. The weighting function makes sharpening of contrasts possible by enhancing boundaries around distinctive anomalous features (MacLeod & Ellis, 2015).

The inversion will improve the model iteratively until the predicted data satisfy an assigned tolerance criterion. In this study, a maximum absolute error was initially set at 0.1 mGal. The simulation ran for 17 iterations during 20 min and resulted in a 3-D model with density contrasts that range from -0.64 g/cm^3 to 0.3 g/cm^3 and lie within a geologically reasonable density variation for the study area. The Bouguer density was then added to each cell to obtain the density distribution. Finally, the results were gridded to a higher resolution of 100 × 100 × 100 m rectangular cells using an isotropic inverse distance weighting interpolator (Shepard, 1968) to enhance the presentation of the model recovered from the inversion (Golden Software LCC, 2018).

---

[19] Density of 1.9 g/cm^3

[20] Density of 2.65 g/cm^3

4.7.3 The 3-D gravity inversion model result

The 3-D gravity modeling in the eastern part of the municipality of Isa, Kagoshima Prefecture, was carried out to define the underground volume of the hydrothermal alteration zone. For carrying out the modeling, a volume of 10 × 10 km and 5 km deep, whose coordinate is 32°00'N and 130°41'E at the center, was selected, see Figure 4-20. This modeling method has voxel cell-size of 250 × 250 × 50 m. The Figure 4-21 shows the 3-D gravity inversion model grid carried out using VOXI™ (Geosoft, 2018).

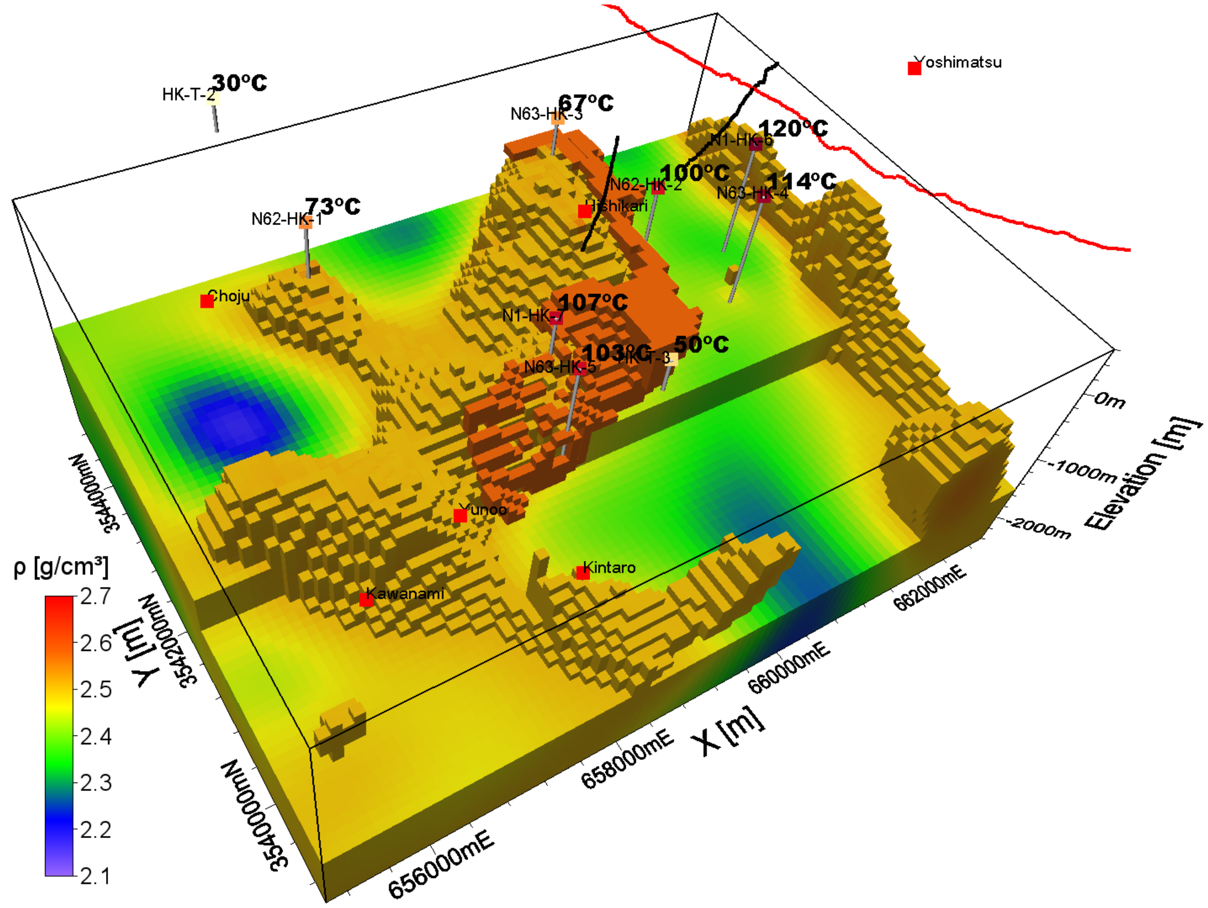

Figure 4-21. 3-D inversion model grid. The brown structure located aside of the high dense body in the center might be the hydrothermal reservoir with the volume of about 0.93 km^3, and an average block density value of 2.45 g/cm^3. The grid is plotted using Voxler 3-D program (Golden Software LCC, 2018).

The gravity inversion model (Figure 4-21) shows a significant body located at 300 m deep, which extends until the lowermost of the model, in the Hishikari hot spring zone. This anomaly has a density contrast of 0.09 g/cm^3, which represents an average density of 2.5485 g/cm^3, and fills a volume of 4.03 km^3. This consolidated mass, which might be either a fossilized intrusive volcanic body or hydrothermally altered rocks, appears to control the ore deposits in this municipality (Renderos et al., 2013). According to Urashima & Izawa (1983), this mineralization hydrothermal altered rock close to the Hishikari gold mine consists basically of quartz, adularia and clay minerals. Moreover, they emphasized that even though the Hishikari gold deposit is the first significant gold concentration discovered in the sedimentary basements in Japan, the mine has magmatic source. This magmatic origin indicates that the basement did not play an essential role as the source material for the ore constituents. The ores may be of magmatic origin either. The assumed rhyolitic plug underneath the ore deposit was significant serving as the conduit (vertical fracture system) for the rising ore solution, and the related magmatic ore solution was a primary source for sulfur and possibly gold (Ishihara et al., 1986). The unusually high-grade ores of the Hishikari deposit can be explained by the strong magmatic concentration of gold in the primary magmatic hydrothermal solution. The Hishikari mineralization model is illustrated in Figure 3-3.

A general geothermal resource conceptual model proposed by Cumming (2009) and Stimac et al. (2008), suggested three altered zones such as Smectite zone (Smectite-Zeolite mineral), Argillic zone (illite-smectite, albite, calcite, wairakite), and Propylitic zone (chlorite, epidote, illite, muscovite, biotite). Smectite alteration is characterized by the formation of Smectite clay and low to atmospheric temperature alteration minerals. Argillic alteration is characterized by the formation of illite and other low to moderate temperature minerals; and propylitic alteration has high temperature minerals resembling chlorite, epidote, biotite and quartz, with lesser quantities of calcite and albite (Mielke et al., 2015). As reported by Wyering (2014), there is a relationship between effective porosity and density of the rocks in geothermal fields, i.e., $\phi = -0.0285\rho + 77.8$. The study suggested that the Propylitic altered rocks in an Andesite deposits have a density of 2.38-2.6 g/cm^3, and an effective porosity of 5-12 %. This suggestion might explain the altered zone, which is mainly Andesite, below the Hishikari gold mine which has the highest density values found in the 3-D inversion model, i.e., 2.5485 g/cm^3.

In addition, Figure 4-21 shows a brown structure located aside of the high dense body in the center which might be the hydrothermal reservoir with about 0.93 km^3 big, and an average block density value of 2.45 g/cm^3. This structure corresponds with the results found by NEDO (1991) in its report (Figure 3-8), i.e., the possible geothermal reservoir orientation might trend NE-SW starting at Uonogoe place and ending close to the well N63-HK-5. In this region representing an area of 4.006 km^2 large, the fluid inclusion temperature of the veins indicates that the high temperature and dominant hydrothermal activity reached a maximum of 240 °C. Moreover, a possible recharge zone (well N63-HK-4) is situated on the side of the inferred reservoir. The characteristic of this area consists of fractured andesite and dacite structures. Figure 4-22 shows the possible location of the geothermal resource in red-dot, and a recharge zone in red-mesh.

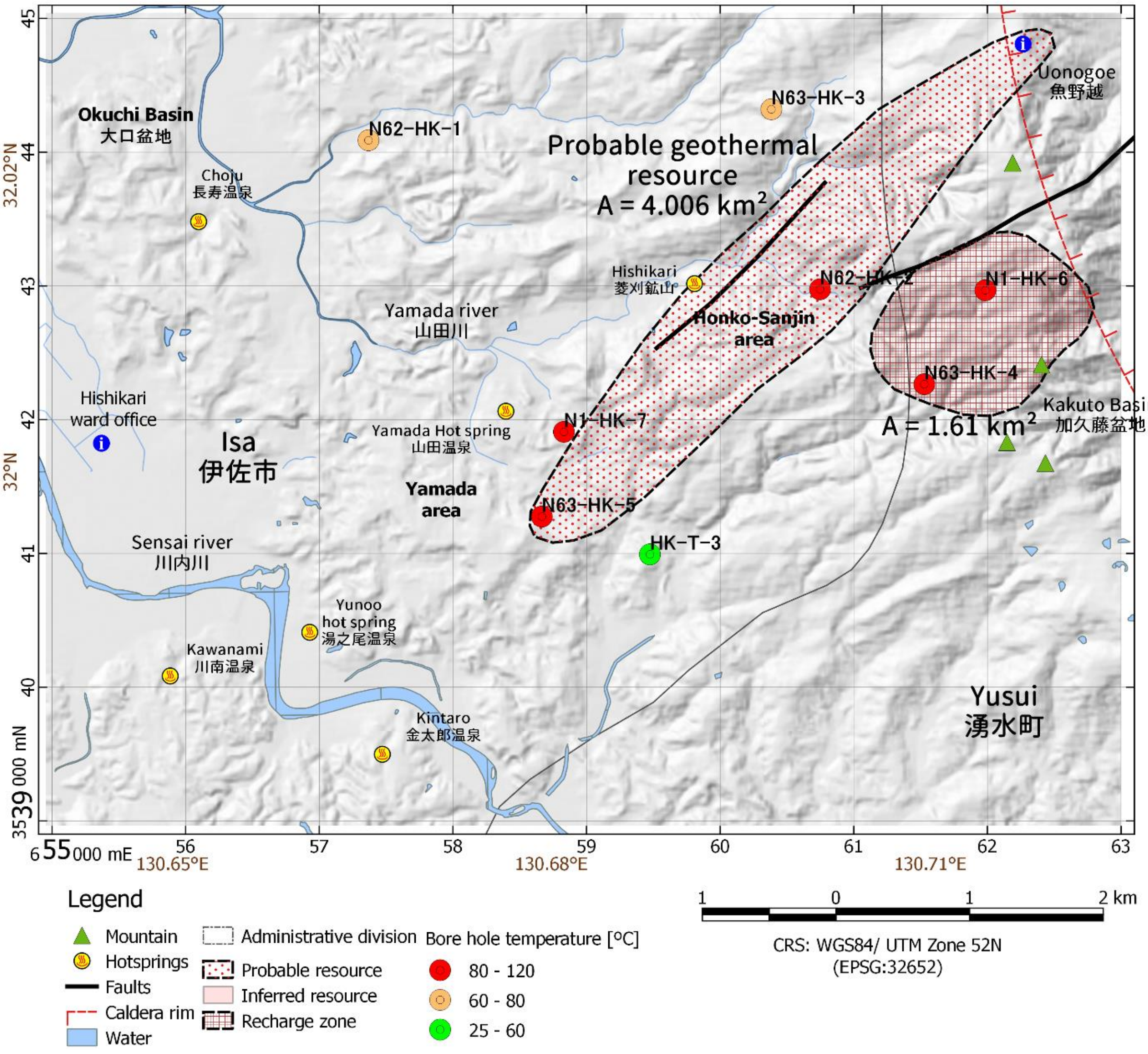

Figure 4-22. Probable geothermal resource area of 4.006 km^2 in red-dot pattern.

Into this 3-D model analysis, a planar slice at elevation of -1,000 m a.s.l (Figure 4-23), was extracted from the inversion model, then overlain on a shaded relief map and plotted alongside faults. The density map shows values ranging from 2.17 to 2.67 g/cm^3. In particular, located in the center of the map, the highest density value of 2.5-2.6 g/cm^3 is found. This particular body represents the propylitic alteration activity that is rich in minerals and where the gold mine is set up; likewise, the structure has a trend NE-SW, i.e., the anomaly is aligned along with the regional trending shown by lineaments map in Figure 3-4, and corresponds with the Kagoshima graben. As well, the Kakuto basin rim is evident in the east.

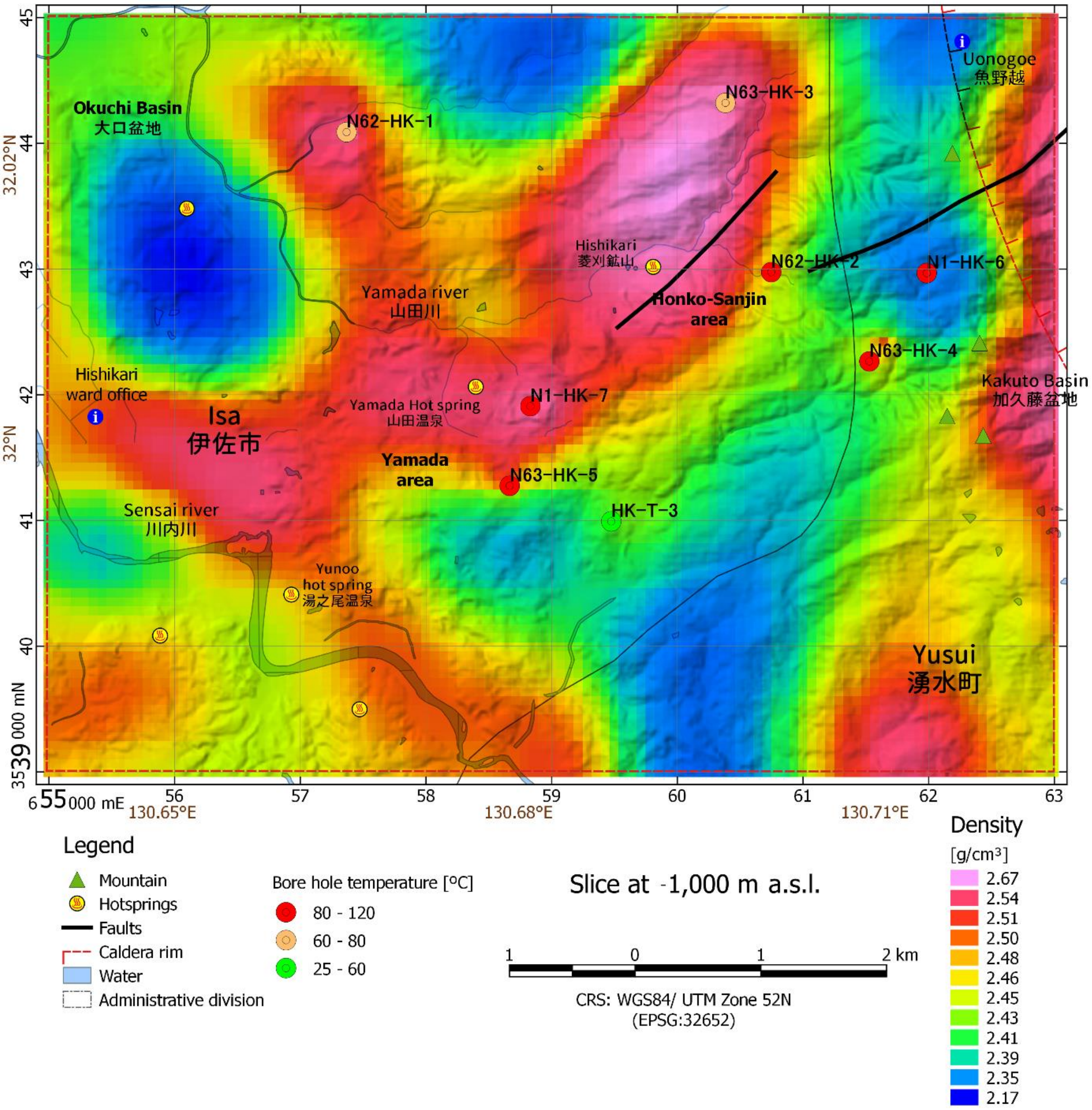

Figure 4-23. A planar view of density distribution at -1,000 m a.s.l. elevation.

The orientation of tectonic faults shown in Figure 4-23 appears to delimit the lateral extent and intensity in distributions of the dense body beneath the Hishikari gold mine. The relationship is still apparently visible despite the depth difference between surface structures and the dense body. The location of hydrothermal activities in most cases describes the zones of high thermal anomalies generally located close to or on the fault structures. This fault structures offer a pathway for fluids to rise to the surface showing zones of hydrothermal upwelling. In addition, the presence of a hot spring in the center of the area appears to be connected to the fault system. However, the hydrothermal manifestations of the hot springs Yunoo, Kintaro, and Kawanami make evident an old fault system that has been covered by sediment dragged by the Sendai River.

4.8 Conclusion

The main aim of conducting gravity study was to attempt to analyze and interpret the gravity data for delineating the geothermal reservoir boundary in the municipality of Isa, Kagoshima. Accordingly, the corresponding researchers conducted 2-D and 3-D gravity modeling in the current research. This modeling is an essential stage of the complete gravity analysis in the region. This is the filtering gravity methods, i.e., Horizontal-Derivative and Tilt-Derivative, can quickly detect steep gradients and indicate the location of faults or geological boundaries, however, they cannot estimate geological structure depth and shape. For this purpose, an area of 10 × 10 km was selected with the available gravity data of 175 stations. Applying several corrections such as latitude correction, free-air correction, Bouguer correction and terrain correction, and using the Bouguer density estimation methods, the analysis obtained a Bouguer Density of 2.458 g/cm^3. The Bouguer Anomaly result shows a high value at the center, which extends 5.61 km^2 horizontally and could represent the probable geothermal resource. According to the Kagoshima geological map, volcanic and sedimentary rocks are the dominant type of rocks in this area. Cretaceous Shimanto Supergroup controls the fundamental structure of the deepest element. This arrangement is typically composed of sandstone, shale, acidic tuff with subordinate conglomerates, and their alterations, also Pliocene volcanic rocks and alluvial deposits. Similarly, Kakuto and Okuchi Basin, which are located at east and west respectively, control the region. The 2-D gravity modeling was carried out requiring a density contrast between the two assumed layers, i.e., the basement and the low-density deposit, and thus a value of 0.4 g/cm^3 was assigned. Likewise, the horizontal size of the cells was set at 250 m. The profile A and B which trends NNW-SSE and NW-SE respectively in the center of the selected area, ISA municipality, indicate that the Sedimentary underground structure is located around 1,400 m, 250 m, and 700 m deep at Okuchi basin, Yamada Onsen, and Sendai River respectively. Also, the inversion profile evidences the borders of the propylitic reservoir which shows high gravity values. The last profile C which trends NE-SW in the center of the selected area, indicates that the sedimentary underground structure is located around 600 m, 520 m, 450 m, 950 m, 600 m deep at Kakuto basin, Uonogoe, well N62-HK-2, well N63-HK-5, and Sendai river respectively.

For a better understanding of the region, the authors also carried out 3-D gravity modeling. The result shows an area which has density values below 2.4 g/cm^3 and the zone NE-SW direction that starts at the Uonogoe area and ends at the Yamada area. Besides, there is a large anomaly located in the central area that has density values above 2.55 g/cm^3. This anomaly represents the hydrothermal alteration zone that hosts the propylitic altered rocks having precious minerals such as gold and silver. Between these evidenced zones, it could be inferred the location of the geothermal reservoir which has a volume of 0.93 km^3, a superficial area of 4.006 km^2, and an average block density value of 2.45 g/cm^3. This model will be used to evaluate the geothermal power potential in the region.

Although the results obtained from the inversion model are encouraging, there are some limitations. First of all, there is lack of extra new gravity data for adjusting the results. Secondly, an accurate geological map showing detailed faults system and lithologic cross-section that validate the gravity inversion is missing. Lastly, it is constrained the model in this study by including density estimates of lithologies interpreted from drill hole cuttings, but the exploration wells were located around 1-5 km of separation, i.e., the geological structures and hydrothermal condition could be different from each other.

Chapter 5

Assessment of geothermal energy potential in the eastern part of Isa

5.1 Overview

Until now, the geothermal resource in the hot spring close to the Municipality of Isa has not been used for power generation purpose although Geological Survey of Japan had carried out several preliminary geothermal assessments. They showed that the power potential density is around 20 kW/km^2 in the Municipality of Yusui in the Abundance map (MOE, 2011), see Figure 1-12. This map shows the Renewable Energy Introduction Potential Map and Basic Zoning Information, Fiscal Year 2011. For calibrating the previous value obtained by Government of Japan, the gravity data in the previous chapter was analyzed, and reviewed the past reports carried out by NEDO (1991).

When geothermal exploration starts, sometimes the provided data are either limited or missing. Consequently, a simple technique called volumetric method is used for estimating the energy available from the geothermal reservoir (Muffler & Cataldi, 1978). The calculation of the geothermal energy stored in a volume is based on reservoir characteristics and carried out by using the stochastic Monte Carlo simulation. To implement the simulation, a Python-based stochastic library, called the Geothermal Power Potential Evaluation (GPPeval) developed in Chapter 2, is used (Pocasangre & Fujimitsu, 2018).

5.2 Reservoir's parameters in the study area

For estimating the geothermal potential, the Volumetric Method is applied. The calculation of the geothermal energy stored in a volume is based on the range of reservoir parameters and carried out by using the stochastic Monte-Carlo simulation and the Geothermal Power Potential Evaluation library (GPPeval) (Pocasangre & Fujimitsu, 2018; Zaher et al., 2012).

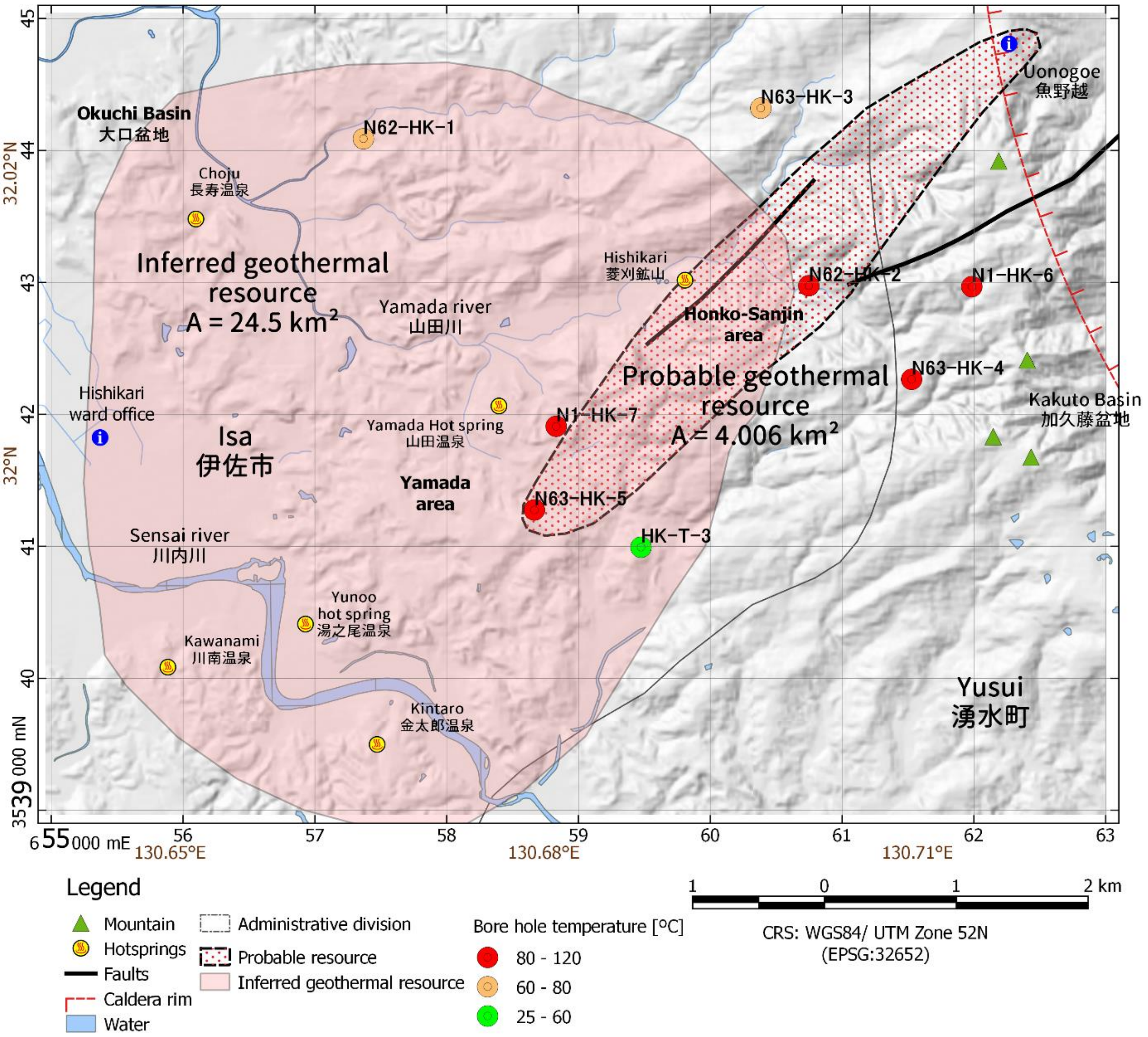

Figure 5-1. Inferred and probable geothermal resource of 24.5 and 4.006 km^2 respectively.

The methodology needs parameters such as reservoir area (A) and thickness (h), reservoir temperature (T_r), abandon temperature (T_a), average rock porosity (ϕ), rock specific heat (Cr) and density (ρ_r), fluid specific heat (Cf) and density (ρf), heat recovery factor (RF), electrical conversion efficiency (ηe), plant net capacity factor (PF), and lifespan (t). Equations (2-1) and (2-5) in Chapter 2 are the total heat stored in the geothermal reservoir (Q_T) and the geothermal power potential assessment (P) respectively. The parameters are described as following:

1. Area and Thickness (Table 5-1).

The selected surface area has two scenarios: a) Inferred resource reserves have a slightly smaller chance of recovery energy, but have a sound basis from surface exploration (e.g., springs, fumaroles, resistivity anomalies) to declare that a reservoir may exist. The inferred area is shown in Figure 5-1 which represents 24.5 km^2 large; b) probable geothermal resource is the most likely recoverable energy, with sufficient reservoir temperature indicators from either nearby wells or geothermometers along natural surface discharges that characterize the resource temperature and chemistry. The probable geothermal resource area is shown in Figure 5-1 which represents 4.006 km^2 large.

The reservoir thickness is usually obtained directly from either electromagnetics methods or drilling and well measurements. In this case, the value of 500 m thick is assigned based on the geothermal conceptual model developed by NEDO (1991) and shown in Figure 3-8.

Table 5-1. Area and thickness summary of the geothermal reservoir.

Property	Unit	Geothermal resource	
		Inferred	Probable
Area	km^2	24.5	4.006
Thickness	m	500	500

2. Reservoir and abandon temperature (Table 5-2).

To apply the Monte Carlo simulation, the hot spring parameters which were provided by the Geological Survey of Japan were used (Sakaguchi et al., 2000). The parameter for the inferred geothermal reservoir are the geo-thermometer of 117.6 °C, 143.6 °C, and 151.4 °C from Chalcedony (Chal), Conductive cooling (Qcond), and Na-K-Ca respectively (Fournier, 1973; Fournier & Rowe, 1966; Fournier & Truesdell, 1973). Likewise, the Hishikari hot spring has a superficial temperature of 65.9 °C, type of fluid of Na-HCO_3·Cl, pH of 6.6, and volumetric fluid discharge of 60 l/min. Furthermore, well's logging temperature of 110-125 °C which were interpolated and plotted into the conceptual model was used (NEDO, 1991). Lastly, the abandon temperature for a binary power plant which has a temperature difference of 5 °C at the pinch point is 105.36 °C, see Chapter 2 (Garg & Combs, 2015).

Table 5-2. Reservoir and abandon temperature summary.

Property	Unit	Geothermal resource	
		Inferred	Probable
Reservoir temperature	°C	117.6 to 151.4	110 to 125
Abandon temperature	°C	105.36	105.36

3. Rock properties: porosity, density, and specific heat (Table 5-3).

Using literature, it was obtained the rock properties for the inferred geothermal resource, i.e., andesite density of 2.61±0.2 g/cm^3, dacite density of 2.58±0.23 g/cm^3, sedimentary rocks density of 1.2-2.7 g/cm^3, and alluvium density of 1.540-1.98 g/cm^3 (Jacoby & Smilde, 2009; Mielke et al., 2015). For the probable geothermal reservoir, it was used the data provided by NEDO (1991) shown in the rock properties of the study area, Table 4-3, i.e., andesite density of 2.135 g/cm^3, dacite density of 2.33 g/cm^3, and sedimentary rock density of 2.64 g/cm^3 (Faye et al., 2018). Similarly, the specific heat of 0.92 to 2.39 kJ/kg-°C and 0.775 to 0.81 kJ/kg-°C for the inferred and probable geothermal reservoir respectively were selected (Schön, 2015).

The porosity that was described in Chapter 2 could be reasonably assumed that is a direct linear function of the recovery factor, at least as a conservative approximation (Bodvarsson, 1974; Nathenson, 1975). Figure 2-3 shows the correlation between the recovery factor (RF) and porosity (ϕ) assuming the geothermal recovery factor to be independent of reservoir temperature under an intergranular flow model. The porosity of 8 % for the inferred geothermal resource and 2.8 to 16.6 % for the probable geothermal resource were selected using the information shown in Table 4-3.

Table 5-3. Porosity, density, and specific heat summary.

Property	Unit	Geothermal resource	
		Inferred	Probable
Density	g/cm^3	2.1 to 2.7	2.33 to 2.64
Porosity	%	8.0	2.8 to 16.6
Rock specific heat	kJ/kg-°C	0.92 to 2.39	0.775 to 0.81

4. Fluid properties: density and specific heat (Table 5-4).

The fluid parameters were calculated using the saturation table of water (Wagner & Kretzschmar, 1998).

Table 5-4. Density of the reservoir fluid summary.

Property	Unit	Geothermal resource	
		Inferred	Probable
Density	g/cm^3	0.91537 to 0.94495	0.93889 to 0.95092
Fluid specific heat	kJ/kg-°C	4.2479 to 4.3164	4.237 to 4.2599

5. Heat recovery factor.

The recovery factor depends on the permeability structure (e.g., fracture vs. matrix, permeability anisotropy, faulting), production and injection well depths and patterns, and the thermal (i.e., heat and fluid recharge from depth) and hydraulic boundary conditions (i.e., recharge/discharge along the ground surface and assumed lateral boundaries of the geothermal reservoir). Many reservoir properties that affect the thermal recovery factor are likely to be poorly known until the reservoir has been producing for several years. Therefore, specification of the thermal recovery factor for a given reservoir is often a matter of conjecture. Some estimations of the thermal recovery factor based on both theoretical grounds and data from operating hydrothermal fields suggest that the appropriate range for fracture-dominated geothermal reservoirs is 0.08–0.20 (Williams, 2014). In this case the geothermal reservoir is assumed to contain hot permeable rock and single phase liquid water.

6. Electrical conversion efficiency.

The conversion efficiency is the amount of geothermal energy that can be converted into electricity. This parameter is limited by the second law of thermodynamics, and it is also a function of the optimum plant design and the efficiency of different components, i.e., the conversion efficiency depends on each geothermal power plant. In the case of low-enthalpy applications, the conversion efficiency for several operating Organic Rankine Cycle (ORC) power plants is analyzed by applying an exergy efficiency analysis or so-called second law efficiencies. Most operating ORC power plants have relatively low (< 25 %) second law efficiencies (DiPippo, 2004).

7. Plant net capacity factor and lifespan.

The Ministry of Environment of Japan suggests a plant net capacity factor and Lifespan of 90 % and 20 years respectively (Ministry of the Environment Government of Japan, 2011).

5.3 Geothermal power potential assessment in Isa

The geothermal power potential assessment is presented below using the Python implementation called GPPeval (Pocasangre & Fujimitsu, 2018). The simulation was run several times. The number of trials until reducing the root mean square (RMS) of the calculations were controlled, i.e., the RMS values after 1,000 and 10,000 trials were 0.12 and 0.04, respectively. However, running more than 10,000 trials did not significantly change the RMS and only augments the execution time. The reservoir parameters, Table 5-5, were prepared using an external CSV file as was shown in Figure 2-5, and edited using a simple ASCII editor.

Table 5-5 considers the following central assumptions (Garg & Combs, 2015; Kang, 2012):

1. An ORC Binary Geothermal Power Plant that uses to heat a secondary working fluid (isobutane) was proposed, and the spent brine is injected back into the reservoir. The turbine inlet pressure is assumed to be 20 bars; the saturation temperature for isobutane at the latter pressure is 100.36 °C (NIST, 2017). Isobutane is assumed to be saturated at the turbine inlet. With a temperature differential of 5 °C at the pinch point, the temperature of the brine at the pinch point is 105.36 °C.
2. The conversion efficiency of the power plant of less than 25 % was assumed according to USGS.
3. The thickness was not calculated in this dissertation, therefore, a fixed 500 m value is used based on NEDO (1991) conceptual model (Figure 3-8).

Table 5-5. Input reservoir parameters in Isa region.

Reservoir Properties	Inferred Geothermal Resource			Probable Geothermal Resource		
	Min	Most Likely	Max	Min	Most Likely	Max
Reservoir Area, A[km^2]	1.0	12.25	24.5	0.2	2.0	4.006
Thickness, h[m]		500			500	
Reservoir Temp., Tr[°C]	117.6	134.5	151.4	110.0	110.0	125.0
Abandon Temp., Ta[°C]		105.36			105.36	
Porosity, ϕ		0.08		0.028	0.097	0.166
Rock SH C_r[kJ/kg °C]	0.92	1.655	2.39	0.775	0.793	0.81
Water SH, C_f[kJ/kg °C]	4.25	4.285	4.32	4.24	4.24	4.26
Rock Density ρ_r[kg/m^3]	2100	2400	2700	2330	2458	2640
Water Density, ρ_f[kg/m^3]	915.4	930.2	945.0	939.0	951.0	951.0
Recovery Factor, RF	0.08	0.14	0.2	0.08	0.14	0.2
Conversion Efficiency, η_e	0.1	0.175	0.25	0.1	0.175	0.25
Plant Net Capacity Factor, PF	0.8	0.85	0.9	0.8	0.85	0.9
Lifespan, t[years]		20			20	

5.3.1 Interpretation of Monte Carlo simulation results

The results are divided into two scenarios, the inferred and probable geothermal resource. The interpretation is shown as following:

- The inferred geothermal resource simulation presented in Figure 5-2 shows possible inference when the output greater than or equal to 4.266 MWe is 90 % (i.e., proven reserves), and when the capacity greater than or equal to 16.19 MWe is 41.4 % (i.e., proven + probable reserves). Additionally, the probability that the output is greater than or equal to 40.03 MWe is only 5 % (i.e., proven

+ probable + possible or maximum reserves), after which, the preliminary upper limit power potential assessment is 174.1 kWe/km^2 for a maximum of 20 years. These results imply that the field could initially support a 4.266 MWe geothermal power plant for 20 years maximum with a possible expansion to 16.19 MWe, subject to further delineation drilling and availability of field performance data. Finally, the risk that the field could not sustain 4.266 MWe is equal to or less than 10 % can be affirmed. However, this interpretation will be subject to further investigations for obtaining and validating the new data, i.e., results are subject to further delineation drilling and availability of field performance data and considering that the geothermal power plant has single OCR system due to the very low temperature.

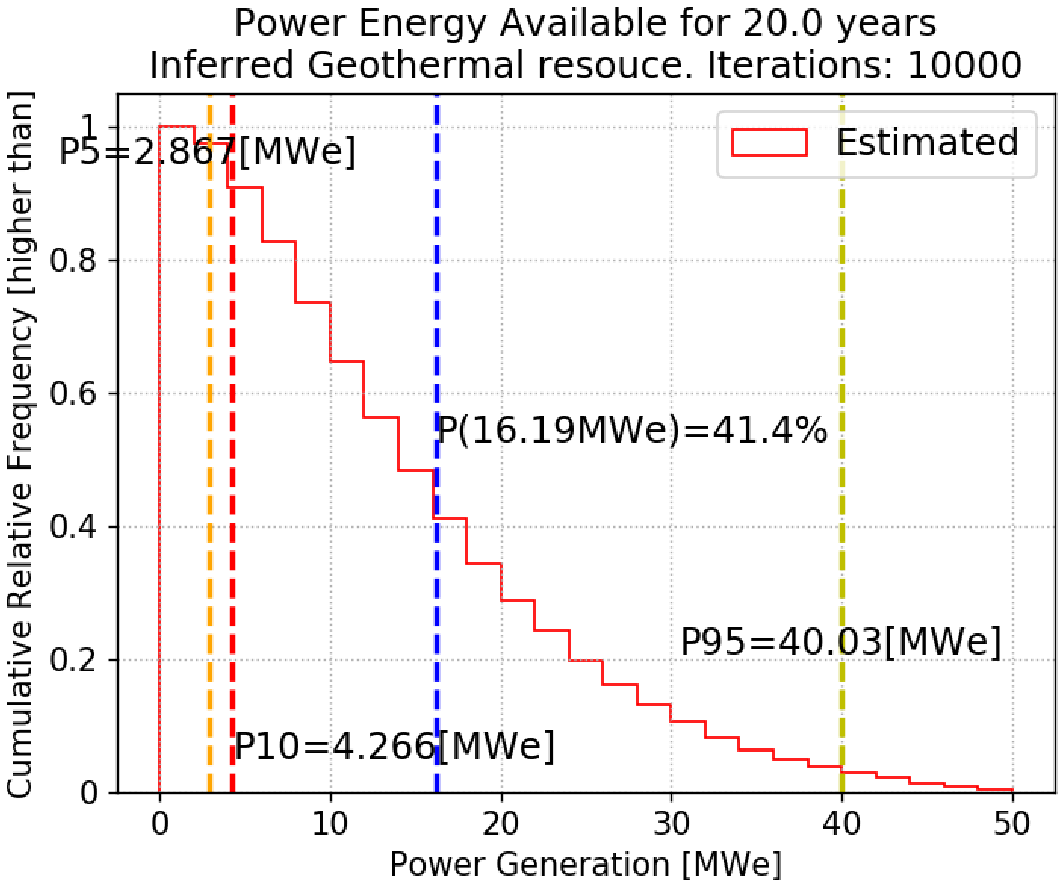

Figure 5-2. Cumulative frequency distribution (CFD) of the municipality of Isa. Case: Inferred geothermal resource. This simulation was run for 20 years.

- The probable geothermal resource simulation presented in Figure 5-3 shows possible inference when the output greater than or equal to 121.9 kWe is 90 %

(i.e., proven reserves), and when the capacity greater than or equal to 227.9 kWe is 74.26 % (i.e., proven + probable reserves). Additionally, the probability that the output is greater than or equal to 1.272 MWe is only 5 % (i.e., proven + probable + possible or maximum reserves), after which, the preliminary power upper limit potential assessment is 30.43 kWe/km^2 for a maximum of 20 years. These results imply that the field could initially support a 121.9 kWe geothermal power plant for 20 years maximum with a possible expansion to 227.9 kWe, subject to further delineation drilling and availability of field performance data. Finally, the risk that the field could not sustain 121.9 kWe is equal to or less than 10 % can be affirmed. However, this interpretation will be subject to further investigations for obtaining and validating the new data, i.e., results are subject to further delineation drilling and availability of field performance data and considering that the geothermal power plant has single OCR system due to the very low temperature.

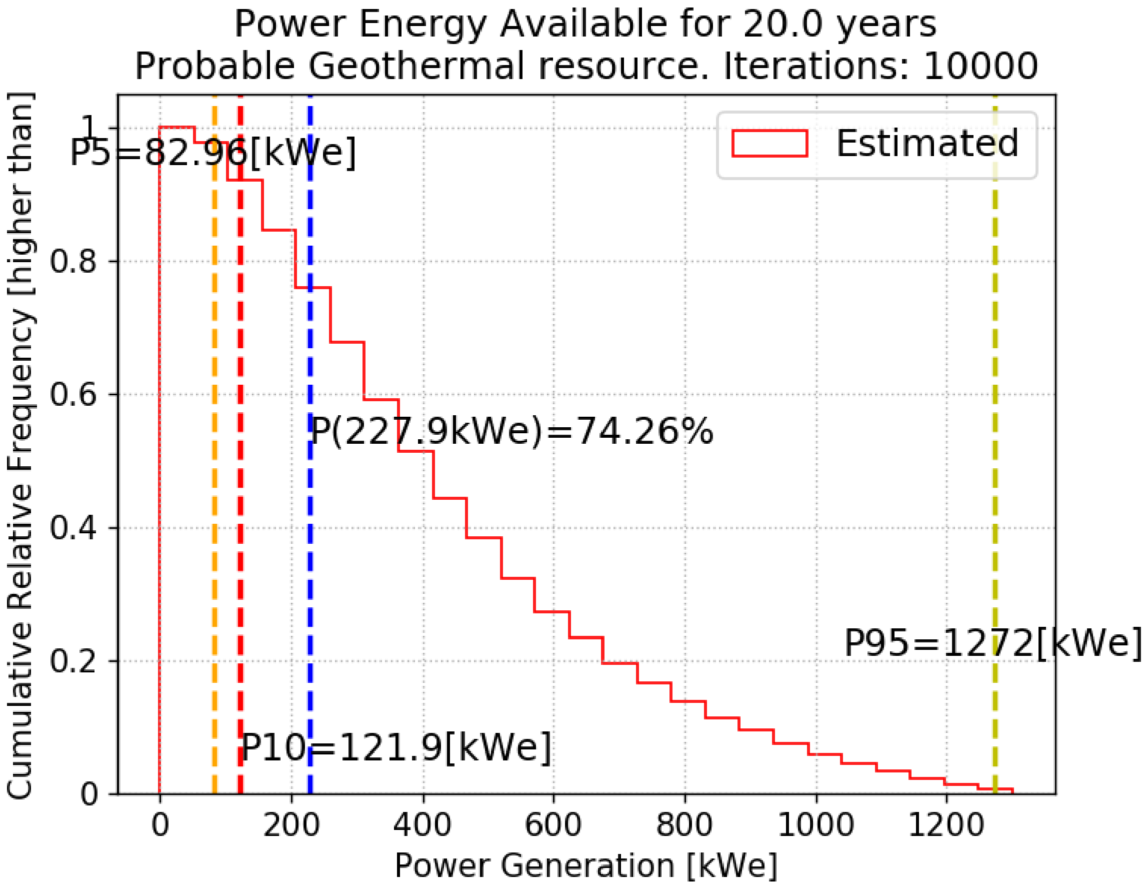

Figure 5-3. Cumulative frequency distribution (CFD) of the municipality of Isa. Case: Probable geothermal resource. This simulation was run for 20 years.

The following Table 5-6 shows the Monte Carlo simulations result summary for Inferred and Probable geothermal resources:

Table 5-6 Power Potential assessment results.

Scenarios	Power potential assessment [kWe]			Density
	P10 %	Most Likely	P95 %	[kWe/km^2]
1) Inferred geothermal resource	4,266.0	16,190.0	40,030.0	174.1
2) Probable geothermal resource	121.9	227.9	1,272.0	30.4

In Chapter 1 (Renewable energy introduction potential map, Figure 1-12), the abundance map of the Isa, Ebino, and Yusui municipalities were described. In this map, the Ministry of the Environment of Japan plotted the geothermal power potential assessments. Consequently, they said in its report that the power potential density is around 20 kW/km^2 in the vicinity of the Municipality of Yusui. Afterward, revising the values shown in Table 5-6, it is said that the Inferred geothermal resource, i.e., 4.27 MWe and 174.1 kWe/km^2, is moderately big, and does not indicate the precise power potential. On the other hand, the adjusted value of the probable geothermal resource, i.e., 121.9 kWe and 30.4 kWe/km^2, that was calculated both processing the data provided by NEDO (1991), and running 2-D and 3-D modeling suggests more precise power potential and closes to the latter one calculated by the Government.

5.4 Conclusion

Until now, the geothermal resource in the hot spring close to the Municipality of Isa has not been used for power generation purpose although the Geological Survey of Japan had carried out several preliminary geothermal assessments. They showed that the power potential density is around 20 kW/km^2 in the Municipality of Yusui in the Abundance map. For adjusting the latter value, two scenarios were simulated, i.e., the inferred and probable geothermal resource. The central objective is to use the volumetric method to estimate the electrical energy production ability from a geothermal liquid-dominated reservoir, and to code a

Python-based stochastic library with suitable methods for running the simulation for an Inferred and probable geothermal resource. As a result of running the simulation, the frequency distribution, which has 10,000 iterations, shows a possible inference that the outputs that are greater than or equal to 4.27 MWe and 121.9 kWe is 90 % for the inferred and probable geothermal resource respectively. After that, the preliminary power potential assessment densities are 174.1 kWe/km^2 and 30.4 kWe/km^2 for the inferred and probable geothermal resource respectively during 20 years. The result, using only the probable geothermal resource, implies that the field could initially support a 121.9 kWe power plant for 20 years maximum and a possible expansion to 227.9 kWe is subject to further delineation drilling and availability of field performance data. As a final point, revising the values shown in Table 5-6, it is said that the Inferred geothermal resource, i.e., 4.27 MWe and 174.1 kWe/km^2, is moderately significant, and does not indicate the precise power potential. On the other hand, the adjusted value of the probable geothermal resource, i.e., 121.9 kWe and 30.4 kWe/km^2, that was calculated both processing the data provided by NEDO (1991), and running 2-D and 3-D modeling suggests more precise power potential and closes to the latter one calculated by the Government. Nevertheless, the concluding results need to be corrected by further geoscientific investigations including inversion modelings of the Isa area because in this dissertation only gravity data was analyzed. The studies could be a precise gravity survey, magneto-telluric (MT), time-domain electromagnetic methods (TDEM), seismic logging, as well as numerical simulation, e.g., USGS Hydrotherm[21] and TOUGH2[22].

---

[21] https://volcanoes.usgs.gov/software/hydrotherm/

[22] https://tough.lbl.gov/

Chapter 6

General Conclusions

6.1 Introduction

A new world energy economy is emerging as fossil fuel prices rise, oil insecurity deepens, nuclear power plant accident recently in Japan and moreover concerns with pollution and climate instability cast a shadow over the future of coal. Consequently, the great energy transition from fossil fuels to renewable sources of energy is in progress. Geothermal energy provides one of such an important alternatives. The relationship of intense volcanic activity with the Earth's tectonic plate boundary has resulted in a world-wide distribution of geothermal energy which is an important alternative renewable energy source for the developed and developing countries as a whole.

Japan is one of the most tectonically active countries in the world, with nearly 200 volcanoes and tremendous geothermal energy resources. Because of this tectonic activity, Japan has two periods before the earthquake in 2011 and later. The event changed the energy prospect of renewable energy. Japan has about 28,000 hot springs that are naturally discharging or artificially drilled. An estimation suggests that, using 1,500 hotter wells and springs among them, as much as 723 MWe could be generated without additional drillings. Currently, 21 electric power units at 18 geothermal sites are in operation with a total capacity of 542 MWe, which amounts to about 2.3 % of its potential. Most are located in Tohoku and Kyushu regions. Total geothermal power capacity in Japan has changed little since

1995. In an early stage, a 42 MWe geothermal power generation project at Wasabizawa, Akita, has been carried out by Mitsubishi Material Company and J-Power and expected to be commenced to operate middle 2019 (JOGMEC, 2015). In addition, a new geothermal power plant went online in Japan newly. The plant in Iwate started operations already in late January 2019 with a rated output of 7.499 MWe in Matsuo-Hachimantai District (Richter, 2019).

The study area for this dissertation is in Isa City, Kagoshima Prefecture (鹿児島県伊佐市) which is located in the inland area at the northern end of Kagoshima Prefecture, approximately 75 km north of Kagoshima City. Located in the southern part of Kyushu Island, it is considered one of the wealthiest places in Japan. The zone is blessed as a result of the hydrothermal manifestations and volcanic activity as they have been depositing several minerals into geologic structures or fractures, e.g., gold. For this dissertation, the study was focused on hydrothermal manifestations of low enthalpy fluids in Isa area, i.e., Hishikari, Yunoo, Kawanami, and Kintaro hot springs. The temperature at the surface and in the borehole is around 60 °C and 120 °C respectively (Sakaguchi et al., 2000).

Until now, the geothermal resource in the hot spring close to the Municipality of Isa has not been used for power generation purpose although Geological Survey of Japan had carried out several preliminary geothermal assessments. They show that the power potential density is around 20 kW/km^2 in the Municipality of Yusui in the Abundance map (Ministry of the Environment Government of Japan, 2011). For calibrating the previous value obtained by Government of Japan, the gravity data for figuring out geothermal reservoir border and the geothermal power potential assessment was analyzed. For this purpose, an area of 10 × 10 km, whose coordinates are 31.97°N to 32.06°N and 130.64°E to 130.75°E, was selected.

6.2 Geothermal power assessment tool

The primary purpose of this chapter are to use the volumetric method to estimate the electrical energy production ability from a geothermal liquid-dominated reservoir, and to code a Python-based stochastic library with suitable methods for running the simulation. The calculation of geothermal energy stored in a volume is based on the range of reservoir parameters and carried out using a stochastic Monte Carlo simulation. During early exploration, estimates of essential reservoir parameters are poorly constrained, but application of the USGS “heat in place” evaluation method along with Monte Carlo simulations produces a wide distribution for the probable power potential. The USGS volumetric “heat in place” method, together with Monte Carlo simulations, are a useful tool for assessing the electrical capacity of a geothermal reservoir.

Although licensed software is available for carrying out these simulations, an open-source programming language was selected, Python. The resulting stochastic library is called the Geothermal Power Potential Evaluation, GPPeval. The new library utilizes the standard numerical modules, Numpy and Scipy, but also the Matplotlib module for graphical visualization, and the Mcerp module for performing non-order specific error propagation or uncertainty analysis. The GPPeval is structured as three essential objects including a geothermal power plant module, a Monte Carlo simulation module, and a tools module.

Finally, to demonstrate how the Python-based stochastic library can be used for assessing the geothermal power potential, an assessment of hot spring data in the municipality of Nombre de Jesus, El Salvador is presented. After running the stochastic simulation, the frequency distribution shows that the field could initially support a 9.16 MWe power plant for 25 years and a possible expansion to 17.1 MWe. However, the geothermal power potential must be investigated further to obtain and validate the new data.

6.3 Field characteristics of Isa, Kagoshima

The regional geology and structural setting of the study area in the eastern part of Isa, Kagoshima, have attracted much researches, and some review papers have been written due to the importance of gold mine exploitation. The area is an ancient volcanic region, and one of the most important gold mines in Japan is located in this area, Hishikari gold mine. In 1973 the Taio Mining Co., a subsidiary of the Sumitomo Metal Mining Co., Ltd. (SMM), acquired the mineral rights. In the neighborhood of Hishikari region, specifically in the eastern part of Isa City, the fundamental structure in the most profound element is controlled by Cretaceous Shimanto Supergroup; additionally Quaternary volcanic rocks. The topography, ranging from 200 to 600 m in elevation, comprises densely timbered, hilly terrain separated by small valleys cultivated mainly with rice. The atmospheric temperatures range from a low of -7 ℃ to a high of 35 °C. The vein system can be classified as an epithermal gold-silver-bearing quartz-adularia vein deposit.

The analysis of the orientation of structures completed using rose diagram shows the azimuths direction of the local distribution of lineaments trending ENE-WSW. The angular tendency corresponds pretty well to that of the faults, the general trend from lineaments matched with the regional trend of Kagoshima Graben.

As a final point, scientists consider that several types of geothermal systems have been formed in the past as a result of the change in the volcanic activity in the Hishikari area. They inferred that the most superior geothermal system of this type was formed around 0.91 to 1.15 Ma close to Mount Kurozono (黒園山) site. The fluid inclusion temperature of the veins indicates that the high temperature and dominant hydrothermal activity reached a maximum of 240 °C. The large-scaled deformation zone accompanied by the mineralization of gold and silver were also formed at this time. Considering the distribution of the land temperature and the temperature of the reservoir, the center of the hydrothermal activity is the one near the Uonogoe (魚野越) field in the eastern end of this area. It indicates the possibility that there is a deep underground geothermal potential where the Hishikari upper part andesite was volcanically active. The extrapolated temperature using well logging shows a value of 144 °C.

6.4 Gravity data analysis and interpretation

The main aim of conducting gravity study was to attempt to analyze and interpret the gravity data for delineating the geothermal reservoir boundary in the municipality of Isa, Kagoshima. Accordingly, the corresponding researchers conducted 2-D and 3-D gravity modeling in the current research. This modeling is an essential stage of the complete gravity analysis in the region. This is the filtering gravity methods, i.e., Horizontal-Derivative and Tilt-Derivative, can quickly detect steep gradients and indicate the location of faults or geological boundaries, however, they cannot estimate geological structure depth and shape. For this purpose, an area of 10 × 10 km was selected with the available gravity data of 175 stations. Applying several corrections such as latitude correction, free-air correction, Bouguer correction and terrain correction, and using the Bouguer density estimation methods, the analysis obtained a Bouguer Density of 2.458 g/cm^3. The Bouguer Anomaly result shows a high value at the center, which extends 5.61 km^2 horizontally and could represent the probable geothermal resource. According to the Kagoshima geological map, volcanic and sedimentary rocks are the dominant type of rocks in this area. Cretaceous Shimanto Supergroup controls the fundamental structure of the deepest element. This arrangement is typically composed of sandstone, shale, acidic tuff with subordinate conglomerates, and their alterations, also Pliocene volcanic rocks and alluvial deposits. Similarly, Kakuto and Okuchi Basin, which are located at east and west respectively, control the region.

The 2-D gravity modeling was carried out requiring a density contrast between the two assumed layers, i.e., the basement and the low-density deposit, and thus a value of 0.4 g/cm^3 was assigned. Likewise, the horizontal size of the cells was set at 250 m. The profile A and B which trends NNW-SSE and NW-SE respectively in the center of the selected area, ISA municipality, indicate that the Sedimentary underground structure is located around 1,400 m, 250 m, and 700 m deep at Okuchi basin, Yamada Onsen, and Sendai River respectively. Also, the inversion profile evidences the borders of the propylitic reservoir which shows high gravity values. The last profile C which trends NE-SW in the center of the selected area, indicates that the sedimentary underground structure is located around 600 m, 520 m, 450 m, 950 m, 600 m deep at Kakuto basin, Uonogoe, well N62-HK-2, well N63-HK-5, and Sendai river respectively.

For a better understanding of the region, the authors also carried out 3-D gravity modeling. The result shows an area which has density values below 2.4 g/cm^3 and the zone NE-SW direction that starts at the Uonogoe area and ends at the Yamada area. Besides, there is a large anomaly located in the central area that has density values above 2.55 g/cm^3. This anomaly represents the hydrothermal alteration zone that hosts the propylitic altered rocks having precious minerals such as gold and silver. Between these evidenced zones, it could be inferred the location of the geothermal reservoir which has a volume of 0.93 km^3, a superficial area of 4.006 km^2, and an average block density value of 2.45 g/cm^3. This model will be used to evaluate the geothermal power potential in the region.

Although the results obtained from the inversion model are encouraging, there are some limitations. First of all, there is lack of extra new gravity data for adjusting the results. Secondly, an accurate geological map showing detailed faults system and lithologic cross-section that validate the gravity inversion is missing. Lastly, it is constrained the model in this study by including density estimates of lithologies interpreted from drill hole cuttings, but the exploration wells were located around 1-5 km of separation, i.e., the geological structures and hydrothermal condition could be different from each other.

6.5 Assessment of geothermal energy potential in the study area

Until now, the geothermal resource in the hot spring close to the Municipality of Isa has not been used for power generation purpose although the Geological Survey of Japan had carried out several preliminary geothermal assessments. They showed that the power potential density is around 20 kW/km^2 in the Municipality of Yusui in the Abundance map. For adjusting the latter value, two scenarios were simulated, i.e., the inferred and probable geothermal resource. The central objective is to use the volumetric method to estimate the electrical energy production ability from a geothermal liquid-dominated reservoir, and to code a Python-based stochastic library with suitable methods for running the simulation for an Inferred and probable geothermal resource. As a result of running the simulation, the frequency distribution, which has 10,000 iterations, shows a possible inference that the outputs that are greater than or equal to 4.27 MWe and 121.9 kWe is 90 % for the inferred and probable geothermal resource respectively. After that, the preliminary power potential assessment densities are 174.1 kWe/km^2 and 30.4 kWe/km^2 for the inferred and probable geothermal resource respectively during 20 years. The result, using only the probable geothermal resource, implies that the field could initially support a 121.9 kWe power plant for 20 years maximum and a possible expansion to 227.9 kWe is subject to further delineation drilling and availability of field performance data. As a final point, revising the values shown in Table 5-6, it is said that the Inferred geothermal resource, i.e., 4.27 MWe and 174.1 kWe/km^2, is moderately significant, and does not indicate the precise power potential. On the other hand, the adjusted value of the probable geothermal resource, i.e., 121.9 kWe and 30.4 kWe/km^2, that was calculated both processing the data provided by NEDO (1991), and running 2-D and 3-D modeling suggests more precise power potential and closes to the latter one calculated by the Government. Nevertheless, the concluding results need to be corrected by further geoscientific investigations including inversion modelings of the Isa area because in this dissertation only gravity data was analyzed. The studies could be a precise gravity survey, magneto-telluric (MT), time-domain electromagnetic methods (TDEM), seismic logging, as well as numerical simulation, e.g., USGS Hydrotherm and TOUGH2.

References

Abe, I., Suzuki, H., Isogami, A., & Goto, T. (1986). Geology and development of the Hishikari mine. *Mining Geology*, *36*, 117–130.

Abebe, T., Mazzarini, F., Innocenti, F., & Manetti, P. (1993). The Yerer-Tullu Wellel Extensional Structure (Central Ethiopia): Evidences from Remote Sensing, Petrologic and Geochronologic Data. In *Journal of African Earth Sciences* (Vol. 17, pp. 145–165). IEEE. https://doi.org/10.1109/IGARSS.1995.520285

AIST National Institute of Advanced Industrial Science and Technology. (2009). Geothermal Potential Map in Japan. Digital Geoscience Map GT-4. *CD-ROM*. Tsukuba, Ibaraki, Japan.

AIST National Institute of Advanced Industrial Science and Technology. (2014). Hot spring power plant project, Niigata. Retrieved from http://www.aist.go.jp/

Akaike, H. (1998). Likelihood and the Bayes procedure. In *Selected Papers of Hirotugu Akaike* (pp. 309–332). Springer, New York, NY. https://doi.org/10.1007/978-1-4612-1694-0_24

Aravena, D., Muñoz, M., Morata, D., Lahsen, A., Parada, M. Á., & Dobson, P. (2016). Assessment of high enthalpy geothermal resources and promising areas of Chile. *Geothermics*, *59*, 1–13. https://doi.org/10.1016/j.geothermics.2015.09.001

Arima, T., Fujimitsu, Y., & Nishijima, J. (2013). Estimation of Subsurface Structure in the Western Fukuoka City from Gravity Data. *Procedia Earth and Planetary Science*, *6*, 163–168. https://doi.org/http://dx.doi.org/10.1016/j.proeps.2013.01.022

Askari, A. (2014). Edge detection of gravity anomaly sources via the tilt angle , total horizontal derivative , total horizontal derivative of the tilt angle and new normalized total horizontal derivative. *Scholars Journal of Engineering and Technology*, *2*(6B), 842–846. Retrieved from http://saspublisher.com/wp-content/uploads/2014/10/SJET26B842-846.pdf

Banerjee, B., & Das Gupta, S. P. (1977). Gravitational attraction of a rectangular parallelepiped. *GEOPHYSICS*, *42*(5), 1053–1055. https://doi.org/10.1190/1.1440766

Barbosa, R. D., & Pereira, J. G. (2013). Inversão 3D de dados Magnéticos na Região de Mara Rosa - Goiás, Brasil, utilizando Geosoft VOXI. In *13th International Congress of the Brazilian Geophysical Society & EXPOGEF, Rio de Janeiro, Brazil, 26–29 August 2013* (pp. 520–525). Society of Exploration Geophysicists and Brazilian Geophysical Society. https://doi.org/10.1190/sbgf2013-109

Battaglia, M., Roberts, C., & Segall, P. (1999). Magma intrusion beneath Long Valley caldera confirmed by temporal changes in gravity. *Science*, *285*(5436), 2119–2122. https://doi.org/10.1126/science.285.5436.2119

Bertani, R. (2012). Geothermal power generation in the world 2005-2010 update report. *Geothermics*, *41*(2012), 1–29. https://doi.org/10.1016/j.geothermics.2011.10.001

Bertani, R. (2015). Geothermal Power Generation in the World 2010 – 2014 Update Report. *Proceedings World Geothermal Congress*, *2015*(April), 1–19. https://doi.org/10.1016/j.geothermics.2011.10.001

Bodvarsson, G. (1974). Geothermal resource energetics. *Geothermics*, *3*(3), 83–92. https://doi.org/10.1016/0375-6505(74)90001-7

Bowie, W. (1912). *Effect of topography and isostatic compensation on gravity*. Washington.

Briggs, I. C. (1974). Machine contouring using minimum curvature. *Geophysics*, *39*(1), 39–48. https://doi.org/10.1190/1.1440410

Brueck, D., & Tanner, S. (2001). *Python 2.1 Bible*. New York: Hungry Minds, Inc.

Bullard, E. C. (1936). Gravity Measurements in East Africa. *Philosophical Transactions of the Royal Society A: Mathematical, Physical and Engineering Sciences*, *235*(757), 445–531. https://doi.org/10.1098/rsta.1936.0008

Campos, T. (1988). Geothermal resources of El Salvador. Preliminary assessment. *Geothermics*, *17*(2–3), 319–332. https://doi.org/10.1016/0375-6505(88)90061-2

Canny, J. (1986). A Computational Approach to Edge Detection. *IEEE Transactions on Pattern*

Analysis and Machine Intelligence, *PAMI-8*(6), 679–698. https://doi.org/10.1109/TPAMI.1986.4767851

Carlos, D. U., Uieda, L., & Barbosa, V. C. F. (2016). How two gravity-gradient inversion methods can be used to reveal different geologic features of ore deposit — A case study from the Quadrilátero Ferrífero (Brazil). *Journal of Applied Geophysics*, *130*, 153–168. https://doi.org/10.1016/J.JAPPGEO.2016.04.011

Carmichael, R. S., & Henry, G. (1977). Gravity exploration for groundwater and bedrock topography in glaciated areas. *Geophysics*, *42*(4), 850–859. https://doi.org/10.14203/risetgeotam2017.v27.295

Cataldi, R., Lazzarotto, A., Muffler, P., Squarci, P., & Stefani, G. (1978). Assessment of geothermal potential of central and southern Tuscany. *Geothermics*, *7*(2–4), 91–131. https://doi.org/10.1016/0375-6505(78)90003-2

Chen, J., Li, J., Zhang, Z., & Ni, S. (2014). Long-term groundwater variations in Northwest India from satellite gravity measurements. *Global and Planetary Change*, *116*, 130–138. https://doi.org/10.1016/J.GLOPLACHA.2014.02.007

Clotworthy, A. W., Ussher, G. N. H., Lawless, J. V., & Randle, J. B. (2006). Towards an industry guideline for geothermal reserves determination. *Transactions - Geothermal Resources Council*, (January).

Consejo Nacional de Energía Gobierno de El Salvador. (2010). National Energy Policy of El Salvador 2010 - 2024. San Salvador, El Salvador: Gobierno de EL Salvador.

Consejo Nacional de Energía Gobierno de El Salvador. (2014). *Updating of the indicative plan for the expansion of the Electricity Generation in El Salvador 2014-2024*. San Salvador, El Salvador. Retrieved from http://estadisticas.cne.gob.sv/images/boletines/estudios/

Cooper, G. R. J., & Cowan, D. R. (2006). Enhancing potential field data using filters based on the local phase. *Computers and Geosciences*, *32*(10), 1585–1591. https://doi.org/10.1016/j.cageo.2006.02.016

Cordell, L., & Grauch, V. J. S. (1985). Mapping basement magnetization zones from aeromagnetic data in the San Juan Basin, New Mexico. In W. J. Hinze (Ed.), *The Utility of Regional Gravity and Magnetic Anomaly Maps* (pp. 181–197). Society of Exploration Geophysicists. https://doi.org/10.1190/1.0931830346

Cordell, L., & Henderson, R. (1968). Iterative Three-Dimensional Solution of Gravity Anomaly Data Using a Digital Computer. *Geophysics*, *33*(4), 596–601. https://doi.org/10.1190/1.1439955

Cumming, W. (2009). Geothermal resource conceptual models using surface exploration data. In *Thirty-Fourth Workshop on Geothermal Reservoir Engineering, Stanford University* (p. 6). Stanford, California. Retrieved from http://citeseerx.ist.psu.edu/viewdoc/download?doi=10.1.1.505.6121&rep=rep1&type=pdf

Dahlin, T., Bernstone, C., & Loke, M. H. (2002). Case History A 3-D resistivity investigation of a contaminated site at Lernacken , Sweden. *GEOPHYSICS*, *67*(6), 1692–1700.

Dickson, M. H., & Fanelli, M. (2006). *Geothermal Energy: Utilization and Technology*.

Ding, L., & Goshtasby, A. (2001). On the Canny edge detector. *Pattern Recognition*, *34*(3), 721–725. https://doi.org/10.1016/S0031-3203(00)00023-6

DiPippo, R. (2004). Second Law assessment of binary plants generating power from low-temperature geothermal fluids. *Geothermics*, *33*(5), 565–586. https://doi.org/10.1016/J.GEOTHERMICS.2003.10.003

DiPippo, R. (2012). Geothermal Power Plants. In *Comprehensive Renewable Energy* (Second Edi, Vol. 7, pp. 209–239). North Dartmouth, Massachusetts: Elsevier. https://doi.org/10.1016/B978-0-08-087872-0.00708-3

DiPippo, R. (2015). Geothermal power plants: Evolution and performance assessments. *Geothermics*, *53*, 291–307. https://doi.org/10.1016/J.GEOTHERMICS.2014.07.005

Drewes, H., Kuglitsch, F., Adám, J., & Rózsa, S. (2016). The International Gravimetric Bureau. In “The Geodesist’s Handbook 2016”. *Journal of Geodesy*, *90*(10), 907–1205. https://doi.org/10.1007/s00190-016-0948-z

Ekneligoda, T. C., & Henkel, H. (2010). Interactive spatial analysis of lineaments. *Computers and Geosciences*, *36*(8), 1081–1090. https://doi.org/10.1016/j.cageo.2010.01.009

Ellis, R. (2012). Iterative Reweighted Inversion. Geosoft Technical Note.

Ellis, R., & MacLeod, I. (2013). Constrained voxel inversion using the cartesian cut cell method. *ASEG Extended Abstracts*, *2013*(1), 1. https://doi.org/10.1071/ASEG2013ab222

Farhi, W., Boudella, A., Saibi, H., & Bounif, M. O. A. (2016). Integration of magnetic, gravity, and well data in imaging subsurface geology in the Ksar Hirane region (Laghouat, Algeria). *Journal of African Earth Sciences*, *124*, 63–74. https://doi.org/10.1016/J.JAFREARSCI.2016.09.013

Faye, G. D., Yamaji, A., Yonezu, K., Tindell, T., & Watanabe, K. (2018). Paleostress and fluid-pressure regimes inferred from the orientations of Hishikari low sulfidation epithermal gold veins in southern Japan. *Journal of Structural Geology*, *110*(March), 131–141. https://doi.org/10.1016/j.jsg.2018.03.002

Fedi, M., Cella, F., D'Antonio, M., Florio, G., Paoletti, V., & Morra, V. (2018). Gravity modeling finds a large magma body in the deep crust below the Gulf of Naples, Italy. *Scientific Reports*, *8*(1), 8229. https://doi.org/10.1038/s41598-018-26346-z

Feng, W., Zhong, M., Lemoine, J.-M., Biancale, R., Hsu, H.-T., & Xia, J. (2013). Evaluation of groundwater depletion in North China using the Gravity Recovery and Climate Experiment (GRACE) data and ground-based measurements. *Water Resources Research*, *49*(4), 2110–2118. https://doi.org/10.1002/wrcr.20192

Fournier, R. O. (1973). Silica in thermal waters: Laboratory and field investigations. *Proc. Int. Symp. on Hydrogeochemistry and Biogeochemistry, Japan, 1970*, *1*(Hydrogeochemistry. Clark), 122–139.

Fournier, R. O., & Rowe, J. J. (1966). Estimation of underground temperatures from the silica content of water from hot springs and wet-steam wells. *American Journal of Science*, *264*(9), 685–697. https://doi.org/10.2475/ajs.264.9.685

Fournier, R. O., & Truesdell, A. H. (1973). An empirical Na-K-Ca geothermometer for natural waters. *Geochimica et Cosmochimica Acta*, *37*, 1255–1275.

Fukao, Y., Yamamoto, A., & Nozaki, K. (1981). A Method of Density determination for Gravity Corrections. *Journal of Physics of the Earth*, *29*, 163–166.

Fullagar, P. K., Pears, G. A., & McMonnies, B. (2008). Constrained inversion of geologic surfaces — pushing the boundaries. *The Leading Edge*, *27*(1), 95–105.

Garg, S. K., & Combs, J. (2015). A reformulation of USGS volumetric "heat in place" resource estimation method. *Geothermics*, *55*, 150–158. https://doi.org/10.1016/J.GEOTHERMICS.2015.02.004

Gavin, H. P. (2019). *The Levenberg-Marquardt algorithm for nonlinear least squares curve-fitting problems*. Retrieved from http://people.duke.edu/~hpgavin/ce281/lm.pdf

Gawad, A. E. A., Donia, A. M. A., & Elsaid, M. (2016). Processing of Landsat 8 Imagery and Ground Gamma-Ray Spectrometry for Geologic Mapping and Dose-Rate Assessment, Wadi Diit along the Red Sea Coast, Egypt. *Open Journal of Geology*, *06*(08), 911–930. https://doi.org/10.4236/ojg.2016.68069

GEA. (2015). Annual U.S. & Global Geothermal Power Production Report. *Geothermal Energy Association*, 21.

Geological Survey of Japan. (2013). Gravity Database of Japan, DVD Edition. Tsukuba, Ibaraki Prefecture: Geological Survey of Japan, National Institute of Advanced Industrial Science and Technology AIST.

Geosoft. (2018). VOXI Earth Modelling. Retrieved from http://www.geosoft.com/products/voxi-earth-modelling/

Geospatial Information Authority of Japan. (2017). *Topographic Map of Japan. Quadrants: 4830-05-06, 4730-75-76*. Tsukuba, Ibaraki Prefecture: Ministry of Land, Infrastructure, Transport and Tourism. Geographical Survey Institute. Retrieved from http://www.gsi.go.jp

Gobierno de El Salvador, Consejo Nacional de Energía, & Cooperación Internacional del Japón JICA. (2012). Master Plan for the Development of Renewable Energy El Salvador 2011.

Golden Software LCC. (2018). Voxler 3D V4.3.771 (x86_64). Retrieved from https://www.goldensoftware.com

Golman, B. (2016). Transient kinetic analysis of multipath reactions: An educational module using the IPython software package. *Education for Chemical Engineers*, *15*, 1–18. https://doi.org/10.1016/J.ECE.2015.12.002

Götze, H.-J. (2011). International Gravity Formula. In *Encyclopedia of Solid Earth Geophysics* (pp. 611–612). Springer. https://doi.org/10.1007/978-90-481-8702-7_102

Grauch, V. J. S., & Cordell, L. (1987). Limitations of determining density or magnetic boundaries from the horizontal gradient of gravity or pseudogravity data. *GEOPHYSICS*, *52*(1), 118–121. https://doi.org/10.1190/1.1442236

GRSJ Geothermal Research Society of Japan. (2010). Geothermal Energy Japan. Resources and Technologies, *1991*, 1998–2001. Retrieved from http://grsj.gr.jp/en/all.pdf

Guglielmetti, L., Comina, C., Abdelfettah, Y., Schill, E., & Mandrone, G. (2013). Integration of 3D geological modeling and gravity surveys for geothermal prospection in an Alpine region. *Tectonophysics*, *608*, 1025–1036. https://doi.org/10.1016/J.TECTO.2013.07.012

Guttag, J. (2015). *Introduction to computation and programming using Python : with application to understanding data* (Second Edi). One Rogers Street Cambridge MA 02142-1209: The MIT Press. Retrieved from https://mitpress.mit.edu/books/introduction-computation-and-programming-using-python-1

Hammer, S. (1939). Terrain corrections for gravimeter stations. *Geophysics*, *4*(3), 184–194. https://doi.org/10.1190/1.1440495

Harrison, K. (2018). Monte Carlo simulation and Python. Retrieved from https://pythonprogramming.net/monte-carlo-simulator-python/

Harsh, G., & Sukanta, R. (2007). *Geothermal Energy: An Alternative resource for the 21st century* (First Edit). Elseiver B.V.

Hashim, M., Ahmad, S., Johari, M. A. M., & Pour, A. B. (2013). Automatic lineament extraction in a heavily vegetated region using Landsat Enhanced Thematic Mapper (ETM+) imagery. *Advances in Space Research*, *51*(5), 874–890. https://doi.org/10.1016/j.asr.2012.10.004

Heath, M., Sarkar, S., Sanocki, T., & Bowyer, K. (1996). Comparison of edge detectors: a methodology and initial study. In *Proceedings CVPR IEEE Computer Society Conference on Computer Vision and Pattern Recognition* (pp. 143–148). IEEE. https://doi.org/10.1109/CVPR.1996.517066

Hinze, W., Frese, V., & Saad, A. H. (2013a). *Gravity and magnetic exploration: Principles, practices, and applications*. Cambridge University Press. Retrieved from https://books.google.co.jp/books?hl=en&lr=&id=tCc2aHkKTwQC&oi=fnd&pg=PR11&dq=Gravity+and+Magnetic+Exploration:+Principles,+Practices,+and+Applications&ots=uxS-glx9tl&sig=G4Nc7444sAm4jreo0K--Y86oXGE

Hinze, W., Frese, V., & Saad, A. H. (2013b). *Oasis montaj Tutorial. Gravity and Magnetic Exploration Principles, Practices and Applications*. Cambridge University Press.

Hinze, Willian. (2003). Bouguer reduction density, why 2.67? *Geophysics*, *68*(5), 1559–1560. https://doi.org/10.1190/1.1620629

Hofmann-Wellenhof, B., & Moritz, H. (2006). *Physical geodesy*. Springer Science & Business Media. Retrieved from https://books.google.co.jp/books?hl=en&lr=&id=yTbFyZVLIk4C&oi=fnd&pg=PA1&dq=Hofmann-Wellenhof+and+Moritz,+2006&ots=ribcadHneV&sig=y88YczaskCPlnzjlqXsNKsSeIOI

Hosseini, S. A. A., Ardejani, F. D., Tabatabaie, S. H., & Hezarkhani, A. (2013). Edge Detection in Gravity Field of the Gheshm Sedimentary Basin. *Int J Min & Geo-Eng*, *47*(1), 41–50.

Hung, L. Q., Batelaan, O., & De Smedt, F. (2005). Lineament extraction and analysis, comparison of LANDSAT ETM and ASTER imagery. Case study: Suoimuoi tropical karst catchment, Vietnam. In M. Ehlers & U. Michel (Eds.), *Remote Sensing for Environmental Monitoring, GIS Applications, and Geology V* (Vol. 5983, p. 59830T). International Society for Optics and Photonics. https://doi.org/10.1117/12.627699

Hunt, T. M. (1970). Gravity Changes at Wairakei Geothermal Field, New Zealand. *GSA Bulletin*, *81*(2), 529–536. https://doi.org/10.1130/0016-7606(1970)81[529:gcawgf]2.0.co;2

Ibaraki, K., & Suzuki, R. (1993). Gold-Silver Quartz-Adularia Veins of the Main, Yamada and Sanjin Deposits, Hishikari Gold Mine; A Comparative Study of Their Geology and Ore Deposits. *Resource Geology*, *14*(Special Issue), 1–11.

Ibaraki, K., Yokoyama, T., Kawazaki, K., & Suzuki, R. (1992). Gold prospecting by integrated geological, geochemical and geophysical study; A case study of the discovery of the Yamada deposit at the Hishikari Mine. *29th IGCC*, *Abstract*, 769.

Ingram, D. M., Causon, D. M., & Mingham, C. G. (2003). Developments in Cartesian cut cell methods. *Mathematics and Computers in Simulation*, *61*(3–6), 561–572. https://doi.org/10.1016/S0378-4754(02)00107-6

Inkscape Project. (2019). Inkscape. A professional quality vector graphics software, v0.92. Retrieved from https://inkscape.org/

Institute for Sustainable Energy policies ISEP. (2015). Renewable Energy Prospects. Retrieved from https://www.isep.or.jp/en/

Ishihara, S., Sakamaki, Y., Sasaki, A., Teraoka, Y., & Terashima, S. (1986). Role of the Basement in the Genesis of the Hishikari Gold-Quartz Vein Deposit, Southern Kyushu, Japan. *Mining Geology*, *36*(6). Retrieved from https://www.jstage.jst.go.jp/article/shigenchishitsu1951/36/200/36_200_495/_pdf/-char/ja

Izawa, E., & Nakae, Y. (1983). Xonotlite, truscottite and gyrolite from gold veins in Kyushu. *Mineral Society*, (Annun Meeting), 14.

Izawa, E., & Urashima, Y. (1987). Paleo-geothermal Systems in Island-arc Settings of the Western Pacific Rim. *Kagoshima University Research Center for the South Pacific Occasional Papers, "Paleo-Geothermal and Active Geothermal Sysyems" Paleo-Geothermal*, *11*, 71–86. Retrieved from http://hdl.handle.net/10232/16105

Izawa, E., Urashima, Y., Ibaraki, K., Suzuki, R., Yokoyama, T., Kawasaki, K., Koga, A., & Taguchi, S. (1990). The Hishikari gold deposit: high-grade epithermal veins in Quaternary volcanics of southern Kyushu, Japan. *Journal of Geochemical Exploration*, *36*(1–3), 1–56. https://doi.org/10.1016/0375-6742(90)90050-K

Jacoby, W., & Smilde, P. L. (2009). *Gravity interpretation: fundamentals and application of gravity inversion and geological interpretation* (1st Ed.). Gutenberg-Universitat Mainz, Germany: Springer-Verlag Berlin Heidelberg.

JOGMEC Japan Oil Gas and Metals National Corporation. (2015). *Current Situation of geohermal Power Generation in Japan*. Tokyo. Retrieved from http://www.jogmec.go.jp

Kageyama, Y., Nishida, M., & Oi, T. (2000). Analysis of the segments extracted by automated lineament detection. In *International Geoscience and Remote Sensing Symposium (IGARSS)* (Vol. 1, pp. 289–291). IEEE.

Kanda, I., Fujimitsu, Y., & Nishijima, J. (2019). Geological structures controlling the placement and geometry of heat sources within the Menengai geothermal field, Kenya as evidenced by gravity study. *Geothermics*, *79*(December 2018), 67–81. https://doi.org/10.1016/j.geothermics.2018.12.012

Kang, S. H. (2012). Design and experimental study of ORC (organic Rankine cycle) and radial turbine using R245fa working fluid. *Energy*, *41*(1), 514–524. https://doi.org/10.1016/J.ENERGY.2012.02.035

Karcol, R., Mikuška, J., Marušiak, I., Karcol, R., Mikuška, J., & Marušiak, I. (2017). Normal Earth Gravity Field Versus Gravity Effect of Layered Ellipsoidal Model. In *Understanding the Bouguer Anomaly* (pp. 63–77). Elsevier. 10.1016/B978-0-12-812913-5.00003-8

Karnieli, A., Meisels, A., Fisher, L., & Arkin, Y. (1996). Automatic extraction and evaluation of geological linear features from digital remote sensing data using a Hough transform. *Photogrammetric Engineering and Remote Sensing*, *62*(5), 525–531.

Klein, C., Lovekin, J., & Sanyal, S. (2004). New geothermal site identification and qualification. In *GeothermEx Inc. report P500-04-051* (pp. 1–8). California Energy Commission. Retrieved from http://www.energy.ca.gov/reports/500-04-051.PDF

Komagata, S., Iga, H., Nakamura, H., & Minohara, Y. (1970). The status of geothermal utilization in Japan. *Geothermics*, *2*, 185–196. https://doi.org/10.1016/0375-6505(70)90019-2

Komazawa, M. (1995). Gravimetric analysis of Aso Volcano and its interpretation. *Journal of the Geodetic Society of Japan*, *41*(1), 17–45.

Kondoh, K. (1986). Exploration and development of Hishikari gold mine. *Mining Geology*, *36*, 1–9.

Krieger, L., & Peacock, J. R. (2014). MTpy: A Python toolbox for magnetotellurics. *Computers and Geosciences*, *72*, 167–175. https://doi.org/10.1016/j.cageo.2014.07.013

Kroese, D. P., Brereton, T., Taimre, T., & Botev, Z. I. (2014). Why the Monte Carlo method is so important today. *Wiley Interdisciplinary Reviews: Computational Statistics*, *6*(6), 386–392. https://doi.org/10.1002/wics.1314

LaFehr, T. R. (1991a). An exact solution for the gravity curvature (Bullard B) correction. *Geophysics*, *56*(8), 1179–1184. https://doi.org/10.1190/1.1443138

LaFehr, T. R. (1991b). Standardization in gravity reduction. *Geophysics*, *56*(8), 1170–1178. https://doi.org/10.1190/1.1443137

Lawson, C. L. (1961). *Contribution to the theory of linear least maximum approximation*. Ph. D. dissertation, Univ. Calif. Retrieved from https://ci.nii.ac.jp/naid/10028990173/

Lee, A. (2014). Mcerp: Real-time latin-hypercube sampling-based Monte Carlo Error Propagation. Retrieved from http://pythonhosted.org/mcerp/index.html

Li, L., Huang, D., Han, L., & Ma, G. (2014). Optimised edge detection filters in the interpretation of potential field data. *Exploration Geophysics*, *45*(3), 171–176. https://doi.org/10.1071/EG13059

Li, Y., & Oldenburg, D. W. (1998). 3-D inversion of gravity data. *Geophys. J. Int*, *63*(1), 109–119. https://doi.org/10.1190/1.1444302

Li, Y., & Oldenburg, D. W. (2000). Incorporating geological dip information into geophysical inversions. *GEOPHYSICS*, *65*(1), 148–157.

Ma, G., & Li, L. (2012). Edge detection in potential fields with the normalized total horizontal derivative. *Computers and Geosciences*, *41*, 83–87. 10.1016/j.cageo.2011.08.016

MacLeod, I., & Ellis, R. (2015). Quantitative Magnetization Vector Inversion. In *Extended Abstracts of 14th SAGA Biennial Technical Meeting and Exhibition 2015* (pp. 1–5).

MacQueen, P., Zurek, J., & Williams-Jones, G. (2016). Connected magma plumbing system between Cerro Negro and El Hoyo Complex, Nicaragua revealed by gravity survey. *Journal of Volcanology and Geothermal Research*, *327*, 375–384. https://doi.org/10.1016/j.jvolgeores.2016.09.002

Marghany, M., & Hashim, M. (2010). Lineament mapping using multispectral remote sensing satellite data. *Research Journal of Applied Sciences*, *5*(2), 126–130. https://doi.org/10.3923/rjasci.2010.126.130

Mariita, N. O. (2012). Strengths and weaknesses of gravity and magnetics as exploration tools for geothermal energy. In *Short Course VII on Exploration for Geothermal Resources, Kenya, Oct. 27 – Nov. 18, 2012* (p. 8). Retrieved from https://orkustofnun.is/gogn/unu-gtp-sc/UNU-GTP-SC-15-0402.pdf

Matsuhisa, Y., Morishita, Y., & Sato, T. (1985). Oxygen and carbon isotope variations in gold-bearing hydrothermal veins in the Kushikino mining area, southern Kyushu, Japan. *Economic Geologic*, *80*, 283–293.

Matthew, M. W., Adler-Golden, S. M., Berk, A., Felde, G., Anderson, G. P., Gorodetzky, D., Paswaters, S., & Shippert, M. (2002). Atmospheric correction of spectral imagery: evaluation of the FLAASH algorithm with AVIRIS data. In *Proceedings of Applied Imagery Pattern Recognition Workshop.* (pp. 157–163). IEEE Comput. Soc. https://doi.org/10.1109/AIPR.2002.1182270

METI Ministry of Economy Trade and Industry. (2015). Long-term Energy Supply and Demand Outlook. Retrieved from https://www.meti.go.jp/english/press/2015/pdf/0716_01a.pdf

METI Ministry of Economy Trade and Industry. (2016). Settlement of FY 2016 Purchase Prices and FY 2016 Surcharge Rates under the Feed-in Tariff Scheme for Renewable Energy in Japan. Retrieved from https://www.meti.go.jp/english/press/2016/0318_03.html

Mielke, P., Prieto, A., Bignall, G., & Sass, I. (2015). Effect of Hydrothermal Alteration on Rock Properties in the Tauhara Geothermal Field, New Zealand. In *World Geothermal Congress 2015* (p. 15).

MOE Ministry of the Environment Government of Japan. (2011). Renewable Energy Introduction Potential Map and Basic Zoning Information FY2011. Retrieved from http://www.env.go.jp/earth/ondanka/rep/EN/

MOE Ministry of the Environment Government of Japan. (2013). *Commissioned Project on Precision Survey and Analysis of Geothermal Power Generation Introduction Potential (FY 2013).* Retrieved from https://www.env.go.jp/earth/report/h26-04/summary_en.pdf

Monterrosa, M., & La Geo. (2007). *Geothermal Resource Assessment of Central American Countries: El Salvador*. San Salvador, El Salvador: United Nations University, geothermal Training Program.

Mountrakis, G., & Luo, L. (2011). Enhancing and replacing spectral information with intermediate structural inputs: A case study on impervious surface detection. *Remote Sensing of Environment*, *115*(5), 1162–1170. https://doi.org/10.1016/j.rse.2010.12.018

Muffler, P., & Cataldi, R. (1978). Methods for regional assessment of geothermal resources. *Geothermics*, *7*(2–4), 53–89. https://doi.org/10.1016/0375-6505(78)90002-0

Muffler, P., & Guffanti, M. (1978). Assessment of geothermal resources of the United States-1978. U.S. Geological Survey Circular 790.

Murata, Y. (1990). Estimation of Bouguer reduction density using ABIC minimization method. *Journal of Seismology Society of Japan*, *43*, 327–339.

Murata, Y. (1993). Estimation of optimum average surficial density from gravity data: An objective Bayesian Approach. *Journal of Geophysical Research: Solid Earth*, *98*(B7), 12097–12109. https://doi.org/10.1029/93JB00192

Murata, Y., & Noro, H. (1993). Optimization of estimation precedure of Bouguer density by use of the ABIC-minimization method. *Geophysics Exploration (Butsuri-Tansa)*, *46*(2), 120–127.

Nagy, D. (1966). The prism method for terrain corrections using digital computers. *Pure and Applied Geophysics PAGEOPH*, *63*(1), 31–39. https://doi.org/10.1007/BF00875156

Naritomi, K., Nishijima, J., & Fujimitsu, Y. (2015). A monitoring of hot spring aquifer using repeated Microgravity Measurements in Northern part of Beppu, Japan. (International Symposium on Earth Science and Technology 2015, Ed.), *International Symposium on Earth Science and Technology 2015*. Fukuoka 819-0395: Department of Earth Resources Engineering, Kyushu University.

Nasuti, Y., & Nasuti, A. (2018). NTilt as an improved enhanced tilt derivative filter for edge detection of potential field anomalies. *Geophysical Journal International*, *214*(1), 36–45. https://doi.org/10.1093/gji/ggy117

Nathenson, M. (1975). Physical factors determining the fraction of stored energy recoverable from hydrothermal convection systems and conduction-dominated areas. *U.S. Geological Survey Open-File Report*, *75–525*, 50.

National Institute of Standards and Technology NIST. (2017). Thermophysical Properties of Fluid Systems. *SRD 69*. Department of Commerce, USA. Retrieved from https://webbook.nist.gov/chemistry/fluid/

National Registration Center CNR. (2015). Catalog of maps. Retrieved from http://www.cnr.gob.sv/

NEDO New Energy and Industrial Technology Development Organization. (1991). *Geothermal Development Promotion Research Report No 25 Hishikari Area.*

Nettleton, L. L. (1939). Determination of density for reduction of gravimeter observations. *Geophysics*, *4*(3), 176–183. https://doi.org/10.1190/1.0403176

NIMA. (1984). *Department of Defense World Geodetic System 1984; Its Definition and Relationships with Local Geodetic Systems*. Bethesda, Maryland.

Nishijima, J. (2009). A terrain correction program using 50m mesh digital elevation data. In *Geothermal and Volcanological Research Report of Kyushu University(in Japanese with English abstract)* (Vol. 18, pp. 35–38).

Nishijima, J., & Fujimitsu, Y. (2015). Precise Gravity Survey around Minou Fault System, Fukuoka Prefecture, Japan -Relationship between Fault Structures and Hot Springs-. *Journal of the Geothermal Research Society of Japan*, *37*(2), 41–49. https://doi.org/10.11367/grsj.37.41

Nishijima, J., & Naritomi, K. (2017). Interpretation of gravity data to delineate underground structure in the Beppu geothermal field, central Kyushu, Japan. *Journal of Hydrology: Regional Studies*, *11*, 84–95. https://doi.org/10.1016/J.EJRH.2015.11.022

Nishikawaki, C., Matsukuma, T., & Urashima, Y. (1971). Neogene gold-silver ores in Japan. *Mining Geology*, *3*, 409.

Nishizawa, N., & Ibaraki, U. (1985). Exploration of the Hishikari mine. In: Y. Urashima (Editor), Gold-Silver Ores in Japan, no. 3. Min. Metall. Inst. Jpn. *Tokyo*, 1–27.

Noltimier, K. F., Jezek, K. C., Wilson, T. J., & Johnson, A. C. (1998). Evidence for the tectonic segmentation of the Antarctic Peninsula from integrated ERS-1 SAR mosaic and aeromagnetic anomaly data. In *IGARSS '98. Sensing and Managing the Environment. 1998 IEEE International Geoscience and Remote Sensing. Symposium Proceedings. (Cat. No.98CH36174)* (pp. 1439–1441 vol.3). IEEE. https://doi.org/10.1109/IGARSS.1998.691486

Nowell, D. A. G. (1999). Gravity terrain corrections - an overview. *Journal of Applied Geophysics*, *42*(2), 117–134. https://doi.org/10.1016/S0926-9851(99)00028-2

Oldenburg, D. W. (1974). The inversion and interpretation of gravity anomalies. *GEOPHYSICS*, *39*(4), 526–536. https://doi.org/10.1190/1.1440444

Parasnis, D. S. (1986). Gravitational methods. In *Principles of Applied Geophysics* (pp. 61–103). Dordrecht: Springer Netherlands. https://doi.org/10.1007/978-94-009-4113-7_3

Parasnis, D. S., & Cook, A. H. (1952). A study of rock densities in the English Midlands. *Geophysical Journal International*, *6*, 252–271. https://doi.org/10.1111/j.1365-246X.1952.tb03013.x

Parasnis, D. S., Wiley, J., & York, N. (1978). *Applied Geophysics Principles of Applied Geophysics LONDON.*

PCI Geomatics. (2015). *PCI Geomatica user's guide version*. Ontario, Canada.

Perez, F., & Granger, B. E. (2007). IPython: A System for Interactive Scientific Computing. *Computing in Science & Engineering*, *9*(3), 21–29. https://doi.org/10.1109/MCSE.2007.53

Phillips, R. J., & Lambeck, K. (1980). Gravity fields of the terrestrial planets: Long-wavelength anomalies and tectonics. *Reviews of Geophysics*, *18*(1), 27. https://doi.org/10.1029/RG018i001p00027

Pocasangre, C., & Fujimitsu, Y. (2017). Analysis of Preliminary Gravity Data for Figuring Out Geothermal Reservoir Border and Underground Structure in Hishikari Area, Kagoshima Prefecture. *International Symposium on Earth Science and Technology*.

Pocasangre, C., & Fujimitsu, Y. (2018). A Python-based stochastic library for assessing geothermal power potential using the volumetric method in a liquid-dominated reservoir. *Geothermics*, *76*, 164–176. https://doi.org/10.1016/J.GEOTHERMICS.2018.07.009

Pocasangre, C., Fujimitsu, Y., & Nishijima, J. (2018a). Three-dimensional gravity modeling for defining the underground volume of the hydrothermal alteration zone in the eastern part of Isa city , Kagoshima Prefecture. *International Symposium on Earth Science and Technology 2018, Kyushu University*, 1–6.

Pocasangre, C., Fujimitsu, Y., & Nishijima, J. (2018b). Utilization of gravity data for figuring out both the hydrothermal alteration zone and the underground structure so that possible geothermal exploitation in the municipality of Isa , Japan . *Proceedings of the 13th SEGJ International Symposium, 2018. Tokyo*.

Python Software Foundation. (2016). Python Programing Language. Retrieved from https://www.python.org

QGIS Development Team. (2017). QGIS Open Source Geographic Information System v2.18.11. Retrieved from http://www.qgis.org

Rao, P. R., Swamy, K. V., & Murthy, I. V. R. (1999). Inversion of gravity anomalies of three-dimensional density interfaces. *Computers & Geosciences*, *25*(8), 887–896. https://doi.org/10.1016/S0098-3004(99)00051-5

Renderos, R., Matus, A., Magaña, M. I., Tenorio, J., & Cubías, M. (2013). Geochemical Surveying and Conceptual Model of Chilanguera Geothermal System, El Salvador. *Short Course V on Conceptual Modelling of Geothermal Systems, UNU-GTP*, 1–17.

Represas, P., Catalão, J., Montesinos, F. G., Madeira, J., Mata, J., Antunes, C., & Moreira, M. (2012). Constraints on the structure of Maio Island (Cape Verde) by a three-dimensional gravity model: imaging partially exhumed magma chambers. *Geophysical Journal International*, *190*(2), 931–940. https://doi.org/10.1111/j.1365-246X.2012.05536.x

Richter, A. (2019). New 7.4 MW geothermal plant started operations in Iwate, Japan. Retrieved from http://www.thinkgeoenergy.com/

Saadi, N. M., Aboud, E., Hakim, S., & Watanabe, K. (2008). Integrating Data from Remote Sensing, Geology and Gravity for Geological Investigation in the Tarhunah area, Northwest Libya. *International Journal of Digital Earth*, *1*(4), 347–366.

Saga, I., Yagyu, R., & Sato, K. (1955). Gold-silver ores. In Mineral Resources of Japan. *Geological Survey of Japan*, *1*(a), 5–104.

Saibi, H. (2018). Various Geoscientific Investigations of Low-Enthalpy Geothermal Sites in the United Arab Emirates. *Proceedings 43th Geothermal Reservoir Engineering, Stanford University. California, USA*, *SGP-TR-213*, 1–8. Retrieved from https://pangea.stanford.edu/ERE/db/GeoConf/papers/SGW/2018/Saibi.pdf

Saibi, H., Ehara, S., Fujimitsu, Y., & Nishijima, J. (2007). *Numerical modeling based on gravity and hydro-geochemical data, -A case study of Obama geothermal field, southwestern Japan. Degree of Doctor of Engineering in Geothermics, Laboratory of Geothermics*. Kyushu University.

Saito, M., Tarakada, S., Toshimitsu, S., Mizuno, K., & Hoshimizu, H. (2010). *Yatsushiro and a part of Nomo Zaki Geological Map. Scale 1:200,000. NI-52-12,18*. Tsukuba, Ibaraki Prefecture: Geological Survey of Japan.

Sakaguchi, K., Noda, T., Takahashi, M., & Komazawa, M. (2000). *Geothermal Resources Map of Kyushu Area. Scale 1:500,000* (Map Series). Tsukuba, Ibaraki Prefecture: Geological Survey of Japan.

Sakaguchi, K., Uto, K., Teraoka, Y., & Okumura, K. (1997). *Kagoshima Geological Map. Scale 1:200,000. NH-52-7*. Tsukuba, Ibaraki Prefecture: Geological Survey of japan.

Salati, S., Van Ruitenbeek, F. J. A., Van der Meer, F. D., Tangestani, M. H., & Van der Werff, H. (2011). Lithological mapping and fuzzy set theory: Automated extraction of lithological boundary from ASTER imagery by template matching and spatial accuracy assessment. *International Journal of Applied Earth Observation and Geoinformation*, *13*(5), 753–765. https://doi.org/10.1016/j.jag.2011.05.004

Santos, P., & Rivas, J. (2009). Geophysical Conceptual Model of the San Vicente Geothermal Area, El Salvador. *Short Course on Surface Exploration for Geothermal Resources, UNU-GTP and LaGeo*, *2*(17-30 October), 9.

Sanyal, S. (2005). Classification of Geothermal Systems - A Possible Scheme. *Proceedings 30th Geothermal Reservoir Engineering, Stanford University. California, USA*, *SGP-TR-176*. Retrieved from https://pangea.stanford.edu/ERE/pdf/IGAstandard/SGW/2005/sanyal1.pdf

Sanyal, S., & Sarmiento, Z. (2005). Booking Geothermal Energy Reserves. *Transaction, Geothermal Resources Council*, *29*.

Sarmiento, Z. F., & Steingrímsson, B. (2011). Resource Assessment I : Introduction and Volumetric Assessment. *Short Course on Geothermal Drilling, Resource Development and Power Plants, UNU-GTP*, 1–15.

Sawai, O., Kawamura, H., Okada, T., & Itaya, T. (2002). K-Ar ages of volcanic rocks and gold deposits in the Bajo gold area, central Kyushu. *Shigen-Chishitsu*, *52*(2), 121–133. https://doi.org/10.11456/shigenchishitsu1992.52.121

Sawamura, H. (1995). Nature Conservation in Japan. Tokyo: Ministry of the Environment Government of Japan. Retrieved from www.env.go.jp

Schön, J. (2015). *Physical properties of rocks: fundamentals and principles of petrophysics*. (J. Cubitt & W. Holt, Eds.) (2nd Editio). Elsevier.

Scintrex. (2012). *CG-5 Scintrex Autograv TM System Operation Manual*. SCINTREX Limited.

Shepard, D. (1968). A two-dimensional interpolation function for irregularly-spaced data. In *Proceedings of the 1968 23rd ACM national conference on* - (pp. 517–524). New York, New York, USA: ACM Press. https://doi.org/10.1145/800186.810616

Simiyu, S. M. (2010). Status of Geothermal Exploration in Kenya and Future Plans for Its Development. In *World Geothermal Congress 2010* (pp. 25–29).

Smith, W. H. F., & Wessel, P. (1990). Gridding with continuous curvature splines in tension. *Geophysics*, *55*(3), 293–305. https://doi.org/10.1190/1.1442837

SPE. (2001). *Guidelines for the Evaluation of Petroleum Reserves and Resources, a Supplement to the SPE/WPC petroleum Reserves Definitions and the SPE/WPC/AAPG Petroleum Resources Definitions*.

Stimac, J., Nordquist, G., Suminar, A., & Sirad-Azwar, L. (2008). An overview of the Awibengkok geothermal system, Indonesia. *Geothermics*, *37*(3), 300–331. https://doi.org/10.1016/J.GEOTHERMICS.2008.04.004

Sumitomo Metal Mining Co. LTD. (2017). Hishikari mine Facility. Retrieved from http://www.smm.co.jp/E/corp_info/domestic/hishikari/kyoten.html

Taylor, J. (1997). *Introduction to Error Analysis, the Study of Uncertainties in Physical Measurements. University Science Books*. Retrieved from http://adsabs.harvard.edu/abs/1997ieas.book.....T

Telford, W. M., Telford, W. M., Geldart, L. P., Sheriff, R. E., & Sheriff, R. E. (1990). *Applied geophysics* (Vol. 1). Cambridge university press.

Tiwari, V. M., Wahr, J., & Swenson, S. (2009). Dwindling groundwater resources in northern India, from satellite gravity observations. *Geophysical Research Letters*, *36*(18), L18401. https://doi.org/10.1029/2009GL039401

Tontini, F. C., de Ronde, C. E. J., Scott, B. J., Soengkono, S., Stagpoole, V., Timm, C., & Tivey, M. (2015). Interpretation of gravity and magnetic anomalies at Lake Rotomahana: Geological and hydrothermal implications. *Journal of Volcanology and Geothermal Research*, *314*, 84–94. https://doi.org/10.1016/j.jvolgeores.2015.07.002

Tsuyuki, T. (1969). Geological study of hot springs in Kyushu, Japan (5): some hot springs in the Kagoshima graben, with special reference to thermal water reservoir. *Faculty of Science, Kagoshima University (Geology and Biology)*, *2*, 85–101.

Tveite, H. (2015). The QGIS Line Direction Histogram Plugin. Retrieved from http://plugins.qgis.org/plugins/LineDirectionHistogram

Uieda, L. (2018). Verde: Processing and gridding spatial data using Green's functions Software・Review・Repository・Archive. *The Journal of Open Source Software*, *3*(30), 957. https://doi.org/10.21105/joss.00957

Uieda, L., Oliveira Jr, V. C., & Barbosa, V. C. F. (2013). Modeling the Earth with Fatiando a Terra. *Proceedings of the 12th Python in Science Conference*, (Scipy), 90–96. https://doi.org/

Urashima, Y., & Izawa, E. (1982). Hydrothermal alteration observed in exploration drill cores of the Hishikari gold deposit. *Autumn Meeting of Mining Metal. Inst. Japan*, *G*(Proc.), 13–16.

Urashima, Y., & Izawa, E. (1983). Ores from drill-cores of the Hishikari gold deposit. *Maining Geology*, *33*(Abstract), 50.

Uwiduhaye, J. d'Amour, Mizunaga, H., & Saibi, H. (2018). Geophysical investigation using gravity data in Kinigi geothermal field, northwest Rwanda. *Journal of African Earth Sciences*, *139*, 184–192. https://doi.org/10.1016/J.JAFREARSCI.2017.12.016

Wagner, W., & Kretzschmar, H.-J. (1998). *International Steam Tables: Properties of Water and Steam based on the Industrial Formulation IAPWS-IF97* (Second Edi). Springer-Verlag Berlin Heidelberg.

Wakeyama, T., & Ehara, S. (2009). Assessment of Renewable Energy by Using GIS - A Case Study of Unzen City -. *Journal of the Japan Institute of Energy*, *88*(1), 58–69. https://doi.org/10.3775/jie.88.58

Watanabe, Y. (2005). Late Cenozoic evolution of epithermal gold metallogenic provinces in Kyushu, Japan. *Mineralium Deposita*, *40*(3), 307–323. doi.org/10.1007/s00126-005-0025-7

Wessel, P., Smith, W., Eickschen, S., Henstock, T., & Horner-Johnson, B. (2017). The Generic Mapping Tools. Retrieved from https://www.soest.hawaii.edu/gmt/

Williams, C. F. (2014). Evaluating the Volume Method in the Assessment of Identified Geothermal resources. *GRC Transactions*, *38*, 967–974. Retrieved from http://pubs.geothermal-library.org/lib/grc/1033647.pdf

Wyering, L. D. (2014). *The influence of hydrothermal alteration and lithology on rock properties from different geothermal fields with relation to drilling*. University of Canterbury, Department of Geological Sciences Christchurch, New Zealand.

Yamamoto, A. (1999a). Estimating the Optimum Reduction Density for Gravity Anomaly: A Theoretical Overview. *Journal of the Hokkaido University, Faculty of Science, Series VII: Geophysics*, *11*(3), 577–599.

Yamamoto, A. (1999b). Estimating the optimun reduction density for gravity anomaly. A theoretical Overview. *Journal of the Faculty of Science, Hokkaido University. Series 7, Geophysics*, *11*(3), 577–599.

Yamamoto, A. (2002). Spherical terrain corrections for gravity anomaly using a digital elevation model gridded with nodes at every 50 m. In *Journal of the Hokkaido University, Faculty of Science, Series VII: Geophysics* (Vol. 11(6), pp. 845–880). Retrieved from http://hdl.handle.net/2115/8866

Yasuhara, S., Watanabe, K., & Izawa, E. (2003). Zoning of Hydrothermalalteration in the Western Part of the Hishikari Epithermal Gold Deposit, Southern Kyushu, Japan, (Figure 2), 49–53.

Yasukawa, K. (2017). *Geotehrmal use in Japan and Geothermal studies in FREA, AIST 2017*. Koriyama, Fukushima Prefecture. Retrieved from http://www.aist.go.jp

Yasukawa, K., Noda, T., Muraoka, H., Adachi, M., Matsunaga, I., & Ehara, S. (2010). Long-Term Prospects of Geothermal Energy Uses and Their Environmental Effects in Japan, (Apr), 1–4.

Zaher, M. A. (2011). *Geothermal Exploration and Numerical Modeling at Gulf of Suez, Egypt*. Kyushu University, Earth Resources Engineering Department. Degree of Doctor of Engineering.

Zaher, M. A., Saibi, H., Mansour, K., Khalil, A., & Soliman, M. (2018). Geothermal exploration using airborne gravity and magnetic data at Siwa Oasis, Western Desert, Egypt. *Renewable and Sustainable Energy Reviews*, *82*, 3824–3832. https://doi.org/10.1016/J.RSER.2017.10.088

Zaher, M. A., Saibi, H., Nishijima, J., Fujimitsu, Y., Mesbah, H., & Ehara, S. (2012). Exploration and assessment of the geothermal resources in the Hammam Faraun hot spring, Sinai Peninsula, Egypt. *Journal of Asian Earth Sciences*, *45*, 256–267. https://doi.org/10.1016/j.jseaes.2011.11.007

Zaher, M. A., Saibi, H., Nouby, M. El, Ghamry, E., & Ehara, S. (2011). A preliminary regional geothermal assessment of the Gulf of Suez, Egypt. *Journal of African Earth Sciences*, *60*(3), 117–132. https://doi.org/10.1016/J.JAFREARSCI.2011.02.006

Zakir, F. A., Qari, M. H. T., & Mostafa, M. E. (1999). Technical note A new optimizing technique for preparing lineament density maps. *International Journal of Remote Sensing*, *20*(6), 1073–1085. https://doi.org/10.1080/014311699212858

Zarrouk, S. J., & Moon, H. (2014). Efficiency of geothermal power plants: A worldwide review. *Geothermics, Department of Engineering Science, University of Auckland, New Zealand*, *51*(November 2012), 142–153. https://doi.org/10.1016/j.geothermics.2013.11.001